ulm university universität
uulm

Channel-SLAM: Multipath Assisted Positioning

DISSERTATION

zur Erlangung des akademischen Grads eines

DOKTOR-INGENIEURS

(Dr.-Ing.)

der Fakultät für Ingenieurwissenschaften,
Informatik und Psychologie der Universität Ulm

von

Christian Gentner
aus Aalen

Betreuer:	Prof. Dr.-Ing. Uwe-Carsten Fiebig
	Prof. Dr.-Ing. Martin Bossert
Amtierender Dekan:	Prof. Dr. rer. nat. Frank Kargl

Ulm, 12. Juli 2018

Abstract

In wireless propagation transmitted signals are reflected, scattered and diffracted by objects. Especially in urban canyons or inside buildings, the signal reaching the receiving antenna consists of multiple replicas of the transmitted signal, which are called multipath components. The positioning accuracy might be drastically reduced due to the distorted received signal by multipath components. Hence, positioning algorithms need to mitigate the impact of multipath components on the received signal to obtain an accurate position estimate.

With this thesis, we propose a paradigm shift in how to process the received signal in order to provide accurate position estimation for mobile receivers: rather than mitigating multipath components we propose an algorithm to exploit multipath. We call this algorithm Channel-SLAM. The basic idea of Channel-SLAM is to interpret multipath components as signals emitted from so called virtual transmitters. These virtual transmitters are inherently time synchronized to the physical transmitter and static in their positions. In this thesis, we show that the presence of multipath components allows positioning even if signals of only one physical transmitter are receivable. The concept of virtual transmitters considers multipath propagation occurring due to multiple number of reflections, diffractions or scattering as well as the combination of these effects. Specifically, we derive a generic signal model to describe virtual transmitters, where a distinct model detection for reflection, diffraction or scattering is not necessary.

To use the information of the multipath components, Channel-SLAM estimates the position of the virtual transmitters without the necessity of any prior information such as a room-layout. The novelty of the algorithm is to estimate the position of the receiver and the virtual transmitters simultaneously, which can be interpreted as simultaneous localization and mapping (SLAM) with radio signals. Instead of mapping the physical environment, Channel-SLAM maps the virtual transmitter positions and interprets them as landmarks. To ease the computational complexity, a hierarchical particle filter based on Rao-Blackwellization is derived that estimates the position of each virtual transmitter using a separated particle filter. The derived hierarchical particle filter

allows to use a different amount of particles in each particle filter associated to a virtual transmitter. Additionally, we show that the number of particles can by dynamically adapted during runtime which enables a significant performance gain.

In order to quantitatively analyze the performance and location accuracy of Channel-SLAM, the posterior Cramér-Rao lower bound for Channel-SLAM is derived. Based on simulations, the position accuracy of Channel-SLAM is compared to the posterior Cramér-Rao lower bound. Especially for higher signal to noise ratios and beneficial geometric relations, the performances of the position estimations of the virtual transmitters using Channel-SLAM are close to the posterior Cramér-Rao lower bound.

We verify the performance of Channel-SLAM using broadband signals in different scenarios. With our experiments we show that Channel-SLAM is able to accurately estimate the mobile receiver position by exploiting multipath propagation even without the prior information on the physical transmitter position. Furthermore, we confirm that Channel-SLAM is able to determine virtual transmitter positions accurately.

Contents

Chapter 1

Introduction

1.1 Positioning in Challenging Environments

With the proliferation of smartphones, the expectation on the position accuracy is increasing [SGLSJBLR12]. Today, most smartphones are equipped with global navigation satellite systems (GNSSs) receivers which allow to use applications on the smartphones for navigation [BVD16] and provide sufficient position accuracies for mass market application in open sky conditions. GNSSs consist of synchronized satellites where each satellite transmits a periodic unique radio signal. By measuring the arrival times, called time of arrivals (TOAs), the distance between the satellites at known locations and the receiver can be estimated. The position of the receiver can be obtained by trilateration from the estimated distances to a minimum number of four satellites. With GNSSs accurate position estimates can be obtained in line-of-sight (LoS) conditions. The LoS propagation path is the direct path between the physical transmitter and the receiver. However, indoors or in urban canyons the GNSS positioning accuracy might be drastically reduced. In these situations, the received GNSS signals might be blocked, degraded by multipath effects or received with low power. To enhance the positioning performance indoors, different methods and sensor systems can provide position information rather than relying on GNSSs [LDBL07, GLN09, NK11, Har13, MPS14, DCD15]. Most of the indoor positioning systems use local infrastructure like positioning with radio frequency identification (RFID) [Li211], mobile communication base-stations [STK05,Zha02], wireless local area networks (WLANs) [KK04b] or ultra-wideband (UWB) [WS02, MCC+06, SW10b]. Especially, using WLAN for indoor positioning is a common approach because WLAN infrastructure is widely deployed [LHC13, BP00]. However, also these wireless radio technologies experience multipath and non-line-of-sight (NLoS) propagation. In

NLoS situations the direct path is shadowed or blocked. Thus, the transmitted signal travels not directly from the physical transmitter to the receiver, it is reflected, diffracted or scattered before arriving at the receiver. The traveled distance of the first detectable path has a delay offset to the geometrical line-of-sight (GLoS) path. Therefore, most of the indoor positioning methods using WLAN are not based on distance estimation. Instead fingerprinting approaches are very common which measure the received signal strengths (RSSs) of signals coming from nearby WLAN transmitters [LDBL07,KK04a,KK04b]. Fingerprinting approaches consist typically of a training phase and a positioning phase: In the training phase, RSSs measurements are recorded and stored at defined locations together with the measurement location in order to generate a RSSs map of the environment. During positioning phase, the position of the receiver can be estimated by correlating the measured RSS with the preconstructed map. The coordinates corresponding to the closest RSS match are returned as an estimate for the receiver position. The main drawback of the fingerprinting approach is that generation and maintenance of the RSSs maps is time-consuming and expensive when performed over wide areas.

1.2 Mitigating Multipath Propagation

Multipath propagation of signals is particularly problematic for the delay estimation [Mau12, SW10a, SWW10, SW08]. When multipath propagation occurs, the transmitted signal arrives at the receiver via multiple propagation paths. These propagation paths with different delays are caused by reflections, diffractions and scattering of the radio signal. Hence, the signal at the receiving antenna consists of multiple replicas of the transmitted signal, which are called multipath components (MPCs). The delay estimation problem arises when MPCs degrade the ability to determine the delay of the LoS path. If the differences in propagation time between MPCs are less than the reciprocal of the transmission bandwidth, the MPCs are observed as the envelope of their sum [Mau12, SW10a, SWW10, SW08]. Standard distance estimation methods cannot resolve multipath propagation and are biased in multipath propagation environments [PS96, Mau12, SW10a, SWW10, SW08]. In order to mitigate the influence of multipath propagation on the distance estimate, algorithms like [TFvDN95, ANU08, FTH$^+$99, KRW10, CFPFR09] estimate the channel impulse response (CIR). Prominent classes of algorithms are based on maximum likelihood [TFvDN95, ANU08, FTH$^+$99] or on recursive Bayesian filters [KRW10, CFPFR09].

To retrieve the distance between the physical transmitter and the receiver, the propagation path with the smallest delay of the CIR is treated as the LoS path. Even

these advanced multipath mitigation algorithms reduce the multipath effects only to a certain degree due to limited signal bandwidth and measurement noise [KRW10]. Additionally, treating the smallest delay as the LoS path may result in weak positioning performance in NLoS situations.

1.3 Exploiting Multipath Propagation

This thesis proposes a paradigm shift in how to process the received signal in order to provide accurate position estimation for mobile receivers: rather than mitigating multipath we propose to exploit multipath. Analog to this thesis, multipath exploitation instead of mitigation is attracting more and more interest. The authors of [DT09] show that the surrounding environment can be estimated using multipath propagation with a non-static UWB radar. By extracting information on different features like walls, edges and corners from the measured CIRs, the surrounding environment is reconstructed. This idea was extended in [DT10], where these features are used as landmarks to navigate with a simultaneous localization and mapping (SLAM) approach [SC86,SSC86,LDw91,DB06,BD06]. Similarly, [LTDU11] describes a SLAM approach to estimate the room dimensions as well as the receiver position based on UWB by using single time reflected MPCs. Additionally, acoustic multipath components, hence, echoes coming from an acoustic source and received by multiple microphones can be used to estimate the room geometry [Plu13, DPW$^+$13]. Furthermore, [KDV16] use a single microphone located on a moving robot and acoustic echoes from an acoustic source to estimate jointly the robot's trajectory and the geometry of the room.

Besides estimating the room geometry, the authors of [TSRF06, KWC13] exploit multipath propagation for positioning of mobile terminals with multipath fingerprinting algorithms. The multipath fingerprinting algorithms rely on memorized CIRs, which are measured and memorized for all possible receiver locations together with the known coordinates of each CIR in an aforementioned training phase. During the positioning phase, the multipath fingerprinting algorithms compare an estimated CIR to the memorized CIRs, where the coordinates corresponding to the closest CIR match are returned as an estimate for the receiver position.

Other multipath assisted positioning algorithms, like [SW09, FLMW13, LMLW15, MWK14, WM12] use reflected MPCs as signals emitted from virtual transmitters (VTs). Fig. 1.1 summarizes the idea of [SW09, FLMW13, LMLW15, MWK14, WM12] with receiver 1 and receiver 2. The transmitted signal from the physical transmitter is reflected on a reflecting surface, i.e. a wall, and reaches the receiver 1 and receiver 2. As shown in Fig. 1.1, these reflected MPCs can be considered as direct paths from

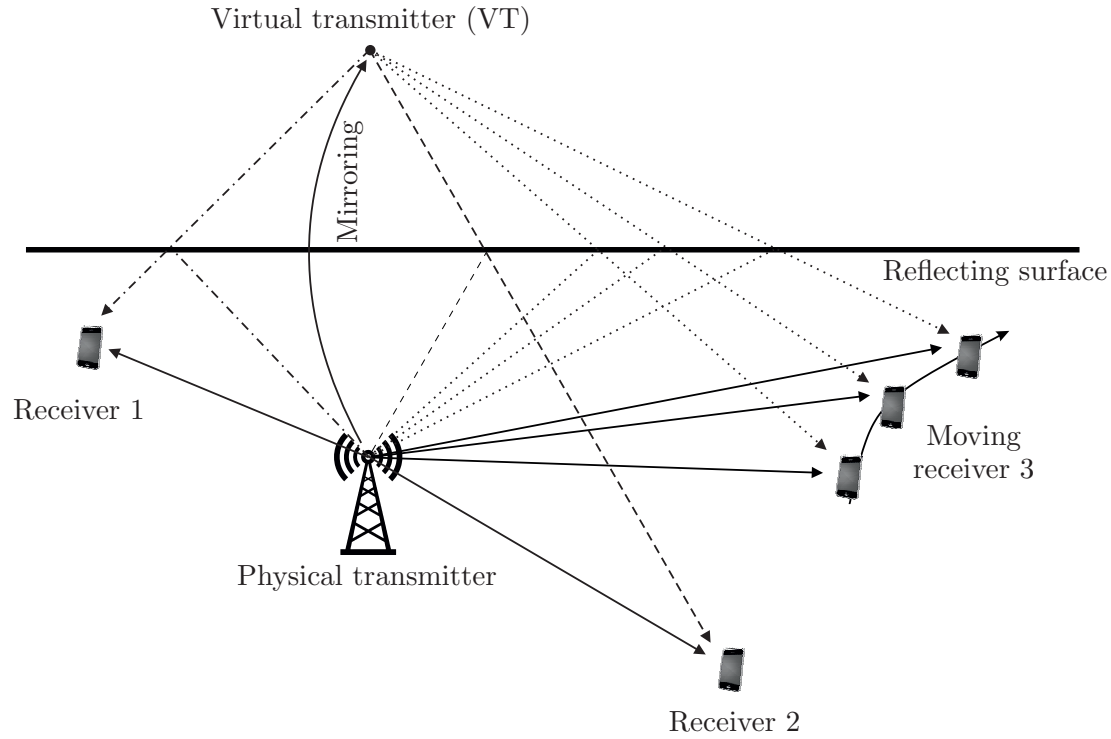

Figure 1.1. *Multipath component which are reflected on a wall can be considered as direct paths from a virtual transmitter. The position of the virtual transmitter can be obtained by mirroring the physical transmitter position at the wall.*

a VT. The position of the VT can be obtained by mirroring the position of the physical transmitter at the wall. Hence, in order to use the reflected MPCs for locating the receiver, the knowledge of the positions of walls and of the physical transmitter is required to precalculate the VT positions.

1.4 Aim of this Thesis

State-of-the-art multipath assisted positioning algorithms require fingerprinting databases or prior information on the building layout and physical transmitter positions in order to calculate VT positions. Hence, not only an accurate knowledge of the physical transmitter positions and building layout are necessary; the building layout must be stationary during positioning phase and doors, windows or furniture must not be moved. Furthermore, algorithms like [SW09, FLMW13, LMLW15, KAT13, MWK14, WM12, DT09, DT10, LTDU11] use only reflected multipath signals for positioning whereas scattered and diffracted MPCs are not considered for positioning.

The aim of the thesis is to propose a novel multipath assisted positioning algorithm referred to as Channel-SLAM. Channel-SLAM considers a moving receiver and is suitable for GNSS denied areas like indoor environments. Similarly to other multipath

assisted positioning approaches, Channel-SLAM interprets MPCs as LoS signals emitted from VTs. Fig. 1.1 shows an example of Channel-SLAM, where receiver 3 receives during its movement two MPCs for each time step: a LoS signal and a signal which is reflected on a wall. When the receiver is moving, the reflection point is moving on the surface as well. However, we can interpret the reflected signal as being emitted from a VT which position is constant for the whole receiver movement. Inherently, the VT is time synchronized to the physical transmitter.

Compared to state-of-the-art multipath assisted positioning algorithms, Channel-SLAM has the following advantages:

- In addition to the reflected signals as shown in Fig. 1.1, Channel-SLAM considers also paths occurring due to multiple number of reflections, diffractions or scattering as well as the combination of these effects. We derive a generic model to describe each MPC as a LoS path being emitted from a VT with unknown but fixed position where a distinct model detection for reflection, diffraction or scattering is not necessary. These VTs are inherently time synchronized to the physical transmitter and static in their positions. Thus, each received MPC increases the number of transmitters which may result in a more accurate position estimate or may enable positioning when the number of physical transmitters is insufficient. As a consequence, the presence of several MPCs allows position estimation even if signals of only one physical transmitter are receivable. Interpreting all MPCs as signals originated from VTs, Channel-SLAM enables positioning also in situations where the position of the physical transmitter is unknown.

- Channel-SLAM does not require any prior information on the building layout and can operate with only one single fixed physical transmitter. To use the information of the MPCs, Channel-SLAM is based on recursive Bayesian filtering and estimates the receiver position, velocity, clock bias and the VT positions simultaneously. This simultaneous estimation can be interpreted as SLAM with radio signals, see [SC86, LDw91, DB06, LKK+11]. Usually, SLAM approaches estimate the user position and build a map of the environment simultaneously. Instead of mapping the environment, Channel-SLAM maps the VT positions and interprets them as landmarks. As a consequence, Channel-SLAM is not affected by changes in the environment.

- Channel-SLAM does not rely on UWB signals. UWB signals have the advantage to provide an accurate CIR estimation due to the fine delay resolution. However, UWB signals have to be of low power to be harmless to other systems which limits the coverage distance. Instead, Channel-SLAM considers wideband

signals which can be used to cover larger distances. Estimating the CIR is though more challenging with wideband signals than with UWB signals, but works well as elaborated in this work.

In order to use Channel-SLAM we propose a two level approach in this thesis: On the first level, the multipath parameters for each MPC are estimated based on the received wireless signal where we assume that the physical transmitter emits continuously known wideband signals. For consistency between different time instances, the multipath parameter estimation algorithm needs to include a path association such that distinct propagation paths are individually tracked over sequential time instances. We use the algorithm called Kalman enhanced super resolution tracking (KEST), for the estimation and tracking of MPCs [JWFP12]. On the second level, we propose two different implementations of Channel-SLAM: The first implementation of Channel-SLAM assumes that the receiver is equipped with a linear antenna array aligned in moving direction [GJW$^+$16]. Hence, additional to the estimated delays, Channel-SLAM uses angle of arrival (AoA) measurements to improve the positioning accuracy. Because of ambiguities in the estimation of the VT positions, the physical transmitter position and an initial prior information on the receiver position and moving direction to define the coordinate system are mandatory. The second implementation of Channel-SLAM uses only a single receiving antenna [GPU$^+$17b]. To resolve the ambiguities, the second implementation of Channel-SLAM fuses additional information coming from an inertial measurement unit (IMU) to obtain heading information of the moving receiver. The heading information of the IMU allows to improve the performance of Channel-SLAM by resolving ambiguities. Thus, Channel-SLAM requires only the initial prior information on the receiver position and moving direction to define the coordinate system.

1.5 Structure of this Thesis and Major Contributions

This thesis comprises six chapters. Chapter 2.1 provides technical background on multipath propagation, multipath parameter estimation algorithms and the principles of positioning.

Chapter 3 gives an overview of the state-of-the-art of recursive Bayesian filtering. First, we present as an optimal Bayesian filters the Kalman filter (KF), thereafter we introduce as suboptimal Bayesian filters the extended Kalman filter (EKF) and

particle filters (PFs) in linear domain and logarithmic domain [GZJ18]. The last part of Chapter 3 describes briefly the SLAM approach based on recursive Bayesian filtering.

In Chapter 4, the Channel-SLAM algorithm is proposed and explained in all its details. First, we address the signal model to describe each MPC as a signal emitted from a VT. Then, we describe the Channel-SLAM algorithm based on recursive Bayesian filtering by a Rao-Blackwellized particle filter (RBPF). The contents of this chapter have appeared in [GJ13, GJW+16, GPU+17b, GZJ18].

In Chapter 5, we quantitatively analyze the performance and location accuracy of Channel-SLAM by deriving the posterior Cramér-Rao lower bound (PCRLB). We evaluate and compare the position precision of Channel-SLAM to the derived PCRLB based on simulations. The contents of this chapter have appeared in [GJW+16].

In Chapter 6 the performance of Channel-SLAM is evaluated by three measurement campaigns using a channel sounder. The first measurement campaign considers a short track in an indoor scenario where the receiver is mounted on a model train and equipped with a linear antenna array. The second measurement campaign considers a moving pedestrian, carrying a single receiving antenna and an IMU. To show that Channel-SLAM is able to estimate the VT position as well as the pedestrian position accurately, we conducted the second measurement campaign in front of a hangar with metallic doors which act as a reflecting surface for the radio signal. The third measurement campaign considers a pedestrian moving inside a building. The moving pedestrian carries equivalently to the second measurement campaign a single receiving antenna and an IMU. The contents of this chapter have appeared in [GJW+16, GPU+17b].

Finally, Chapter 7 concludes this work and discusses possible directions for future research.

Chapter 2

Multipath Propagation and Position Estimation

In the first part of this chapter we provide a survey of propagation mechanisms and the different propagation effects of the wireless channel. Furthermore, we describe the effect of band-limited signals in multipath propagation channels and the estimation of the MPC. In the second part we describe distance estimation error sources and their effect on the position estimation.

2.1 Multipath Propagation and Estimation

2.1.1 Multipath Propagation

The signal transferred through a wireless channel is altered by additive noise, interference, signal attenuation and multipath propagation. Multipath propagation is experienced when the transmitted signal arrives at the receiver via several propagation paths. Hence, the signal at the receiving antenna consists of a superposition of multiple versions of the transmitted signal, which are called MPCs. In acoustics or in optics, MPCs are often referred to echoes or rays. The MPC with the smallest possible propagation delay, the direct path is referred to the LoS path. The LoS path represents the connection line between the physical transmitter and the receiver and has an absolute propagation delay proportional to the geometrical distance divided by the speed of light. For notational conveniences, the LoS propagation path is considered also as a MPC in this thesis. All other propagation paths have longer delays than the LoS path and are caused by reflections, diffractions and scattering of the impinging radio signal. These propagation paths experience differences in attenuation, delay and phase shift while traveling from the physical transmitter to the receiver.

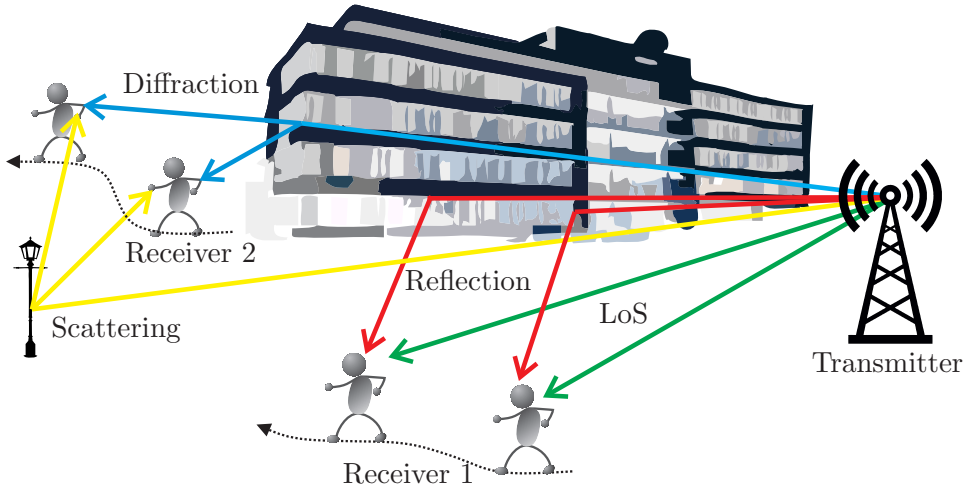

Figure 2.1. *Typical multipath scenario with a physical transmitter and two different receiver positions. The different physical propagation effects are shown by the different colors.*

Fig. 2.1 illustrates a multipath scenario with a physical transmitter and two receivers, where the different physical propagation effects are shown by different colors. Receiver 1 receives two MPCs, the LoS path indicated in green and a MPC which is reflected at the front of the building indicated in red. Reflections occur on smooth surfaces where the strength of the reflected signal depends on the reflection coefficient, which in turn depends on the electric properties of the surface [Par00]. Fig. 2.1 depicts by receiver 2 a NLoS situation where the direct path is blocked by the building. Even though the direct path, i.e. the LoS path, is blocked, receiver 2 receives a signal: it is the signal (indicated by the blue line) which is diffracted on the edge of the building and a signal (indicated by the yellow line) which is scattered at the lamp post. Diffraction describes the bending of waves around edges. The propagation effect of scattering occurs if a radio signal impinges an object, i.e. a lamp post, where the impinging energy of the incoming wave is reflected in all directions [Rap96, BS87]. Geometrically, scattering can be described as a fixed point, i.e. the lamp post, in the pathway of the MPC.

As indicated by the moving receivers in Fig. 2.1, the received signal has geometrical dependencies on the physical transmitter, the receiver positions and the environment. In case of short motion of the physical transmitter, receiver or objects that interact with the emitted signal the multipath propagation parameters are highly correlated. This is indicated in Fig. 2.1, where the MPCs are received for both receiver positions of the moving receiver 1 and receiver 2.

Mathematically, the behavior of the multipath channel can be described by the time variant CIR $h(t_k, \tau)$ where t_k indicates the discrete time step, and τ is the delay

of the MPC [Bel63]. According to [Bel63], the CIR $h(t_k, \tau)$ can be assumed to be constant for a short time interval T at time t_k and time index k, with

$$h(t_k, \tau) = \sum_{i=0}^{N(t_k)-1} \alpha_i(t_k)\, \delta\left(\tau - \tau_i(t_k)\right) , \tag{2.1}$$

for $T_0 \leq t_k \leq T_0 + T$, where $N(t_k)$ is the number of MPCs, $\tau_i(t_k)$ is the delay, $\alpha_i(t_k)$ the complex amplitude of the i-th MPC, and $\delta(\cdot)$ stands for the Dirac distribution [Tur72]. Generally, the CIR is a summation of an infinitive number of MPCs, however, a practical receiver is only capable of capturing signals whose powers are above a certain sensitivity level, thus, $N(t_k)$ MPCs. Considering a transmitted signal $s(t_k)$ with a length smaller than T, the received noiseless signal $y(t_k)$ is the convolution of the transmitted signal $s(t_k)$ and the CIR $h(t_k, \tau)$, hence,

$$\begin{aligned} y(t_k) &= s(t_k) * h(t_k, \tau) && (2.2)\\ &= \int_{-\infty}^{\infty} h(t_k, \tau)\; s(t_k - \tau)\, \mathrm{d}\tau && (2.3)\\ &= \sum_{i=0}^{N(t_k)-1} \alpha_i(t_k)\; s(t_k - \tau_i(t_k)) \; . && (2.4) \end{aligned}$$

The time variant CIR $h(t_k, \tau)$ of (2.1) is the most popular way to describe the channel. As shown in Fig. 2.2, the channel can also be described by:

- The time variant channel transfer function $H_h(t_k, f)$ which describes the time-variant fading effects of the multipath components of the channel in the frequency domain.

- The Doppler variant CIR $S(\nu_k, \tau)$ which describes the dispersion in delay and Doppler frequency of the channel.

- The Doppler variant channel transfer function $D(\nu_k, f)$ which describes the double Fourier transform of the time-variant weight function, where the time-variance is shown in both frequency domains.

These functions completely describe the behavior of the channel in time and/or frequency domain. As indicated in Fig. 2.2, these functions can be derived from each other by the Fourier transform $\mathscr{F}\{\cdot\}$ [Bel63], where $\mathscr{F}_{t_k}\{\cdot\}$ is the discrete-time Fourier transform with respect to t_k and $\mathscr{F}_f^{-1}\{\cdot\}$ denotes the inverse discrete-time Fourier transform with respect to f.

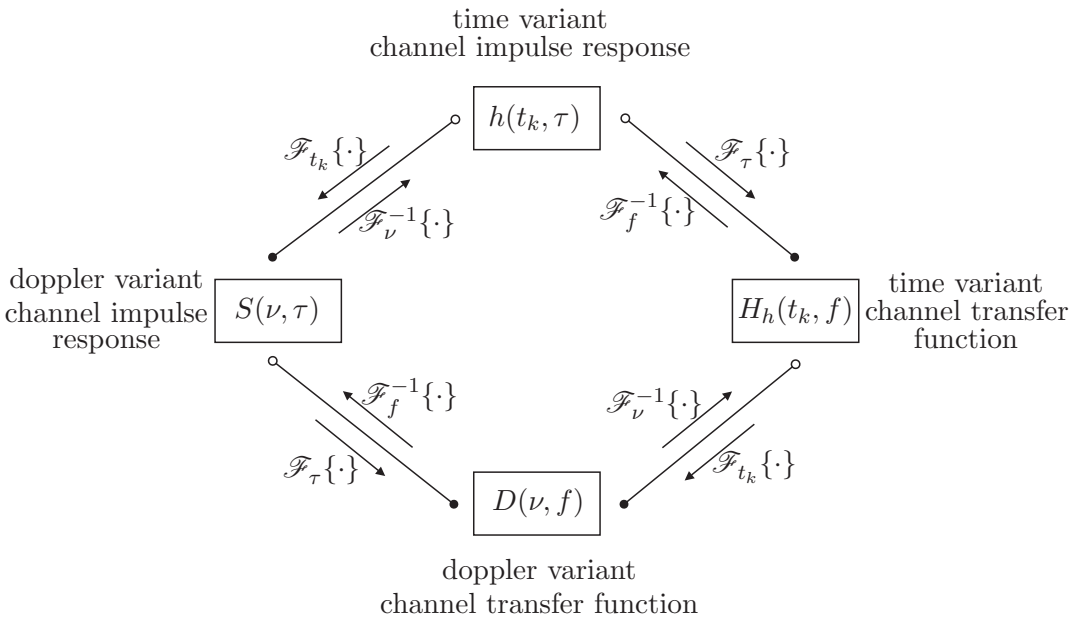

Figure 2.2. *Pairwise relations by the Fourier transform of the channel functions.*

2.1.2 Bandlimited Received Signal

In the following, we assume that the transmitted signal $s(t_k)$ is band-limited with bandwidth B and time-limited with a length smaller than T. Additionally, we consider a receiver equipped with a linear antenna array. Using multiple antennas at the receiver, the angle between the received MPC and a given coordinate axis can be determined which is called AoA. Thus, the signal received by the l-th antenna at time t_k sampled with rate B, bin indices $m = 0, \ldots, M-1$ and the delay $\tau_m = \frac{m}{B}$ can be written as

$$y_l(t_k, \tau_m) = \sum_{i=0}^{N(t_k)-1} \alpha_i(t_k)\, a_l(\theta_i(t_k))\, s(\tau_m - \tau_{i,l}(t_k)) + n(\tau_m) \tag{2.5}$$

$$= \tilde{y}_l(t_k, \tau_m) + n(\tau_m)\,, \tag{2.6}$$

for $T_0 \leq t_k \leq T_0 + T$, where $a_l(\theta_i(t_k))$ denotes the response of the l-th receiving antenna with respect to the phase center, $\theta_i(t_k)$ the AoA, $\tilde{y}_l(t_k, \tau_m)$ is the sum of all paths' contributions and $n(\tau_m)$ denotes the white circular symmetric normal distributed receiver noise with variance σ_n^2. The expression given in (2.5) considers a linear antenna array only, which can be extended to other types of antenna arrays able to measure the two dimensional AoA separately. For the later derivations and evaluations in Chapter 5, we write the sampled received signal of (2.5) in matrix notation, as

$$\boldsymbol{Y}(t_k) = \begin{bmatrix} y_1(t_k, \tau_0) & \cdots & y_1(t_k, \tau_m) & \cdots & y_1(t_k, \tau_{M-1}) \\ \vdots & \ddots & \vdots & \ddots & \vdots \\ y_L(t_k, \tau_0) & \cdots & y_L(t_k, \tau_m) & \cdots & y_L(t_k, \tau_{M-1}) \end{bmatrix} \tag{2.7}$$

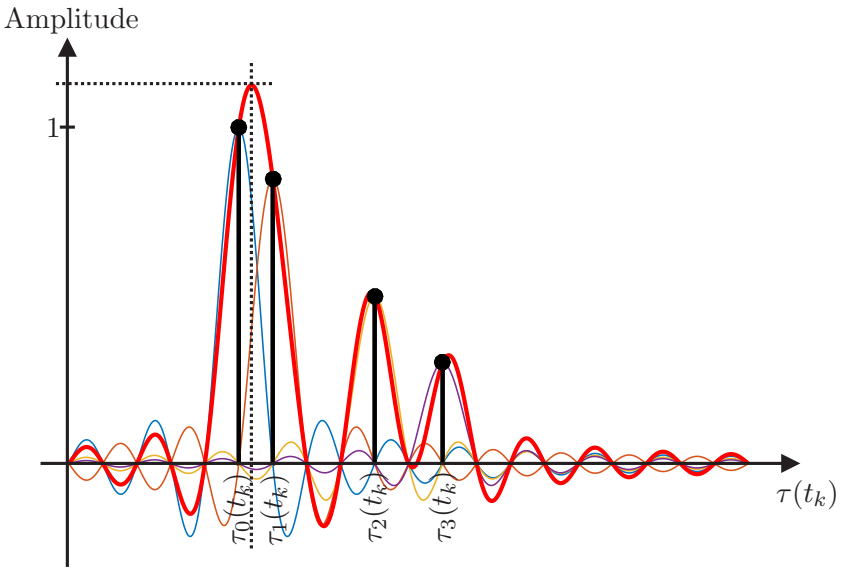

Figure 2.3. *Illustration of the effect of band-limitation. The transmitted signal* $s(t_k) = sinc\,(t_k B) = \frac{\sin(\pi t_k B)}{\pi t_k B}$ *is a band-limited signal with bandwidth* B *and transmitted trough a multipath channel with 4 MPCs indicated in black. The received signal is the superposition, hence, convolution of the transmitted signal with the CIR indicated in red.*

and similarly the sum of all paths' contribution for all antennas $l = 1, \ldots, L$, as

$$\tilde{\mathbf{Y}}(t_k) = \begin{bmatrix} \tilde{y}_1(t_k, \tau_0) & \cdots & \tilde{y}_1(t_k, \tau_m) & \cdots & \tilde{y}_1(t_k, \tau_{M-1}) \\ \vdots & \ddots & \vdots & \ddots & \vdots \\ \tilde{y}_L(t_k, \tau_0) & \cdots & \tilde{y}_L(t_k, \tau_m) & \cdots & \tilde{y}_L(t_k, \tau_{M-1}) \end{bmatrix}. \tag{2.8}$$

The CIR of (2.1) is represented as the sum of delayed and weighted Dirac distributions, each representing an individual MPC, with a sparse structure [Shu06]. However, this sparse structure of the received measured signal $\boldsymbol{Y}(t_k)$ is degraded by additive noise and band-limitation of the physical transmitter and receiver hardware [Shu06]. Fig. 2.3 illustrates by an example the effect of band-limitation. The ideal CIR of (2.1) is shown in black with four MPCs and normalized real valued amplitudes, where the first MPC has a delay of $\tau_0(t_k)$, the second $\tau_1(t_k) = \tau_0(t_k) + 1/B$, the third $\tau_2(t_k) = \tau_0(t_k) + 4/B$ and the fourth $\tau_3(t_k) = \tau_0(t_k) + 6/B$ at time t_k. We assume that the physical transmitter emits a band-limited signal with rectangular power spectral density (PSD) which corresponds to the time domain signal $s(t_k) = \text{sinc}\,(t_k B) = \frac{\sin(\pi t_k B)}{\pi t_k B}$ with bandwidth B. The signal arriving at $\tau_0(t_k)$ corresponds to the LoS propagation path and the distance estimate $d(t_k)$ between the physical transmitter and the receiver can be directly

obtained by $d(t_k) = \tau_0(t_k) \cdot c$, where c denotes the speed of light. As indicated by the red curve in Fig. 2.3, the received signal is a superposition of multiple versions of the transmitted signal. Especially, the maximum amplitude of the received signal is shifted to the right caused by the closely spaced first and second MPC. As visualized by the dashed lines, algorithms which detect the maximum peak as the LoS path might be biased in multipath propagation environments [PS96].

2.1.3 Multipath Propagation Estimation

In order to obtain the sparse structure of the CIR from the measurements, multipath estimation algorithms are necessary [KV96]. We can distinguish between static and dynamic multipath estimation algorithms. These algorithms fit a measured band-limited CIR $h(t_k, \tau)$ at discrete time steps t_k and sampled delay τ, to a given model. Snapshot-based multipath estimation algorithms independently estimate the CIR for each time step t_k. Examples for snapshot-based multipath estimation algorithms are parametric spectral estimators like multiple signal classification (MUSIC) [Sch86], ESPRIT [RK89, HN95] or deterministic parametric estimators like the expectation maximization (EM) [DLR77], RIMAX [Ric] or the space-alternating generalized expectation-maximization (SAGE) [FTH+99] which are based on maximum likelihood (ML). A crucial problem in snapshot-based multipath estimation is the model order detection, i.e., the number of MPCs for each time step which has been investigated in e.g. [SS04, XRK94]. In contrast, dynamic multipath estimation algorithms incorporate the previous time information of a dynamic measurement scenario. As aforementioned, in a dynamic measurement scenario with a moving receiver and/or a moving physical transmitter, propagation paths can be observed for a certain time duration. This time duration depends on the physical transmitter, receiver positions and on the surrounding environment, see e.g. [JWFPF12, WJ12a, Leh05, SRK09]. Algorithms like [RSZ94, KRW10, JWFP12, CFPFR09, SRK09, WJG+16] allow to model the time evolution for each MPC, e.g. [JWFPF12, JWFP12] use a KF, [SRK09] a EKF or [KRW10] a PF to track the MPCs.

In this thesis, we use the dynamic multipath estimation algorithm named KEST [JWFP12, WJD10, Wan15, Jos13] for estimating and tracking MPCs. Fig. 2.4 shows a flow chart of KEST which consists of several SAGE-Kalman filters running in parallel. KEST estimates the MPCs

$$\hat{\boldsymbol{\Phi}}(t_k) = \left[\hat{\boldsymbol{\phi}}_0(t_k), \hat{\boldsymbol{\phi}}_1(t_k), \ldots, \hat{\boldsymbol{\phi}}_{N(t_k)-1}(t_k)\right], \tag{2.9}$$

where the i-th MPC is characterized by its parameters

$$\hat{\boldsymbol{\phi}}_i(t_k) = \left[\hat{\alpha}_i(t_k), \hat{\theta}_i(t_k), \hat{\tau}_i(t_k)\right]^T, \tag{2.10}$$

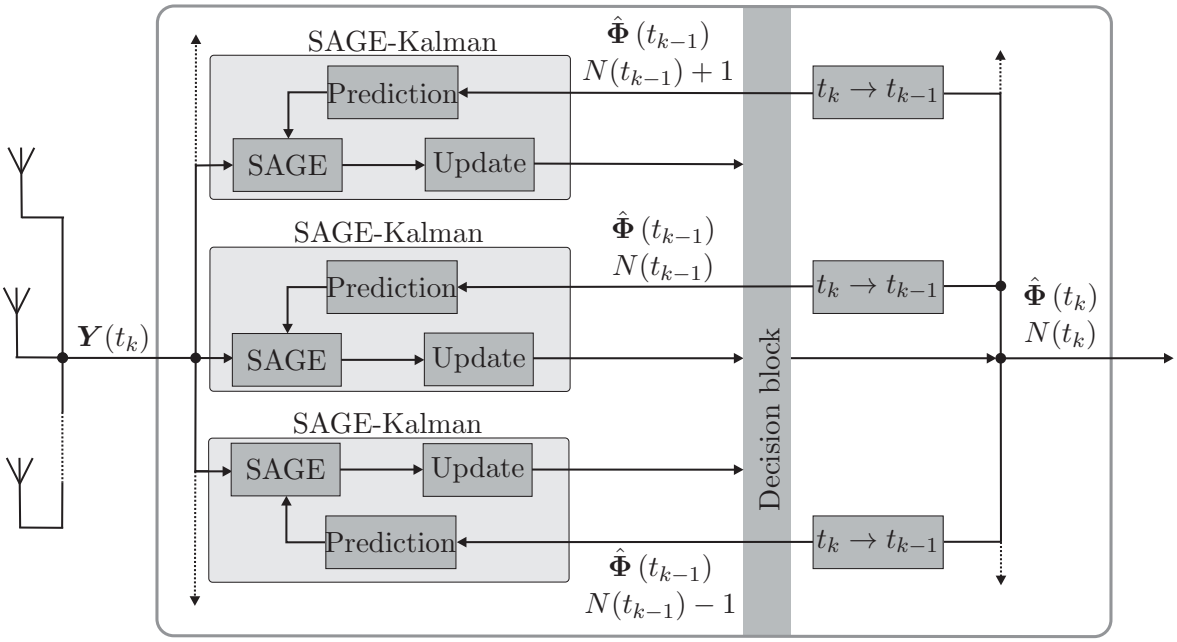

Figure 2.4. *Flow chart of KEST which estimates and tracks the channel parameters* $\hat{\mathbf{\Phi}}(t_k)$ *by several SAGE-Kalman filters running in parallel.*

with the estimated complex amplitude $\hat{\alpha}_i(t_k)$, AoA $\hat{\theta}_i(t_k)$ and delay $\hat{\tau}_i(t_k)$ at time step t_k. Additionally, KEST tracks the parameter changes $\Delta\hat{\mathbf{\Phi}}(t_k)$ of the MPCs, which are for simplicity not shown in Fig. 2.4. Each SAGE-Kalman filter consists of a KF which tracks the MPCs $\hat{\mathbf{\Phi}}(t_k)$ and a SAGE estimator. Please note, KEST can use any ML estimator. KF consists of two steps, a prediction and an update step (see Section 3.2 for a detailed description). In general the number of MPCs $N(t_k)$ is unknown and needs to be detected for each time step t_k. Hence, the KF uses the model order $N(t_{k-1})$ and the MPCs $\hat{\mathbf{\Phi}}(t_{k-1})$ from the last time step t_{k-1} to predict the MPCs of the current time step t_k using a linear system model with additive normal distributed noise. The predicted MPCs are used to initialize the SAGE algorithm. Afterwards, the SAGE estimates are the inputs of the update step of the KF. Because changes in the model order are possible at each time step, KEST runs several SAGE-Kalman filters in parallel and erases and initializes MPCs. After parallel processing of the SAGE-Kalman filters, the decision block decides the model order based on the residuals. For further details about KEST, see [JWFP12, WJD10, Wan15, Jos13].

The authors of [JWFP12, WJD10, Wan15, Jos13] show that KEST is superior compared to the snapshot-based multipath estimation algorithms. Even in critical scenarios where two MPCs are close in state-space, KEST is able to effectively keep on tracking two MPCs. Additionally, KEST allows to smoothly and continuously model the evolution of the CIR which is essential for Channel-SLAM.

2.2 Radio Based Positioning

Positioning describes methods to determine the location of objects and persons. GNSS receivers are well known to deliver very good position estimates under open sky conditions [ME05, PS96, Kap05, HL98]. Also signals from terrestrial radio systems can be used for radio based positioning and might be helpful to augment GNSS [SCGL05, GG05, Gez08]. By measuring the signal travel times from multiple physical transmitters at known locations to the receiver, the receiver position can be obtained. Assuming ideal wave propagation conditions and a receiver clock which is synchronized to the physical transmitter time, the distance between the physical transmitter i at position $\boldsymbol{r}_{t,i}$ and the receiver can be calculated as

$$d_i(t_k) = c \cdot (t_{a,i}(t_k) - t_{t,i}(t_k)) = \|\boldsymbol{r}_{t,i} - \boldsymbol{r}_u(t_k)\| \,, \tag{2.11}$$

where $t_{a,i}(t_k)$ is the arrival time called TOA, $t_{t,i}(t_k)$ is the time step of transmission of physical transmitter i and $\boldsymbol{r}_u(t_k)$ the receiver position. As shown in Fig. 2.5 by the dashed circles, the distances $d_i(t_k)$ defines a circle centered at the physical transmitter position $\boldsymbol{r}_{t,i}$ with radius $d_i(t_k)$. The receiver position can be estimated by trilateration: finding the unique intersection of the circles as indicated by the cross. Similarly, positioning in three dimensions can be interpreted by finding the unique intersection of several spheres.

However, usually the receiver clock is not synchronized to the physical transmitter time. As the physical transmitters are synchronized, the measured travel times at the receiver have a common clock bias $b_u(t_k)$ which has to be estimated in addition to the receiver position. Hence, we obtain from (2.11) the pseudorange $\rho_i(t_k)$, which is the pseudo distance between the physical transmitter i and the receiver, with

$$\rho_i(t_k) = d_i(t_k) + c \cdot b_u(t_k) \,. \tag{2.12}$$

Most positioning algorithms assume that the signals propagate on a direct path, i.e. the LoS path, from the physical transmitters to the receiver. However, in NLoS propagation conditions, the direct path between the physical transmitter is blocked and the signal travels not directly, but is reflected, diffracted or scattered before arriving at the receiver. Thus, the traveled distance of the first detectable path at $\tau_0(t_k)$ introduces a NLoS bias $\epsilon_{n,i}(t_k)$ to the GLoS path at $\tau_G(t_k)$ which is the dominant error source for mobile positioning [CS98] as illustrated in Fig. 2.6a by an example. Additional to NLoS propagation, the direct signal path between the physical transmitter and the receiver may be interfered by multipath which adds a multipath error $\epsilon_{m,i}(t_k)$

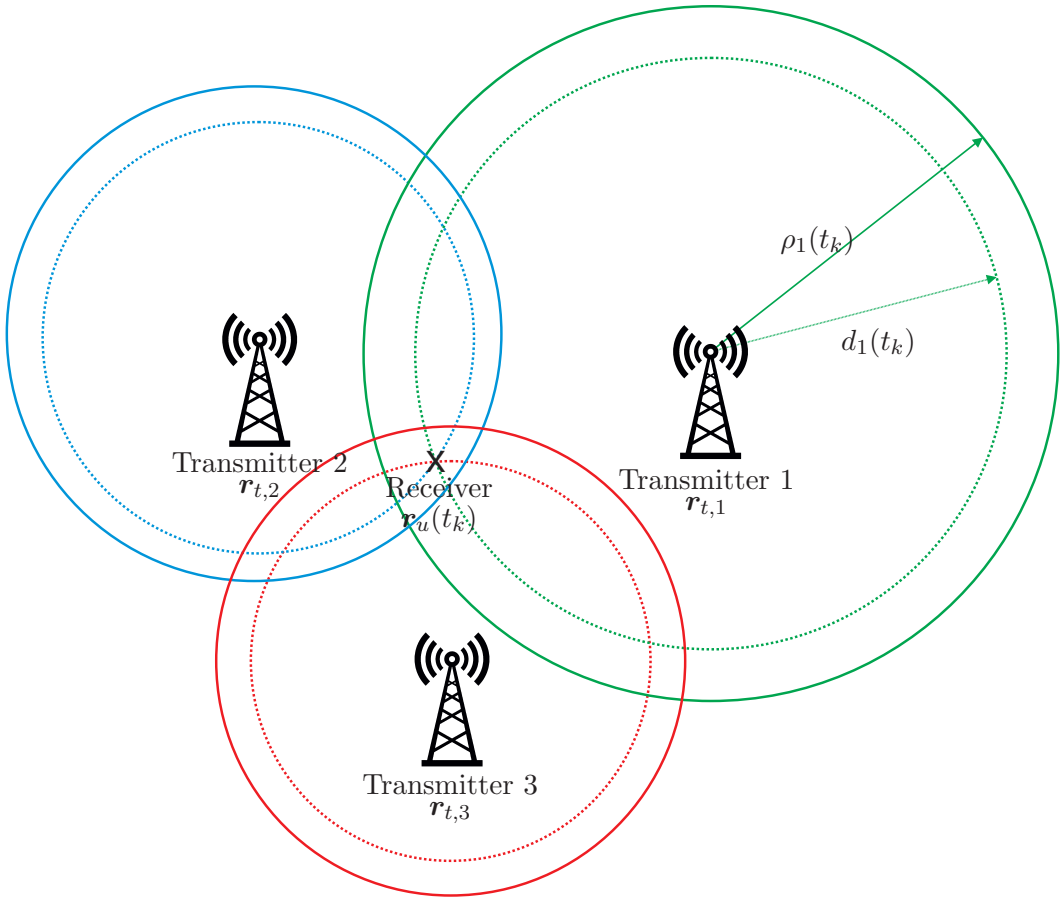

Figure 2.5. *Two dimensional positioning of a receiver at position $\boldsymbol{r}_u(t_k)$ with trilateration using circles. The intersection point of circles, with center at the physical transmitter positions $\boldsymbol{r}_{t,i}$ and radius of the geometrical distance $d_i(t_k)$ between the physical transmitter i and the receiver. However, the measured distance $\rho_i(t_k)$ is different from the true geometrical distance $d_i(t_k)$.*

[PS96]. An example of the multipath error is illustrated in Fig. 2.6b, the maximum amplitude of the received signal is shifted to the right caused by the closely spaced MPCs. Hence, algorithms which detect the maximum peak as the LoS path might be biased in multipath propagation environments [PS96] as visualized by the dashed lines. Furthermore, the pseudorange $\rho_i(t_k)$ is subject to a number of inaccuracies introduced at the physical transmitter and receiver side, which are residual errors $\epsilon_{r,i}(t_k)$ coming from thermal noise and hardware effects. Taking these error sources into account, the pseudorange $\rho_i(t_k)$ is

$$\rho_i(t_k) = d_i(t_k) + c \cdot (b_u(t_k) + \epsilon_{m,i}(t_k) + \epsilon_{n,i}(t_k) + \epsilon_{r,i}(t_k)) \ . \tag{2.13}$$

As indicated in Fig. 2.5, the pseudorange $\rho_i(t_k)$ is different from the true geometrical distance $d_i(t_k)$ and may introduce a positioning error. To deal with these kind of error

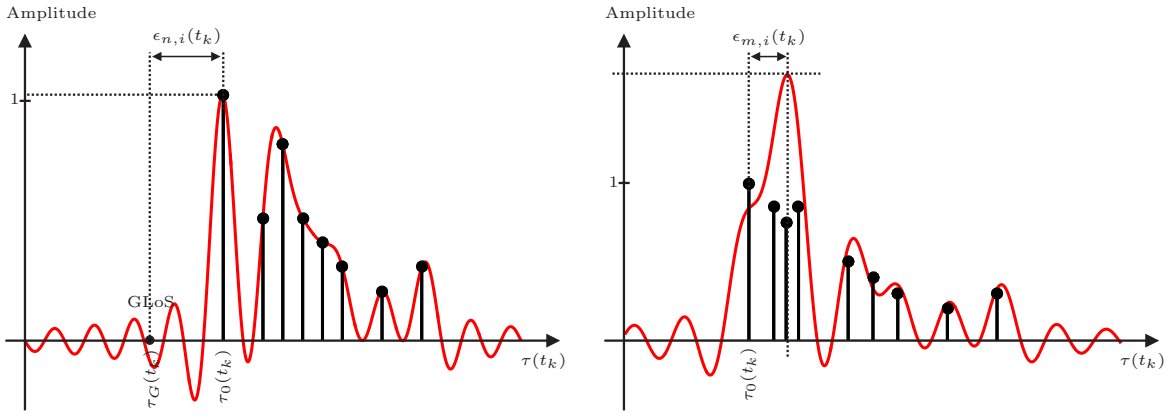

(a) *NLoS propagation conditions introduce a NLoS bias $\epsilon_{n,i}(t_k)$. The propagation time along the GLoS path is defined by $\tau_G(t_k)$; $\tau_0(t_k)$ is the propagation time of the first detectable MPC.*

(b) *Multipath propagation might introduce a multipath error $\epsilon_{m,i}(t_k)$ caused by closely spaced MPCs.*

Figure 2.6. *Illustration of the NLoS bias $\epsilon_{n,i}(t_k)$ and multipath error $\epsilon_{m,i}(t_k)$ for the measured band-limited CIR of the physical transmitter i.*

sources, the errors have to be modeled, see e.g. [WJMD09, GMK+12], and mitigated as mentioned in Section 2.1.3. Please note, the pseudorange defined in (2.13) only includes the errors occurring from transmissions from terrestrial radio systems, GNSS pseudoranges include additional inaccuracies e.g. from the atmosphere or satellite, see [ME05, PS96, Kap05, HL98].

To obtain the receiver position from the pseudorange $\rho_i(t_k)$ different methods with different complexity and restrictions are available, where we can distinguish between snapshot-based and dynamic position estimation algorithms [SZT08, Men13]. Snapshot-based position estimation algorithms use only the parameters available at a specific time step. Several approaches exist to solve the underlying problem which belongs to the class of nonlinear optimization problems. Examples are [CS98] which is based on ML or [CSMC04] which is based on least square (LS). Dynamic position estimation algorithms use information about previous estimates. In dynamic position estimation algorithms, it is assumed that the receiver follows a certain path which can be integrated directly in the estimation problem in terms of transition or movement models. Well-known methods for dynamic position estimation algorithms are based on recursive Bayesian filtering, see Chapter 3, e.g. KF [Kal60], EKF [SSM62, WB95] or PF [AMGC02].

Chapter 3

Recursive Bayesian Filtering

In the first part of this chapter, we introduce the principle of recursive Bayesian filtering. Thereafter, we describe in Section 3.2 the KF, in Section 3.3 the EKF, and in Section 3.4 PFs as examples of recursive Bayesian filters. The last part of this chapter discusses SLAM which is often solved by recursive Bayesian filtering.

3.1 Introduction to Recursive Bayesian Filtering

Dynamic systems can be described by state-space models where the state is only observable by noisy measurements. Hence, the state is estimated using sequentially arriving noisy measurements of the system. Usually, prior knowledge on the system dynamics exists, which can be used to propose or apply restrictions on the state evolution. The optimal approach to use the prior knowledge of the system dynamics and the measurements in the estimation process is recursive Bayesian filtering. Recursive Bayesian filtering refers to the Bayesian way of formulating the estimation of the state of a time-varying system which is indirectly observed through noisy measurements.

Fig. 3.1 illustrates the relation of the states and measurements over adjacent time instants by a dynamic Bayesian network (DBN). The true state at discrete time instant t_k is modeled by a random variable $\mathbf{x}(t_k)$ following a hidden Markov model (HMM). In a HMM, the state of interest $\mathbf{x}(t_k)$ cannot be observed directly and is estimated from the measurements $\mathbf{z}(t_k)$. In our application we assume a first-order HMM, i.e. the state $\mathbf{x}(t_k)$ depends only on the state $\mathbf{x}(t_{k-1})$ and is independent from states $\mathbf{x}(t_{0:k-2})$. As indicated in Fig. 3.1, we can describe the dynamic estimation based on a discrete time formulation by two models:

1. The transition model,

$$\mathbf{x}(t_k) = \mathbf{f}(\mathbf{x}(t_{k-1}), \mathbf{n}_t(t_k)), \tag{3.1}$$

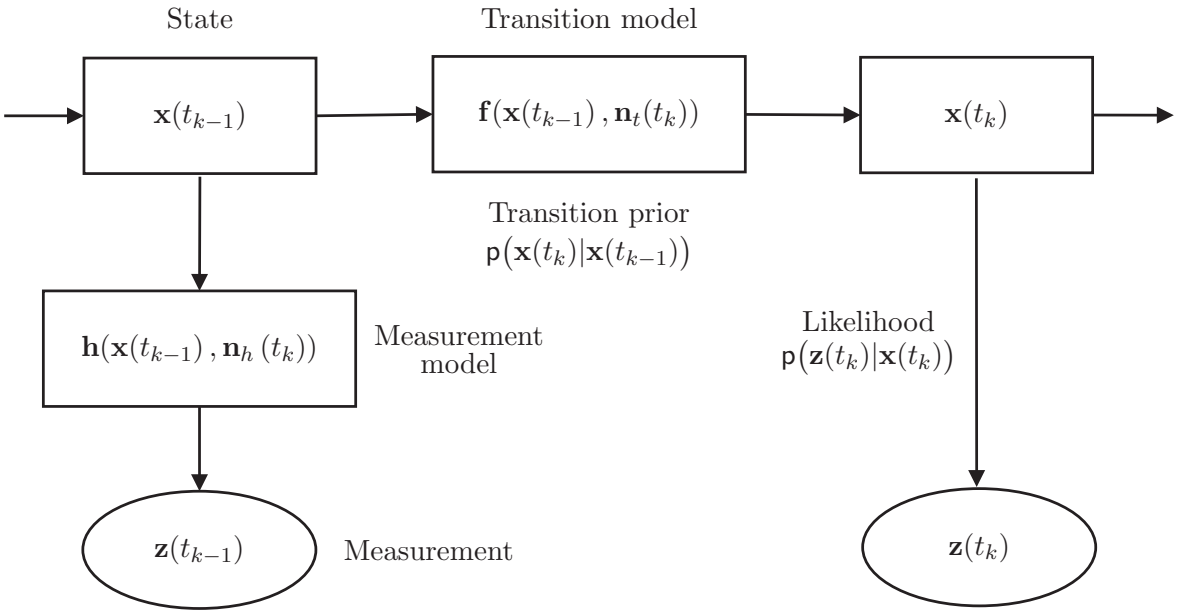

Figure 3.1. *First-order HMM representing the dynamic system with state* $\mathbf{x}(t_k)$ *and meaurements* $\mathbf{z}(t_k)$*. The state is a hidden variable, which cannot be observed directly and is estimated from the measurements* $\mathbf{z}(t_k)$*.*

which describes the state evolution from time instant t_{k-1} to time instant t_k employing a possibly nonlinear function $\mathbf{f}(\cdot,\cdot)$ and process noise $\mathbf{n}_t(t_k)$. We may express the transition model in a probabilistic way as the transition prior $\mathsf{p}\big(\mathbf{x}(t_k)|\mathbf{x}(t_{k-1})\big)$ which is the conditional probability distribution of the state $\mathbf{x}(t_k)$ at time instant t_k given the previous state $\mathbf{x}(t_{k-1})$.

2. The measurement model,

$$\mathbf{z}(t_k) = \mathbf{h}(\mathbf{x}(t_k), \mathbf{n}_h(t_k)), \tag{3.2}$$

which relates the state vector to the measurements at time instant t_k with a possibly nonlinear function $\mathbf{h}(\cdot,\cdot)$ and the measurement noise $\mathbf{n}_h(t_k)$. Similar to the transition model, we may express the measurement model in a probabilistic way with the likelihood $\mathsf{p}\big(\mathbf{z}(t_k)|\mathbf{x}(t_k)\big)$ which is the conditional probability distribution of the measurement $\mathbf{z}(t_k)$ at time instant t_k conditioned the current state $\mathbf{x}(t_k)$.

From a Bayesian perspective, an unknown probability density function (PDF) of the state $\mathbf{x}(t_k)$ is estimated recursively by measurements over time. In order to obtain the PDF of the state $\mathbf{x}(t_k)$, the posterior density $\mathsf{p}\big(\mathbf{x}(t_k)|\mathbf{z}(t_{1:k})\big)$ has to be calculated and might be obtained by two steps, the prediction and the update step. In the prediction

step, the PDF $\mathsf{p}\big(\mathbf{x}(t_k)|\mathbf{z}(t_{1:k-1})\big)$ of the state is calculated based on the prior according to

$$\mathsf{p}\big(\mathbf{x}(t_k)|\mathbf{z}(t_{1:k-1})\big) = \int \mathsf{p}\big(\mathbf{x}(t_k)|\mathbf{x}(t_{k-1})\big)\mathsf{p}\big(\mathbf{x}(t_{k-1})|\mathbf{z}(t_{1:k-1})\big)\mathrm{d}\mathbf{x}(t_{k-1}) \;, \tag{3.3}$$

assuming a first-order HMM with the transition prior $\mathsf{p}\big(\mathbf{x}(t_k)|\mathbf{x}(t_{k-1})\,,\mathbf{z}(t_{1:k-1})\big) = \mathsf{p}\big(\mathbf{x}(t_k)|\mathbf{x}(t_{k-1})\big)$. During the update step, the measurement $\mathbf{z}(t_k)$ is used to correct the prediction based on the measurement model to obtain the required posterior density of the current state, with

$$\mathsf{p}\big(\mathbf{x}(t_k)|\mathbf{z}(t_{1:k})\big) = \frac{\mathsf{p}\big(\mathbf{z}(t_k)|\mathbf{x}(t_k)\big)\mathsf{p}\big(\mathbf{x}(t_k)|\mathbf{z}(t_{1:k-1})\big)}{\mathsf{p}\big(\mathbf{z}(t_k)|\mathbf{z}(t_{1:k-1})\big)}, \tag{3.4}$$

where

$$\mathsf{p}\big(\mathbf{z}(t_k)|\mathbf{z}(t_{1:k-1})\big) = \int \mathsf{p}\big(\mathbf{z}(t_k)|\mathbf{x}(t_k)\big)\mathsf{p}\big(\mathbf{x}(t_k)|\mathbf{z}(t_{1:k-1})\big)\mathrm{d}\mathbf{x}(t_k)\,. \tag{3.5}$$

In many applications, we are interested in a point estimate of the state instead of the posterior density $\mathsf{p}\big(\mathbf{x}(t_k)|\mathbf{z}(t_{1:k})\big)$. To obtain a point estimate, we can determine the maximum a posteriori (MAP) estimate as

$$\hat{\mathbf{x}}_{\mathrm{MAP}}(t_k) = \arg\max_{\mathbf{x}(t_k)} \mathsf{p}\big(\mathbf{x}(t_k)|\mathbf{z}(t_{1:k})\big)\,, \tag{3.6}$$

or the expectation

$$\hat{\mathbf{x}}_{\mathrm{MMSE}}(t_k) = \int \mathbf{x}(t_k)\,\mathsf{p}\big(\mathbf{x}(t_k)|\mathbf{z}(t_{1:k})\big)\,\mathrm{d}\mathbf{x}(t_k) \;. \tag{3.7}$$

which is equivalent to the minimum mean square error (MMSE) estimate. For a symmetric posterior densities, the MAP and MMSE criteria are equivalent.

The prediction and update equations (3.3) and (3.4) may not always be analytically solvable. Solutions are Gaussian filters like KF, EKF which represent the posterior density by a multivariate normal distribution. The KF introduced in Section 3.2 is an optimal Bayesian filter which can be used if the considered system is linear and the probabilistic model is Gaussian. However, most of the real world problems are nonlinear. In such cases we need to resort into sub-optimal Bayesian filters, like the EKF introduced in Section 3.3. Also the EKF behaves poorly when the degree of nonlinearity becomes high. Hence, nonlinear filters like PFs introduced in Section 3.4 approximate the posterior density with a finite number of parameters and are suitable for multivariate data and nonlinear/non-Gaussian processes. Section 3.2, Section 3.3 and Section 3.4 show examples of recursive Bayesian filters. Other recursive Bayesian filters can be found in literature see [Che03, AMGC02, RAG04].

3.2 Kalman Filter

The KF [Kal60] is an optimal implementation of recursive Bayesian filters. It is based on the assumption that the posterior density can be characterized by the mean and the variance of a Gaussian at every time instant. Thus, the KF recursively computes the mean and the covariance of the Gaussian posterior density $\mathsf{p}\big(\mathbf{x}(t_k)|\mathbf{z}(t_{1:k})\big)$ over time instants t_k. Additionally, the transition model of (3.1) is restricted to a linear function with

$$\mathbf{x}(t_k) = \mathbf{F}(t_k)\mathbf{x}(t_{k-1}) + \mathbf{n}_t(t_k)\,, \tag{3.8}$$

where $\mathbf{F}(t_k)$ is a known matrix and $\mathbf{n}_t(t_k)$ is the transition noise drawn from a Gaussian distribution with covariance $\mathbf{Q}(t_k)$. Equivalently, the measurement model of (3.2) is a linear function with

$$\mathbf{z}(t_k) = \mathbf{H}(t_k)\mathbf{x}(t_{k-1}) + \mathbf{n}_h\left(t_k\right)\,, \tag{3.9}$$

where $\mathbf{H}(t_k)$ is a known matrix and $\mathbf{n}_h\left(t_k\right)$ is the measurement noise drawn from a Gaussian distribution with covariance $\mathbf{R}(t_k)$. Using these assumptions, the KF can be derived based on (3.3) and (3.4) with

$$\begin{aligned}
\mathsf{p}\big(\mathbf{x}(t_k)|\mathbf{z}(t_{1:k-1})\big) &= \mathcal{N}(\mathbf{x}(t_k)\,;\mathbf{m}(t_k|t_{k-1})), \mathbf{P}(t_k|t_{k-1}))\,, &(3.10)\\
\mathsf{p}\big(\mathbf{x}(t_k)|\mathbf{z}(t_{1:k})\big) &= \mathcal{N}(\mathbf{x}(t_k)\,;\mathbf{m}(t_k|t_k), \mathbf{P}(t_k|t_k))\,, &(3.11)
\end{aligned}$$

where $a \sim \mathcal{N}(a; \mu_a, \sigma_a^2)$ denotes a Gaussian distributed random variable a with mean μ_a, variance σ_a^2 and

$$\begin{aligned}
\mathbf{m}(t_k|t_{k-1}) &= \mathbf{F}(t_k)\mathbf{m}(t_{k-1}|t_{k-1})\,, &(3.12)\\
\mathbf{P}(t_k|t_{k-1}) &= \mathbf{Q}(t_{k-1}) + \mathbf{F}(t_k)\mathbf{P}(t_{k-1}|t_{k-1})\mathbf{F}^T(t_k)\,, &(3.13)\\
\mathbf{m}(t_k|t_k) &= \mathbf{m}(t_k|t_{k-1}) + \mathbf{K}(t_k)\left(\mathbf{z}(t_k) - \mathbf{H}(t_k)\mathbf{m}(t_k|t_{k-1})\right)\,, &(3.14)\\
\mathbf{P}(t_k|t_k) &= \mathbf{P}(t_k|t_{k-1}) - \mathbf{K}(t_k)\mathbf{H}(t_k)\mathbf{P}(t_k|t_{k-1})\,, &(3.15)\\
\mathbf{K}(t_k) &= \mathbf{P}(t_k|t_{k-1})\mathbf{H}^T(t_k)\left(\mathbf{H}(t_k)\mathbf{P}(t_k|t_{k-1})\mathbf{H}^T(t_k) + \mathbf{R}(t_k)\right)^{-1}\,, &(3.16)
\end{aligned}$$

where $\mathbf{K}(t_k)$ is the Kalman gain which specifies the impact of the new measurement in the new posterior estimate. The KF is computationally efficient and is optimal in the Bayesian sense if the mentioned assumptions hold. However, most of the real world problems are nonlinear where the KF cannot be used and sub-optimal algorithms like the EKF introduced in the following section have to be used.

3.3 Extended Kalman Filter

A sub-optimal implementation of recursive Bayesian filters for more general nonlinear problems is the EKF [SSM62, WB95]. In the EKF, a local linearization of the transition

and measurement equations is made to approximate the nonlinearity starting from an initial guess. According to the Gaussian assumptions, the prediction and update equations can be approximated as

$$\mathsf{p}\big(\mathbf{x}(t_k)|\mathbf{z}(t_{1:k-1})\big) \approx \mathcal{N}(\mathbf{x}(t_k)\,;\mathbf{m}(t_k|t_{k-1})),\mathbf{P}(t_k|t_{k-1}))\,, \tag{3.17}$$

$$\mathsf{p}\big(\mathbf{x}(t_k)|\mathbf{z}(t_{1:k})\big) \approx \mathcal{N}(\mathbf{x}(t_k)\,;\mathbf{m}(t_k|t_k),\mathbf{P}(t_k|t_k))\,, \tag{3.18}$$

with

$$\mathbf{m}(t_k|t_{k-1}) = \mathbf{f}(\mathbf{m}(t_{k-1}|t_{k-1}))\,, \tag{3.19}$$

$$\mathbf{P}(t_k|t_{k-1}) = \mathbf{Q}(t_{k-1}) + \mathbf{F}(t_k)\mathbf{P}(t_{k-1}|t_{k-1})\mathbf{F}^T(t_{k-1})\,, \tag{3.20}$$

$$\mathbf{m}(t_k|t_k) = \mathbf{m}(t_k|t_{k-1}) + \mathbf{K}(t_k)\left(\mathbf{z}(t_k) - \mathbf{h}(\mathbf{m}(t_k|t_{k-1}))\right)\,, \tag{3.21}$$

$$\mathbf{P}(t_k|t_k) = \mathbf{P}(t_k|t_{k-1}) - \mathbf{K}(t_k)\mathbf{H}(t_k)\mathbf{P}(t_k|t_{k-1})\,, \tag{3.22}$$

$$\mathbf{K}(t_k) = \mathbf{P}(t_k|t_{k-1})\hat{\mathbf{H}}^T(t_k)\left(\mathbf{H}(t_k)\mathbf{P}(t_k|t_{k-1})\hat{\mathbf{H}}^T(t_k) + \mathbf{R}(t_k)\right)^{-1}, \tag{3.23}$$

where $\mathbf{K}(t_k)$ is the Kalman gain. The local linearization of $\mathbf{f}(\cdot)$ and $\mathbf{h}(\cdot)$ around $\mathbf{m}(t_{k-1}|t_{k-1})$ and $\mathbf{m}(t_k|t_{k-1})$ are denoted by $\mathbf{F}(t_k)$ and $\mathbf{H}(t_k)$ with

$$\mathbf{F}(t_k) = \left.\frac{\mathrm{d}\mathbf{f}(x)}{\mathrm{d}x}\right|_{x=\mathbf{m}(t_{k-1}|t_{k-1})}\,, \tag{3.24}$$

$$\mathbf{H}(t_k) = \left.\frac{\mathrm{d}\mathbf{h}(x)}{\mathrm{d}x}\right|_{x=\mathbf{m}(t_k|t_{k-1})}\,. \tag{3.25}$$

The linearization of the functions in the EKF can yield highly unstable filters when the local linearity assumption does not hold. Also the approximation of $\mathsf{p}\big(\mathbf{x}(t_k)|\mathbf{z}(t_{1:k})\big)$ by a Gaussian may fail if the density is non-Gaussian or the nonlinearity is too high. Hence, other filters based on the KF have been proposed, which are not introduced in this thesis but can be found e.g. in [WVDM00, RAG04, Che03]. In the following section we introduce PFs which are suitable for nonlinear/non-Gaussian processes.

3.4 Particle Filters

In this section we give a short introduction to particle filtering. First we introduce the sequential importance sampling (SIS) PF which forms the basis of most PF implementations. Several flavors of PFs have been developed over the last few years. They differ in their choice of the importance sampling density and the resampling step. We focus on the sequential importance resampling (SIR) PF, regularized PF and Rao-Blackwellized PF. Rao-Blackwellized PF forms the basis of the PF implementation of Channel-SLAM described in Chapter 4. Section 3.4.6 introduces a novel PF in

logarithmic domain (log-domain) published in [GZJ18] which uses the Jacobian logarithm to describe all steps of the PF, including weight update, weight normalization, resampling and point estimations in log-domain.

3.4.1 Sequential Importance Sampling Particle Filter

PFs are based on sequential Monte Carlo methods which implement recursive Bayesian filters by Monte Carlo integrations [GSS93, AMGC02, RAG04, Gus10]. PFs approximate the probability density of the state vector $\mathbf{x}(t_k)$ at time step t_k by N_p particles. Assuming a first-order HMM, the posterior density $\mathsf{p}\big(\mathbf{x}(t_k)|\mathbf{z}(t_{1:k})\big)$ is approximated as

$$\mathsf{p}\big(\mathbf{x}(t_k)|\mathbf{z}(t_{1:k})\big) \approx \sum_{j=1}^{N_p} w^{(j)}(t_k)\, \delta\left(\mathbf{x}(t_k) - \mathbf{x}^{(j)}(t_k)\right) , \tag{3.26}$$

where $\delta(\cdot)$ stands for the Dirac distribution, $\mathbf{x}^{(j)}(t_k)$ denotes the particle state vector and $w^{(j)}(t_k)$ denotes the normalized weight. The particles are drawn according to the concept of importance sampling from the importance density $\mathsf{q}\big(\mathbf{x}(t_k)|\mathbf{x}^{(j)}(t_{k-1}), \mathbf{z}(t_k)\big)$ such that

$$w^{*(j)}(t_k) = w^{(j)}(t_{k-1}) \frac{\mathsf{p}\big(\mathbf{z}(t_k)|\mathbf{x}^{(j)}(t_k)\big)\mathsf{p}\big(\mathbf{x}^{(j)}(t_k)|\mathbf{x}^{(j)}(t_{k-1})\big)}{\mathsf{q}\big(\mathbf{x}^{(j)}(t_k)|\mathbf{x}^{(j)}(t_{k-1}), \mathbf{z}(t_k)\big)}, \tag{3.27}$$

and

$$w^{(j)}(t_k) = \frac{w^{*(j)}(t_k)}{\sum_{i=1}^{N_p} w^{*(i)}(t_k)} . \tag{3.28}$$

with the likelihood distribution $\mathsf{p}\big(\mathbf{z}(t_k)|\mathbf{x}^{(j)}(t_k)\big)$ and the transition prior distribution $\mathsf{p}\big(\mathbf{x}^{(j)}(t_k)|\mathbf{x}^{(j)}(t_{k-1})\big)$ [AMGC02]. For $N_p \to \infty$, the approximation used in (3.26) approaches $\mathsf{p}\big(\mathbf{x}(t_k)|\mathbf{z}(t_{1:k})\big)$. PFs have the advantage not being restricted to linear models or Gaussian distributions. By (3.26) and (3.27) the SIS PF can be described as shown in Algorithm 1 by a pseudo-code which is the basis of most PFs. Algorithm 1 is evaluated at each time step t_k, where $\{\mathbf{x}^{(j)}(t_k), w^{(j)}(t_k)\}_{j=1}^{N_p}$ denotes the set for the particle states $\mathbf{x}^{(j)}(t_k)$ and weights $w^{(j)}(t_k)$ with $j = 1, \ldots, N_p$ for time instant t_k. The SIS PF sequentially calculates the particle states $\mathbf{x}^{(j)}(t_k)$ and weights $w^{(j)}(t_k)$ with the measurements $\mathbf{z}(t_k)$.

3.4.2 Degeneracy in Particle Filters

A crucial problem of the SIS PF is degeneracy. Degeneracy occurs when all particles except one have low weights and do not contribute anymore to the computation of the posterior PDF, i.e. the distribution estimation degenerates. A suitable measure

Algorithm 1: Sequential importance sampling (SIS) PF

$\{\mathbf{x}^{(j)}(t_k), w^{(j)}(t_k)\}_{j=1}^{N_p} = \text{SIS}\left(\{\mathbf{x}^{(j)}(t_{k-1}), w^{(j)}(t_{k-1})\}_{j=1}^{N_p}, \mathbf{z}(t_k)\right)$

for $j = 1 : N_p$ **do**

  Draw: $\mathbf{x}^{(j)}(t_k) \sim \mathsf{q}\big(\mathbf{x}^{(j)}(t_k)|\mathbf{x}^{(j)}(t_{k-1}), \mathbf{z}(t_k)\big)$;

  Calculate: $w^{*(j)}(t_k)$ according to (3.27);

Calculate: $W(t_k) = \sum_{j=1}^{N_p} w^{*(j)}(t_k)$;

for $j = 1 : N_p$ **do**

  Normalize: $w^{(j)}(t_k) = \frac{w^{*(j)}(t_k)}{W(t_k)}$;

of degeneracy is the effective sample size N_{eff} [GSS93, AMGC02, RAG04, Che03]. A widely used approximation for the effective sample size is

$$N_{\text{eff}} = \frac{1}{\sum_{j=1}^{N_p}(w^{(j)}(t_k))^2} = \frac{\left(\sum_{j=1}^{N_p}(w^{*(j)}(t_k))\right)^2}{\sum_{j=1}^{N_p}(w^{*(j)}(t_k))^2}\,, \tag{3.29}$$

with $1 \leq N_{\text{eff}} \leq N_p$. Small values of N_{eff} indicate a severe degeneracy and vice versa. Alternative effective sample size approximations can be found e.g. in [MEL17].

Using a very large number of particles N_p is one solution to avoid the degeneracy problem, however, impractical in most applications due to the high computational time and effort. Additionally, very large number of particles N_p may introduce numerical errors due to number representation during normalization [GZJ18]. In practical systems the degeneracy problem is resolved by choosing an appropriate importance density or by resampling.

Importance Density

An appropriate choice of the importance density $\mathsf{q}\big(\mathbf{x}^{(j)}(t_k)|\mathbf{x}^{(j)}(t_{k-1}), \mathbf{z}(t_k)\big)$ is essential, i.e. [AMGC02] proposes different importance density functions. The choice of an optimal importance density function minimizes the variance of the weights and hence, reduces the degeneracy problem, see [DFMR00]. The most popular and convenient way is to set the importance density to be equal to the transitional prior distribution, with

$$\mathsf{q}\big(\mathbf{x}(t_k)|\mathbf{x}^{(j)}(t_{k-1}), \mathbf{z}(t_k)\big) \triangleq \mathsf{p}\big(\mathbf{x}(t_k)|\mathbf{x}^{(j)}(t_{k-1})\big)\,, \tag{3.30}$$

which simplifies the weight update in (3.27) to

$$w^{*(j)}(t_k) = w^{(j)}(t_{k-1})\mathsf{p}\big(\mathbf{z}(t_k)|\mathbf{x}^{(j)}(t_k)\big)\,. \tag{3.31}$$

The authors of [AMGC02] calculate additionally the optimal importance density for the special case where the measurements are more informative than the transition model. Hence, the likelihood $\mathsf{p}\big(\mathbf{z}(t_{1:k})|\mathbf{x}^{(j)}(t_{k-1})\big)$ has a lower variance than the prior distribution $\mathsf{p}\big(\mathbf{x}(t_k)|\mathbf{x}^{(j)}(t_{k-1})\big)$. This optimal importance density requires the ability to sample from $\mathsf{p}\big(\mathbf{z}(t_k)|\mathbf{x}^{(j)}(t_{k-1})\big)$ and to evaluate the integral over the new state. However, we are only able to sample from the distribution $\mathsf{p}\big(\mathbf{z}(t_k)|\mathbf{x}^{(j)}(t_{k-1})\big)$ if its Gaussian distributed or when $\mathbf{x}(t_{k-1})$ is a member of a finite set.

Resampling

The basic idea of the resampling method is to eliminate particles with low weights and reproduce particles with high weights. For example, the generic PF extends the SIS PF by a resampling step to prevent degeneration as shown in Algorithm 3 by a pseudo-code. Whenever a significant degeneracy is observed in the generic PF, i.e. N_{eff} is less than a threshold N_{thr} the particles are resampled. Resampling is hence required in the PF when the true distribution differs from the distribution of the proposal. Resampling generates a new set $\{\tilde{\mathbf{x}}^{(j)}(t_k), \tilde{w}^{(j)}(t_k) = N_p^{-1}\}_{j=1}^{N_p}$ with uniform distributed weights generated from $\{\mathbf{x}^{(j)}(t_k), w^{(j)}(t_k)\}_{j=1}^{N_p}$. In this way particles with high weights are duplicated and particles with low weight are eliminated. After the resampling procedure, all particles have the same weight. Algorithm 2 shows a pseudo-code of the systematic resampling algorithm [Kit96] which is a standard resampling algorithm with low complexity and used in Section 4.3. First, the estimated sampled cumulative distribution function (CDF) is constructed, presented by a vector $\mathbf{c}$ with length N_p and element $[\mathbf{c}]_j$ with $j = 1, \ldots, N_p$. According to the estimated sampled CDF, particles are resampled. Also other types of resampling algorithms exist in literature: multinomial resampling, residual resampling and local Monte Carlo resampling, see e.g. [LC98, CCF99, Che03] for more details.

3.4.3 Sampling Importance Resampling Particle Filter

The SIR PF is a wildly spread PF and was first proposed in [GSS93] under the name bootstrap filter. Algorithm 4 shows a pseudo-code of the SIR PF, which is derived from the SIS PF. The SIR PF sets the importance density to be equal to the transitional prior distribution as stated in (3.30) and resampling is performed at every time step, thus the weight update of (3.31) simplifies to

$$w^{*(j)}(t_k) \propto \mathsf{p}\big(\mathbf{z}(t_k)|\mathbf{x}^{(j)}(t_k)\big). \tag{3.32}$$

Fig. 3.2 illustrates by an example the evaluation of the SIS PF for one time instant t_k with the actual probability distributions of interest and three steps of particle filtering:

Algorithm 2: Resampling algorithm

$\{\tilde{\mathbf{x}}^{(j)}(t_k), \tilde{w}^{(j)}(t_k)\}_{j=1}^{N_p} = \text{Resampling}\left(\{\mathbf{x}^{(j)}(t_k), w^{(j)}(t_k)\}_{j=1}^{N_p}\right)$

Initialize the CDF: $[\mathbf{c}]_1 = w^{(1)}(t_k)$;

for $j = 2 : N_p$ **do**

  Construct CDF: $[\mathbf{c}]_j = [\mathbf{c}]_{j-1} + w^{(j)}(t_k)$;

$i = 1$;

Draw starting point: $[\mathbf{u}]_1 \sim \mathcal{U}\left[0, N_p^{-1}\right]$;

for $j = 1 : N_p$ **do**

  $[\mathbf{u}]_j = [\mathbf{u}]_1 + N_p^{-1}(j-1)$;

  while $[\mathbf{u}]_j > [\mathbf{c}]_i$ **do**

    $i = i + 1$;

  Assign: $\left\{\tilde{\mathbf{x}}^{(j)}(t_k), \tilde{w}^{(j)}(t_k)\right\} = \left\{\mathbf{x}^{(i)}(t_k), N_p^{-1}\right\}$;

Algorithm 3: Generic-PF

$\{\mathbf{x}^{(j)}(t_k), w^{(j)}(t_k)\}_{j=1}^{N_p} = \text{Generic}\left(\{\mathbf{x}^{(j)}(t_{k-1}), w^{(j)}(t_{k-1})\}_{j=1}^{N_p}, \mathbf{z}(t_k)\right)$

for $j = 1 : N_p$ **do**

  Draw: $\mathbf{x}^{(j)}(t_k) \sim \mathsf{q}\big(\mathbf{x}^{(j)}(t_k)|\mathbf{x}^{(j)}(t_{k-1}), \mathbf{z}(t_k)\big)$;

  Calculate: $w^{*(j)}(t_k)$ according to (3.27);

Calculate: $W(t_k) = \sum_{j=1}^{N_p} w^{*(j)}(t_k)$;

for $j = 1 : N_p$ **do**

  Normalize: $w^{(j)}(t_k) = \frac{w^{*(j)}(t_k)}{W(t_k)}$;

Calculate $N_{\text{eff}} = \frac{1}{\sum_{j=1}^{N_p}(w^{(j)}(t_k))^2}$;

if $N_{\text{eff}} < N_{\text{thr}}$ **then**

  Resample with Algorithm 2: Obtaining $\left\{\mathbf{x}^{(j)}(t_k), w^{(j)}(t_k)\right\}_{j=1}^{N_s}$;

drawing, weighting and resampling. The solid curve represents the distributions of interest, which is approximated by the particles where the sizes of the particles reflect the value of their weight. After resampling, particles with high weights are duplicated, particles with low weights are eliminated and all particles have the same weight. The next time instant, the particles are drawn according to the transition model.

Algorithm 4: Sequential importance resampling (SIR) PF

$\{\mathbf{x}^{(j)}(t_k), w^{(j)}(t_k)\}_{j=1}^{N_p} = \mathrm{SIR}\left(\{\mathbf{x}^{(j)}(t_{k-1}), w^{(j)}(t_{k-1})\}_{j=1}^{N_p}, \mathbf{z}(t_k)\right)$

for $j = 1 : N_p$ **do**

  Draw: $\mathbf{x}^{(j)}(t_k) \sim \mathsf{p}\big(\mathbf{x}^{(j)}(t_k)|\mathbf{x}^{(j)}(t_{k-1})\big)$;

  Calculate: $w^{*(j)}(t_k) = \mathsf{p}\big(\mathbf{z}(t_k)|\mathbf{x}^{(j)}(t_k)\big)$;

Calculate: $W(t_k) = \sum_{j=1}^{N_p} w^{*(j)}(t_k)$;

for $j = 1 : N_p$ **do**

  Normalize: $w^{(j)}(t_k) = \frac{w^{*(j)}(t_k)}{W(t_k)}$;

Resample with Algorithm 2: Obtaining $\left\{\mathbf{x}^{(j)}(t_k), w^{(j)}(t_k)\right\}_{j=1}^{N_s}$;

3.4.4 Regularized Particle Filter

The regularized PF is based on the SIS PF and addresses the effect that resampling introduces the problem of loss of diversity among the particles [MOLG01, AMGC02]. The loss of diversity occurs due to the fact that particles are drawn from a discrete distribution rather than a continuous distribution in the resampling step. Particles drawn from the discrete distribution might be identical in the state which gives a poor representation of the posterior density. Whereas the SIR resamples from the discrete approximation (3.26), the regularized PF resamples from a continuous approximation of the posterior density. Thus, in the regularized PF, samples are drawn from

$$\mathsf{p}\big(\mathbf{x}(t_k)|\mathbf{z}(t_{1:k})\big) \approx \sum_{j=1}^{N_p} w^{(j)}(t_k)\ \mathrm{K}(\mathbf{x}(t_k) - \mathbf{x}^{(j)}(t_k))\,, \tag{3.33}$$

where $\mathrm{K}(\mathbf{x}(t_k) - \mathbf{x}^{(j)}(t_k))$ is a kernel function centered at $\mathbf{x}^{(j)}(t_k)$ with bandwidth σ_{K} and normalized weights $w^{(j)}(t_k)$.

3.4.5 Rao-Blackwellized Particle Filter

PF based on the SIS PF have the disadvantage that the computational complexity grows exponentially with the dimension of the state size. The RBPF [CR96,

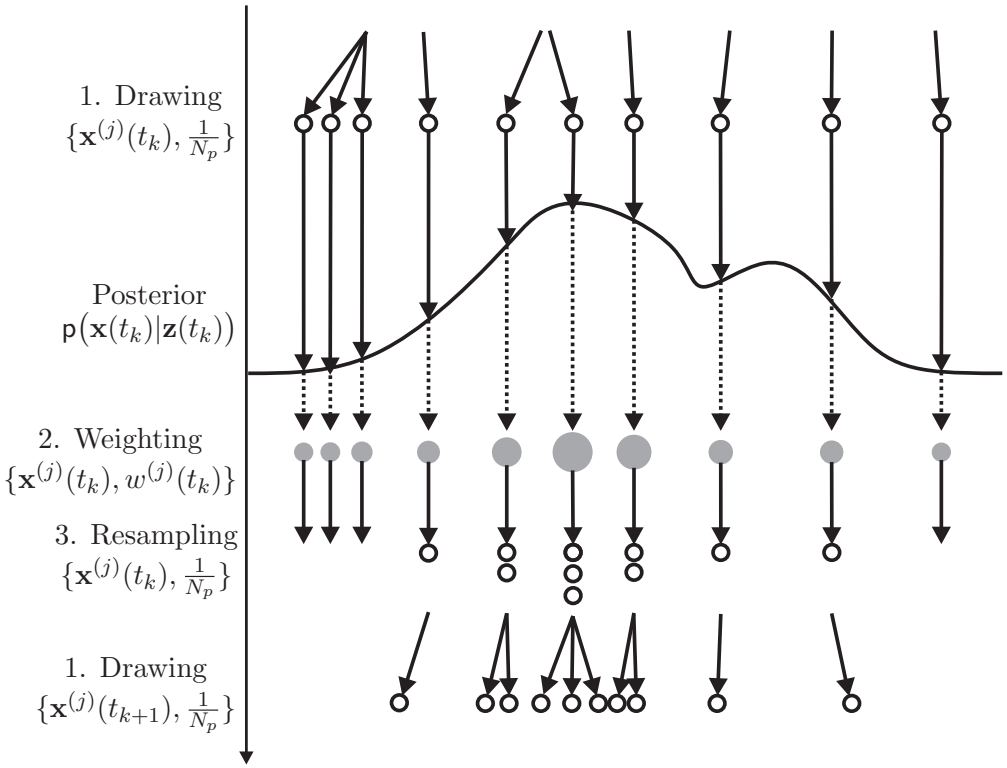

Figure 3.2. *Graphical illustration of the SIR PF steps: drawing, weighting, resampling. The sizes of the particles reflect their weights.*

DGK01,DFMR00,Che03], also known as marginalized PF, marginalizes out sub-states. Thus, the state vector $\mathbf{x}(t_k)$ is partitioned into sub-state vectors $\mathbf{r}(t_k)$ and $\mathbf{y}(t_k)$ with $\mathbf{x}(t_k) = [\mathbf{r}(t_k)^T, \mathbf{y}(t_k)^T]^T$ and the posterior density $\mathsf{p}\big(\mathbf{x}(t_k)|\mathbf{z}(t_{1:k})\big)$ can be written as

$$\begin{aligned} \mathsf{p}\big(\mathbf{x}(t_k)|\mathbf{z}(t_{1:k})\big) &= \mathsf{p}\big(\mathbf{r}(t_k), \mathbf{y}(t_k)|\mathbf{z}(t_{1:k})\big) \\ &= \mathsf{p}\big(\mathbf{y}(t_k)|\mathbf{z}(t_{1:k}), \mathbf{r}(t_k)\big)\ \mathsf{p}\big(\mathbf{r}(t_k)|\mathbf{z}(t_{1:k})\big)\,. \end{aligned} \tag{3.34}$$

For instants the sub-state $\mathbf{y}(t_k)$ can be updated analytically and efficiently using any optimal Bayesian filter such as KF, while $\mathbf{r}(t_k)$ cannot be represented parametrically and a PF is used for the estimation. Hence, the RBPF contains additionally to the sample $\mathbf{r}^{(j)}(t_k)$ from $\mathsf{p}\big(\mathbf{r}(t_k)|\mathbf{z}(t_{1:k})\big)$ a parametric representation of $\mathsf{p}\big(\mathbf{y}(t_k)|\mathbf{z}(t_{1:k}), \mathbf{r}^{(j)}(t_k)\big)$ for each particle j. Using a RBPF allows that the state dimension can be kept small enough to be feasible for a PF by representing parts of the state space using e.g. parametrical functions.

3.4.6 Particle Filter in Logarithm Domain

For numerical stability reasons, weights are often computed and stored in the log-domain, which is also computationally efficient when the distributions involved contain expo-

nentials or products. From (3.27), we obtain the update equation in log-domain with

$$\begin{aligned} \hat{w}^{*(j)}(t_k) &= \hat{w}^{(j)}(t_{k-1}) + \ln\big(\mathsf{p}\big(\mathbf{z}(t_k)|\mathbf{x}^{(j)}(t_k)\big)\big) \\ &\quad + \ln\big(\mathsf{p}\big(\mathbf{x}^{(j)}(t_k)|\mathbf{x}^{(j)}(t_{k-1})\big)\big) - \ln\big(\mathsf{q}\big(\mathbf{x}(t_k)|\mathbf{x}^{(j)}(t_{k-1}), \mathbf{z}(t_k)\big)\big)\,, \end{aligned} \tag{3.35}$$

where we define with

$$\begin{aligned} \hat{w}^{(j)}(t_k) &= \ln\left(w^{(j)}(t_k)\right), \\ \hat{w}^{*(j)}(t_k) &= \ln\left(w^{*(j)}(t_k)\right), \end{aligned} \tag{3.36}$$

the log-domain weights (log-weights) $\hat{w}^{(j)}(t_k)$ and $\hat{w}^{*(j)}(t_k)$ for particle j. After calculating the weights $\hat{w}^{*(j)}(t_k)$ in log-domain, the weights are transferred for further processing to the linear domain with $w^{*(j)}(t_k) = e^{\hat{w}^{*(j)}(t_k)}$ for $j = 1, \ldots, N_p$ and are normalized with (3.28).

In order to obtain a more stable PF implementation, the weights $\hat{w}^{*(j)}(t_k)$ can be transferred to the linear domain by

$$w^{+(j)}(t_k) = e^{\hat{w}^{*(j)}(t_k) - \max\limits_{l}(\hat{w}^{*(l)}(t_k))}\,, \tag{3.37}$$

such that

$$w^{(j)}(t_k) = \frac{w^{+(j)}(t_k)}{\sum_{i=1}^{N_p} w^{+(i)}(t_k)}\,, \tag{3.38}$$

see e.g. [LFS+12, GZJ18]. In Algorithm 5, we show a pseudo-code of the Generic PF where the weights are calculated in log-domain according to (3.35), normalized and transferred to the linear domain according to (3.37). Further improvements can be obtained if the weights $\hat{w}^{*(j)}(t_k)$ are directly propagated in log-domain if resampling is not necessary.

In [GZJ18], we investigate a different approach, where the transformation from the log-domain to the linear domain is not necessary. Hence, [GZJ18] introduces the weight calculation, weight normalization, resampling and point estimations in log-domain. To compute all these steps of the PF in log-domain, we obtain for the approximation of the posterior filtered density from (4.19)

$$\mathsf{p}\big(\mathbf{x}(t_k)|\mathbf{z}(t_{1:k})\big) \approx \sum_{j=1}^{N_p} e^{\hat{w}^{(j)}(t_k)}\, \delta\left(\mathbf{x}(t_k) - \mathbf{x}^{(j)}(t_k)\right)\,, \tag{3.39}$$

using (3.35) and (3.36). The normalization of the log-weight can be calculated directly in log-domain as a simple subtraction, with

$$\hat{w}^{(j)}(t_k) = \hat{w}^{*(j)}(t_k) - \hat{W}(t_k)\,, \tag{3.40}$$

Algorithm 5: Generic-PF in linear domain with weight calculation in log-domain (Generic Lin-Log-PF)

$\{\mathbf{x}^{(j)}(t_k), w^{(j)}(t_k)\}_{j=1}^{N_p} = \text{Generic-Lin-Log}\left(\{\mathbf{x}^{(j)}(t_{k-1}), w^{(j)}(t_{k-1})\}_{j=1}^{N_p}, \mathbf{z}(t_k)\right)$

for $j = 1 : N_p$ **do**

  Draw: $\mathbf{x}^{(j)}(t_k) \sim \mathfrak{q}\big(\mathbf{x}^{(j)}(t_k)|\mathbf{x}^{(j)}(t_{k-1}), \mathbf{z}(t_k)\big)$;

  Transfer: $\hat{w}^{(j)}(t_k) = \ln\left(w^{(j)}(t_k)\right)$;

  Calculate: $\hat{w}^{*(j)}(t_k)$ according to (3.35);

for $j = 1 : N_p$ **do**

  Transfer and Normalize: $w^{+(j)}(t_k) = e^{\hat{w}^{*(j)}(t_k) - \max\limits_{l}(\hat{w}^{*(l)}(t_k))}$;

Calculate: $W(t_k) = \sum_{j=1}^{N_p} w^{+(j)}(t_k)$;

for $j = 1 : N_p$ **do**

  Normalize: $w^{(j)}(t_k) = \frac{w^{+(j)}(t_k)}{W(t_k)}$;

Calculate $N_{\text{eff}} = \frac{1}{\sum_{j=1}^{N_p}(w^{(j)}(t_k))^2}$;

if $N_{\text{eff}} < N_{\text{thr}}$ **then**

  Resample with Algorithm 2: Obtaining $\left\{\mathbf{x}^{(j)}(t_k), w^{(j)}(t_k)\right\}_{j=1}^{N_s}$;

where $\hat{W}(t_k)$ denotes the normalization factor with

$$\hat{W}(t_k) = \ln\left(\sum_{i=1}^{N_p} e^{\hat{w}^{*(i)}(t_k)}\right) . \tag{3.41}$$

To compute the normalization factor $\hat{W}(t_k)$ of (3.41) without transferring the log-weights to the linear domain, the Jacobian logarithm [EPG94, KB90] can be used. The Jacobian logarithm computes the logarithm of a sum of two exponentials $\ln(e^{\delta_1} + e^{\delta_2})$ using the $\max(\cdot)$ operator and adding a correction term, i.e.,

$$\ln(e^{\delta_1} + e^{\delta_2}) = \max(\delta_1, \delta_2) + \ln\left(1 + e^{-|\delta_2 - \delta_1|}\right) . \tag{3.42}$$

With (3.42) and as derived in [RVH95], the expression $\ln\left(\sum_{l=1}^{n} e^{\delta_l}\right)$ can be calculated iteratively as

$$\ln(e^{\delta_1} + \cdots + e^{\delta_n}) = \ln(\Delta + e^{\delta_n}) = \max\left(\ln(\Delta), \delta_n\right) + \ln\left(1 + e^{-|\ln(\Delta) - \delta_n|}\right) , \tag{3.43}$$

where $\delta = \ln\left(e^{\delta_1} + \cdots + e^{\delta_{n-1}}\right)$ and $\Delta = e^{\delta_1} + \cdots + e^{\delta_{n-1}}$. Hence, using the Jacobian logarithm allows to compute operations such as summations like in (3.41) efficiently in

the log-domain. We express (3.43) by an iterative algorithm shown in Algorithm 6 by a pseudo-code, i.e.,

$$\ln\left(\sum_{l=1}^{n} e^{\delta_l}\right) = \text{Jacob}\big(\{\delta_l\}_{l=1}^{n}\big)\,, \tag{3.44}$$

where $\{\delta_l\}_{l=1}^{n}$ defines the set for δ_l with $l = 1, \ldots, n$. Thus, the normalization factor

Algorithm 6: Iterative Jacobian Algorithm

1 $\ln\left(\sum_{l=1}^{n} e^{\delta_i}\right) = \text{Jacob}\big(\{\delta_l\}_{l=1}^{n}\big)$

2 Init: $\Delta_1 = \delta_1$;

3 **for** $l = 2 : n$ **do**

4 $\quad \Delta_l = \max(\delta_l, \Delta_{l-1}) + \ln\left(1 + e^{-|\delta_l - \Delta_{l-1}|}\right)$;

5 $\ln\left(\sum_{l=1}^{n} e^{\delta_i}\right) = \Delta_n$;

$\hat{W}(t_k)$ of (3.41) can be calculated iteratively by

$$\hat{W}(t_k) = \text{Jacob}\big(\{\hat{w}^{*(i)}(t_k)\}_{i=1}^{N_p}\big). \tag{3.45}$$

Hence, we obtain for the log-weight normalization of (3.40),

$$\hat{w}^{(j)}(t_k) = \hat{w}^{*(j)}(t_k) - \text{Jacob}\big(\{\hat{w}^{*(i)}(t_k)\}_{i=1}^{N_p}\big)\,. \tag{3.46}$$

Similar to the description above, the calculation of the effective sampling size, resampling and point estimations can be described in log-domain using the Jacobian logarithm, see [GZJ18]. Algorithm 7 and Algorithm 8 show by pseudo-codes the Generic PF and the systematic resampling algorithm transferred into log-domain. For further details about the PF implementation in log-domain, see [GZJ18].

3.5 Simultaneous Localization and Mapping

Dynamic position estimation algorithms can be implemented using the aforementioned implementations of recursive Bayesian filters. For instance in radio based positioning as introduced in Section 2.2, the location of the receiver is estimated using a transition model and pseudorange measurements between physical transmitters at known locations and the receiver. However, in cases where the locations of the physical transmitters are unknown, the receiver and physical transmitters positions have to be calculated simultaneously. A method to estimate the positions of the receiver and of the physical transmitters at the same time is called SLAM [GU17, GUJ18].

Algorithm 7: Generic-PF in log-domain (Generic Log-PF)

$\{\mathbf{x}^{(j)}(t_k), \hat{w}^{(j)}(t_k)\}_{j=1}^{N_p} = \text{Generic-Log}\left(\{\mathbf{x}^{(j)}(t_{k-1}), \hat{w}^{(j)}(t_{k-1})\}_{j=1}^{N_p}, \mathbf{z}(t_k)\right)$

for $j = 1 : N_p$ **do**

  Draw: $\mathbf{x}^{(j)}(t_k) \sim \mathsf{q}\big(\mathbf{x}^{(j)}(t_k)|\mathbf{x}^{(j)}(t_{k-1}), \mathbf{z}(t_k)\big)$;

  Calculate: $\hat{w}^{*(j)}(t_k)$ according to (3.35);

Calculate: $\hat{W}(t_k) = \text{Jacob}\big(\{\hat{w}^{*(j)}(t_k)\}_{j=1}^{N_p}\big)$;

for $j = 1 : N_p$ **do**

  Normalize: $\hat{w}^{(j)}(t_k) = \hat{w}^{*(j)}(t_k) - \hat{W}(t_k)$;

Calculate $\ln(N_{\text{eff}}) = -\text{Jacob}\big(\{2 \cdot \hat{w}^{(j)}(t_k)\}_{j=1}^{N_p}\big)$;

if $\ln(N_{\text{eff}}) < \ln(N_{\text{thr}})$ **then**

  Resample with Algorithm 8: Obtaining $\big\{\mathbf{x}^{(j)}(t_k), \hat{w}^{(j)}(t_k)\big\}_{j=1}^{N_s}$;

Algorithm 8: Resampling in log-domain

$\{\tilde{\mathbf{x}}^{(j)}(t_k), \tilde{w}^{(j)}(t_k)\}_{j=1}^{N_p} = \text{Log-Resampling}\left(\{\mathbf{x}^{(j)}(t_k), \hat{w}^{(j)}(t_k)\}_{j=1}^{N_p}\right)$

Initialize the cumulative distribution function in log-domain (log-CDF):

$[\mathbf{c}]_1 = \hat{w}^{(1)}(t_k)$;

for $j = 2 : N_p$ **do**

  Construct log-CDF using the Jacobian logarithm:

  $[\mathbf{c}]_j = \max(\hat{w}^{(j)}(t_k), [\mathbf{c}]_{j-1}) + \ln\left(1 + e^{-\left|[\mathbf{c}]_{j-1} - \hat{w}^{(j)}(t_k)\right|}\right)$;

$i = 1$;

Draw starting point: $s \sim \mathcal{U}\left[0, N_p^{-1}\right]$;

for $j = 1 : N_p$ **do**

  $[\mathbf{u}]_j = \ln\big(s + N_p^{-1}(j-1)\big)$;

  while $[\mathbf{u}]_j > [\mathbf{c}]_i$ **do**

    $i = i + 1$;

  Assign: $\big\{\tilde{\mathbf{x}}^{(j)}(t_k), \tilde{w}^{(j)}(t_k)\big\} = \big\{\mathbf{x}^{(i)}(t_k), -\ln(N_p)\big\}$;

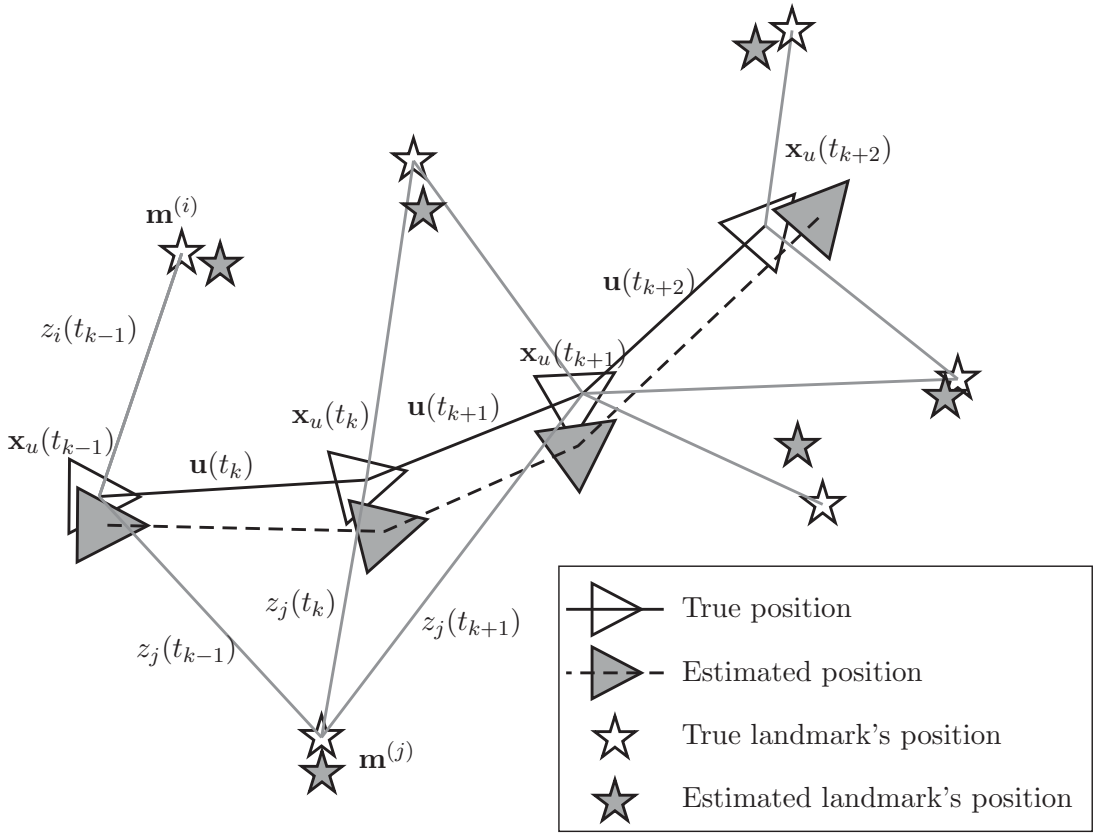

Figure 3.3. *Overview of the SLAM method with a moving object, where the positions of the moving object and of the landmarks are estimated simultaneously.*

In general, SLAM addresses the method of estimating the location of a moving object in an unknown environment and simultaneously builds a map of the environment [SC86, SSC86, LDw91, DB06, BD06]. In SLAM the map and the trajectory are estimated without the need of any prior knowledge of the environment. SLAM was originally presented within the robotics community as a technique to jointly estimate the position of a robot and a map of detected landmarks. In a recursive Bayesian formulation, the SLAM method computes the probability distribution

$$\mathsf{p}\big(\mathbf{x}_u(t_k)\,,\mathbf{m}|\mathbf{z}(t_{1:k})\,\mathbf{u}(t_{1:k})\,,\mathbf{x}_u(t_0)\big)\,, \tag{3.47}$$

with

- The state vector $\mathbf{x}_u(t_k)$ which describes the location and orientation of the moving object.
- The map $\mathbf{m}$ which comprises a set of objects $\mathbf{m} = \{\mathbf{m}^{(i)}\}$ in the environment for $0 \leq i < N_m$, where N_m is the number of objects in the environment and $\mathbf{m}^{(i)}$ specifies the properties, such as positions, of object i whose true location is assumed to be time invariant.

- The control inputs $\mathbf{u}(t_{1:k}) = \left[\mathbf{u}(t_1)^T, \ldots, \mathbf{u}(t_k)^T\right]^T$ are the control inputs for time instant $t_1, \ldots, t_k$, where $\mathbf{u}(t_k)$ is used at time instant t_{k-1} to move the object from state $\mathbf{x}_u(t_{k-1})$ to state $\mathbf{x}_u(t_k)$.
- The measurements $\mathbf{z}(t_{1:k}) = \left[\mathbf{z}(t_1)^T, \ldots, \mathbf{z}(t_k)^T\right]^T$ are the measurements taken of the landmarks from the moving object for time instant $t_1, \ldots, t_k$ and $\mathbf{z}(t_k) = [z_0(t_k), z_1(t_k), \ldots]$ are the measurements at time instant t_k.

The probability distribution of (3.47) describes the joint posterior density of the landmarks' locations and object state given the measurements and control inputs together with the initial state of the object. Fig. 3.3 visualizes the SLAM method: an object moves through an environment and takes relative measurements of a number of landmarks at unknown positions using a sensor located on the object. In order to use the information of the landmarks, the object estimates simultaneously the positions of the object and landmarks. The true locations are never known or measured directly.

Equivalent to Section 3.1, the posterior density $\mathsf{p}\big(\mathbf{x}_u(t_k), \mathbf{m}|\mathbf{z}(t_{1:k})\,\mathbf{u}(t_{1:k}), \mathbf{x}_u(t_0)\big)$ might be obtained recursively by the prediction and update step. In the prediction step, the PDF

$$\begin{aligned}&\mathsf{p}\big(\mathbf{x}_u(t_k), \mathbf{m}|\mathbf{z}(t_{1:k-1}), \mathbf{u}(t_{1:k}), \mathbf{x}_u(t_0)\big) \\ &= \int \mathsf{p}\big(\mathbf{x}_u(t_k)|\mathbf{x}_u(t_{k-1}), \mathbf{u}(t_k)\big)\mathsf{p}\big(\mathbf{x}_u(t_{k-1}), \mathbf{m}|\mathbf{z}(t_{1:k-1}), \mathbf{u}(t_{1:k-1}), \mathbf{x}_u(t_0)\big)\,\mathrm{d}\mathbf{x}_u(t_{k-1})\end{aligned} \tag{3.48}$$

is calculated where we assume a first-order HMM with the transition prior

$$\mathsf{p}\big(\mathbf{x}(t_k)|\mathbf{x}(t_{k-1}), \mathbf{u}(t_k)\big), \tag{3.49}$$

which depends on the state $\mathbf{x}(t_{k-1})$ and the applied control input $\mathbf{u}(t_k)$ and is independent of both, the measurements and the map. During the update step with

$$\begin{aligned}&\mathsf{p}\big(\mathbf{x}_u(t_k), \mathbf{m}|\mathbf{z}(t_{1:k}), \mathbf{u}(t_{1:k}), \mathbf{x}_u(t_0)\big) \\ &= \frac{\mathsf{p}\big(\mathbf{z}(t_k)|\mathbf{x}_u(t_k), \mathbf{m}\big) \cdot \mathsf{p}\big(\mathbf{x}_u(t_k), \mathbf{m}|\mathbf{z}(t_{1:k-1}), \mathbf{u}(t_{1:k}), \mathbf{x}_u(t_{k-1})\big)}{\mathsf{p}\big(\mathbf{z}(t_k)|\mathbf{z}(t_{1:k-1}), \mathbf{u}(t_{1:k})\big)},\end{aligned} \tag{3.50}$$

the measurement $\mathbf{z}(t_k)$ is used to correct the prediction based on the measurement model

$$\mathsf{p}\big(\mathbf{z}(t_k)|\mathbf{x}(t_k), \mathbf{m}\big). \tag{3.51}$$

Equations (3.48) and (3.50) provide a recursive procedure for calculating the joint posterior $\mathsf{p}\big(\mathbf{x}_u(t_k), \mathbf{m}|\mathbf{z}(t_{1:k})\,\mathbf{u}(t_{1:k}), \mathbf{x}_u(t_0)\big)$ for the object state $\mathbf{x}_u(t_k)$ and map $\mathbf{m}$ at time instant t_k based on all measurements $\mathbf{z}(t_{1:k})$ and all control inputs $\mathbf{u}(t_{1:k})$.

As aforementioned, SLAM was originally presented within the robotics community. The most well-known implementations are based on EKF [DNC+01,SC86,SSC86, LDw91], GraphSLAM [TM06] and FastSLAM [MTK+02]. State-of-the-art techniques of SLAM within the robotics community use cameras [DRMS07] and distance measurements, e.g. laser scanners [TBF00] to obtain measurements of the landmarks. In recent years, pedestrian SLAM has become an important research area [BR11,FFL07,SCZ+13, RAK09, KD15, HRMT12, AR12, PBRJ14, Puy17]. For instant [BR11, FFL07, SCZ+13] map the positions of detected WLAN access points or [RAK09,KD15,HRMT12,AR12, PBRJ14, Puy17] build probabilistic maps based on human motion using pedestrian step measurements.

Chapter 4

Multipath Assisted Positioning

In this chapter, the Channel-SLAM algorithm is explained in all its details. Section 4.1 addresses the concept of VTs to represent each MPC as a LoS signal from a VT to the receiver. Then, Section 4.2 describes the Channel-SLAM algorithm: Section 4.2.1 addresses the derivation of Channel-SLAM based on recursive Bayesian filtering; Section 4.2.2 addresses the derivation of the RBPF for Channel-SLAM; Section 4.2.4 describes two different transition models without and with heading information from an IMU; Section 4.3 describes the implementation of the RBPF.

4.1 The Concept of Virtual Transmitters

In order to use MPCs for the localization of a mobile receiver, a model reflecting their parameters in dependency of the receiver position $\boldsymbol{r}_u(t_k)$ needs to be found. In the following, we consider a two dimensional static environment with a physical transmitter at position $\boldsymbol{r}_t$ and a receiver moving along an arbitrary trajectory. We consider the aforementioned propagation effects described in Section 2.1.1: reflection, scattering and diffraction. Both, scattering and diffraction can be geometrically described by a fixed point S at position $\boldsymbol{r}_s$ in the path of the MPC.

In Fig. 4.1, we consider the case of reflection on a smooth surface. The reflection point at position $\boldsymbol{r}_r(t_k)$ is moving on the surface when the receiver is in motion. As indicated by VT_1, we can construct a VT at position $\boldsymbol{r}_{\mathrm{VT},1}$ by mirroring the physical transmitter position at the reflecting surface. The distance between VT_1 and the receiver equals $d_{\mathrm{TR}}(t_k) + d_{\mathrm{RU}}(t_k) = \|\boldsymbol{r}_t - \boldsymbol{r}_r(t_k)\| + \|\boldsymbol{r}_r(t_k) - \boldsymbol{r}_u(t_k)\| = \|\boldsymbol{r}_{\mathrm{VT},1} - \boldsymbol{r}_u(t_k)\|$, which is the geometrical length of the reflected path, i.e. the delay of the MPC multiplied by the speed of light, where $d_{\mathrm{TR}}(t_k)$ is the distance between the physical transmitter and the reflection point and $d_{\mathrm{RU}}(t_k)$ the distance between the reflection point and the receiver. Seen from the receiver side, both, the reflected and the virtual propagation

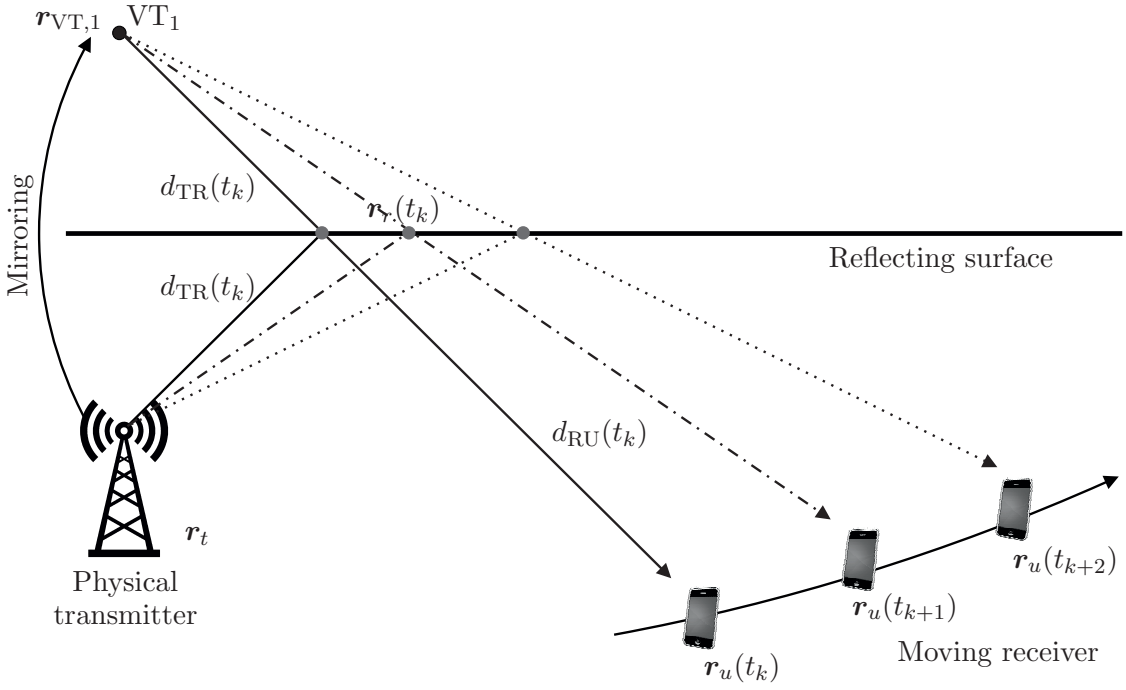

Figure 4.1. *The transmitted signal is reflected on a smooth surface. The position of VT_1 is obtained by mirroring the physical transmitter position at the reflecting surface. Inherently, VT_1 is time synchronized to the physical transmitter.*

paths starting at VT_1 have the same AoA and delay. Therefore, a reflected path can be described as a direct path between VT_1 and the receiver. Inherently, VT_1 is time synchronized to the physical transmitter.

Using the same approach, a VT can be obtained for propagation paths which are reflected multiple times. Fig. 4.2 shows a multiple reflection scenario, where the transmitted signal is reflected twice. If the receiver is moving, the reflection points on both reflecting surfaces at the coordinates $\boldsymbol{r}_{r,j}(t_k)$ for $j = 1, 2$ are moving accordingly. As depicted in Fig. 4.2 by VT_2, we can construct a VT at position $\boldsymbol{r}_{\mathrm{VT},2}$ by mirroring the physical transmitter position at both reflecting surfaces. The distance between the VT_2 and the receiver is equal to $d_{\mathrm{TR}}(t_k) + d_{\mathrm{RR}}(t_k) + d_{\mathrm{RU}}(t_k) = \|\boldsymbol{r}_t - \boldsymbol{r}_{r,1}(t_k)\| + \|\boldsymbol{r}_{r,1}(t_k) - \boldsymbol{r}_{r,2}(t_k)\| + \|\boldsymbol{r}_{r,2}(t_k) - \boldsymbol{r}_u(t_k)\| = \|\boldsymbol{r}_{\mathrm{VT},2} - \boldsymbol{r}_u(t_k)\|$ which is equivalent to the propagation time of the reflected signal multiplied with the speed of light. The distances $d_{\mathrm{TR}}(t_k)$, $d_{\mathrm{RR}}(t_k)$ and $d_{\mathrm{RU}}(t_k)$ are the distances between the physical transmitter and the reflection point on the first reflecting surface; between the reflection points on both reflecting surfaces; between the reflection point on the second reflecting surface and the receiver. Equivalently to Fig. 4.1 the reflected path can be described as a direct path between VT_2 and the receiver. VT_2 is inherently time

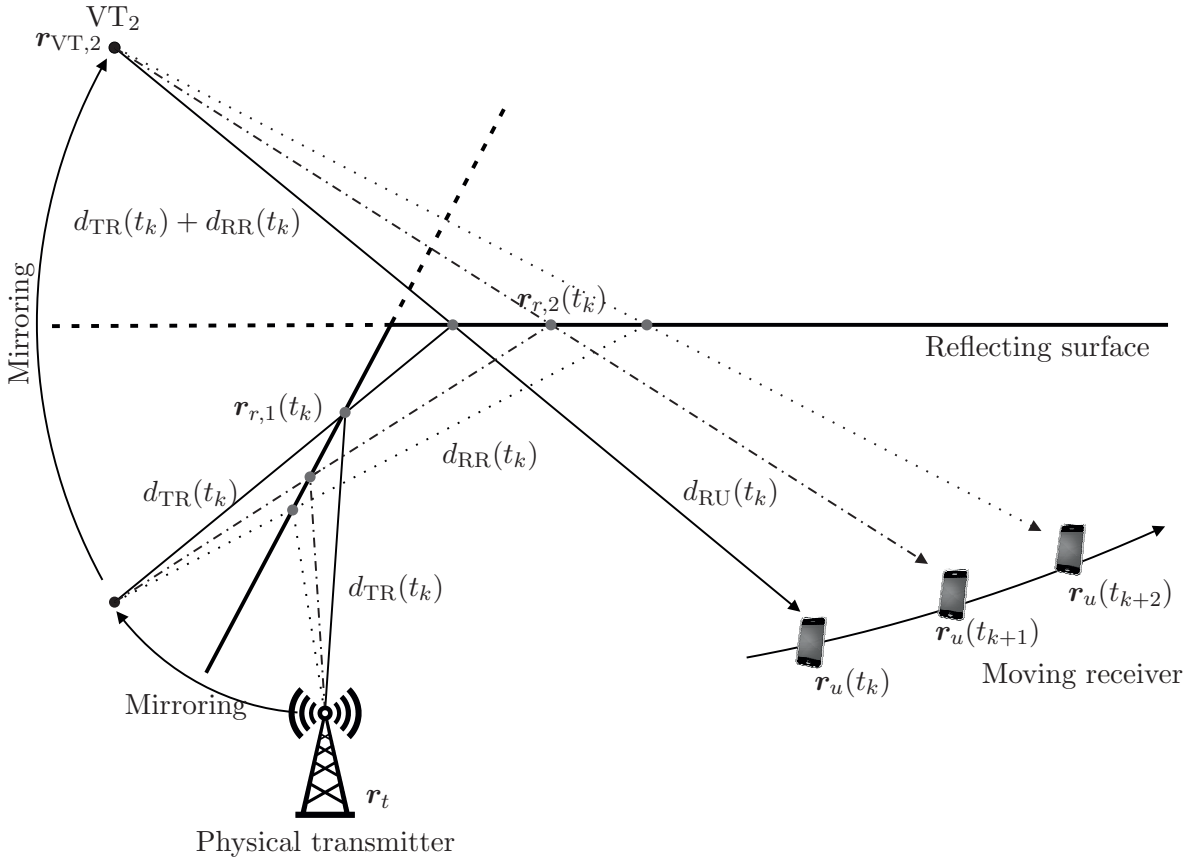

Figure 4.2. *The transmitted signal is reflected on two smooth surfaces. VT_2 is defined by mirroring the physical transmitter position at the first and additionally at the second reflecting surface. Inherently, VT_2 is time synchronized to the physical transmitter.*

synchronized to the physical transmitter and seen from the receiver side, the virtual propagation path starting at VT_2 has the same AoA and delay as the reflected path.

Fig. 4.3 provides a visualization of scattering of the signal at the physical scatterer S at position $\boldsymbol{r}_s$. The geometrical propagation distance of the scattered propagation path is a direct path between S and the receiver with distance $d_{\mathrm{SU}}(t_k)$ and the propagation distance $d_{\mathrm{TS}}(t_k)$ between the physical transmitter and S. Thus, we can construct a VT at the scatterer position $\boldsymbol{r}_{\mathrm{VT},3} = \boldsymbol{r}_s$ as visualized by VT_3 in Fig. 4.3. The propagation distance of the scattered path is $d_{\mathrm{TS}}(t_k) + d_{\mathrm{SU}}(t_k) = \|\boldsymbol{r}_t - \boldsymbol{r}_s\| + \|\boldsymbol{r}_s - \boldsymbol{r}_u(t_k)\| = \|\boldsymbol{r}_{\mathrm{VT},3} - \boldsymbol{r}_u(t_k)\| + d_{\mathrm{VT},3}$ where $d_{\mathrm{TS}}(t_k) = d_{\mathrm{VT},3} > 0$ is constant for all receiver positions $\boldsymbol{r}_u(t_k)$. Hence, the scattered signal can be interpreted as a direct signal from VT_3 to the receiver plus an additional constant propagation distance $d_{\mathrm{VT},3}$.

As indicated in Fig. 4.3 by the winded line, additional interactions between the physical transmitter and S may occur including reflections, scattering and diffractions. Fig. 4.4 provides examples if the last propagation effect is a scatterer before the signal reaches the receiving antenna. In Fig. 4.4, the signal before reaching the scatterer S_2

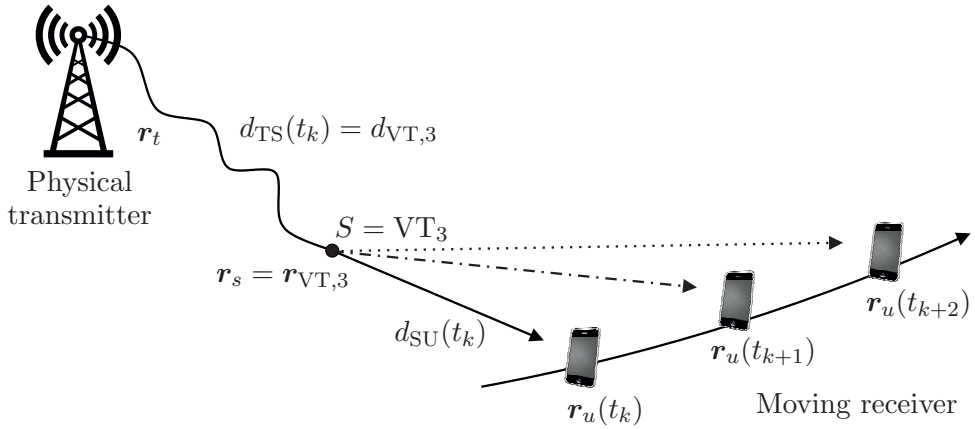

Figure 4.3. *The transmitted signal is scattered at S. VT_3 is defined at the position of S and the additional propagation distance $d_{\mathrm{VT},3}$ equals to $d_{\mathrm{TS}}(t_k)$. Additional interactions between the physical transmitter and S may occur indicated by the winded line.*

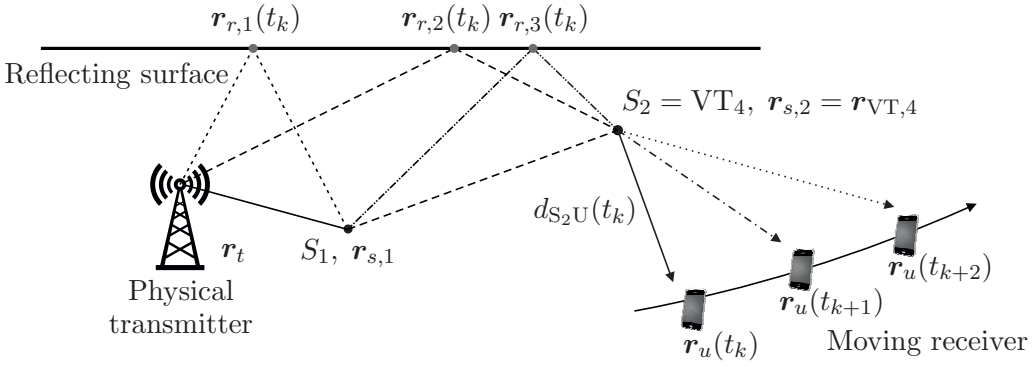

Figure 4.4. *The transmitted signal is scattered at S_2. Before reaching the scatterer S_2, the transmitted signal is either reflected at the reflecting surface, scattered at S_1, scattered at S_1 and afterwards reflected or reflected on the reflecting surface and afterwards scattered at S_1. For all these possibilities, VT_4 is defined at the position of S_2.*

is either reflected at the reflecting surface; scattered at S_1; scattered S_1 and afterwards reflected; reflected and afterwards scattered at S_1. For all of these cases, we can construct a VT at the scatterer S_2 position $\boldsymbol{r}_{\mathrm{VT},4} = \boldsymbol{r}_{s,2}$ as visualized by VT_4 in Fig. 4.4. The propagation distance of the scattered path is $d_{\mathrm{TS_2}}(t_k) + d_{\mathrm{S_2U}}(t_k) = d_{\mathrm{TS_2}}(t_k) + \|\boldsymbol{r}_s - \boldsymbol{r}_u(t_k)\| = \|\boldsymbol{r}_{\mathrm{VT},4} - \boldsymbol{r}_u(t_k)\| + d_{\mathrm{VT},4}$ where $d_{\mathrm{TS_2}}(t_k)$ is the traveled distance between the physical transmitter and scatterer S_2 and $d_{\mathrm{TS_2}}(t_k) = d_{\mathrm{VT},4} > 0$ is constant for all receiver positions $\boldsymbol{r}_u(t_k)$. Hence, the scattered signal can be interpreted as a direct signal from VT_4 to the receiver plus an additional constant propagation distance $d_{\mathrm{VT},4}$.

Fig. 4.5 shows a scenario where the emitted signal from the physical transmitter is first scattered at S and then reflected before it reaches the receiver. When the receiver is moving, the reflection point at position $\boldsymbol{r}_r(t_k)$ in Fig. 4.5 is moving on the surface. Hence, the VT is defined by mirroring the location of the scatterer S at the surface as

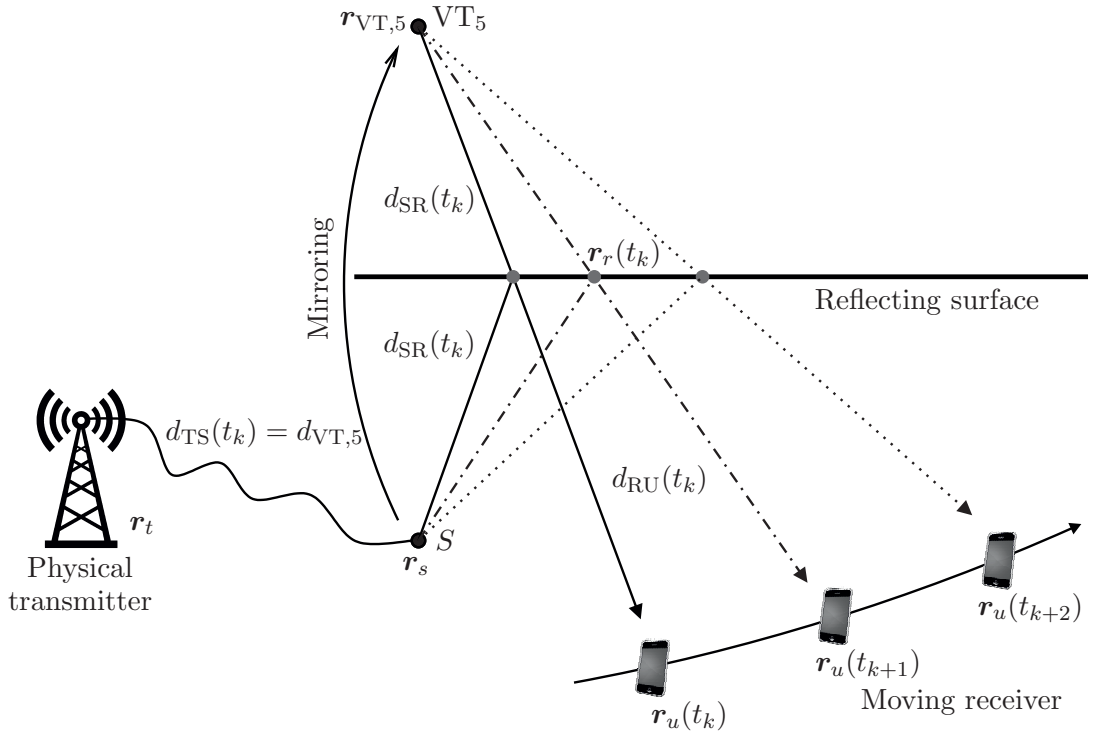

Figure 4.5. *The transmitted signal is scattered and afterwards reflected on a smooth surface. VT_5 is defined by mirroring the location of the scatterer S at the surface; the additional propagation distance $d_{\mathrm{VT},5}$ equals to $d_{\mathrm{TS}}(t_k)$. Additional interactions between the physical transmitter and S may occur indicated by the winded line.*

indicated by VT_5 at position $\boldsymbol{r}_{\mathrm{VT},5}$. The propagation distance is therefore $d_{\mathrm{TS}}(t_k) + d_{\mathrm{SR}}(t_k) + d_{\mathrm{RU}}(t_k) = d_{\mathrm{VT},5} + \|\boldsymbol{r}_s - \boldsymbol{r}_r(t_k)\| + \|\boldsymbol{r}_r(t_k) - \boldsymbol{r}_u(t_k)\| = d_{\mathrm{VT},5} + \|\boldsymbol{r}_{\mathrm{VT},5} - \boldsymbol{r}_u(t_k)\|$, where $d_{\mathrm{TS}}(t_k) = d_{\mathrm{VT},5} > 0$, $d_{\mathrm{SR}}(t_k)$ is the distance between S and $\boldsymbol{r}_r(t_k)$, and $d_{\mathrm{RU}}(t_k)$ is the distance between $\boldsymbol{r}_r(t_k)$ and the receiver. As mentioned before, between the physical transmitter and S additional interactions may occur leading to the same position of VT_5.

Combining the approaches described before leads to the conclusion that the propagation path of any i-th MPC can be equivalently described as a direct path between VT_i and the receiver plus an additional constant propagation distance $d_{\mathrm{VT},i}$. This additional propagation distance is zero, i.e. $d_{\mathrm{VT},i} = 0$, if only reflections occurred on the path between the physical transmitter and the receiver; the additional propagation distance is greater than zero, i.e. $d_{\mathrm{VT},i} > 0$, if the i-th MPC interacts with at least one scatterer. In general, $d_{\mathrm{VT},i}/c$ can be interpreted as a clock bias between the i-th VT and the physical transmitter. In the following, we will denote the position of the VT and the additional propagation distance associated to the i-th MPC at time instant t_k by $\boldsymbol{r}_{\mathrm{VT},i}(t_k)$ and $d_{\mathrm{VT},i}(t_k)$, respectively. The position of the VTs and the additional

propagation distances are constant over time. Nevertheless for notational convenience in the later sections a time dependency on t_k is introduced here.

4.2 Algorithm Derivation

According to the description given in the previous section, a MPC can be represented by a direct path between a VT and the receiver plus an additional propagation distance. However, the receiver position $\boldsymbol{r}_u(t_k)$ as well as the states of the VTs, i.e. $\boldsymbol{r}_{\mathrm{VT},i}(t_k)$ and $d_{\mathrm{VT},i}(t_k)$, are unknown. Additionally, it is unknown whether the MPC is caused by a reflection or an interaction with a scatterer. We assume that a total of $N(t_k)$ propagation paths arrrive at the receiver at time instant t_k. Please note, the number of propagation paths $N(t_k)$ includes all MPCs with the LoS component. Hence, the state vector $\mathbf{x}(t_k)$ that describes the parameters to be estimated at time instant t_k for $N(t_k)$ propagation paths is defined by

$$\mathbf{x}(t_k) = \left[\mathbf{x}_u(t_k)^T, \mathbf{x}_{\mathrm{VT}}(t_k)^T\right]^T , \tag{4.1}$$

with the receiver states

$$\mathbf{x}_u(t_k) = \left[\boldsymbol{r}_u(t_k)^T, \boldsymbol{v}_u(t_k)^T, b_u(t_k)\right]^T , \tag{4.2}$$

where $\boldsymbol{r}_u(t_k)$ is the receiver position, $\boldsymbol{v}_u(t_k)$ the receiver velocity, $b_u(t_k)$ the receiver's clock bias with respect to the phyical transmitter and the VT states

$$\mathbf{x}_{\mathrm{VT}}(t_k) = \left[\mathbf{x}_{\mathrm{VT},0}(t_k)^T, \ldots, \mathbf{x}_{\mathrm{VT},N(t_k)-1}(t_k)^T\right]^T . \tag{4.3}$$

The parameters representing the i-th VT are defined as

$$\mathbf{x}_{\mathrm{VT},i}(t_k) = \left[\boldsymbol{r}_{\mathrm{VT},i}(t_k)^T, d_{\mathrm{VT},i}(t_k)\right]^T , \tag{4.4}$$

where $\boldsymbol{r}_{\mathrm{VT},i}(t_k)$ is the position of the i-th VT for $i = 0, \ldots, N(t_k) - 1$ and $d_{\mathrm{VT},i}(t_k)$ the additional propagation distance. If the physical transmitter position is known, we use for notational conveniences, VT_0 to describe the physical transmitter with known position $\boldsymbol{r}_{\mathrm{VT},0}(t_k) = \boldsymbol{r}_t$ and additional propagation distance $d_{\mathrm{VT},0}(t_k) = 0$. If the physical transmitter position is unknown, the physical transmitter position is estimated as a VT position.

Fig. 4.6 presents the available sensors at the receiver together with the corresponding measurements. As shown on the left, the receiver measures the sampled received signal $\boldsymbol{Y}(t_k)$ as stated in (2.7) assuming that the physical transmitter continuously emits known wideband signals. Based on the received signal $\boldsymbol{Y}(t_k)$, the signal parameters $\hat{\boldsymbol{\Phi}}(t_k)$ with amplitude $\alpha_i(t_k)$, delay $\tau_i(t_k) = \frac{d_i(t_k)}{c}$ and AoA $\theta_i(t_k)$ if an antenna

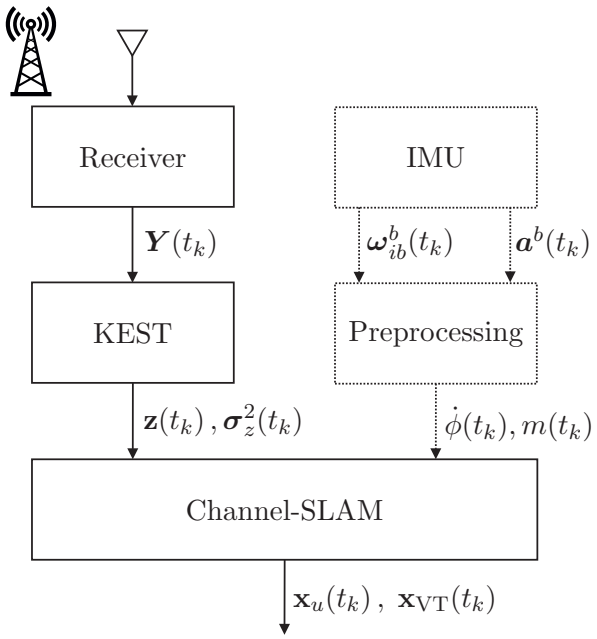

Figure 4.6. *System model consisting of a terrestrial receiver and an IMU.*

array is used are estimated for each MPC $i = 0, \ldots, N(t_k)-1$. For consistency between different time instances, the signal parameter estimation algorithm needs to include a path association such that distinct propagation paths are individually tracked over sequential time instances. As mentioned in Section 2.1.3, we use the algorithm called KEST for the estimation and tracking of MPCs. Also other multipath estimation and tracking algorithms could be applied, e.g. [KRW10, SRK09]. The estimated AoA $\hat{\theta}_i(t_k)$ and propagation path length $\hat{d}_i(t_k) = \hat{\tau}_i(t_k) \cdot c$ of all $N(t_k)$ MPCs of KEST are used as measurements

$$\mathbf{z}(t_k) = [\hat{\boldsymbol{\theta}}(t_k)^T,\ \hat{\boldsymbol{d}}(t_k)^T]^T, \tag{4.5}$$

with

$$\hat{\boldsymbol{\theta}}(t_k) = [\hat{\theta}_0(t_k),\ \ldots\ , \hat{\theta}_{N(t_k)-1}(t_k)]^T\,, \tag{4.6}$$

$$\hat{\boldsymbol{d}}(t_k) = [\hat{d}_0(t_k),\ \ldots\ , \hat{d}_{N(t_k)-1}(t_k)]^T\,, \tag{4.7}$$

in Channel-SLAM with their corresponding variances $\boldsymbol{\sigma}_z^2(t_k) = \left[\boldsymbol{\sigma}_\theta^2(t_k)^T, \boldsymbol{\sigma}_d^2(t_k)^T\right]^T$.

In case of a single receiving antenna, the measurements $\mathbf{z}(t_k)$ include only the estimated propagation path lengths $\hat{\boldsymbol{d}}(t_k)$. Multipath estimation algorithms like KEST cannot distinguish between reflected paths, scattered paths or the combination of both. However, by including the additional propagation distance $d_{\mathrm{VT},i}(t_k)$ in the state vector $\mathbf{x}_{\mathrm{VT},i}(t_k)$, a specific model detection is not necessary, since for reflected paths, scattered paths or the combination of both, the same model can be used. Hence, if the MPC was interacting with a scatterer, Channel-SLAM estimates $d_{\mathrm{VT},i}(t_k) > 0$. If only re-

flections occurred on the propagation path between physical transmitter and receiver, Channel-SLAM estimates $d_{\mathrm{VT},i}(t_k) \approx 0$.

Additionally, as illustrated in Fig. 4.6, an IMU might be used. The IMU provides measurements of the accelerations $\boldsymbol{a}^b(t_k)$ and turn rates $\boldsymbol{\omega}_{ib}^b(t_k)$ in three dimensions. After preprocessing, the heading change $\dot{\phi}(t_k)$ and moving indicator $m(t_k)$ can be used in Channel-SLAM as a control input $\mathbf{u}(t_k)$, with

$$\mathbf{u}(t_k) = \left[\dot{\phi}(t_k), m(t_k)\right]^T \tag{4.8}$$

and is therefore directly integrated into the transition model of the recursive Bayesian filter. The heading information of the IMU allows to improve the performance of Channel-SLAM by resolving ambiguities. Further details about the IMU can be found in Appendix A.

4.2.1 Algorithm Description by Recursive Bayesian Filtering

As introduced in Section 3.1, recursive Bayesian filtering provides a methodology to optimally estimate parameters in non-stationary scenarios. Fig. 4.7 shows the considered DBN of Channel-SLAM using a first-order hidden Markov model. Channel-SLAM requires to calculate the posterior filtered density

$$\mathsf{p}\big(\mathbf{x}(t_k)|\mathbf{z}(t_{1:k}), \mathbf{u}(t_{1:k}), \mathbf{x}_u(t_0)\big), \tag{4.9}$$

considering the aforementioned first-order hidden Markov model. Assuming independency among MPCs, we obtain from (4.9),

$$\begin{aligned}
&\mathsf{p}\big(\mathbf{x}(t_k)|\mathbf{z}(t_{1:k}), \mathbf{u}(t_{1:k}), \mathbf{x}_u(t_0)\big) \qquad (4.10)\\
&= \mathsf{p}\big(\mathbf{x}_u(t_k), \mathbf{x}_{\mathrm{VT}}(t_k)|\mathbf{z}(t_{1:k}), \mathbf{u}(t_{1:k}), \mathbf{x}_u(t_0)\big)\\
&= \mathsf{p}\big(\mathbf{x}_u(t_k)|\mathbf{z}(t_{1:k}), \mathbf{u}(t_{1:k}), \mathbf{x}_u(t_0)\big) \cdot \mathsf{p}\big(\mathbf{x}_{\mathrm{VT}}(t_k)|\mathbf{x}_u(t_k), \mathbf{z}(t_{1:k})\big)\\
&= \mathsf{p}\big(\mathbf{x}_u(t_k)|\mathbf{z}(t_{1:k}), \mathbf{u}(t_{1:k}), \mathbf{x}_u(t_0)\big) \prod_{i=0}^{N(t_k)-1} \mathsf{p}\big(\mathbf{x}_{\mathrm{VT},i}(t_k)|\mathbf{x}_u(t_k), \mathbf{z}_i(t_{1:k})\big),
\end{aligned}$$

where $\mathbf{z}_i(t_k)$ denotes the measurements of the i-th MPC with

$$\mathbf{z}_i(t_k) = \left[\hat{\theta}_i(t_k), \hat{d}_i(t_k)\right]^T. \tag{4.11}$$

The transition prior $\mathsf{p}\big(\mathbf{x}(t_k)|\mathbf{x}(t_{k-1}), \mathbf{u}(t_k)\big)$ used in the prediction step of the recursive Bayesian filter is defined here as

$$\mathsf{p}\big(\mathbf{x}(t_k)|\mathbf{x}(t_{k-1}), \mathbf{u}(t_k)\big) = \mathsf{p}\big(\mathbf{x}_u(t_k)|\mathbf{x}_u(t_{k-1}), \mathbf{u}(t_k)\big) \prod_{i=0}^{N(t_k)-1} \mathsf{p}\big(\mathbf{x}_{\mathrm{VT},i}(t_k)|\mathbf{x}_{\mathrm{VT},i}(t_{k-1})\big), \tag{4.12}$$

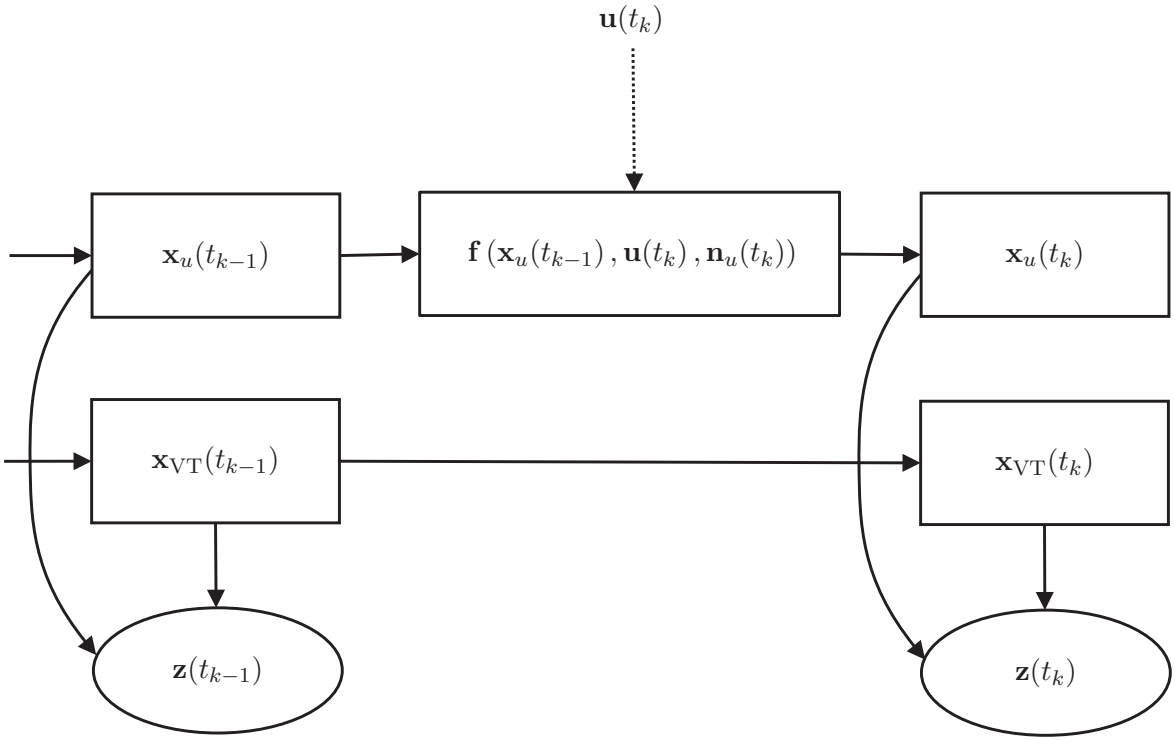

Figure 4.7. *First-order hidden Markov model representing the dynamic system of Channel-SLAM.*

where we assume independence between the transition priors of the receiver state vector $\mathbf{x}_u(t_k)$ and the VT state vectors $\mathbf{x}_{\mathrm{VT},i}(t_k)$ associated to the i-th MPC. The independency among MPCs in (4.12) is based on the well-known uncorrelated scattering assumption in wireless propagation channel modelling [Rap96]. As mentioned in Section 4.1, the state $\mathbf{x}_{\mathrm{VT},i}(t_k)$ is time-invariant, hence, for the transition prior $\mathsf{p}\big(\mathbf{x}_{\mathrm{VT},i}(t_k)|\mathbf{x}_{\mathrm{VT},i}(t_{k-1})\big)$ of the i-th MPC we obtain

$$\mathsf{p}\big(\mathbf{x}_{\mathrm{VT},i}(t_k)|\mathbf{x}_{\mathrm{VT},i}(t_{k-1})\big) = \delta\left(\mathbf{x}_{\mathrm{VT},i}(t_k) - \mathbf{x}_{\mathrm{VT},i}(t_{k-1})\right) . \tag{4.13}$$

For the transition prior $\mathsf{p}\big(\mathbf{x}_u(t_k)|\mathbf{x}_u(t_{k-1}), \mathbf{u}(t_k)\big)$ of the receiver state vector, Section 4.2.4 describes two different transition models indicated by the function $\mathbf{f}\left(\mathbf{x}_u(t_{k-1}), \mathbf{u}(t_k), \mathbf{n}_t(t_k)\right)$ in Fig. 4.7.

Assuming the elements of $\mathbf{z}(t_k)$ to be independent Gaussian distributed conditioned on the current state $\mathbf{x}(t_k)$, $\mathsf{p}\big(\mathbf{z}(t_k)|\mathbf{x}(t_k)\big)$ can be expressed as

$$\mathsf{p}\big(\mathbf{z}(t_k)|\mathbf{x}(t_k)\big) = \mathsf{p}\big(\hat{\boldsymbol{d}}(t_k)|\mathbf{x}(t_k)\big) \cdot \mathsf{p}\big(\hat{\boldsymbol{\theta}}(t_k)|\mathbf{x}(t_k)\big) , \tag{4.14}$$

where

$$\mathsf{p}\big(\hat{\boldsymbol{d}}(t_k)|\mathbf{x}(t_k)\big) = \prod_{i=0}^{N(t_k)-1} \frac{1}{\sqrt{2\pi}\sigma_{d,i}(t_k)} e^{-\frac{(\hat{d}_i(t_k)-d_i(t_k))^2}{2\sigma^2_{d,i}(t_k)}}, \tag{4.15}$$

$$\mathsf{p}\big(\hat{\boldsymbol{\theta}}(t_k)|\mathbf{x}(t_k)\big) = \prod_{i=0}^{N(t_k)-1} \frac{1}{\sqrt{2\pi}\sigma_{\theta,i}(t_k)} e^{-\frac{(\hat{\theta}_i(t_k)-\theta_i(t_k))^2}{2\sigma^2_{\theta,i}(t_k)}}, \tag{4.16}$$

with the propagation distance

$$d_i(t_k) = \|\boldsymbol{r}_u(t_k) - \boldsymbol{r}_{\mathrm{VT},i}(t_k)\| + d_{\mathrm{VT},i}(t_k) + b_u(t_k)\cdot c \tag{4.17}$$

and the AoA

$$\theta_i(t_k) = \arccos\left(\frac{\left(\boldsymbol{r}_{\mathrm{VT},i}(t_k) - \boldsymbol{r}_u(t_k)\right)^T \cdot \boldsymbol{v}_u(t_k)}{\|\boldsymbol{r}_{\mathrm{VT},i}(t_k) - \boldsymbol{r}_u(t_k)\| \cdot \|\boldsymbol{v}_u(t_k)\|}\right), \tag{4.18}$$

for the i-th MPC, where $\sigma^2_{d,i}(t_k)$ and $\sigma^2_{\theta,i}(t_k)$ denote the corresponding variances. Please note that we assume in (4.18) that the linear antenna array is aligned to the direction of $\boldsymbol{v}_u(t_k)$, i.e. the moving direction.

4.2.2 Rao-Blackwellized Particle Filter

In this section a formulation of Channel-SLAM is derived based on Rao-Blackwellization [GJW+16], where the states space of $\mathbf{x}(t_k)$ is partitioned into subspaces. We use PFs to estimate the subspaces representing the VTs inside a PF. The formulation allows to use different numbers of particles in each PF associated to a VT and reduces the computational complexity compared to [GJ13, GJD13, GPJD14]. The reason to use a PF instead of a low complexity EKF is the high degree of nonlinearity of the measurements in (4.18) and (4.17). As shown in Fig. 4.8, the RBPF of Channel-SLAM is based on a superordinate particle filter (super-PF) and subordinate particle filters (sub-PFs): Each particle $j = 1 \dots N_s$ of the super-PF with the state vector $\mathbf{x}_u^{(j)}(t_k) = \left[\boldsymbol{r}_u^{(j)}(t_k)^T, \boldsymbol{v}_u^{(j)}(t_k)^T, b_u^{(j)}(t_k)\right]^T$ consists of $N(t_k)$ sub-PFs. Each sub-PF is represented by the particles $\mathbf{x}_{\mathrm{VT},i}^{(j,a)}(t_k)$ with $a = 1, \dots, N_{P,j,i}(t_k)$ where $N_{P,j,i}(t_k)$ stands for the number of particles in the i-th sub-PF with $i = 0, \dots, N(t_k) - 1$. The number of particles $N_{P,j,i}(t_k)$ in the i-th sub-PF is time dependent because of a grid based reduction method introduced in Section 4.3. In the super-PF, the marginalized posterior filtered density $\mathsf{p}\big(\mathbf{x}_u(t_k)|\mathbf{z}(t_{1:k}), \mathbf{u}(t_{1:k})\big)$ can be approximated by importance samples, see [GJW+16, GPU+17b], as

$$\mathsf{p}\big(\mathbf{x}_u(t_k)|\mathbf{z}(t_{1:k}), \mathbf{u}(t_{1:k})\big) \approx \sum_{j=1}^{N_s} w^{(j)}(t_k)\, \delta\left(\mathbf{x}_u(t_k) - \mathbf{x}_u^{(j)}(t_k)\right), \tag{4.19}$$

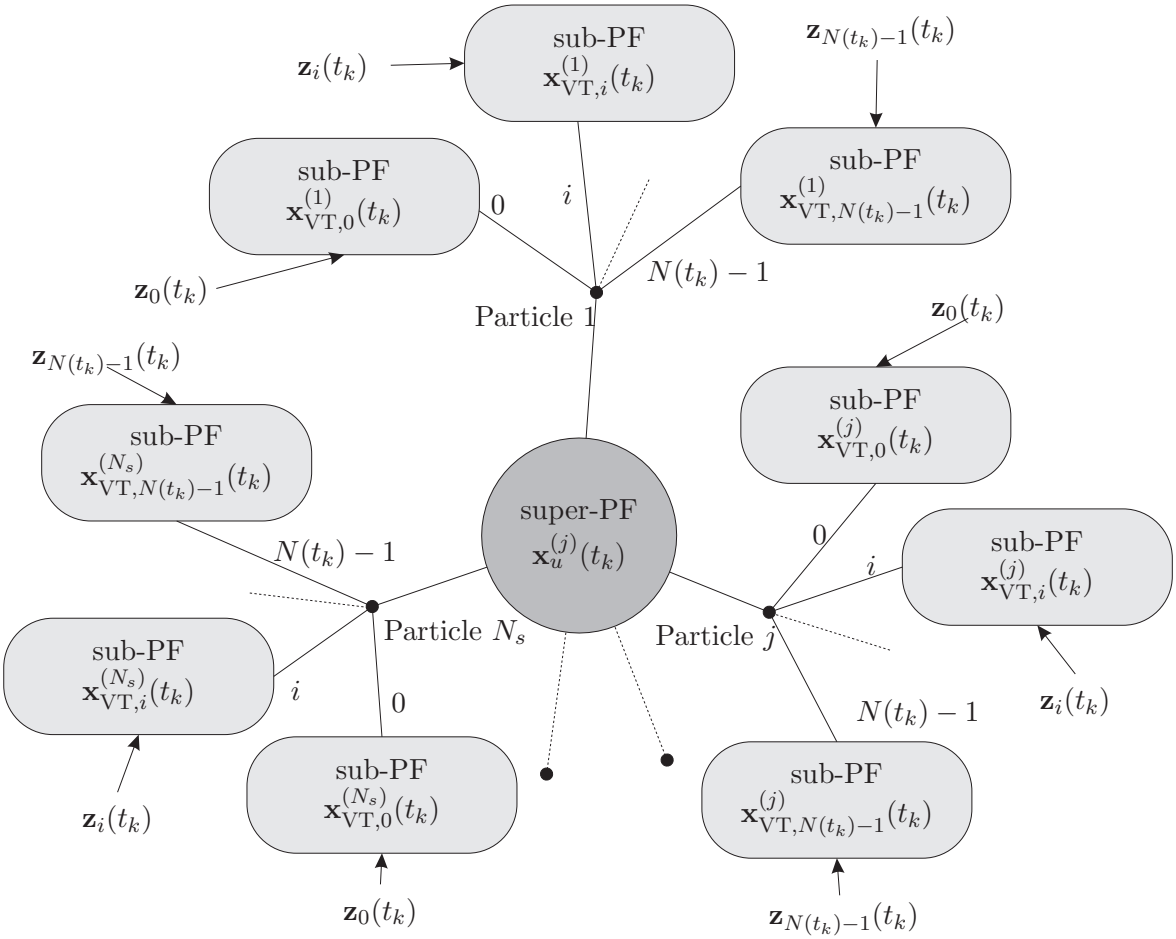

Figure 4.8. *The RBPF of Channel-SLAM is based on a superordinate particle filter (super-PF) and subordinate particle filters (sub-PFs): the sub-PFs estimate the conditional posterior density* $\mathsf{p}\big(\mathbf{x}_{\mathrm{VT},i}(t_k)|\mathbf{x}_u(t_k)\,,\mathbf{z}_i(t_{1:k})\big)$ *of* $\mathbf{x}_{\mathrm{VT},i}(t_k)$ *for the* i*-th VT and the super-PF estimates the marginalized posterior filtered density* $\mathsf{p}\big(\mathbf{x}_u(t_k)|\mathbf{z}(t_{1:k})\,,\mathbf{u}(t_{1:k})\big)$ *of* $\mathbf{x}_u(t_k)$*. Each particle* $j = 1 \ldots N_s$ *of the super-PF consists of* $N(t_k)$ *sub-PFs.*

where

$$w^{(j)}(t_k) \propto w^{(j)}(t_{k-1}) \frac{\mathsf{p}\big(\mathbf{z}(t_k)|\mathbf{x}^{(j)}_u(t_k)\,,\mathbf{z}(t_{k-1})\big)\mathsf{p}\big(\mathbf{x}^{(j)}_u(t_k)|\mathbf{x}^{(j)}_u(t_{k-1})\,,\mathbf{u}(t_k)\big)}{\mathsf{q}\big(\mathbf{x}^{(j)}_u(t_k)|\mathbf{x}^{(j)}_u(t_{k-1})\,,\mathbf{z}(t_k)\,,\mathbf{u}(t_k)\big)} \tag{4.20}$$

is the weight for the j-th particle at time instant t_k which is calculated recursively as described in Appendix B. Using the transition prior as the importance density, hence,

$$\mathsf{q}\big(\mathbf{x}_u(t_k)|\mathbf{x}_u(t_{k-1})\,,\mathbf{z}(t_k)\,,\mathbf{u}(t_k)\big) = \mathsf{p}\big(\mathbf{x}_u(t_k)|\mathbf{x}_u(t_{k-1})\,,\mathbf{u}(t_k)\big)\,, \tag{4.21}$$

we obtain from (4.20)

$$\begin{aligned} w^{(j)}(t_k) &\propto w^{(j)}(t_{k-1}) \cdot \mathsf{p}\big(\mathbf{z}(t_k)|\mathbf{x}_u^{(j)}(t_k)\,,\mathbf{z}(t_{k-1})\big) \\ &\propto w^{(j)}(t_{k-1}) \int \mathsf{p}\big(\mathbf{z}(t_k)|\mathbf{x}_u^{(j)}(t_k)\,,\mathbf{x}_{\mathrm{VT}}(t_k)\,,\mathbf{z}(t_{k-1})\big) \\ &\qquad \times \mathsf{p}\big(\mathbf{x}_{\mathrm{VT}}(t_k)|\mathbf{x}_u^{(j)}(t_k)\,,\mathbf{z}(t_{k-1})\big)\ \mathrm{d}\mathbf{x}_{\mathrm{VT}}(t_k) \\ &\propto w^{(j)}(t_{k-1}) \prod_{i=0}^{N(t_k)-1} \int \mathsf{p}\big(\mathbf{z}_i(t_k)|\mathbf{x}_u^{(j)}(t_k)\,,\mathbf{x}_{\mathrm{VT},i}(t_k)\,,\mathbf{z}_i(t_{k-1})\big) \\ &\qquad \times \mathsf{p}\big(\mathbf{x}_{\mathrm{VT},i}(t_k)|\mathbf{x}_u^{(j)}(t_k)\,,\mathbf{z}_i(t_{k-1})\big)\ \mathrm{d}\mathbf{x}_{\mathrm{VT},i}(t_k)\ , \end{aligned} \tag{4.22}$$

again with the assumption of independency among MPCs. The term $\mathsf{p}\big(\mathbf{x}_{\mathrm{VT},i}(t_k)|\mathbf{x}_u^{(j)}(t_k)\,,\mathbf{z}_i(t_{k-1})\big)$ of (4.22) can be reformulated to

$$\begin{aligned} \mathsf{p}\big(\mathbf{x}_{\mathrm{VT},i}(t_k)|\mathbf{x}_u^{(j)}(t_k)\,,\mathbf{z}_i(t_{k-1})\big) = \int \mathsf{p}\big(\mathbf{x}_{\mathrm{VT},i}(t_k)|\mathbf{x}_{\mathrm{VT},i}(t_{k-1})\,,\mathbf{x}_u^{(j)}(t_k)\,,\mathbf{z}_i(t_{k-1})\big) \\ \times \mathsf{p}\big(\mathbf{x}_{\mathrm{VT},i}(t_{k-1})|\mathbf{x}_u^{(j)}(t_k)\,,\mathbf{z}_i(t_{k-1})\big)\ \mathrm{d}\mathbf{x}_{\mathrm{VT},i}(t_{k-1})\ . \end{aligned} \tag{4.23}$$

In order to calculate (4.23), we consider the stationarity of the VTs for all time instants of (4.13) and that the states of the VTs $\mathbf{x}_{\mathrm{VT},i}(t_{k-1})$ are independent from the receiver states $\mathbf{x}_u^{(j)}(t_k)$ according to (4.12), hence,

$$\begin{aligned} \mathsf{p}\big(\mathbf{x}_{\mathrm{VT},i}(t_k)|\mathbf{x}_{\mathrm{VT},i}(t_{k-1})\,,\mathbf{x}_u^{(j)}(t_k)\,,\mathbf{z}_i(t_{k-1})\big) &= \mathsf{p}\big(\mathbf{x}_{\mathrm{VT},i}(t_k)|\mathbf{x}_{\mathrm{VT},i}(t_{k-1})\big) \\ &= \delta\left(\mathbf{x}_{\mathrm{VT},i}(t_k) - \mathbf{x}_{\mathrm{VT},i}(t_{k-1})\right), \end{aligned} \tag{4.24}$$

and represent $\mathsf{p}\big(\mathbf{x}_{\mathrm{VT},i}(t_{k-1})|\mathbf{x}_u^{(j)}(t_k)\,,\mathbf{z}_i(t_{k-1})\big)$ by $N_{P,j,i}(t_k)$ Kernels $\mathrm{K}(\cdot)$ using a Gaussian kernel based density estimator which is approximated by a regularized PF, see Section 3.4.4, with weight $w_i^{(j,a)}(t_{k-1})$ and bandwidth $\sigma_{\mathrm{K},i}^{(j)}(t_{k-1})$, thus,

$$\mathsf{p}\big(\mathbf{x}_{\mathrm{VT},i}(t_{k-1})|\mathbf{x}_u^{(j)}(t_k)\,,\mathbf{z}_i(t_{k-1})\big) = \sum_{a=1}^{N_{P,j,i}(t_k)} w_i^{(j,a)}(t_{k-1}) \cdot \mathrm{K}(\mathbf{x}_{\mathrm{VT},i}(t_{k-1}) - \mathbf{x}_{\mathrm{VT},i}^{(j,a)}(t_{k-1})). \tag{4.25}$$

Inserting (4.24) and (4.25) in (4.23), we obtain

$$\mathsf{p}\big(\mathbf{x}_{\mathrm{VT},i}(t_k)|\mathbf{x}_u^{(j)}(t_k)\,,\mathbf{z}_i(t_{k-1})\big) \approx \sum_{a=1}^{N_{P,j,i}(t_k)} w_i^{(j,a)}(t_{k-1}) \cdot \mathrm{K}(\mathbf{x}_{\mathrm{VT},i}(t_k) - \mathbf{x}_{\mathrm{VT},i}^{(j,a)}(t_{k-1})). \tag{4.26}$$

Finally, by inserting (4.26) in (4.22), we obtain

$$\begin{aligned} w^{(j)}(t_k) &\propto w^{(j)}(t_{k-1}) \prod_{i=0}^{N(t_k)-1} \sum_{a=1}^{N_{P,j,i}(t_k)} w_i^{(j,a)}(t_{k-1}) \int \mathsf{p}\big(\mathbf{z}_i(t_k)|\mathbf{x}_u^{(j)}(t_k)\,,\mathbf{x}_{\mathrm{VT},i}(t_k)\big) \\ &\quad \times \mathrm{K}(\mathbf{x}_{\mathrm{VT},i}(t_k) - \mathbf{x}_{\mathrm{VT},i}^{(j,a)}(t_{k-1}))\,\mathrm{d}\mathbf{x}_{\mathrm{VT},i}(t_k) \\ &\propto w^{(j)}(t_{k-1}) \prod_{i=0}^{N(t_k)-1} \sum_{a=1}^{N_{P,j,i}(t_k)} \underbrace{w_i^{(j,a)}(t_{k-1})\mathsf{p}\big(\mathbf{z}_i(t_k)|\mathbf{x}_u^{(j)}(t_k)\,,\mathbf{x}_{\mathrm{VT},i}^{(j,a)}(t_k)\big)}_{w_i^{(j,a)}(t_k)}\,, \end{aligned} \tag{4.27}$$

where we use $\mathsf{p}\big(\mathbf{z}_i(t_k)|\mathbf{x}_u^{(j)}(t_k)\,,\mathbf{x}_{\mathrm{VT},i}(t_k)\big) = \mathsf{p}\big(\mathbf{z}_i(t_k)|\mathbf{x}_u^{(j)}(t_k)\,,\mathbf{x}_{\mathrm{VT},i}(t_k)\,,\mathbf{x}_{\mathrm{VT},i}^{(j,a)}(t_{k-1})\big)$ and interpret $\mathrm{K}(\mathbf{x}_{\mathrm{VT},i}(t_k) - \mathbf{x}_{\mathrm{VT},i}^{(j,a)}(t_{k-1}))$ as a density $\mathsf{p}\big(\mathbf{x}_{\mathrm{VT},i}(t_k)|\mathbf{x}_{\mathrm{VT},i}^{(j,a)}(t_{k-1})\big)$ given the particle state $\mathbf{x}_{\mathrm{VT},i}^{(j,a)}(t_{k-1})$ and using $\mathbf{x}_{\mathrm{VT},i}^{(j,a)}(t_k) = \mathbf{x}_{\mathrm{VT},i}^{(j,a)}(t_{k-1})$. Hence, the weight $w_i^{(j,a)}(t_k)$ of the sub-PFs at time instant t_k is

$$w_i^{(j,a)}(t_k) \triangleq w_i^{(j,a)}(t_{k-1}) \cdot \mathsf{p}\big(\mathbf{z}_i(t_k)|\mathbf{x}_u^{(j)}(t_k)\,,\mathbf{x}_{\mathrm{VT},i}^{(j,a)}(t_k)\big). \tag{4.28}$$

4.2.3 Point Estimation

In order to obtain a point estimate of the state, $\hat{\mathbf{x}}(t_k) = \left[\hat{\mathbf{x}}_u(t_k)^T\,,\hat{\mathbf{x}}_{\mathrm{VT}}(t_k)^T\right]^T$, we use the MMSE criterion of (3.7). The MMSE of the RBPF can be derived with (4.19) as

$$\begin{aligned} \hat{\mathbf{x}}(t_k) &= \int \mathbf{x}(t_k)\,\mathsf{p}\big(\mathbf{x}(t_k)|\mathbf{z}(t_{1:k})\,,\mathbf{u}(t_{1:k})\big)\,\mathrm{d}\mathbf{x}(t_k) \\ &= \int_{\mathbf{x}_u(t_k)} \int_{\mathbf{x}_{\mathrm{VT}}(t_k)} \mathbf{x}(t_k)\,\mathsf{p}\big(\mathbf{x}_u(t_k)\,,\mathbf{x}_{\mathrm{VT}}(t_k)|\mathbf{z}(t_{1:k})\,\mathbf{u}(t_{1:k})\big)\,\mathrm{d}\mathbf{x}_u(t_k)\;\mathrm{d}\mathbf{x}_{\mathrm{VT}}(t_k) \\ &= \int_{\mathbf{x}_u(t_k)} \int_{\mathbf{x}_{\mathrm{VT}}(t_k)} \mathbf{x}(t_k)\,\mathsf{p}\big(\mathbf{x}_u(t_k)|\mathbf{z}(t_{1:k})\,,\mathbf{u}(t_{1:k})\big) \\ &\quad \times \mathsf{p}\big(\mathbf{x}_{\mathrm{VT}}(t_k)|\mathbf{x}_u(t_k)\,,\mathbf{z}(t_{1:k})\big)\,\mathrm{d}\mathbf{x}_u(t_k)\;\mathrm{d}\mathbf{x}_{\mathrm{VT}}(t_k) \\ &= \prod_{i=0}^{N(t_k)-1} \int_{\mathbf{x}_u(t_k)} \int_{\mathbf{x}_{\mathrm{VT},i}(t_k)} \mathbf{x}(t_k)\,\mathsf{p}\big(\mathbf{x}_u(t_k)|\mathbf{z}(t_{1:k})\,,\mathbf{u}(t_{1:k})\big) \\ &\quad \times \mathsf{p}\big(\mathbf{x}_{\mathrm{VT},i}(t_k)|\mathbf{x}_u(t_k)\,,\mathbf{z}_i(t_{1:k})\big)\,\mathrm{d}\mathbf{x}_u(t_k)\;\mathrm{d}\mathbf{x}_{\mathrm{VT},i}(t_k)\;, \end{aligned} \tag{4.29}$$

which leads to the approximation of the MMSE for the receiver state

$$\hat{\mathbf{x}}_u(t_k) \approx \sum_{j=1}^{N_s} w^{(j)}(t_k)\;\mathbf{x}_u^{(j)}(t_k)\;, \tag{4.30}$$

and the ith VT

$$\hat{\mathbf{x}}_{\mathrm{VT,i}}(t_k) \approx \sum_{j=1}^{N_s} w^{(j)}(t_k) \sum_{a=1}^{N_{P,j,i}(t_k)} w_i^{(j,a)}(t_k)\;\mathbf{x}_{\mathrm{VT},i}^{(j,a)}(t_k)\;. \tag{4.31}$$

4.2.4 Transition Models

In this thesis, we consider a moving receiver optionally equipped with an IMU. We describe in the following two different transition models reflecting two cases: a receiver not equipped with an IMU referred to as Gaussian-Transition-Model; a receiver equipped with an IMU referred to as IMU-Transition-Model. For both transition models we are using a discrete white noise acceleration model [BSLK04] in a two dimensional Cartesian coordinate system. The receiver state vector $\mathbf{x}_u(t_k) = \left[\boldsymbol{r}_u(t_k)^T, \boldsymbol{v}_u(t_k)^T, b_u(t_k)\right]^T$ as introduced in (4.2) contains the x-y positions

$$\boldsymbol{r}_u(t_k) = \left[r_{u,x}(t_k), r_{u,y}(t_k)\right]^T , \tag{4.32}$$

the corresponding velocities

$$\boldsymbol{v}_u(t_k) = \left[v_{u,x}(t_k), v_{u,y}(t_k)\right]^T \tag{4.33}$$

and the receiver's clock bias $b_u(t_k)$. The state equation for the discrete white noise acceleration model is defined by

$$\mathbf{x}_u(t_k) = \mathbf{A}_u(t_\delta, \dot{\phi}(t_k))\, \mathbf{x}_u(t_{k-1}) + \mathbf{n}_u(t_k) , \tag{4.34}$$

with $t_\delta = t_k - t_{k-1}$, the transition noise $\mathbf{n}_u(t_k)$ and transition matrix

$$\mathbf{A}_u(t_\delta, \dot{\phi}(t_k)) = \begin{cases} \mathbf{A}_{u,L}(t_\delta) & \text{without IMU} \\ \mathbf{A}_{u,I}(t_\delta, \dot{\phi}(t_k)) & \text{with IMU} \end{cases} , \tag{4.35}$$

that will be described in the following. Please note, also other transition models could be applied, see e.g. [GPU+17b, HM95, YFL+03, RABC09, Khi13, PS96, RAG04, KKR12, BSLK04].

Gaussian-Transition-Model

The Gaussian-Transition-Model is a discrete white noise acceleration model [BSLK04], with the transition matrix

$$\mathbf{A}_{u,L}(t_\delta) = \begin{pmatrix} 1 & 0 & t_\delta & 0 & 0 \\ 0 & 1 & 0 & t_\delta & 0 \\ 0 & 0 & 1 & 0 & 0 \\ 0 & 0 & 0 & 1 & 0 \\ 0 & 0 & 0 & 0 & 1 \end{pmatrix} , \tag{4.36}$$

and the covariance matrix $\mathbf{Q}_u(t_\delta) = \mathbf{E}\left[\mathbf{n}_u(t_k) \cdot \mathbf{n}_u(t_k)^H\right]$ with

$$\mathbf{Q}_u(t_\delta) = \begin{pmatrix} \sigma^2_{q_u}\frac{(t_\delta)^3}{3} & 0 & \sigma^2_{q_u}\frac{(t_\delta)^2}{2} & 0 & 0 \\ 0 & \sigma^2_{q_u}\frac{(t_\delta)^3}{3} & 0 & \sigma^2_{q_u}\frac{(t_\delta)^2}{2} & 0 \\ \sigma^2_{q_u}\frac{(t_\delta)^2}{2} & 0 & \sigma^2_{q_u}t_\delta & 0 & 0 \\ 0 & \sigma^2_{q_u}\frac{(t_\delta)^2}{2} & 0 & \sigma^2_{q_u}t_\delta & 0 \\ 0 & 0 & 0 & 0 & \sigma^2_{q_b} \end{pmatrix}, \tag{4.37}$$

where $\sigma^2_{q_u}$ defines the continuous-time process noise intensity, which has to be dimensioned according to the application with physical dimension $\left[\frac{\mathrm{m}^2}{\mathrm{s}^3}\right]$ and $\sigma^2_{q_b}$ the variance of the clock bias following a random walk model [PS96,RAG04]. If physical transmitter and receiver oscillators provide different frequencies, a clock drift parameter has to be considered additionally.

IMU-Transition-Model

The IMU-Transition-Model is based on a discrete white noise acceleration model incorporating additional information from an IMU. We use solely the heading changes from the IMU. The heading changes allow to improve the performance of Channel-SLAM by resolving ambiguities such that AoA measurements are not required anymore. Additionally we consider the moving indicator $m(t_k)$ if the object is moving with $m(t_k) = 1$ or static with $m(t_k) = 0$ based on the amplitude of the inertial measurement. Further details about the used IMU, the coordinate transformation and preprocessing can be found in Appendix A. The IMU-Transition-Model includes the heading changes $\dot{\phi}(t_k)$ in the transition matrix $\mathbf{A}_{u,I}(t_\delta, \dot{\phi}(t_k))$, with

$$\mathbf{A}_{u,I}(t_\delta, \dot{\phi}(t_k)) = \begin{pmatrix} 1 & 0 & t_\delta \cdot m(t_k) & 0 & 0 \\ 0 & 1 & 0 & t_\delta \cdot m(t_k) & 0 \\ 0 & 0 & \cos(\dot{\phi}(t_k)) & -\sin(\dot{\phi}(t_k)) & 0 \\ 0 & 0 & \sin(\dot{\phi}(t_k)) & \cos(\dot{\phi}(t_k)) & 0 \\ 0 & 0 & 0 & 0 & 1 \end{pmatrix} \tag{4.38}$$

and the covariance matrix $\mathbf{Q}_u(t_\delta)$ defined in (4.37). Equivalently to the Gaussian-Transition-Model we use in (4.38) a random walk model for the clock bias [PS96, RAG04].

Algorithm 9: Channel-SLAM for time instant t_k

Input:

Multipath estimates: $\mathbf{z}(t_k)$, $\boldsymbol{\sigma}_z^2(t_k)$;

Control input: $\mathbf{u}(t_k)$;

States and weights for $t_k > t_1$:

$$\left\{ \mathbf{x}_u^{(j)}(t_{k-1}), w^{(j)}(t_{k-1}), \left\{ \left\{ \mathbf{x}_{\mathrm{VT},i}^{(j,a)}(t_{k-1}), w_i^{(j,a)}(t_{k-1}) \right\}_{a=1}^{N_{p,j,i}(t_{k-1})} \right\}_{i=0}^{N(t_{k-1})-1} \right\}_{j=1}^{N_s};$$

Initial prior information: $\mathbf{x}_u(t_0)$ for $t_k = t_1$;

Output:

States and weights for $t_k \geq t_1$:

$$\left\{ \mathbf{x}_u^{(j)}(t_k), w^{(j)}(t_k), \left\{ \left\{ \mathbf{x}_{\mathrm{VT},i}^{(j,a)}(t_k), w_i^{(j,a)}(t_k) \right\}_{a=1}^{N_{p,j,i}(t_k)} \right\}_{i=0}^{N(t_k)-1} \right\}_{j=1}^{N_s};$$

if $t_k = t_1$ **then**
  Initialization using $\mathbf{x}_u(t_0)$, $\mathbf{z}(t_1)$ and $\boldsymbol{\sigma}_z^2(t_1)$;
for $j = 1 : N_s$ **do**
  Draw $\mathbf{x}_u^{(j)}(t_k) \sim \mathsf{p}\big(\mathbf{x}_u^{(j)}(t_k) | \mathbf{x}_u^{(j)}(t_{k-1}), \mathbf{u}(t_k)\big)$;
  if *New MPCs detected* **then**
    Initialize new sub-PFs;
  if *Tracking of MPCs lost* **then**
    Delete corresponding sub-PFs;
  for $i = 0 : N(t_k) - 1$ **do**
    for $a = 1 : N_{P,j,i}(t_k)$ **do**
      Assign $\mathbf{x}_{\mathrm{VT},i}^{(j,a)}(t_k) = \mathbf{x}_{\mathrm{VT},i}^{(j,a)}(t_{k-1})$;
      Calculate $w_i^{(j,a)}(t_k) = w_i^{(j,a)}(t_{k-1})\ \mathsf{p}\big(\mathbf{z}_i(t_k) | \mathbf{x}_u^{(j)}(t_k), \mathbf{x}_{\mathrm{VT},i}^{(j,a)}(t_k)\big)$;
    Calculate total sub-PF weight: $t_{j,i} = \mathrm{SUM}[\{w_i^{(j,a)}(t_k)\}_{a=1}^{N_{P,j,i}(t_k)}]$;
  $w^{(j)}(t_k) = \prod_{i=0}^{N(t_k)-1} t_{j,i}$;
  Resample using Algorithm 10;
  Calculate MMSE $\hat{\mathbf{x}}(t_k)$ according to (4.29);

4.3 Channel-SLAM Implementation

Algorithm 9 provides the pseudo-code of Channel-SLAM, which is executed at every time instant $t_k \geq t_1$ with the estimates $\mathbf{z}(t_k), \boldsymbol{\sigma}_z^2(t_k)$ obtained from KEST and the control input $\mathbf{u}(t_k)$. During the initialization, at time instant $t_k = t_1$, the particles $\{\mathbf{x}_u^{(j)}(t_1)\}_{j=1}^{N_s}$ of the super-PF are initialized according to prior information $\mathbf{x}_u(t_0)$. The particles $\{\mathbf{x}_{\mathrm{VT},i}^{(j,a)}(t_1)\}_{a=1}^{N_{P,j,i}(t_1)}$ of the sub-PFs are initialized depending on $\mathbf{x}_u^{(j)}(t_1)$ and the measurements $\hat{d}_i(t_1)$ and $\hat{\theta}_i(t_1)$ for the i-th MPC. A grid is used to initialize the states of $\mathbf{x}_{\mathrm{VT},i}^{(j,a)}(t_1)$ with $a = 1, \ldots, N_{P,j,i}(t_1)$ of the j-th sub-PF associated to the i-th MPC. Whether a linear antenna array or a single receiving antenna is used, the initialization is done differently:

- **Linear antenna array**
  The positions $\mathbf{r}_{\mathrm{VT},i}^{(j,a)}(t_1)$ of the particles $\{\mathbf{x}_{\mathrm{VT},i}^{(j,a)}(t_1)\}_{a=1}^{N_{P,j,i}(t_1)}$ are distributed such that

$$0 \leq \|\mathbf{r}_{\mathrm{VT},i}^{(j,a)}(t_1) - \boldsymbol{r}_u^{(j)}(t_1)\| \leq \hat{d}_i(t_1) + \Delta_d\,, \tag{4.39}$$

  with spacing Δ_d, hence, there are $N_{d,i} = \lfloor \frac{\hat{d}_i(t_1)}{\Delta_d} \rfloor + 1$ grid points and

$$\begin{aligned} &\hat{\theta}_i(t_1) - K \cdot \sigma_{\theta,i}(t_1) \\ &\qquad \leq \arccos\left(\frac{\left(\mathbf{r}_{\mathrm{VT},i}^{(j,a)}(t_1) - \boldsymbol{r}_u^{(j)}(t_1)\right) \cdot \boldsymbol{v}_u^{(j)}(t_1)}{\|\mathbf{r}_{\mathrm{VT},i}^{(j,a)}(t_1) - \boldsymbol{v}_u^{(j)}(t_1)\| \cdot \|\boldsymbol{v}_u^{(j)}(t_1)\|} \right) \leq \\ &\qquad\qquad \hat{\theta}_i(t_1) + K \cdot \sigma_{\theta,i}(t_1)\,, \end{aligned} \tag{4.40}$$

  with spacing Δ_θ, resulting in $N_{\theta,i} = \lfloor \frac{2K \cdot \sigma_{\theta,i}}{\Delta_\theta} \rfloor + 1$ grid points, where K denotes an empirical constant value. The additional propagation distance is $d_{\mathrm{VT},i}^{(j,a)}(t_1) = \hat{d}_i(t_1) - \|\mathbf{r}_{\mathrm{VT},i}^{(j,a)}(t_1) - \boldsymbol{r}_u^{(j)}(t_1)\|$, where we inherently assume $b_u(t_1) = 0$ for the initialization. Hence, the total number of particles during initialization can be calculated as

$$N_{\mathrm{t}}(t_1) = \sum_{j=1}^{N_p} \sum_{i=0}^{N(t_1)-1} N_{P,j,i}(t_1) = N_p \sum_{i=0}^{N(t_1)-1} N_{d,i} \cdot N_{\theta,i}. \tag{4.41}$$

- **Single receiving antenna**
  The positions $\mathbf{r}_{\mathrm{VT},i}^{(j,a)}(t_1)$ of the particles $\{\mathbf{x}_{\mathrm{VT},i}^{(j,a)}(t_1)\}_{a=1}^{N_{P,j,i}(t_1)}$ are distributed on a grid inside a circle around $\boldsymbol{r}_u^{(j)}(t_1)$ with radius $\hat{d}_i(t_1) + \Delta_d$ such that (4.39) with spacing Δ_d holds. The number of grid points $N_{P,j,i}(t_1)$ can be estimated by the Gauss's circle problem [Har15]. The additional propagation distance is $d_{\mathrm{VT},i}^{(j,a)}(t_1) = \hat{d}_i(t_1) -$

$\|\mathbf{r}_{\mathrm{VT},i}^{(j,a)}(t_1) - \boldsymbol{r}_u^{(j)}(t_1)\|$, where we inherently assume $b_u(t_1) = 0$ for the initialization. Hence, the total number of particles during initialization can be calculated as

$$N_{\mathrm{t}}(t_1) = \sum_{j=1}^{N_p} \sum_{i=0}^{N(t_1)-1} N_{P,j,i}(t_1)\,. \tag{4.42}$$

For each particle j of the super-PF, the receiver state $\mathbf{x}_u^{(j)}(t_k)$ is drawn according to the transition models described in Section 4.2.4. Additionally, an individual MPC may not always be visible while the receiver is moving. Hence, new MPCs appear or existing MPCs disappear after a certain time during the receiver movement. Hence, Channel-SLAM determines at each time instant whether the number of estimated MPCs has changed. In case that new MPCs have been detected, new sub-PFs are added and initialized using (4.39) and (4.40) (cf. Line 6 in Algorithm 9). In case that MPCs disappeared the corresponding sub-PFs are removed (cf. Line 8 in Algorithm 9). Neither KEST nor Channel-SLAM consider re-tracking of previous MPCs. Hence, if the tracking of a MPC has been lost and might be regained, the corresponding VT is initialized without any prior information. According to (4.13) the state $\mathbf{x}_{\mathrm{VT},i}(t_k)$ is time-invariant, hence each sub-PF assigns the states of the VTs with $\mathbf{x}_{\mathrm{VT},i}^{(j,a)}(t_k) = \mathbf{x}_{\mathrm{VT},i}^{(j,a)}(t_{k-1})$ and calculates the weight $w_i^{(j,a)}(t_k)$ using (4.45). Thereafter, the weight $w^{(j)}(t_k)$ is calculated using (4.27) (cf. Line 14 in Algorithm 9). Afterwards, the particles of the sub-PFs and super-PF are resampled. To prevent degeneration, resampling is performed at each time instant. Algorithm 10 shows a pseudo-code of the derived resampling algorithm for Channel-SLAM. The resampling algorithm for Channel-SLAM is based on the systematic resampling algorithm [Kit96]. Please note that Algorithm 10 is split into two parts: Part I shown on Page 55 and Part II shown on Page 56. Similarly to Algorithm 9, the Channel-SLAM resampling algorithm consists of a superordinate and subordinates resampling algorithms. First, the estimated sampled CDF of the super-PF is constructed, presented by a vector $\mathbf{c}_p$ with length N_p and element $[\mathbf{c}_p]_j$ with $j = 1, \ldots, N_p$. According to the estimated sampled CDF of the super-PF, the sub-PFs are eliminated or resampled. The particles of the super-PF with index f are assigned to the resampled particle index j for the assignment of the receiver state (cf. Line 10 in Algorithm 10). Afterwards, the (f, i)-th sub-PF is resampled with $i = 0, \ldots N(t_k) - 1$ using a systematic resampling algorithm, where $\mathbf{c}_b$ represents the estimated sampled CDF of the (f, i)-th sub-PF.

As mentioned before, whenever a new MPC is tracked, many particles are initialized to cover all possible VT positions in each sub-PF. However during the receiver movement many particles of the sub-PFs are resampled at the same grid point because the states of the VTs $\mathbf{x}_{\mathrm{VT},i}(t_k)$ are time-invariant. In order to reduce the number of

particles, we limit the number of resampled particles per grid point to N_m (cf. Line 20 in Algorithm 10). The number of particles per grid point are counted by the function $\mathrm{Bin}(\cdot)$ (cf. Line 24 in Algorithm 10). In order to include the weight of the reduced number of particles, the weight is updated if the particles per bin exceed N_m (cf. Line 28 in Algorithm 10). Afterwards the states of the VTs $\mathbf{x}_{\mathrm{VT},i}^{(j,a)}(t_k)$ are drawn using a Gaussian-Kernel (cf. Line 29 in Algorithm 10). The Gaussian-Kernel has a low bandwidth which does not influence the grid based reduction method.

Algorithm 10: Resampling algorithm for Channel-SLAM (Part I)

Input:

States and weights:

$$\left\{ \mathbf{x}_u^{(j)}(t_k), w^{(j)}(t_k), \left\{ \left\{ \mathbf{x}_{\mathrm{VT},i}^{(j,a)}(t_k), w_i^{(j,a)}(t_k) \right\}_{a=1}^{N_{p,j,i}(t_k)} \right\}_{i=0}^{N(t_k)-1} \right\}_{j=1}^{N_s};$$

Output:

Resampled states and weights:

$$\left\{ \tilde{\mathbf{x}}_u^{(j)}(t_k), \tilde{w}^{(j)}(t_k), \left\{ \left\{ \tilde{\mathbf{x}}_{\mathrm{VT},i}^{(j,a)}(t_k), \tilde{w}_i^{(j,a)}(t_k) \right\}_{a=1}^{N_{p,j,i}(t_k)} \right\}_{i=0}^{N(t_k)-1} \right\}_{j=1}^{N_s};$$

1 Initialize the CDF for super-PF: $[\mathbf{c}_p]_1 = w^{(1)}(t_k)$;

2 **for** $j = 2 : N_s$ **do**

3 Construct CDF for super-PF: $[\mathbf{c}_p]_j = [\mathbf{c}_p]_{j-1} + w^{(j)}(t_k)$;

4 $f = 1$;

5 Draw starting point: $[\mathbf{u}_p]_1 \sim \mathcal{U}[0, N_s^{-1}]$;

Algorithm 10: Continued from Page 55, Resampling algorithm for Channel-SLAM (Part II)

for $j = 1 : N_s$ **do**
  $[\mathbf{u}_p]_j = [\mathbf{u}_p]_1 + N_s^{-1} \cdot (j-1)$;
  while $[\mathbf{u}_p]_j > [\mathbf{c}_p]_f$ **do**
    $f = f + 1$;
  Assign: $\left\{\tilde{\mathbf{x}}_u^{(j)}(t_k), \tilde{w}^{(j)}(t_k)\right\} = \left\{\mathbf{x}_u^{(f)}(t_k), 1/N_s\right\}$;
  for $i = 0 : N(t_k) - 1$ **do**
    Initialize the CDF for (f,i)-th sub-PF: $[\mathbf{c}_b]_1 = w_i^{(f,1)}(t_k)$;
    for $a = 2 : N_{P,i,f}(t_k)$ **do**
      Construct CDF for sub-PF: $[\mathbf{c}_b]_a = [\mathbf{c}_b]_{a-1} + w_i^{(f,a)}(t_k)$;
    $g = 1,\ a_r = 1$;
    for $a = 1 : N_{P,f,i}(t_k)$ **do**
      $[\mathbf{u}_b]_a = [\mathbf{u}_b]_1 + 1/N_{P,i,f}(t_k) \cdot (a-1)$;
      while $[\mathbf{u}_b]_a > [\mathbf{c}_b]_g$ **do**
        $g = g + 1$;
      if Bin $\left(\tilde{\mathbf{x}}_{\mathrm{VT},i}^{(j,a_r)}(t_k)\right) \leq N_m$ **then**
        Assign: $\tilde{\mathbf{x}}_{\mathrm{VT},i}^{(j,a_r)}(t_k) = \mathbf{x}_{\mathrm{VT},i}^{(f,g)}(t_k)$;
        Assign: $\tilde{w}_i^{(j,a_r)}(t_k) = 1/N_{P,j,i}(t_k)$;
        $a_r = a_r + 1$;
      Bin $\left(\tilde{\mathbf{x}}_{\mathrm{VT},i}^{(j,a_r)}(t_k)\right) = \mathrm{Bin}\left(\tilde{\mathbf{x}}_{\mathrm{VT},i}^{(j,a_r)}(t_k)\right) + 1$;
    Update number of particles: $N_{P,j,i}(t_k) = a_r$;
    for $a = 1 : N_{P,j,i}(t_k)$ **do**
      if Bin $\left(\tilde{\mathbf{x}}_{\mathrm{VT},i}^{(j,a)}(t_k)\right) > N_m$ **then**
        Update weight: $\tilde{w}_i^{(j,a)}(t_k) = \tilde{w}_i^{(j,a)}(t_k) \cdot \mathrm{Bin}\left(\tilde{\mathbf{x}}_{\mathrm{VT},i}^{(j,a)}(t_k)\right)/N_m$;
      Draw $\tilde{\mathbf{x}}_{\mathrm{VT},i}^{(j,a)}(t_k) = \tilde{\mathbf{x}}_{\mathrm{VT},i}^{(j,a)}(t_k) + \varepsilon$ with $\varepsilon \sim \mathcal{N}\left(0, \sigma_{\mathrm{K},i}^{(j)}(t_k)\right)$;

4.4 Channel-SLAM in Logarithm Domain

As mentioned in Section 3.4.6, computing the weights in log-domain can provide more accurate results and a more stable implementation. Hence, the RBPF of Channel-SLAM can be transferred to compute all steps in the log-domain using the Jacobian logarithm [EPG94, KB90, RVH95]. From (4.19), we obtain

$$\mathsf{p}\big(\mathbf{x}_u(t_k)|\mathbf{z}(t_{1:k})\,,\mathbf{u}(t_{1:k})\big) \approx \sum_{j=1}^{N_s} e^{\hat{w}^{(j)}(t_k)}\;\delta\left(\mathbf{x}_u(t_k)-\mathbf{x}_u^{(j)}(t_k)\right)\,, \tag{4.43}$$

with the log-weights $\hat{w}^{(j)}(t_k)$ using (3.36). By transferring (4.27) and (4.45) to the log-domain, we obtain

$$\begin{aligned}\hat{w}^{(j)}(t_k) &\propto \hat{w}^{(j)}(t_{k-1}) + \ln\left(\mathsf{p}\big(\mathbf{z}(t_k)|\mathbf{x}_u^{(j)}(t_k)\,,\mathbf{z}(t_{k-1})\big)\right)\\ &= \hat{w}^{(j)}(t_{k-1}) + \sum_{i=1}^{N(t_k)} \ln\left(\sum_{a=1}^{N_{P,i,j}(t_k)} e^{\hat{w}_i^{(j,a)}(t_k)}\right)\\ &= \hat{w}^{(j)}(t_{k-1}) + \sum_{i=1}^{N(t_k)} \mathrm{Jacob}\big(\{\hat{w}_i^{(j,a)}(t_k)\}_{a=1}^{N_{P,i,j}(t_k)}\big)\,,\end{aligned} \tag{4.44}$$

using the Jacabian logarithm of Algorithm 6 and with the log-weights

$$\hat{w}_i^{(j,a)}(t_k) \triangleq \hat{w}_i^{(j,a)}(t_{k-1}) + \ln\left(\mathsf{p}\big(\mathbf{z}_i(t_k)|\mathbf{x}_u^{(j)}(t_k)\,,\mathbf{x}_{\mathrm{VT},i}^{(j,a)}(t_k)\big)\right), \tag{4.45}$$

of the sub-PFs at time instant t_k. According to Section 3.4.6 and [GZJ18] all steps of the PF can be calculated in log-domain including weight normalization, resampling and point estimations in a straightforward manner.

In [GZJ18], we show an example of Channel-SLAM where we clearly observe a higher accuracy using the RBPF implementation in the log-domain if the width of the likelihood distribution is too small in comparison to the width of the prior distribution. However, in the considered scenarios of Chapter 5 and Chapter 6, the proposed RBPF implementation in log-domain does not improve the performance. Hence, we do not consider the RBPF implementation in log-domain in the following.

Chapter 5

Theoretical Performance Evaluations

In this chapter, we evaluate the performance of Channel-SLAM based on simulations. The first part of this chapter describes the derivation of the PCRLB for Channel-SLAM. To verify the position accuracy, the second part compares the performance of Channel-SLAM to the PCRLB and to four state-of-the-art algorithms based on a simulated scenario.

5.1 Posterior Cramér-Rao Lower Bound

The PCRLB is the theoretical performance bound of an unbiased sequential Bayesian estimator [TMN98, VTB07] and can be calculated by the inverse of the posterior information matrix $\mathbf{J}(t_k)$, with

$$\mathbf{E}_{\mathbf{x}(t_k)}\left[\left(\hat{\mathbf{x}}(t_k)-\mathbf{x}(t_k)\right)\left(\hat{\mathbf{x}}(t_k)-\mathbf{x}(t_k)\right)^T\right]=\mathbf{M}(t_k)\succeq\mathbf{J}(t_k)^{-1}\,, \tag{5.1}$$

where $\mathbf{E}_a[\cdot]$ stands for expectation with respect to $\mathsf{p}\big(a\big)$. The inequality in (5.1) means that the difference $\mathbf{M}(t_k)-\mathbf{J}(t_k)^{-1}$ is a positive semi-definite matrix. The posterior information matrix $\mathbf{J}(t_k)$ can be calculated recursively according to [TMN98, VTB07, SS16], with

$$\mathbf{J}(t_k)=\mathbf{D}_{22}(t_k)-\mathbf{D}_{21}(t_k)\left(\mathbf{J}(t_{k-1})+\mathbf{D}_{11}(t_k)\right)^{-1}\mathbf{D}_{12}(t_k)\,, \tag{5.2}$$

where

$$\mathbf{D}_{11}(t_k)=-\mathbf{E}_{\mathbf{x}(t_{k-1}),\mathbf{x}(t_k)|\mathbf{u}(t_k)}\left[\Delta^{\mathbf{x}(t_{k-1})}_{\mathbf{x}(t_{k-1})}\ln\mathsf{p}\big(\mathbf{x}(t_k)|\mathbf{x}(t_{k-1})\,,\mathbf{u}(t_k)\big)\right]\,, \tag{5.3}$$

$$\mathbf{D}_{21}(t_k)=-\mathbf{E}_{\mathbf{x}(t_{k-1}),\mathbf{x}(t_k)|\mathbf{u}(t_k)}\left[\Delta^{\mathbf{x}(t_{k-1})}_{\mathbf{x}(t_k)}\ln\mathsf{p}\big(\mathbf{x}(t_k)|\mathbf{x}(t_{k-1})\,,\mathbf{u}(t_k)\big)\right]=\mathbf{D}_{12}(t_k)^T\,, \tag{5.4}$$

$$\begin{aligned}\mathbf{D}_{22}(t_k)=&-\mathbf{E}_{\mathbf{x}(t_{k-1}),\mathbf{x}(t_k)|\mathbf{u}(t_k)}\left[\Delta^{\mathbf{x}(t_k)}_{\mathbf{x}(t_k)}\ln\mathsf{p}\big(\mathbf{x}(t_k)|\mathbf{x}(t_{k-1})\,,\mathbf{u}(t_k)\big)\right]\\&-\mathbf{E}_{\mathbf{x}(t_k),\mathbf{z}(t_k)|\mathbf{u}(t_k)}\left[\Delta^{\mathbf{x}(t_k)}_{\mathbf{x}(t_k)}\ln\mathsf{p}\big(\mathbf{z}(t_k)|\mathbf{x}(t_k)\big)\right]\,,\end{aligned} \tag{5.5}$$

where ∇_a stands for the first-order partial derivatives with respect to a and Δ_a^b stands for the second-order partial derivatives with $\Delta_a^b \triangleq \nabla_a \nabla_b^T$. To calculate the PCRLB, we combine the time-invariant transition model for the VTs $\mathbf{x}_{\mathrm{VT}}(t_k)$ as introduced in (4.13) and the transition model of the receiver of (4.34) as

$$\mathbf{x}(t_k) = \underbrace{\begin{pmatrix} \mathbf{A}_u(t_\delta, \dot{\phi}(t_k)) & \mathbf{0} \\ \mathbf{0} & \mathbf{I} \end{pmatrix}}_{\mathbf{A}(t_\delta, \dot{\phi}(t_k))} \mathbf{x}(t_{k-1}) + \mathbf{n}_t(t_k)\,, \tag{5.6}$$

with the identity matrix $\mathbf{I}$, the zero matrix $\mathbf{0}$ and the transition noise $\mathbf{n}_t(t_k) \sim \mathcal{N}(0, \mathbf{Q}(t_\delta))$ with covariance matrix

$$\mathbf{Q}(t_\delta) = \begin{pmatrix} \mathbf{Q}_u(t_\delta) & \mathbf{0} \\ \mathbf{0} & \mathbf{0} \end{pmatrix}\,, \tag{5.7}$$

where $\mathbf{Q}_u(t_\delta)$ is defined in (4.37). In case of the linear transition model of (5.6) and Gaussian distributed transition noise, we obtain for (5.3), (5.4) and (5.5)

$$\mathbf{D}_{11}(t_k) = \mathbf{A}(t_\delta, \dot{\phi}(t_k))^T \mathbf{Q}(t_\delta)^{-1} \mathbf{A}(t_\delta, \dot{\phi}(t_k))\,, \tag{5.8}$$

$$\mathbf{D}_{12}(t_k) = -\mathbf{A}(t_\delta, \dot{\phi}(t_k))^T \mathbf{Q}(t_\delta)^{-1}\,, \tag{5.9}$$

$$\mathbf{D}_{22}(t_k) = \mathbf{Q}(t_\delta)^{-1} + \mathbf{C}(t_k)\,, \tag{5.10}$$

where $\mathbf{C}(t_k)$ relates the PCRLB to the measurement model, with

$$\begin{aligned} \mathbf{C}(t_k) &= \mathbf{E}_{\mathbf{x}(t_k), \mathbf{z}(t_k)|\mathbf{u}(t_k)} \left[\Delta^{\mathbf{x}(t_k)}_{\mathbf{x}(t_k)} \ln \mathsf{p}\big(\mathbf{z}(t_k)|\mathbf{x}(t_k)\big) \right] \\ &= \mathbf{E}_{\mathbf{x}(t_k)|\mathbf{u}(t_k)} \left[\mathbf{E}_{\mathbf{z}(t_k)|\mathbf{x}(t_k), \mathbf{u}(t_k)} \left[\Delta^{\mathbf{x}(t_k)}_{\mathbf{x}(t_k)} \ln \mathsf{p}\big(\mathbf{z}(t_k)|\mathbf{x}(t_k)\big) \right] \right]\,, \end{aligned} \tag{5.11}$$

where the term inside the outer expectation is the classic Fisher information matrix [VTB07, Rao45, Cra16, Cra46]. Substituting (5.8), (5.9) and (5.10) into (5.2), we get

$$\mathbf{J}(t_k) = \mathbf{C}(t_k) + \Big(\mathbf{Q}(t_\delta) + \mathbf{A}(t_\delta, \dot{\phi}(t_k)) \mathbf{J}(t_{k-1})^{-1} \mathbf{A}(t_\delta, \dot{\phi}(t_k))^T \Big)^{-1}\,, \tag{5.12}$$

using the matrix inversion lemma. The recursion (5.12) involves computations with the initial posterior Fisher information matrix $\mathbf{J}(t_0)$ calculated from the prior information $\mathsf{p}\big(\mathbf{x}(t_0)\big)$ with

$$\mathbf{J}(t_0) = -\mathbf{E}_{\mathbf{x}(t_k)} \left[\Delta^{\mathbf{x}(t_0)}_{\mathbf{x}(t_0)} \ln \mathsf{p}\big(\mathbf{x}(t_0)\big) \right]\,. \tag{5.13}$$

As mentioned before, the matrix $\mathbf{C}(t_k)$ of (5.11) relates the PCRLB to the measurement at time instant t_k. In order to calculate $\mathbf{C}(t_k)$, we consider both levels, i.e. the signal parameter estimation and Channel-SLAM. In general, a two level approach

performs either equally or worse than an estimator which jointly combines both levels. Thus, the derived PCRLB is based on a theoretical joint approach and considers therefore the best possible estimator. Using $a_l(\theta_i(t_k)) = e^{-j2\pi f_c \tau_{i,l}(t_k)}$ where $\tau_{i,l}(t_k)$ is the delay of the i-th MPC for the l-th antenna element $l = 1 \dots L$, we obtain from (2.5) the signal received by the l-th antenna at time t_k as

$$y_l(t_k, \tau_m) = \sum_{i=0}^{N(t_k)-1} \alpha_i(t_k)\, e^{-j2\pi f_c \tau_{i,l}(t_k)}\, s(\tau_m - \tau_i(t_k)) + n(\tau_m)\,. \tag{5.14}$$

According to the system model in (4.17), the delay $\tau_{i,l}(t_k)$ of the i-th MPC is

$$\tau_{i,l}(t_k) = \left(\|\tilde{\mathbf{d}}_{\mathrm{VT},i,l}(t_k)\| + d_{\mathrm{VT},i}(t_k) \right) \frac{1}{c} + b_u(t_k) \tag{5.15}$$

and

$$\tilde{\mathbf{d}}_{\mathrm{VT},i,l}(t_k) = \boldsymbol{r}_{\mathrm{VT},i}(t_k) - \left(\boldsymbol{r}_u(t_k) + \frac{\boldsymbol{v}_u(t_k) \cdot (l-1) \cdot d}{\|\boldsymbol{v}_u(t_k)\|} \right), \tag{5.16}$$

where d defines the spacing between adjacent antennas. From (5.14), the discrete channel transfer function in dependence on $\mathbf{x}(t_k)$ can be written as

$$\mu(\omega_m, l; \mathbf{x}(t_k)) = \sum_{i=0}^{N(t_k)-1} \alpha_{i,l}(t_k) e^{-j(2\pi f_c + \omega_m)\, \tau_{i,l}(t_k)}\,, \tag{5.17}$$

where f_c is the carrier frequency, ω_m defines the discrete circular frequency at index $m = 0 \dots M-1$ and $\alpha_{i,l}(t_k)$ the complex amplitude of the i-th MPC.

Finally, we obtain for (5.11)

$$\mathbf{C}(t_k) = \mathbf{E}_{\mathbf{x}(t_k)|\mathbf{u}(t_k)} \left[2\, \Re\Big\{ \left(\nabla_{\mathbf{x}(t_k)} \boldsymbol{\mu}(\mathbf{x}(t_k)) \right)^H \mathbf{R}(t_k)^{-1} \left(\nabla_{\mathbf{x}(t_k)} \boldsymbol{\mu}(\mathbf{x}(t_k)) \right) \Big\} \right], \tag{5.18}$$

see [Kay93, RAG04, VTB07], where $\mathbf{R}(t_k) = \sigma_n^2 \mathbf{I}$ is the covariance matrix, $\Re\{\cdot\}$ denotes the real part and

$$\begin{aligned} \boldsymbol{\mu}(\mathbf{x}(t_k)) = [&\mu(\omega_0, 1; \mathbf{x}(t_k)), \dots, \mu(\omega_0, L; \mathbf{x}(t_k)), \\ &\dots, \mu(\omega_{M-1}, 1; \mathbf{x}(t_k)), \dots, \mu(\omega_{M-1}, L; \mathbf{x}(t_k))]^T\,. \end{aligned}$$

The derivatives of $\boldsymbol{\mu}(\mathbf{x}(t_k))$ with respect to the receiver position $\boldsymbol{r}_u(t_k)$, velocity $\boldsymbol{v}_u(t_k)$, clock bias $b_u(t_k)$, i-th VT position $\boldsymbol{r}_{\mathrm{VT},i}(t_k)$ and corresponding additional distance $d_{\mathrm{VT},i}(t_k)$ are

$$\nabla_{\boldsymbol{r}_u(t_k)}\boldsymbol{\mu}(\mathbf{x}(t_k)) = \sum_{i=0}^{N(t_k)-1} \left\{ \frac{j(2\pi f_c + \omega_m)\alpha_{i,l}(t_k)e^{-j(2\pi f_c+\omega_m)\tau_{i,l}(t_k)}}{c \cdot \|\boldsymbol{r}_{\mathrm{VT},i}(t_k) - (\boldsymbol{r}_u(t_k) + \frac{\boldsymbol{v}_u(t_k)\cdot(l-1)\cdot d}{\|\boldsymbol{v}_u(t_k)\|})\|} \cdot \tilde{\mathbf{d}}_{\mathrm{VT},i,l}(t_k) \right\}, \tag{5.19}$$

$$\begin{aligned}\nabla_{\boldsymbol{v}_u(t_k)}\boldsymbol{\mu}(\mathbf{x}(t_k)) = \sum_{i=0}^{N(t_k)-1} \Bigg\{ & \frac{j\cdot(l-1)\cdot d\cdot(2\pi f_c + \omega_m)\alpha_{i,l}(t_k)e^{-j(2\pi f_c+\omega_m)\tau_{i,l}(t_k)}}{c \cdot \|\boldsymbol{r}_{\mathrm{VT},i}(t_k) - (\boldsymbol{r}_u(t_k) + \frac{\boldsymbol{v}_u(t_k)\cdot(l-1)\cdot d}{\|\boldsymbol{v}_u(t_k)\|})\|} \\ & \times \left(\frac{\mathbf{I}}{\|\boldsymbol{v}_u(t_k)\|} - \frac{\boldsymbol{v}_u(t_k)\cdot\boldsymbol{v}_u(t_k)^T}{\|\boldsymbol{v}_u(t_k)\|^3} \right) \cdot \tilde{\mathbf{d}}_{\mathrm{VT},i,l}(t_k) \Bigg\},\end{aligned} \tag{5.20}$$

$$\nabla_{b_u(t_k)}\boldsymbol{\mu}(\mathbf{x}(t_k)) = \sum_{i=0}^{N(t_k)-1} -j(2\pi f_c + \omega_m)\alpha_{i,l}(t_k)e^{-j(2\pi f_c+\omega_m)\tau_{i,l}(t_k)}, \tag{5.21}$$

$$\nabla_{\boldsymbol{r}_{\mathrm{VT},i}(t_k)}\boldsymbol{\mu}(\mathbf{x}(t_k)) = \frac{-j(2\pi f_c + \omega_m)\alpha_{i,l}(t_k)e^{-j(2\pi f_c+\omega_m)\tau_{i,l}(t_k)}}{c \cdot \|\boldsymbol{r}_{\mathrm{VT},i}(t_k) - (\boldsymbol{r}_u(t_k) + \frac{\boldsymbol{v}_u(t_k)\cdot(l-1)\cdot d}{\|\boldsymbol{v}_u(t_k)\|})\|} \cdot \tilde{\mathbf{d}}_{\mathrm{VT},i,l}(t_k), \tag{5.22}$$

$$\nabla_{d_{\mathrm{VT},i}(t_k)}\boldsymbol{\mu}(\mathbf{x}(t_k)) = -j(2\pi f_c + \omega_m)\alpha_{i,l}(t_k)e^{-j(2\pi f_c+\omega_m)\tau_{i,l}(t_k)}\frac{1}{c}. \tag{5.23}$$

5.2 Evaluations Based on Simulations

We evaluate the performance of Channel-SLAM for an artificial two dimensional scenario with a static physical transmitter, a moving receiver, a reflecting surface and a scatterer, shown in Fig. 5.1. Based on simulations, the position precision of Channel-SLAM is evaluated and compared to the derived PCRLB. Fig. 5.1 shows two tracks: Track I indicated in blue is simulated using the Gaussian-Transition-Model with $\sigma^2_{q_u} = 0.1\left[\frac{\mathrm{m}^2}{\mathrm{s}^3}\right]$. For Track I, the receiver is equipped with a 3-element linear antenna array aligned to the direction of movement with an element-spacing of 0.5λ, where λ is the wave length. Track II indicated in cyan is simulated using the IMU-Transition-Model described in Section 4.2.4 with $\sigma^2_{q_u} = 0.01\left[\frac{\mathrm{m}^2}{\mathrm{s}^3}\right]$, where the IMU is modeled as a random generator and the motion indicator is set to $m(t_k) = 1$. Track II is simulated for a receiver equipped with the aforementioned 3-element linear antenna array and with a single receiving antenna.

The receiver is moving on both tracks for 20 s with a system sampling interval of $t_\delta = 0.1\,\mathrm{s}$. During the receiver movement, the LoS path between the physical transmitter and the receiver is present for $t_k \leq 10\,\mathrm{s}$ and has a normalized amplitude of 1. For $10\,\mathrm{s} < t_k \leq 20\,\mathrm{s}$, the LoS path between the physical transmitter and the receiver is not received anymore. Please note, the simulations show by a simplified

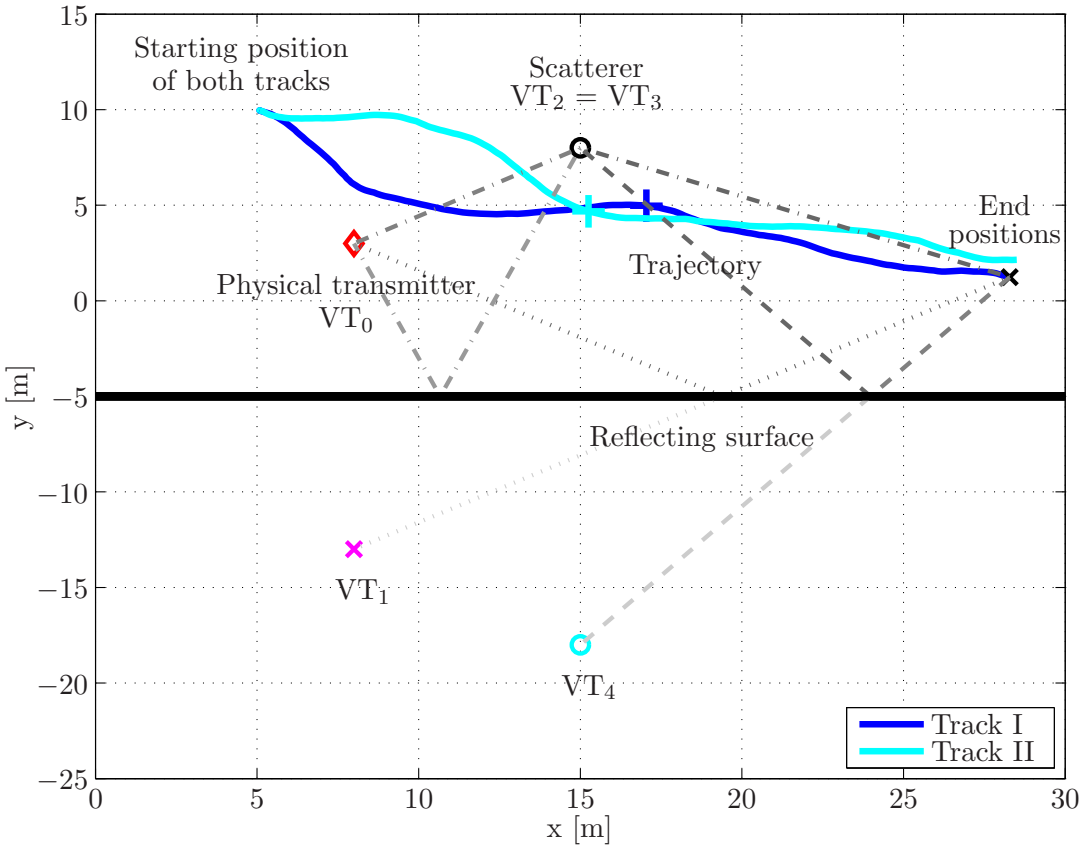

Figure 5.1. *Simulated scenario with a fixed physical transmitter, a moving receiver, a reflecting surface and a scatterer. The figure shows two different tracks, in blue Track I for Gaussian-Transition-Model and in cyan Track II for IMU-Transition-Model, where the crosses indicate the receiver position at* $t_k = 10\,\mathrm{s}$*. The signal reaches the receiving antenna via five different propagation paths: the LoS path for* $0\,\mathrm{s} \leq t_k \leq 10\,\mathrm{s}$*, a reflected path, a path which is scattered, a path which is first reflected and afterwards scattered and a path which is scattered and afterwards reflected. The figure shows also the theoretical and virtual propagation paths for a receiver at the end of Track I.*

scenario that even when the LoS path is not present anymore, Channel-SLAM is able to estimate the receiver position using MPCs. Additional to the LoS path, the signal reaches the receiving antenna via four different propagation paths at each time instant t_k during the whole receiver movement: a reflected path with normalized amplitude of $1/2$ associated to VT_1, a scattered path with normalized amplitude of $1/3$ associated to VT_2, a path which is first reflected and afterwards scattered with normalized amplitude of $1/4$ associated to VT_3 and a path which is first scattered and afterwards reflected with normalized amplitude of $1/6$ associated to VT_4. The band-unlimited CIRs for each time instant t_k are bandlimited to a bandwidth of 100 MHz and transmitted on a carrier frequency of $f_c = 1.51\,\mathrm{GHz}$. The simulations are performed for different signal-to-noise-

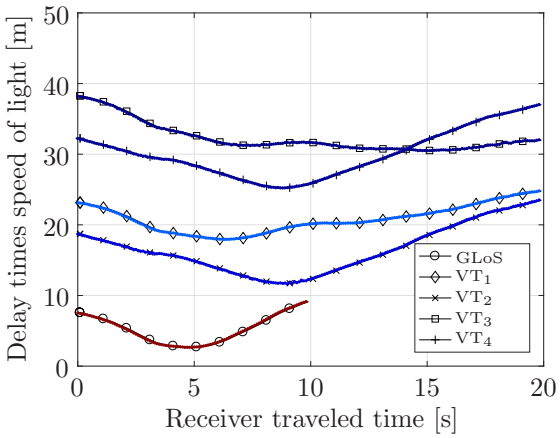

(a) *Estimated propagation distances for Track I*

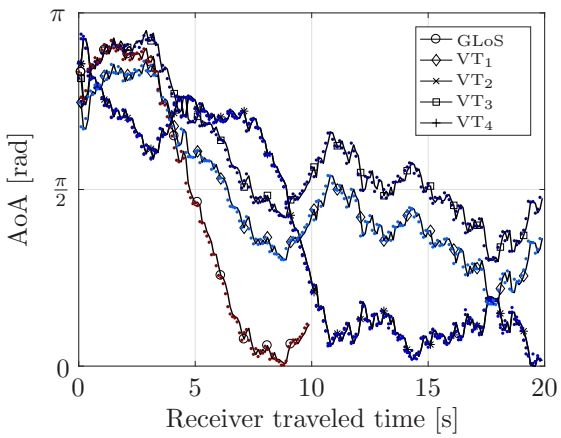

(b) *Estimated AoAs for Track I*

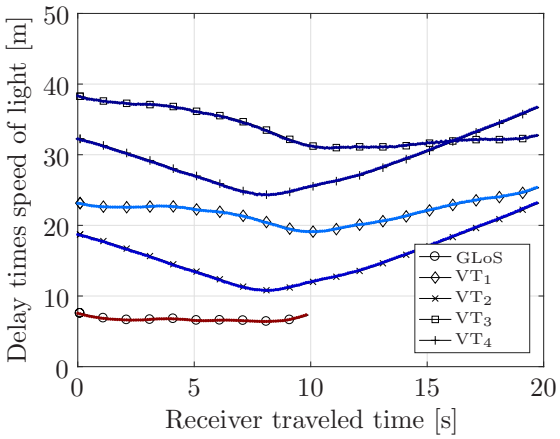

(c) *Estimated propagation distances for Track II*

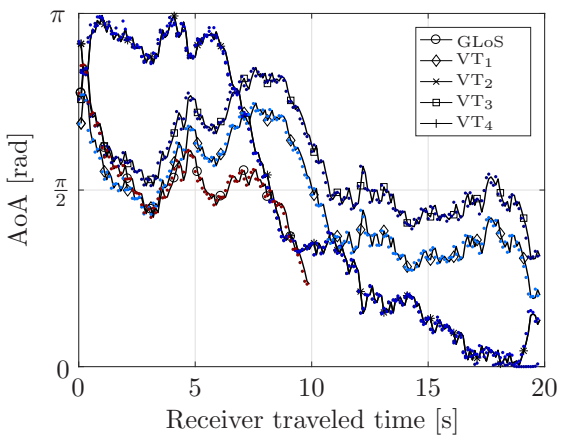

(d) *Estimated AoAs for Track II*

Figure 5.2. *Examples of the estimation results obtained by KEST for the estimated propagation distances and AoAs as a function of the receiver traveled time for SNR* = 24 dB *for Track I in Fig. 5.2a, Fig. 5.2b and Track II in Fig. 5.2c, Fig. 5.2d both using a linear antenna array. The black lines indicate the theoretical propagation distances and AoAs of the GLoS path and paths of* VT_1*,* VT_2*,* VT_3 *and* VT_4*.*

ratios (SNRs) which are calculated as $\text{SNR} = \frac{\|\tilde{\mathbf{Y}}(t_k)^2\|}{L\,M\,\sigma_n^2}$, where $\|\tilde{\mathbf{Y}}(t_k)\|^2$ is the power of all paths' contributions $\tilde{\mathbf{Y}}(t_k)$, see (2.5). Additionally, we add an artificial clock bias to verify the clock bias estimation capabilities. As mentioned in Section 4.1, the VT position of the reflected signal path is determined by mirroring the physical transmitter position at the reflecting surface, indicated by VT_1 in Fig. 5.1 with $d_{\text{VT},1}(t_k) = 0$. The position of the scatterer is equivalent to the position of both VT_2 and VT_3 with $d_{\text{VT},2}(t_k) = \|\boldsymbol{r}_t - \boldsymbol{r}_s\| = 8.6\,\text{m}$ and $d_{\text{VT},3}(t_k) = \|\boldsymbol{r}_{\text{VT},1} - \boldsymbol{r}_s\| = 22.1\,\text{m}$, respectively. The position of VT_4 can be determined by mirroring the location of the scatterer at the reflecting surface with the additional propagation distance $d_{\text{VT},4}(t_k) = d_{\text{VT},2}(t_k)$.

Fig. 5.1 visualizes the theoretical and virtual propagation paths for a receiver at the end of Track I.

During the simulations, KEST is used with a fixed model order of $N(t_k) = 5$ for $0\,\mathrm{s} \leq t_k \leq 10\,\mathrm{s}$ and $N(t_k) = 4$ for $10\,\mathrm{s} < t_k \leq 20\,\mathrm{s}$. Fig. 5.2 shows two examples of KEST results for SNR = 24 dB with the estimated propagation distances and estimated AoAs as a function of the receiver traveled time for Track I in Fig. 5.2a and Fig. 5.2b, and for Track II in Fig. 5.2c and Fig. 5.2d for a receiver equipped with the aforementioned linear antenna array. The figures indicate by the black lines the theoretical propagation distances and AoAs. At time instant $t_k = 14.2\,\mathrm{s}$ the delay of the propagation paths associated to VT_3 and VT_4 are equal for Track I and at time instant $t_k = 16.2\,\mathrm{s}$ for Track II. However, because of different amplitudes, phases and AoAs of these MPCs, KEST is able to track both MPCs separately, see also [JWFP12]. In case of using only a single receiving antenna, the accuracy of the delay estimation would be reduced. Especially, when the delays of the MPCs associated to VT_3 and VT_4 are equal, the estimation error is in the order of 10 cm for a SNR = 24 dB.

Channel-SLAM is evaluated for five different cases summarized in Table 5.1. The cases are denoted by (a)-(e) and correspond to the sub-figures (a) - (e) in Fig. 5.5, Fig. 5.6, Fig. 5.7, Fig. 5.8 and Fig. 5.9. For the initialization of Channel-SLAM, we use prior information $\mathsf{p}\big(\mathbf{x}_u(t_0)\big)$ which includes a two-dimensional uniform distribution of 1 m width centered around the starting position for $\boldsymbol{r}_u(t_0)$. Additionally, the speed vector $\|\boldsymbol{v}_u(t_0)\|$ is initialized using a uniform distribution between 0 m/s and 2 m/s and a uniform direction of 60° width around the true moving direction. Please note that an unknown starting position and direction or larger initial uncertainties may result in a biased and rotated coordinate system for the estimation. For $\Delta_d, \Delta_\theta, K$, we use empirical values as $\Delta_d = 0.5\,\mathrm{m}, \Delta_\theta = 0.5°, K = 5$. In the cases (a),(b),(c), we consider for conveniences the first propagation path $i = 0$ as the LoS path, indicated by VT_0 in Fig. 5.1 with a known fixed position $\boldsymbol{r}_{\mathrm{VT},0}(t_k) = \boldsymbol{r}_t$ and $d_{\mathrm{VT},0}(t_k) = 0$. As mentioned in Section 1.4, the heading changes enable that Channel-SLAM operates without the prior information on the physical transmitter position. Thus, in the cases (d) and (e), the position of the physical transmitter is estimated by Channel-SLAM as the position of VT_0 using the KEST estimates of the first propagation path. If Channel-SLAM has no prior information on the physical transmitter position, the coordinate system has to be defined by the prior information on the initial receiver position and speed. Thus, for the cases (d) and (e), the moving direction is assumed to be known to define the coordinate system. Unless otherwise noted, the simulations are performed using $N_s = 6000$ particles in the super-PF, whereas the number of particles for the sub-PFs for each propagation path with $i = 0, \ldots, 4$ is different depending on the

Table 5.1. *Description of five different cases for the Channel-SLAM evaluations.*

(a)	**Track I - Linear Antenna Array** Channel-SLAM uses the KEST estimates of Track I where the receiver is equipped with the 3-element linear antenna array, uses the Gaussian-Transition-Model and has prior information on the physical transmitter position.
(b)	**Track II - Linear Antenna Array** Channel-SLAM uses the KEST estimates of Track II where the receiver is equipped with the 3-element linear antenna array, uses the IMU-Transition-Model and has prior information on the physical transmitter position.
(c)	**Track II - Single Receiving Antenna** Channel-SLAM uses the KEST estimates of Track II where the receiver is equipped with the single receiving antenna, uses the IMU-Transition-Model and has prior information on the physical transmitter position.
(d)	**Track II - Linear Antenna Array - NLoS** Channel-SLAM uses the KEST estimates of Track II where the receiver is equipped with the 3-element linear antenna array, uses the IMU-Transition-Model and has no prior information on the physical transmitter position.
(e)	**Track II - Single Receiving Antenna - NLoS** Channel-SLAM uses the KEST estimates of Track II where the receiver is equipped with a single receiving antenna, uses the IMU-Transition-Model and has no prior information on the physical transmitter position.

estimated delay and AoA of each propagation path. Additionally, the simulations are performed using the Channel-SLAM implementation with the dynamical adaptation of the number of particles as introduced in Section 4.3 in Algorithm 10. We limit the number of particles per bin to $N_m = 30$ and the grid size to $\Delta_d = 0.5\,\text{m}$. Later in this section, we show that the dynamical adaption does not affect the position accuracy. Furthermore, we draw for each simulation run randomly a clock bias. Please note, the clock bias can be estimated only for the cases (a) - (c) and VT_0 is only estimated in (d) and (e), hence, the sub-figures (a) - (c) in Fig. 5.5, Fig. 5.6 and Fig. 5.9 do not show the curve for VT_0 and (d) - (e) do not show the curve for the clock bias.

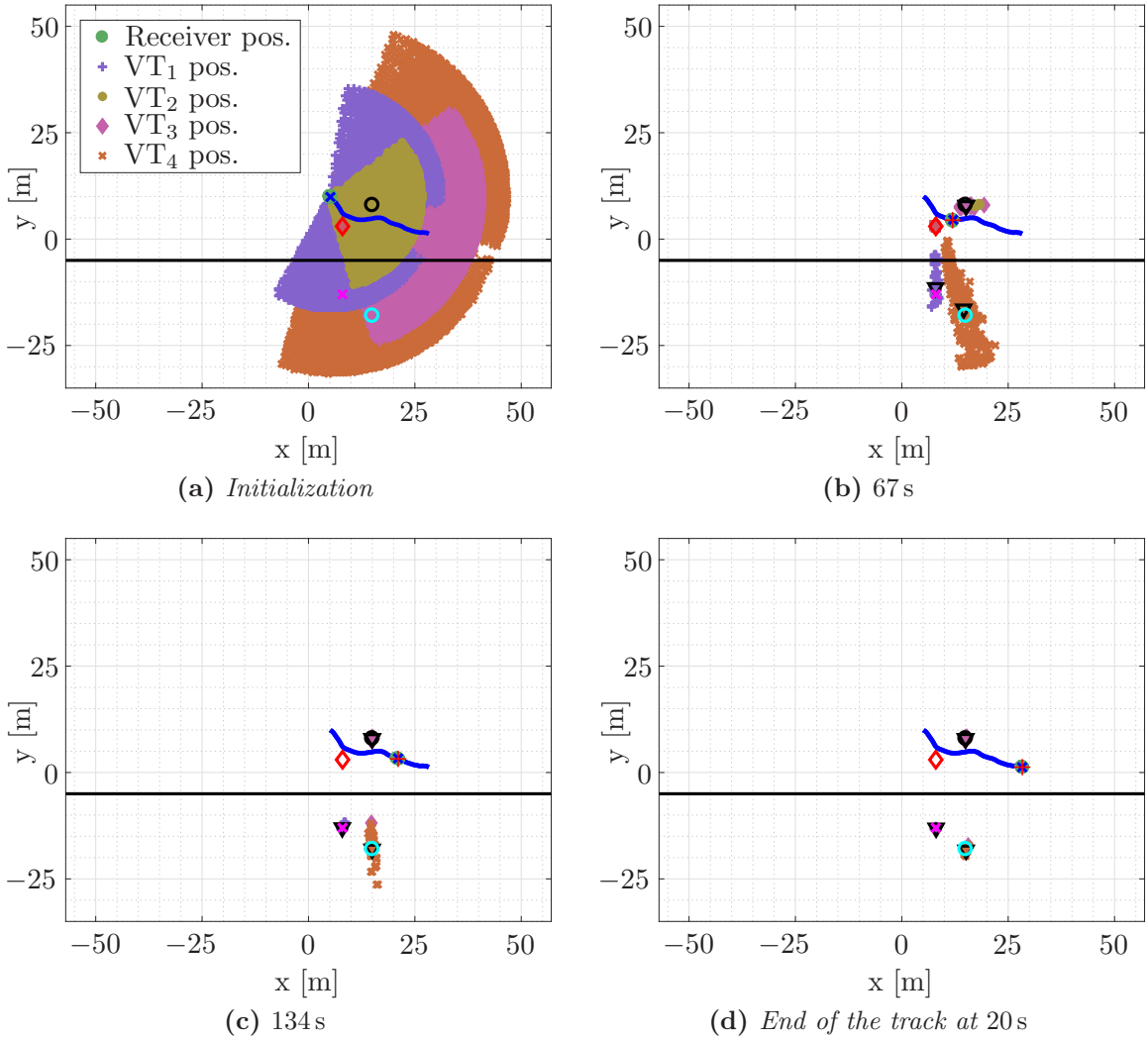

(a) *Initialization* **(b)** 67 s

(c) 134 s **(d)** *End of the track at* 20 s

Figure 5.3. *Four different time instants of the estimations of Channel-SLAM for Track I if a linear antenna array is used, i.e. case (a).*

Fig. 5.3 and Fig. 5.4 illustrate the PF estimations of the receiver position and VT positions of Channel-SLAM by four different time instants for case (a) in Fig. 5.3 and

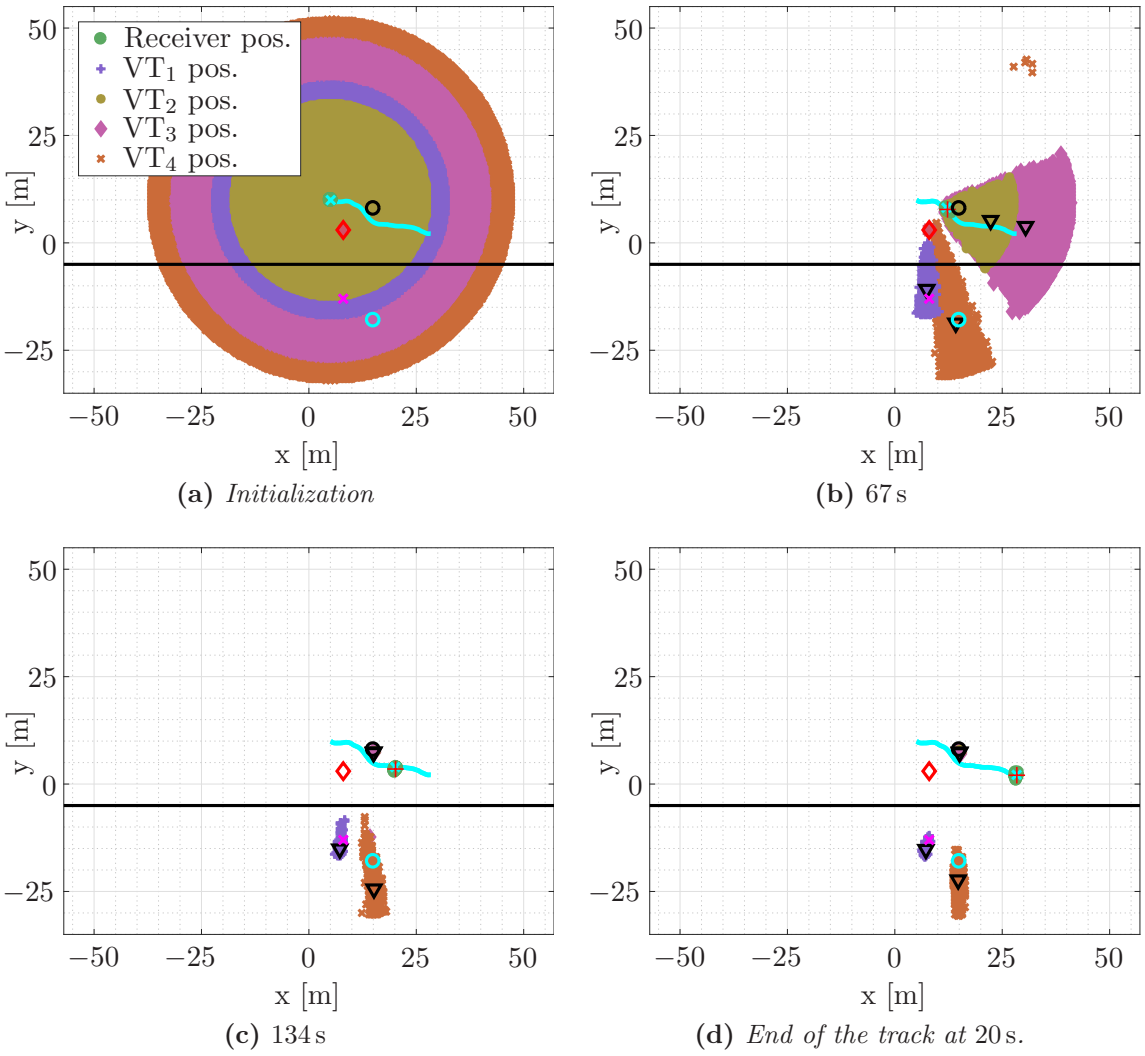

(a) *Initialization* **(b)** 67 s

(c) 134 s **(d)** *End of the track at* 20 s.

Figure 5.4. *Four different time instants of the estimations of Channel-SLAM for Track II if a single receiving antenna is used, i.e. case (c).*

for case (c) in Fig. 5.4. Fig. 5.3 and Fig. 5.4 indicate similar to Fig. 5.1 by the magenta cross the position of VT_1, by the black circle the position of VT_2 and VT_3, and by the cyan circle the position of VT_4. Additionally, Track I is indicated in Fig. 5.3 in blue and Track II is indicated in cyan in Fig. 5.4 with the corresponding ground truth positions indicated by the blue and cyan crosses. The PF estimations of the VT positions are indicated by different colors. The black triangles show the corresponding MMSE estimates of the VT positions for $t_k > t_1$. Additionally, the green circles indicate the PF estimations of the receiver position and the red plus indicates the MMSE estimate of the receiver position. Fig. 5.3a shows the initialization, according to the delay and AoA measurements, all possible VT positions are initialized on a grid around the receiver position. The position of a VT is ambiguous because a distinction between

Table 5.2. *Four different algorithms to compare to Channel-SLAM.*

Alg. I	Positioning algorithm with perfect knowledge of all VT positions $\boldsymbol{r}_{\mathrm{VT},i}(t_k)$ and additional propagation distances $d_{\mathrm{VT},i}$, with $0 = 1 \ldots 4$, including the physical transmitter position. This algorithm can be seen as a lower bound for Channel-SLAM.
Alg. II	Positioning algorithm using only the reflected and the LoS signal, assuming prior information on the physical transmitter position and perfect knowledge of the geometry, hence, the knowledge of the states of VT_0 and VT_1. This reflects algorithms in [LMLW15, MWK14]. For $t_k > 10$, the algorithm uses only the reflected path for positioning.
Alg. III	Positioning algorithm which considers the first arrived propagation path as the LoS path and assuming the prior information on the physical transmitter position. Hence, the algorithm interprets the second propagation path (scattered path) as the LoS path for $t_k > 10$ and represents a multipath mitigation algorithm similar to [CFPFR09].
Alg. IV	Positioning algorithm using only the LoS path and assuming the prior information on the physical transmitter position. For $t_k > 10$, the algorithm estimates the position using the prediction model. Therefore, the algorithm could be described as a multipath mitigation algorithm including an ideal NLoS detection.

propagation paths arriving from the left and the right of the linear antenna array is not possible. During the receiver movement, the uncertainty on the estimated VTs' positions reduces. At the end of the track we obtain for the receiver and VT positions accurate position estimates. If a single receiving antenna is used as illustrated in Fig. 5.4, the VT positions are initialized on a grid with spacing of 0.5m in a circular area around the starting position with the radius of the estimated delay, see Fig. 5.4a. During the receiver movement, the uncertainty on the estimated positions of the VTs reduces. However, after $t_k = 67\,\mathrm{s}$, there are still ambiguities on the position estimates of the VTs on the left and on the right of the receiver for VT_2, VT_3 and VT_4. Because of the direction changes of the receiver, the ambiguity in the VT positions can be solved and we obtain an accurate position estimate at the end of the track.

To see the positioning performance of Channel-SLAM in relation to other algorithms, we compare Channel-SLAM to four different algorithms named as Alg. I to Alg. IV described in Table 5.2. Similarly to Channel-SLAM, these algorithms use the delays and AoAs of the estimated MPCs provided by KEST as input, use the

same transition model, assume the same prior information on the receiver position and velocity, and are implemented using PFs with $N_s = 6000$ particles. In contrast to Channel-SLAM, we assume for Alg. I to Alg. IV that the receivers are synchronized to the physical transmitter, i.e. the clock biases are zero.

Fig. 5.5, Fig. 5.6, Fig. 5.7, Fig. 5.8 and Fig. 5.9 summarizes the evaluations. As mentioned before, the sub-figures hold for the 5 cases (a) to (e) according to Table 5.1.

Fig. 5.5 shows the root mean square errors (RMSEs) of the estimated positions of the VTs, receiver positions and clock biases as a function of the receiver traveled time. The RMSE of the estimated receiver position is calculated as $\mathrm{RMSE}_u(t_k) = \sqrt{\mathbf{E}\{\|\boldsymbol{r}_u(t_k) - \hat{\boldsymbol{r}}_u(t_k)\|^2\}}$, of the estimated i-th VT position as $\mathrm{RMSE}_{\mathrm{VT},i}(t_k) = \sqrt{\mathbf{E}\{\|\boldsymbol{r}_{\mathrm{VT},i}(t_k) - \hat{\boldsymbol{r}}_{\mathrm{VT},i}(t_k)\|^2\}}$ and of the clock bias estimation times the speed of light in meters as $\mathrm{RMSE}_b(t_k) = \sqrt{\mathbf{E}\{\|b_u(t_k) - \hat{b}_u(t_k)\|^2\}} \cdot c$. Whereas the solid lines indicate the RMSE for the simulations, the dashed lines indicate the corresponding curves calculated using the PCRLB. The vertical dashed line indicates the time when the LoS path is not received anymore.

Overall we can conclude that in all figures the RMSEs for the estimated VT positions follow a similar shape: At the starting position, Channel-SLAM and the PCRLB are based on the same prior information. During the receiver movement the position estimates of the VTs converge and hence, the RMSEs decrease. The PCRLB shows the theoretical performance bound which has lower RMSEs than the PF estimations. However, the PCRLB and PF estimations follow a similar shape. Because the positions of VT_2 and VT_3 are identical, the curves for the PCRLBs of these VTs are equivalent. Additionally, the parameter estimations of VT_2 and VT_3 are more accurate than for VT_1 and VT_4, because VT_2 and VT_3 are closer to the track than VT_1 and VT_4, hence, the delays and AoAs are changing more significantly. As mentioned before, we can observe the convergence of the position estimations of VT_2 and VT_3 by the fast drop after 7.5s for the linear antenna array and 9s for the single receiving antenna. Additionally, without the prior information on the physical transmitter position, the position accuracy is slightly decreased, however, we are still able to obtain a position estimation error at the end of the track lower than 1 m when a single receiving antenna is used. Please note, the clock bias can be estimated only if the position of the physical transmitter position is known. In the cases where the physical transmitter is unknown, the clock bias is estimated inherently in the additional distance $d_{\mathrm{VT},i}(t_k)$ of all VTs and cannot be resolved.

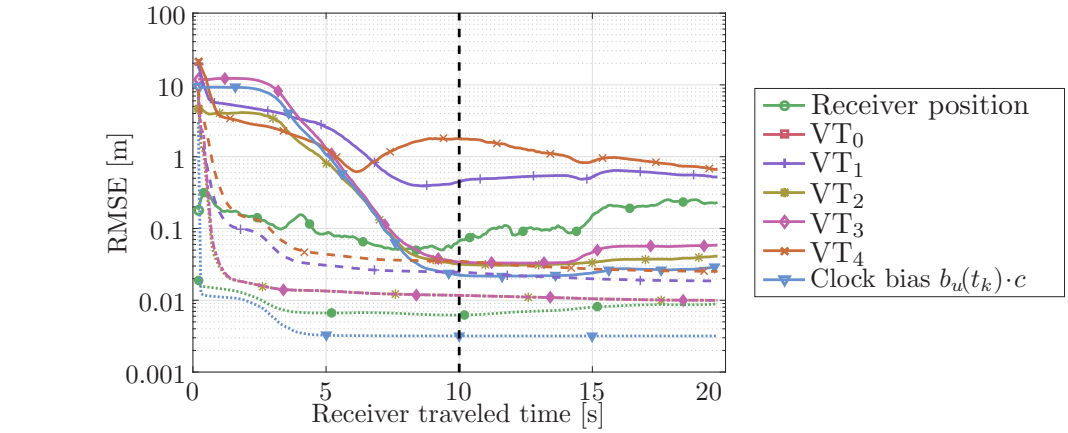

(a) *Track I - Linear Antenna Array*

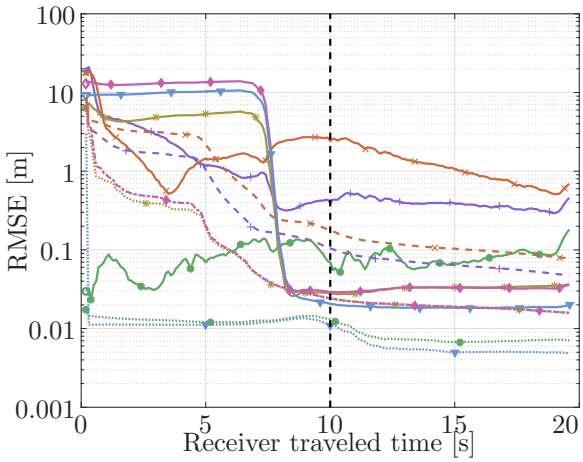

(b) *Track II - Linear Antenna Array*

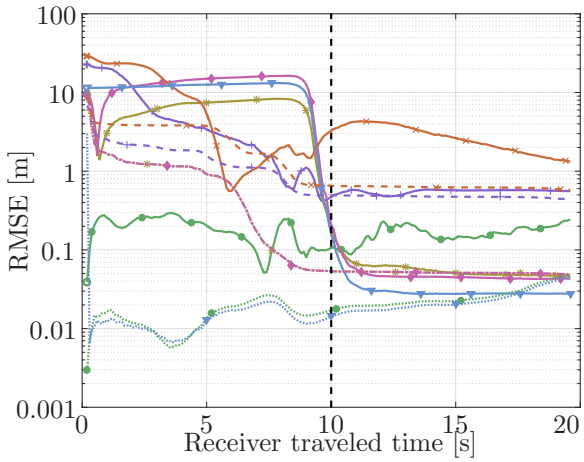

(c) *Track II - Single Receiving Antenna*

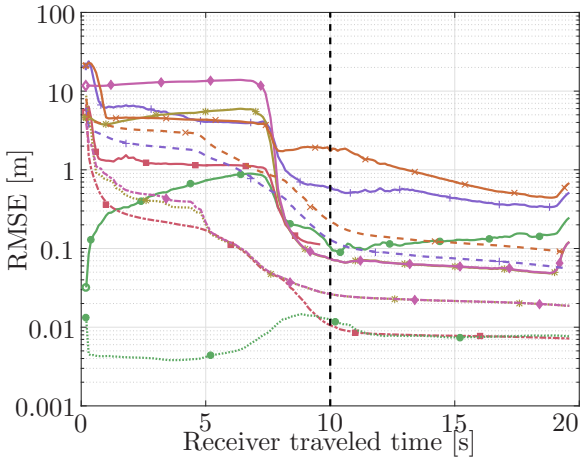

(d) *Track II - Linear Antenna Array - NLoS*

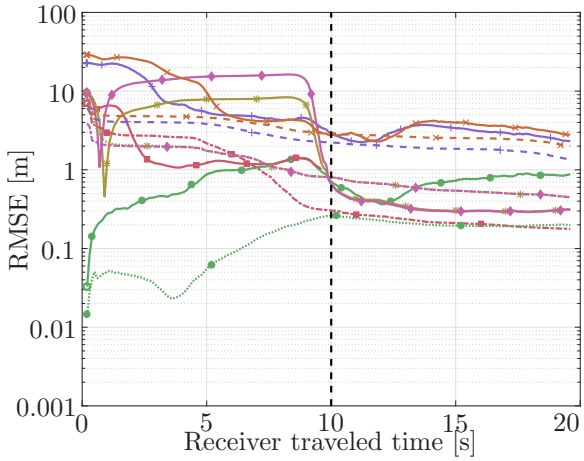

(e) *Track II - Single Receiving Antenna - NLoS*

Figure 5.5. *RMSEs of the estimated receiver positions, VT positions and clock biases as a function of the receiver traveled time for cases (a) - (e) see Table 5.1. The dashed lines represent the corresponding curves calculated by the PCRLBs. Additionally, the vertical dashed line indicates the time when the LoS component is lost. Please note, the clock bias can be estimated only for the cases (a) - (c) and VT_0 is only estimated in (d) and (e).*

Fig. 5.6 shows the RMSEs as a function of the SNR for the receiver and VT positions at the end of the track, i.e. $t_k = 20\,\mathrm{s}$. Similar to Fig. 5.5, the solid lines indicate the RMSEs for the simulations and the dashed lines indicate the corresponding curves calculated using the PCRLB. For low SNRs, it is difficult for KEST to accurately estimate all five MPCs because of the measurement noise. The non-accurate CIR estimations of KEST causes directly estimation errors on the VT and receiver positions of Channel-SLAM. Hence, the position estimation errors of the receiver position and VTs increases for low SNRs. For higher SNRs, the RMSEs of VT_2 and VT_3 are close to the curves for the PCRLB. In all evaluations, the position accuracy increases with the SNR. As mentioned before, the positions of VT_2 and VT_3 are identical and can be estimated more accurately than the positions of VT_1 and VT_4. We can observe that the prior information on the physical transmitter position is not essential for Channel-SLAM if an IMU is used. Even without the prior information on the physical transmitter position accurate position estimation is possible. The physical transmitter position can be estimated as a VT with a position error below 0.04 m if a linear antenna array is used and 0.3 m for a single receiving antenna for SNRs $\geq 12\,\mathrm{dB}$. By using a linear antenna array, we observe a strong dependency of the accuracy on the SNR. For the cases (a), (b) and (d) the position estimation accuracy increases significantly for SNRs $\geq 12\,\mathrm{dB}$. This effect is not visible in the PCRLB and is most likely caused by estimation errors of KEST. By using a linear antenna array, the positioning accuracy increases by a factor of 10 compared to a single receiving antenna. However, we are still able to obtain a position accuracy at the end of the track below 1 m for SNRs $\geq 16\,\mathrm{dB}$ even if the physical transmitter position is unknown.

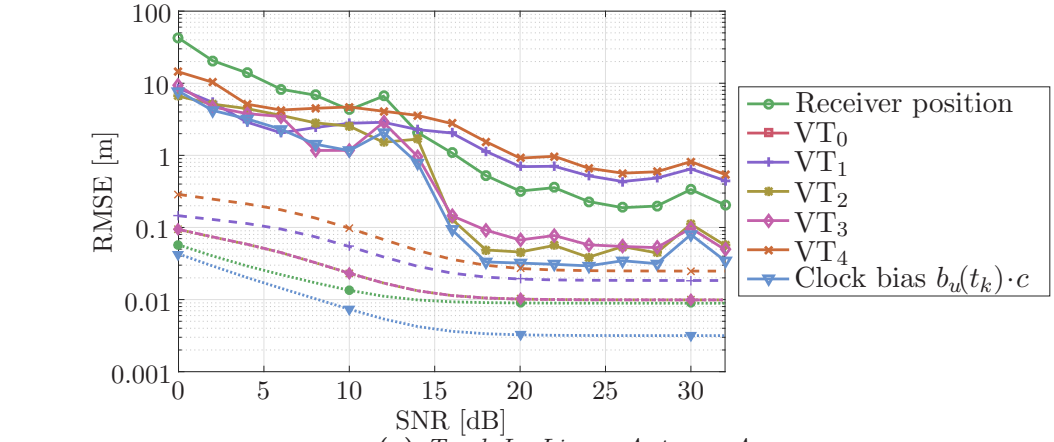

(a) *Track I - Linear Antenna Array*

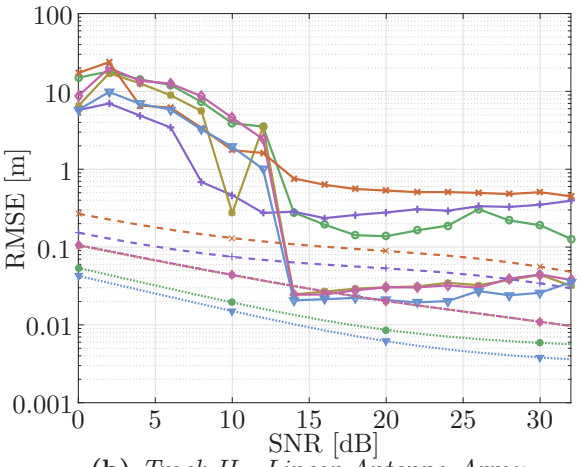

(b) *Track II - Linear Antenna Array*

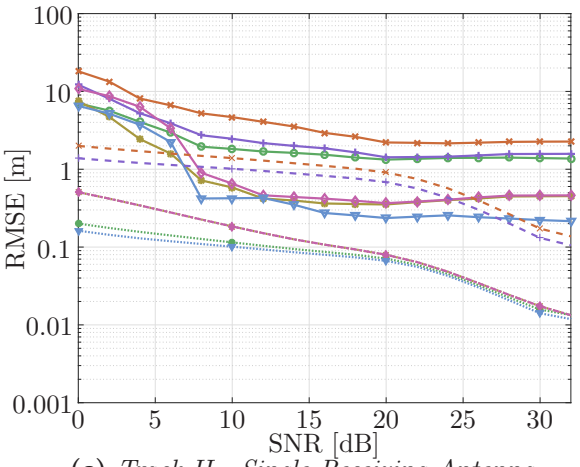

(c) *Track II - Single Receiving Antenna*

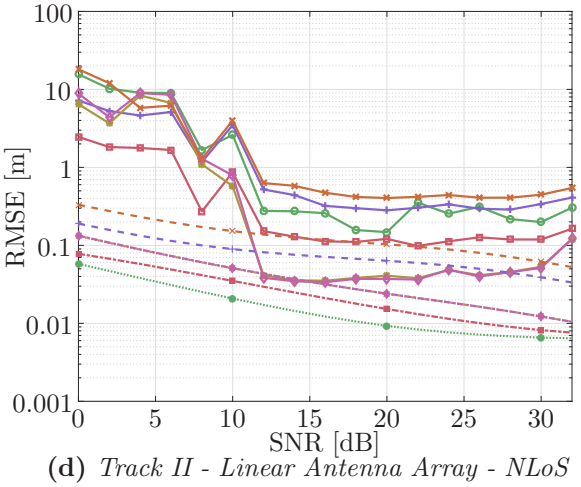

(d) *Track II - Linear Antenna Array - NLoS*

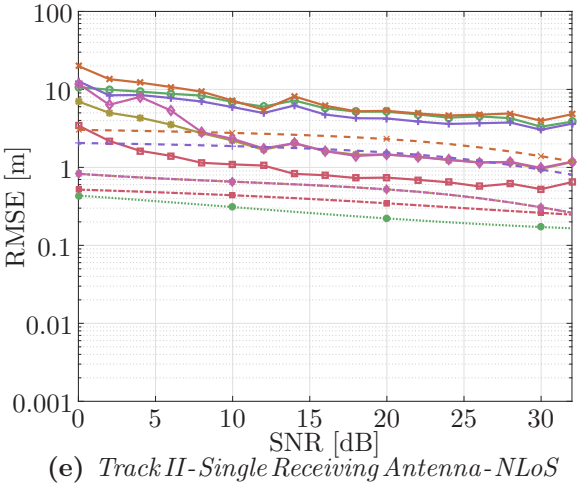

(e) *Track II - Single Receiving Antenna - NLoS*

Figure 5.6. *RMSEs of the estimated receiver positions, VT positions and clock biases as a function of the SNR for cases (a) - (e) see Table 5.1. The dashed lines represent the corresponding curves calculated by the PCRLBs. Please note, the clock bias can be estimated only for the cases (a) - (c) and* VT_0 *is only estimated in (d) and (e).*

Fig. 5.7 shows the RMSEs as a function of the receiver traveled time for Channel-SLAM and Alg. I - IV. The vertical dashed line indicates the time when the LoS path is not received anymore. Additionally, we compare in Fig. 5.7 the RMSEs of two Channel-SLAM implementation, using the dynamical adaptation of the number of particles as introduced in Section 4.3 in Algorithm 10 referred to as Dynamic-Channel-SLAM and without dynamical adaptation referred to as RBPF-Channel-SLAM. At the starting time, the RMSE for all algorithms are similar because of the same prior information. Alg. I can be interpreted as a lower bound and estimates the receiver position with the lowest RMSE. Alg. II shows similar results, as long as the LoS path prevails. When the LoS path is absent, the RMSEs increase because the number of transmitters reduces to one. Estimating the receiver positions with only one propagation path, like Alg. III and Alg. IV, the worst position accuracy is obtained compared to Alg. I, Alg. II and Channel-SLAM. Furthermore, we see that we obtain similar RMSEs for Dynamic-Channel-SLAM and RBPF-Channel-SLAM. However, if we have a look on the number of used particles, as shown in Fig. 5.8, we see a major computational performance gain of Dynamic-Channel-SLAM compared to RBPF-Channel-SLAM. Fig. 5.8 shows the total number of particles $N_{\mathrm{t}}(t_k)$ calculated according to (4.42) for $N_p = 6000$ as a function of the receiver traveled time. At the beginning, both Channel-SLAM algorithms are initialized with the same number of particles. As soon as the receiver is moving, the estimations of the VT positions converge resulting in a reduction of the number of particles for Dynamic-Channel-SLAM. Especially at the end of the track, Dynamic-Channel-SLAM uses 5 times less particles than RBPF-Channel-SLAM if a linear antenna array is used and 35 times less particles if a single receiving antenna is used.

Fig. 5.9 shows the RMSEs for the receiver and VT positions at the end of the tracks, i.e. $t_k = 20\,\mathrm{s}$, as a function of the number of particles in the super-PF. As mentioned before, the number of particles for the sub-PFs for each MPC with $i = 0, \ldots, 4$ is different depending on the estimated delay and AoA of each MPC and dynamically adapts during the receiver movement. The more particles for the super-PF are used, the higher the accuracy of Channel-SLAM: For the case (a) - (d), the receiver positions can be estimated in average with RMSEs lower than $0.3\,\mathrm{m}$ with $N_s > 2000$. For the case (e), the receiver position can be estimated in average with a RMSE lower than $2\,\mathrm{m}$ with $N_s > 2000$.

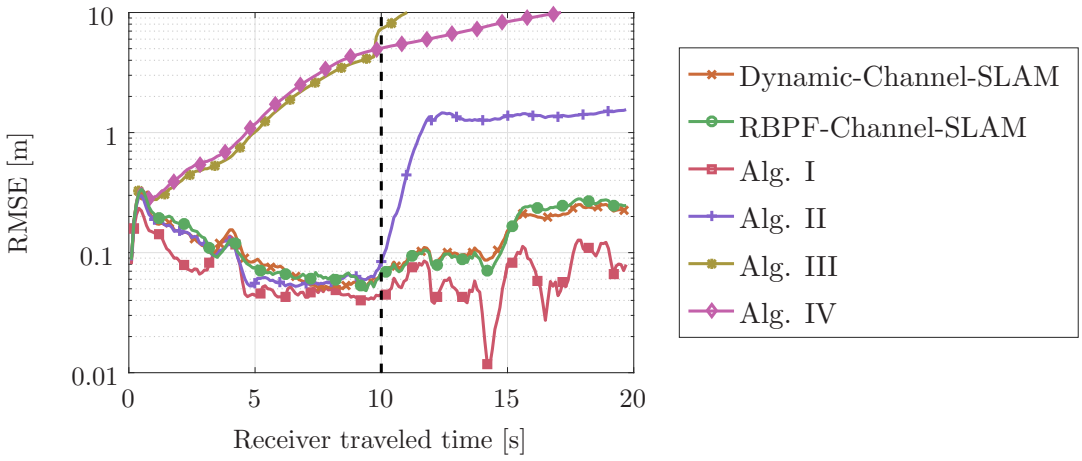

(a) *Track I - Linear Antenna Array*

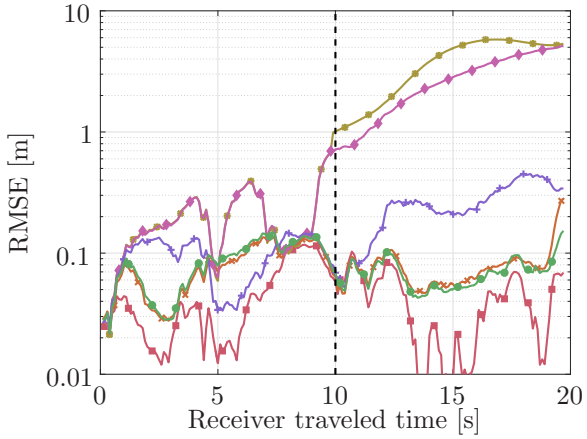

(b) *Track II - Linear Antenna Array*

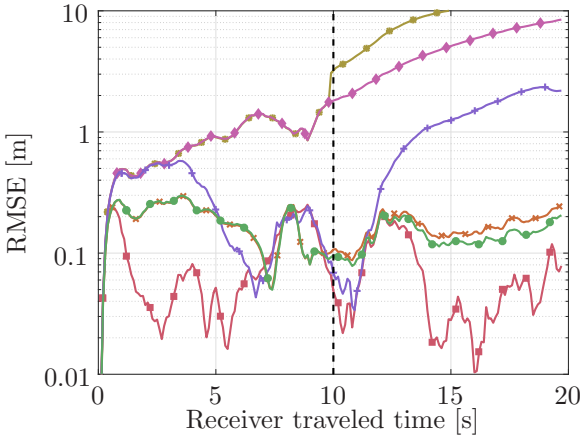

(c) *Track II - Single Receiving Antenna*

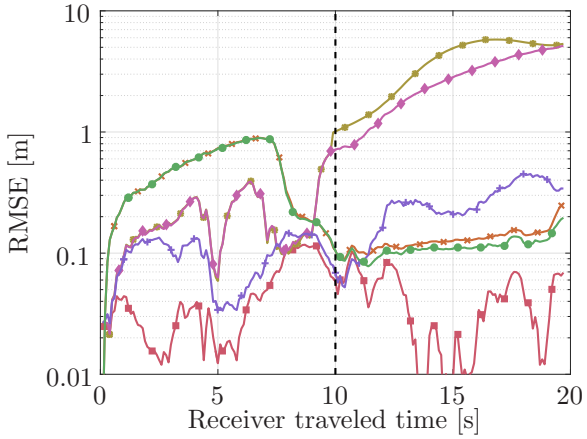

(d) *Track II - Linear Antenna Array - NLoS*

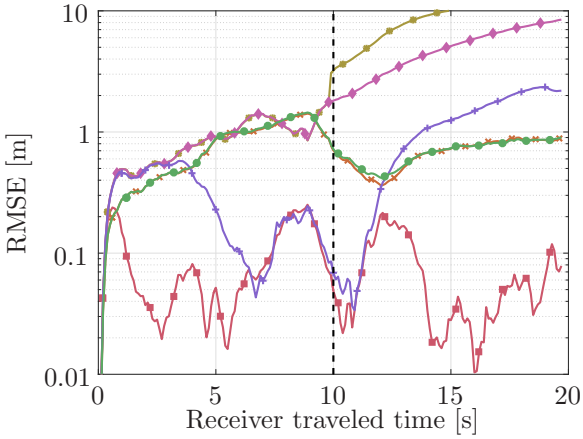

(e) *Track II - Single Receiving Antenna - NLoS*

Figure 5.7. *RMSEs of the estimated receiver positions as a function of the receiver traveled time for different algorithms, see Table 5.2, and cases (a) - (e), see Table 5.1. The vertical dashed line indicates the time instant when the LoS path is lost.*

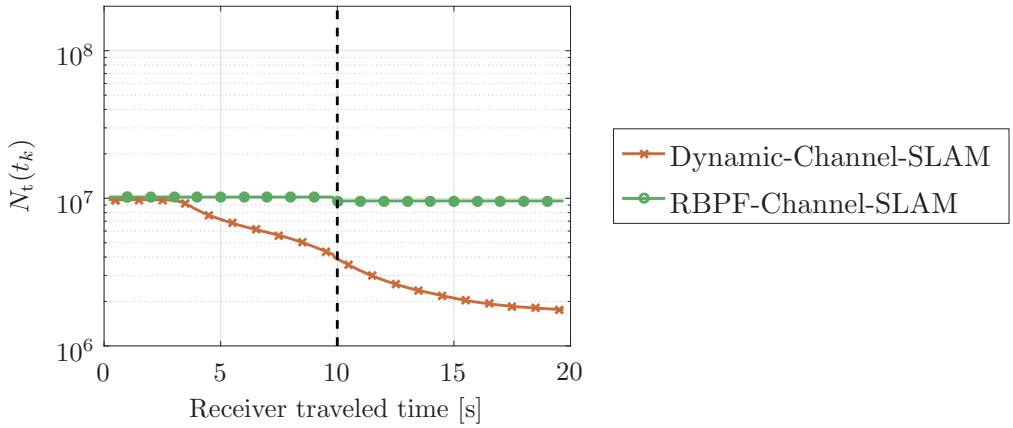

(a) *Track I - Linear Antenna Array*

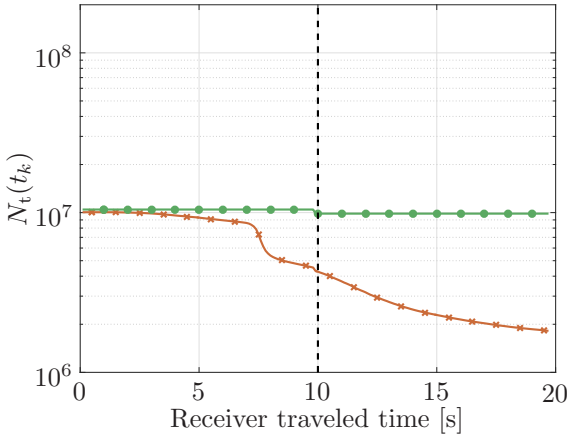

(b) *Track II - Linear Antenna Array*

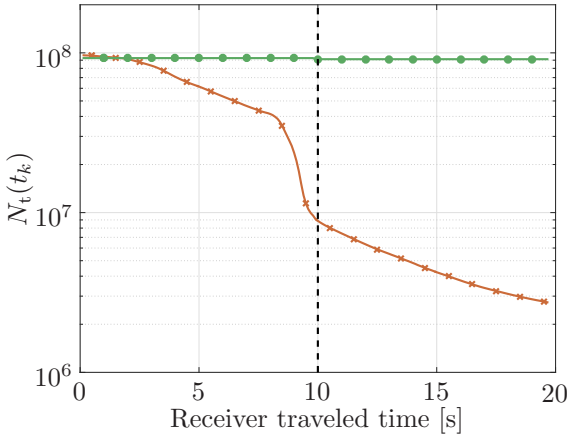

(c) *Track II - Single Receiving Antenna*

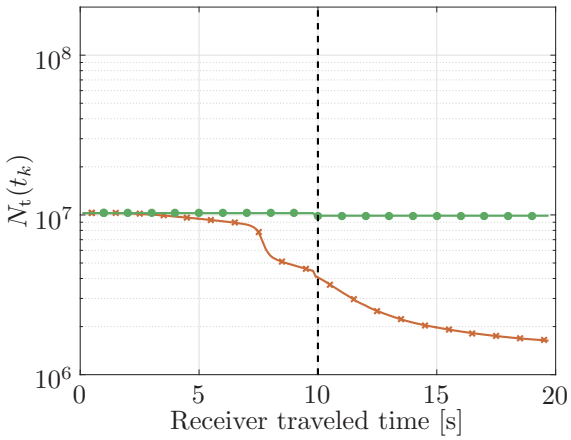

(d) *Track II - Linear Antenna Array - NLoS*

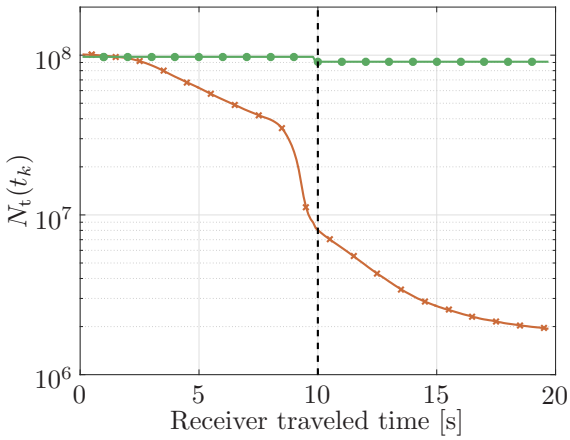

(e) *Track II - Single Receiving Antenna - NLoS*

Figure 5.8. *Total number of particles $N_t(t_k)$ as a function of the receiver traveled time for Dynamic-Channel-SLAM and RBPF-Channel-SLAM for cases (a) - (e) see Table 5.1. The vertical dashed line indicates the time instant when the LoS path is lost.*

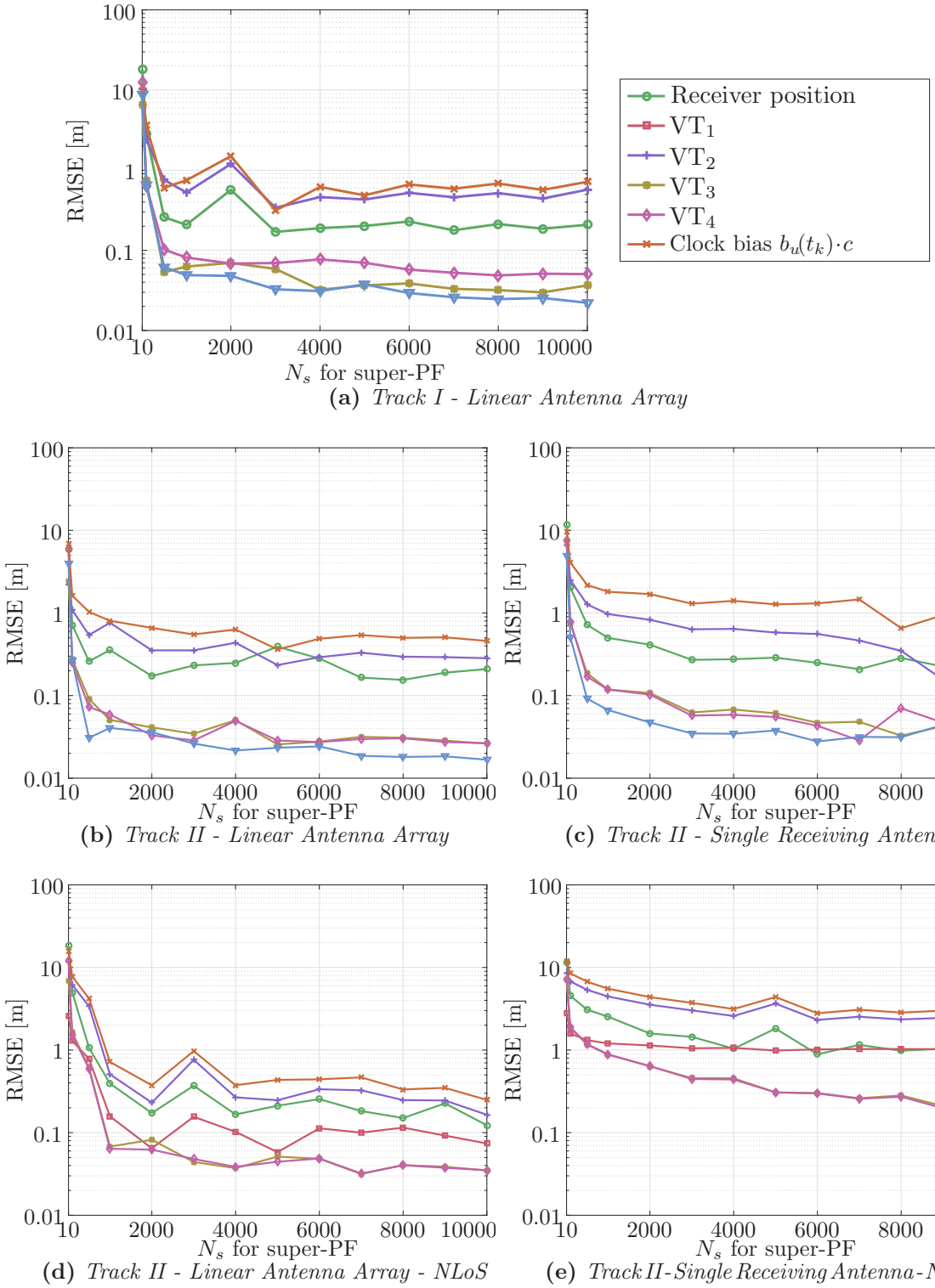

(a) *Track I - Linear Antenna Array*

(b) *Track II - Linear Antenna Array*

(c) *Track II - Single Receiving Antenna*

(d) *Track II - Linear Antenna Array - NLoS*

(e) *Track II - Single Receiving Antenna - NLoS*

Figure 5.9. *RMSEs of the estimated receiver positions, estimated VT positions and estimated clock bias as a function of the number of particles at the end of the track at* $t_k = 20\,\mathrm{s}$ *for cases (a) - (e) see Table 5.1. Please note, the clock bias can be estimated only for the cases (a) - (c) and* VT_0 *is only estimated in (d) and (e).*

Chapter 6

Performance Evaluations

This chapter describes the performance evaluation of Channel-SLAM based on three different measurement campaigns. The first measurement campaign considers an indoor scenario where the receiving antenna is mounted on a model train described in Section 6.2. The second and third measurement campaigns explore a walking pedestrian carrying a single receiving antenna and an IMU. In the second measurement campaign described in Section 6.3, the pedestrian walks outdoors in front of a hangar with metallic doors. The hangar acts as a reflecting surface for the radio signal. In the third measurement campaign described in Section 6.4, the pedestrian enters a building, walks inside the building and leaves the building afterwards.

6.1 Measurement Equipment

The measurement campaigns are conducted using the MEDAV RUSK-DLR broadband channel sounder. The channel sounder consists of a physical transmitter and a receiver to sound the wireless channel. In the following we describe the channel sounder based on the configuration used for the measurement campaigns in this work. For further details about the channel sounder and different configurations or applications see e.g. [Leh05, Jos13, Wan15]. To sound the channel, the channel sounder uses a single-input single-output (SISO) mode [TLRT05]. Hereby, the physical transmitter emits a multitone spread spectrum signal with $N = 1281$ sub-carriers with equal gains spaced by $f_\Delta = \frac{1}{T_p}$ at a carrier frequency of $f_c = 1.51\,\text{GHz}$ and bandwidth $B = 100\,\text{MHz}$. This transmitted signal is similar to an orthogonal frequency-division multiplexing (OFDM) signal and is periodically transmitted with a period duration of $T_p = 12.8\,\mu\text{s}$. In all considered measurements, the physical transmitter is static in its position and emits the multitone signal with a power of 100 mW. On the receiver side, the CIR snapshots are repeatedly

Table 6.1. *Channel sounder settings*

Parameter	Value
Measurement type	SISO
Carrier frequency	1.51 GHz
Bandwidth B	100 MHz
Number of sub-carriers N	1281
Sub-carrier spacing Δf	78.125 kHz
Transmit power	100 mW
Signal period T_p	12.8 μs
Measurement rate T_g	1.024 ms
Transmitter antenna	Omni-directional (V-polarized)
Receiver antenna	Omni-directional (V-polarized)
ADC	8 bit, 320 MHz

measured in a time grid of $T_g = 1.024\,\text{ms}$. In the following sections, we describe two different receiver-setups which are used in the measurement campaigns.

6.1.1 Moving Model Train

Fig. 6.1 shows the first measurement setup with a static physical transmitter and a mobile receiver. To prevent time drifts during the measurements, the physical transmitter and the receiver are connected to the same rubidium clock, see Fig. 6.1a. The receiving antenna is mounted on an experimental platform realized using a model train which moves on a model railroad track, see Fig. 6.1b. To prevent wheel slipping, the model train is driven by a cogwheel. Additionally, the model train is equipped with a rotary encoder which counts the number of motor turns and generates 500 impulses per motor turn which are stored simultaneously with the captured CIR snapshots. The number of motor turns corresponds linearly to the traveled distance of the mobile platform. By storing the number of motor turns synchronously with the measured CIR snapshots, we obtain the ground truth of the receiver for each captured CIR snapshot [Jos13, Wan15]. To measure the track layout and physical transmitter location the tachymeter TPS1200 from Leica Geosystems AG was used, which has an accuracy in subcentimeter domain. Hence, the traveled distance can be exactly mapped onto a three dimensional coordinate and results in a precisely measured position for each CIR snapshot. As mentioned before, the channel sounder is used in SISO mode, hence, we

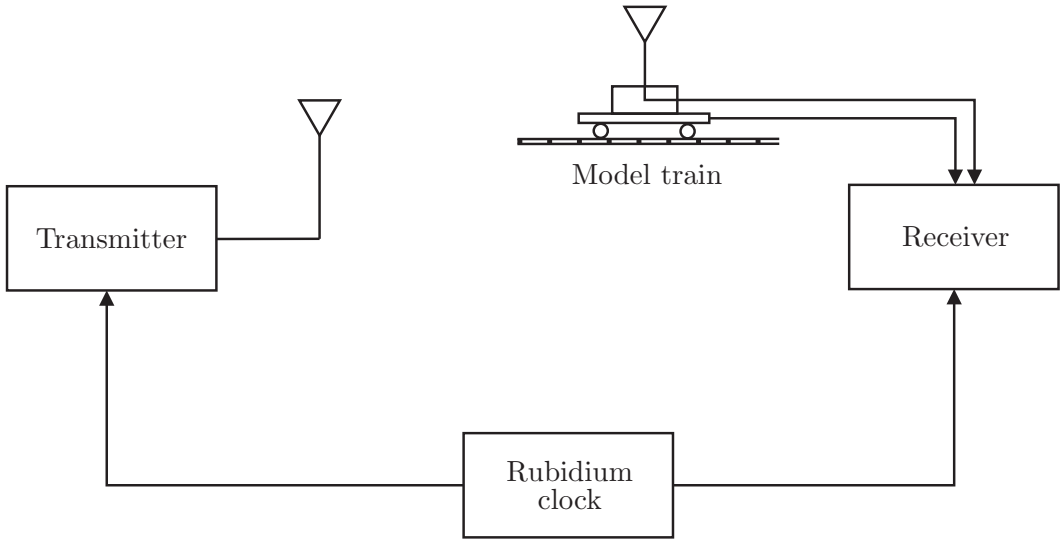

(a) *Block diagram of the measurement setup with a static physical transmitter and a mobile receiver where the receiving antenna is mounted on a model train. Transmitter and receiver use the same rubidium clock for synchronization.*

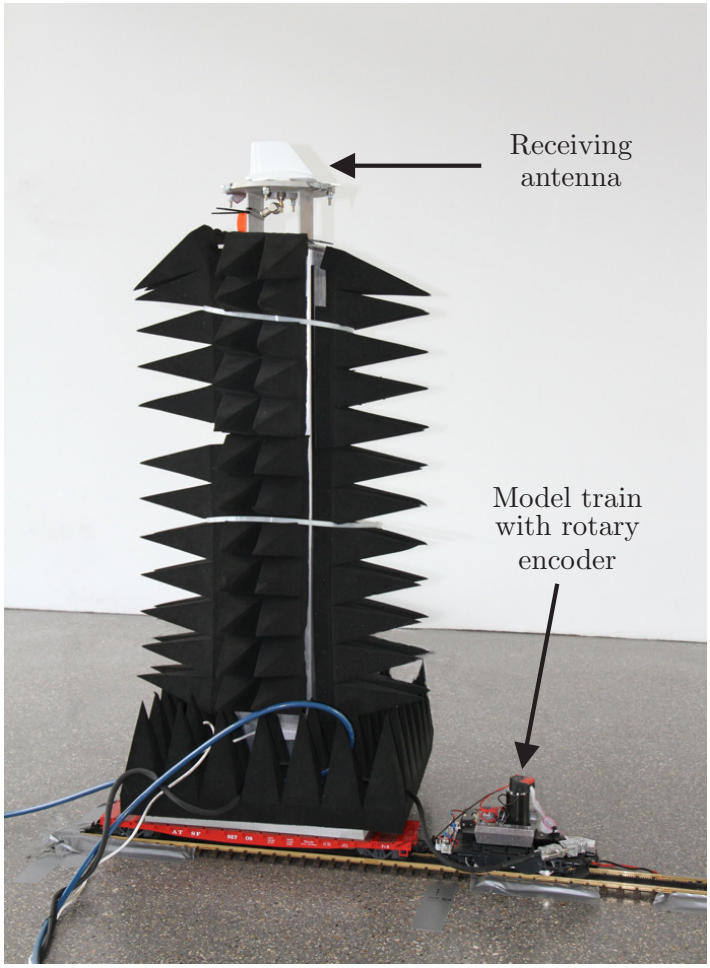

(b) *The model train used as a mobile platform with the receiving antenna mounted on top.*

Figure 6.1. *Measurement setup using a model train.*

do not have a linear antenna array as used in Section 5.2. However, with the accurate knowledge of the traveled distance, it is possible to form virtually a linear antenna array from the time-variant measurements, see [WJ12b]. In the considered measurements in Section 6.2, the model train travels with a speed of roughly $0.05\,{}^{\mathrm{m}}/_{\mathrm{s}}$ resulting in a spatial distance between two adjacent CIR measurements of 0.0512 mm. We form a 3-element linear antenna array with an element-spacing of 0.3λ with the wave length $\lambda = {}^{1}/_{f_c}$.

6.1.2 Walking Pedestrian

Fig. 6.2 shows the second measurement setup with a static physical transmitter and a pedestrian, where the receiving antenna is mounted on a pole attached on the backpack of the pedestrian. Additionally, the pedestrian is equipped with a hand-held equipment including a Xsens IMU (MTI-G-700) and a laptop which stores the IMU measurements. In order to obtain the ground truth of the receiver movement, a prism is mounted next to the antenna at the pole above the pedestrian. The prism is tracked by the aforementioned tachymeter which sends the measured coordinates to the laptop that records the coordinates simultaneously with the IMU measurements. To synchronize all devices, the laptop is additionally connected by cable to the channel sounder. Thus, we are able to obtain the ground truth of the receiver for each captured CIR snapshot. Although, the synchronization between the IMU and the channel sounder might be in the ms scale only, the influence on the position estimation is negligible because of the low pedestrian speed of around 0.7 m/s. Similar to the measurement setup in Section 6.1.1, the physical transmitter and the receiver are connected to the same Rubidium clock to prevent time drifts during the measurements.

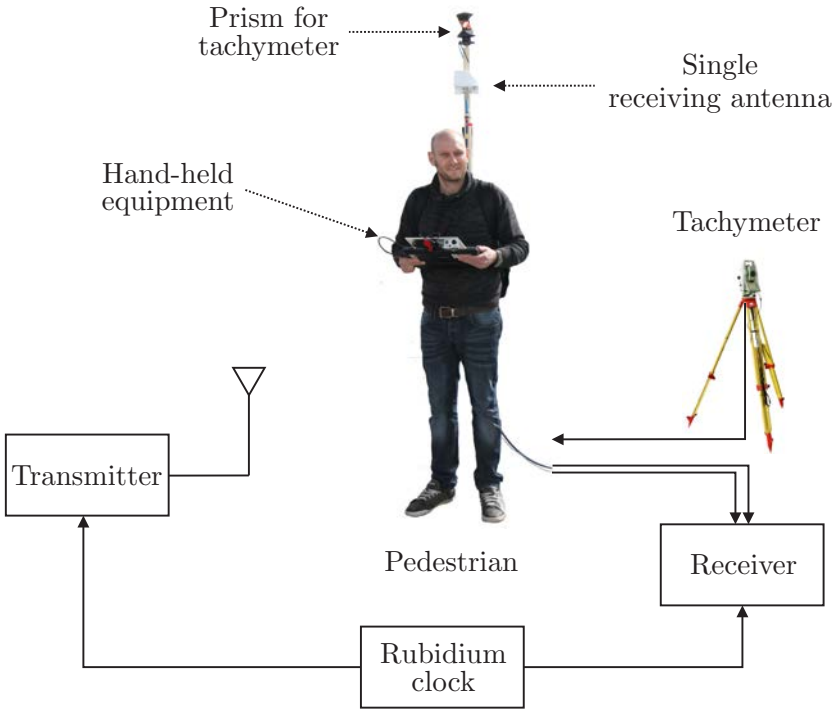

Figure 6.2. *Block diagram of the second measurement setup with a static physical transmitter and a pedestrian. The pedestrian carries the receiving antenna which is mounted on a stick next to a prism for measuring the ground truth of the moving receiver. The pedestrian holds a hand-held device which consists of an IMU and a laptop. For synchronization, physical transmitter and receiver use the same rubidium clock.*

6.2 Moving Model Train - Indoor Measurements

In this section, we evaluate Channel-SLAM in an indoor environment, indicated in Fig. 6.3 where we consider similarly to the simulations in Section 5.2 a LoS to NLoS transition. The transmit antenna was located in the lobby of the office building as visualized by the red diamond in Fig. 6.3, and the receiving antenna was mounted on the model train, see Section 6.1.1. The model train was running on the pre-measured track with a length of 23 m as indicated by the blue line in the office building, starting in the lobby and entering the meeting room after 14m with a travel speed of $0.05\,^{\mathrm{m}}/_{\mathrm{s}}$. Fig. 6.4 visualizes the antenna platforms on the left, the lobby on the upper right and the meeting room on the lower right. The left figure shows in the foreground the receiving antenna mounted on the top of the experimental platform on a height of 1.2 m and in the background the transmit antenna mounted on a tripod with the same height.

Fig. 6.5 shows the recorded CIRs as a function of the receiver traveled distance, where the color indicates the received power. The vertical dashed lines in Fig. 6.6 and Fig. 6.7 indicate the traveled distance when the receiver is entering the meeting room (cf. Fig. 6.3) and the black line indicates the GLoS path length. Fig. 6.6 and Fig. 6.7 show the estimated propagation distances and AoAs of KEST as a function of the receiver traveled distance. Only MPCs which are visible to the receiver for more than 5 m of movement are visualized. As shown in Fig. 6.6 and Fig. 6.7, many MPCs can be tracked for several meters of receiver movement. Channel-SLAM considers an underdetermined system, therefore, long tracked MPCs are preferable. Hence, for the evaluations, Channel-SLAM only uses those MPCs which are visualized in Fig. 6.6 and Fig. 6.7. Channel-SLAM could use all detected MPCs, however, this would increase the computational complexity. The LoS path is visible to the receiver until the receiver enters the meeting room. Due to limited bandwidth and MPCs that are close to the LoS path, KEST is not able to resolve all MPCs properly. Hence, the KEST estimation of the LoS path length is not identical to the GLoS path length.

Similarly to the simulations in Section 5.2, prior information on $\mathbf{x}_u(t_0)$ has been used. We apply a uniform distribution of 1 m width around the starting position $\boldsymbol{r}_u(t_0)$ and a uniform distributed speed between 0 m/s and 0.2 m/s for $\|\boldsymbol{v}_u(t_0)\|$ while the speed direction is drawn from a uniform distribution of 60° width around the moving direction. For the evaluation, Channel-SLAM uses $N_s = 6000$ particles in the super-PF. We limit the number of particles per bin to $N_m = 30$ and the grid size to $\Delta_d = 0.5\,\mathrm{m}$. For notational conveniences, the first propagation path, i.e. $i = 0$, is considered as the LoS path to the physical transmitter and, therefore, the position $\boldsymbol{r}_{\mathrm{VT},0}(t_k) = \boldsymbol{r}_t$ is equal

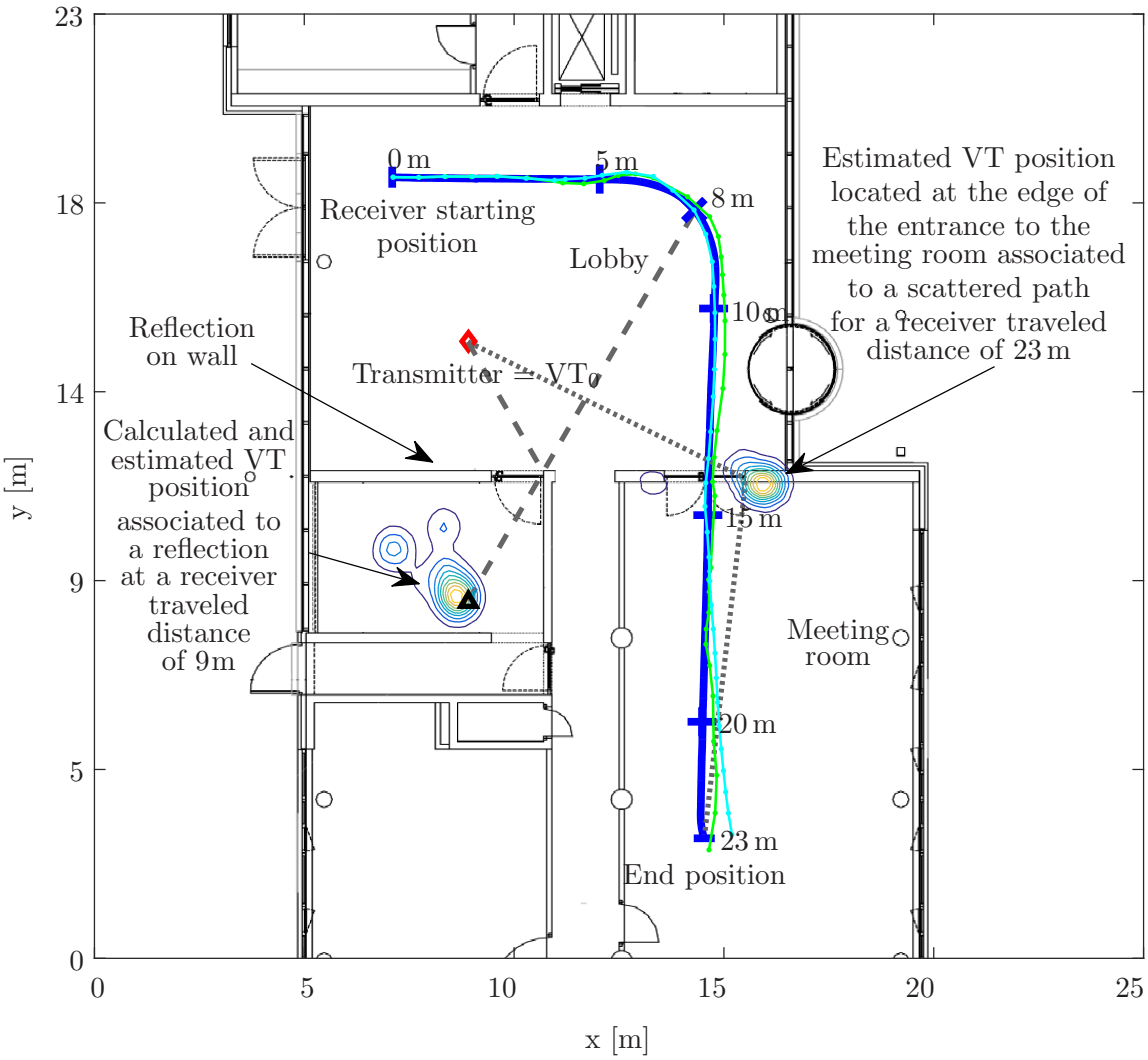

Figure 6.3. *Measurement scenario with a static physical transmitter and a moving receiver. The receiver is moving on the track as indicated in blue, starting in the lobby and entering after 14 m the meeting room. The green and cyan lines indicate the receiver position estimations of Channel-SLAM for two independent runs based on the same measurement data. Additionally, the PDFs of two estimated VT positions are shown, see also Fig. 6.6 and Fig. 6.7.*

to the physical transmitter position and $d_{\mathrm{VT},0}(t_k) = 0$. Compared to the simulations in the previous section, the number of tracked MPCs changes, hence, the number of sub-PFs changes accordingly. The number of used MPCs and respectively the number of VTs changes between 2 at the starting point and up to 7 at the end of the track. In Fig. 6.3, we show by the green and cyan lines two examples of the MMSE point estimates of the receiver position for two different PF evaluations based on the same

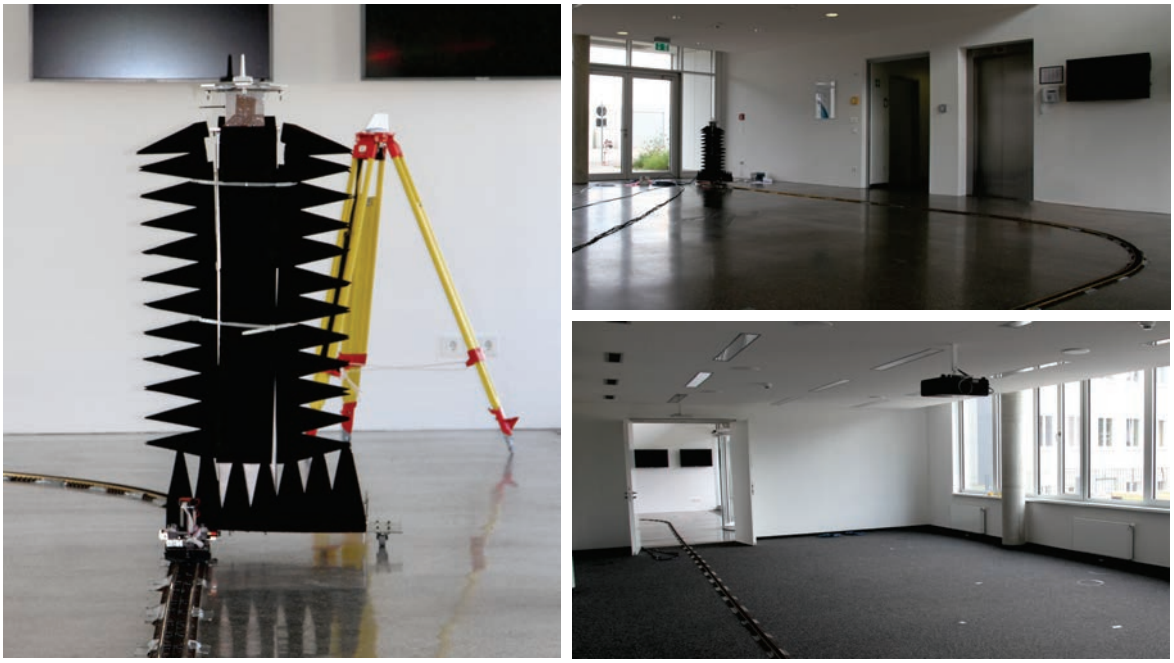

Figure 6.4. *Measurement scenario: the left figure shows in front the receiving antenna mounted on the top of the experimental train and in the background the transmit antenna mounted on a tripod. The left figure shows the lobby on top and below the meeting room with the pre-measured tracks.*

measurement data. Estimations with PFs include randomness, hence, even based on the same measurement data, the MMSE estimates differ for each evaluation unless the number of particles is infinite. Additionally, Fig. 6.3 visualizes two VTs that result from a reflected and scattered propagation path:

- On the left side of Fig. 6.3, the position of the VT occurring due to a reflection is displayed together with the estimated PDF obtained from Channel-SLAM for a receiver travelled distance of 8m. The black triangle denotes the calculated VT position based on the calculated propagation path indicated by the grey dashed lines. Fig. 6.6 and Fig. 6.7 compares additionally the delay and AoA estimate of KEST to the calculated theoretical delay and AoA indicated by the dashed lines. The theoretical delays and AoAs are calculated based on the known physical transmitter and receiver positions as well as on the room-layout measured by the tachymeter.

- On the right side of Fig. 6.3, the position of the VT occurring due to scattering is displayed together with the estimated PDF from Channel-SLAM for a receiver travelled distance of 23m. The VT is located at the edge of the entrance to the meeting room and corresponds, therefore, most probably to a scattered path

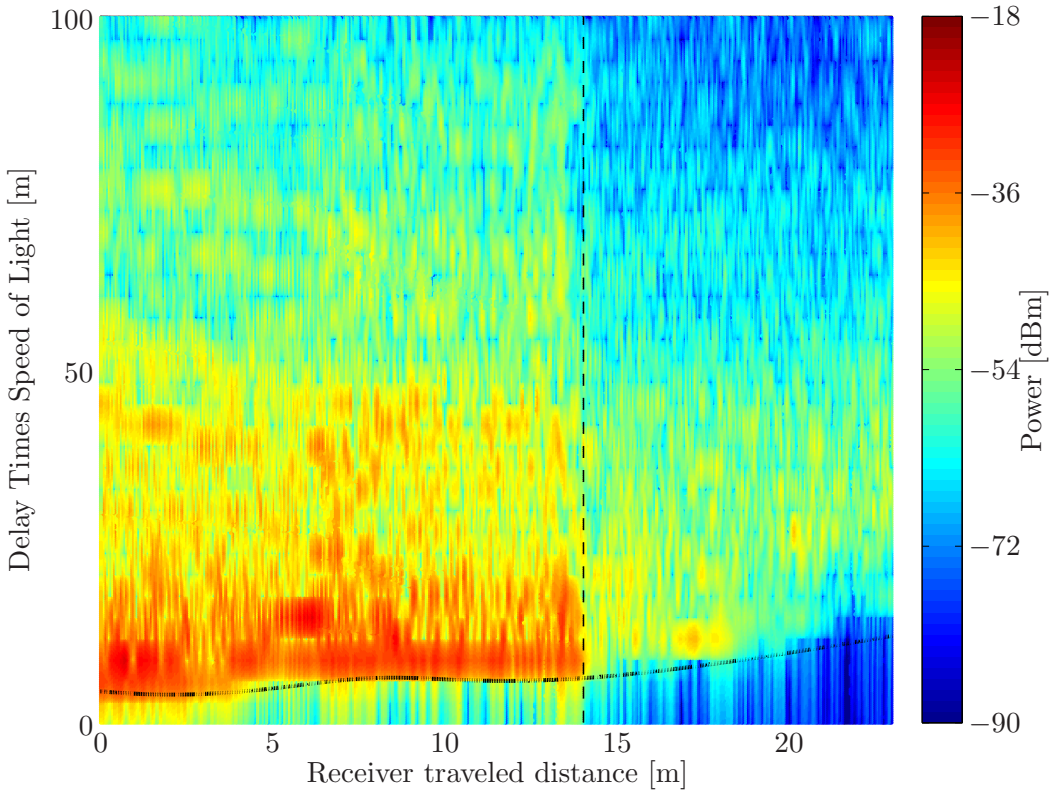

Figure 6.5. *Recorded CIRs as a function of the receiver traveled distance. The vertical black dashed line indicates the traveled distance at which the mobile receiver enters the meeting room. The black solid line indicates the GLoS path length.*

which explains the rather low received power for that MPC. Again, the theoretical delay and AoA of the MPC is visualized in Fig. 6.3, Fig. 6.6 and Fig. 6.7 as dotted lines.

Please note, by using a linear antenna array, two hypotheses of the VT position, on both sides of the linear antenna array are equally likely as long as the receiver moves along a straight line. Neither Channel-SLAM nor KEST can resolve the ambiguity. Hence, Channel-SLAM estimates the position of the VT on both sides of the antenna array that is aligned to the moving direction of the receiver. However, as long as the receiver moves on a straight track, both hypotheses do not influence the receiver position estimation. By turning, the ambiguity can be solved if the LoS path is present and the physical transmitter position is known. Therefore, for the considered reflected signal in Fig. 6.3, Fig. 6.6 and Fig. 6.7, the ambiguity problem can be solved because the receiver turns at the receiver traveled distance between 5m and 10m.

Because Channel-SLAM uses a PF, each evaluation result includes randomness. We performed 200 independent evaluations using Channel-SLAM based on the same measurement data visualized by the estimated CIRs in Fig. 6.6 and Fig. 6.7. In Fig. 6.8,

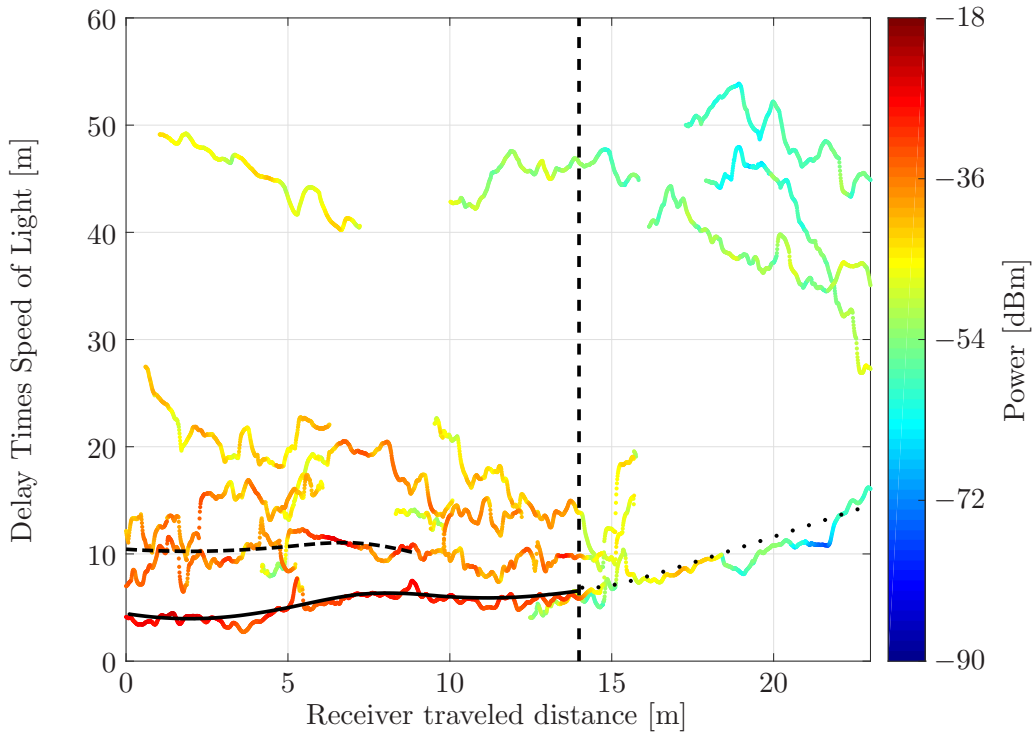

Figure 6.6. *Estimation results of KEST for the estimated propagation distances of the CIR as a function of the receiver traveled distance. Only MPCs that are visible to the receiver for more than* 5 m *are shown. The vertical black dashed line indicates the traveled distance at which the mobile receiver enters the meeting room. The black solid line indicates the GLoS path length, the black dashed line the theoretical propagation distance associated to a reflected path and the black dotted line the theoretical propagation distance associated to the scattered path shown in Fig. 6.3.*

the green curve shows the average $\mathrm{RMSE}_u(t_k)$ for all evaluations and time instants. The vertical dashed line indicates the traveled distance when the receiver is entering the meeting room. Because of the initialization of the receiver position using prior information, the position error at the beginning of the track is rather low. Afterwards, the $\mathrm{RMSE}_u(t_k)$ is varying between 0.6m and 1.1m. Nevertheless, an average position accuracy below 1.1m can be achieved within this indoor scenario. Similarly to Section 5.2, Fig. 6.8 shows also the RMSEs of Alg. III and Alg. IV. The description of Alg. III and Alg. IV can be found in Table 5.2. At the starting time, all algorithms perform similarly because of the same initialization. Because Alg. III and Alg. IV use only one MPC for positioning, the uncertainty increases during the receiver movement. After the LoS path is not received anymore, we obtain a better position estimation accuracy with Alg. III than with Alg. IV. Even if Alg. III uses the wrong MPC as the LoS path, the positioning estimation accuracy is higher than using only the transition model like Alg. IV.

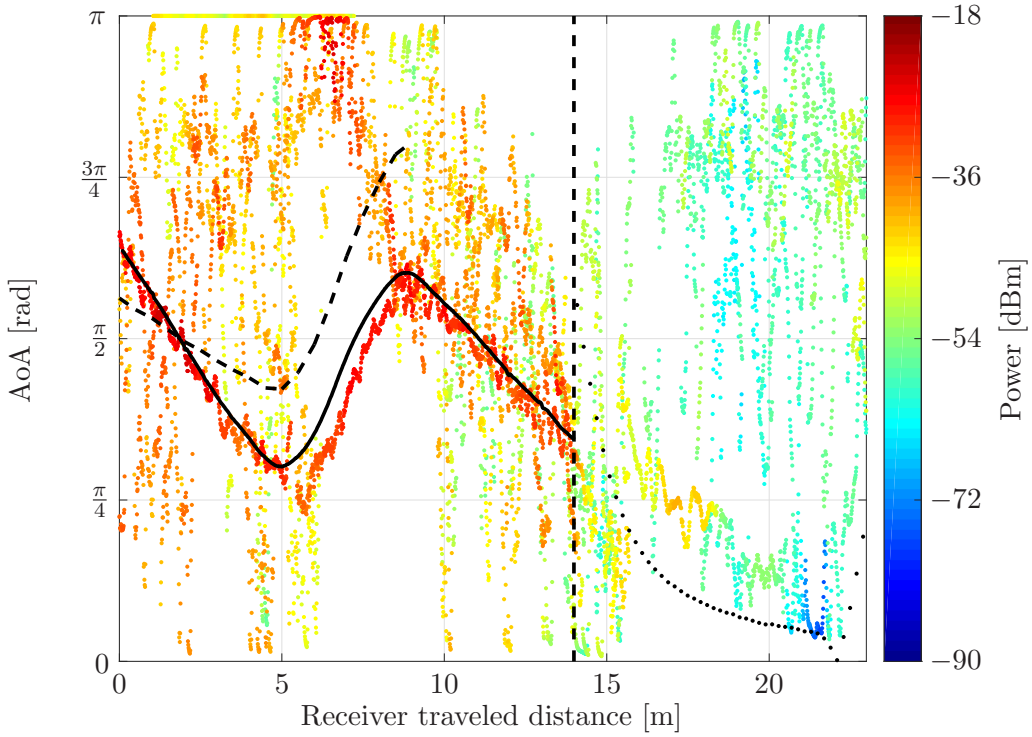

Figure 6.7. *Similar to Fig. 6.6, the figure shows the estimation results of KEST for the estimated AoAs of the CIR as a function of the receiver traveled distance.*

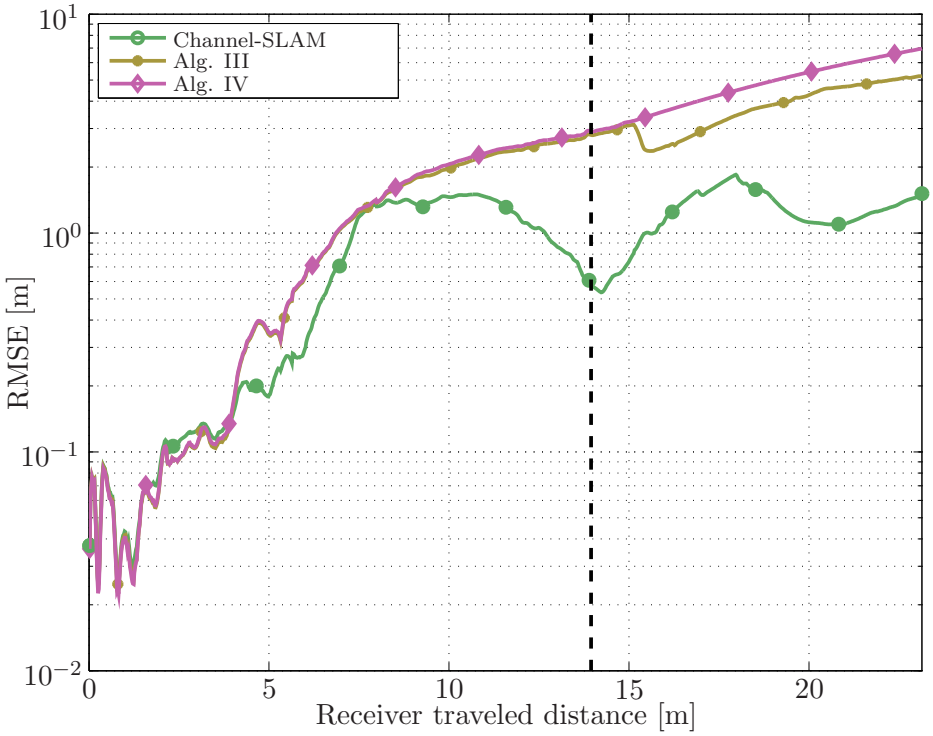

Figure 6.8. *$RMSE_u(t_k)$ as a function of the receiver traveled distance for Channel-SLAM, Alg. III and Alg. IV, see Table 5.2. The vertical black dashed line indicates the traveled distance at which the mobile receiver enters the meeting room.*

Figure 6.9. *Measurement scenario: the measurements were conducted in front of a hangar with metallic doors.*

6.3 Walking Pedestrian - Outdoor Measurements

In this section, we evaluate the derived algorithm based on channel measurements on an airfield in front of a hangar and chain-link fences, shown in Fig. 6.9. The measurements use the setup as described in Section 6.1.2, with a single static physical transmitter and a walking pedestrian. Fig. 6.10 shows the scenario by a top view with the physical transmitter position in red, the track in blue, the starting-position in green and the end-position in magenta. The pedestrian moves on the indicated track of Fig. 6.10 for 155s (distance of 111m) in front of a hangar with metallic doors. During the whole pedestrian movement, the LoS path between the physical transmitter and the receiver is present.

Fig. 6.11 shows the recorded CIRs and Fig. 6.12 the estimation results of KEST for the CIR as a function of the pedestrian moving time, where the color indicates the received power. In Fig. 6.12, we extracted only long visible MPCs from the KEST estimates. The black circled line in Fig. 6.12 indicates the GLoS path length, which matches perfectly to the KEST estimates for the first path. Additionally, other MPCs are tracked by KEST for a long time. The metallic doors of the hangar act as a reflecting surface for the transmitted wireless signal. Hence, we can obtain the position of VT_1 by mirroring the physical transmitter position at the reflecting surface as mentioned in Section 4.1. Additionally, the chain-link fences indicated by Fence 1, Fence 2, Fence 3 act as reflecting surfaces. Hence, we obtain VT_2, VT_3, VT_4 by mirroring the physical transmitter position at Fence 1, Fence 2 and Fence 3 as indicated in Fig. 6.10. The positions of the hangar, Fence 1, Fence 2 and Fence 3 are measured

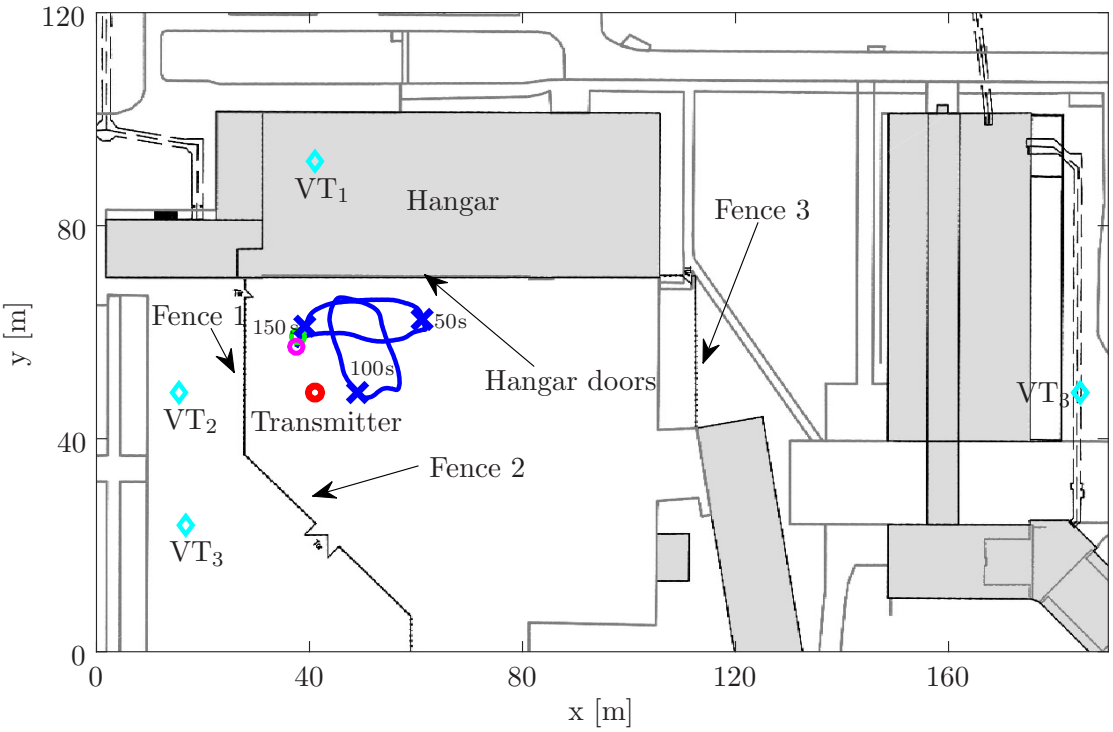

Figure 6.10. *Measurement scenario with a static physical transmitter and a moving receiver (pedestrian). The pedestrian moves on the blue track for* 155 s*, in total* 111 m*. The starting-position and end-position are indicated by the green and magenta circles. The metallic doors of the hangar and the chain-link fences act as reflecting surfaces for the transmitted wireless signal.*

using the tachymeter, thus, we are able to calculate the positions of VT_1, VT_2, VT_3 and VT_4 according to Section 4.1. Based on the calculated VT positions, we are able to determine the theoretical propagation distances between these VTs and the walking pedestrian for all time instants. We can see that the theoretical propagation distances indicated by the black lines in Fig. 6.12 match to the KEST estimates.

The evaluations are performed using $N_s = 2000$ particles in the super-PF, whereas the number of particles for the sub-PFs for each MPC is different depending on the estimated delay of each MPC. For the initialization of Channel-SLAM, we use prior information $\mathsf{p}\big(\mathbf{x}_u(t_0)\big)$. The prior information includes the starting position and moving direction, whereas the speed is initialized using a uniform distribution between 0 m/s and 1 m/s. We limit the number of particles per bin to $N_m = 30$ and the grid size to $\Delta_d = 1$ m. We compare Channel-SLAM with and without the prior information on the physical transmitter position. With the prior information on the physical transmitter

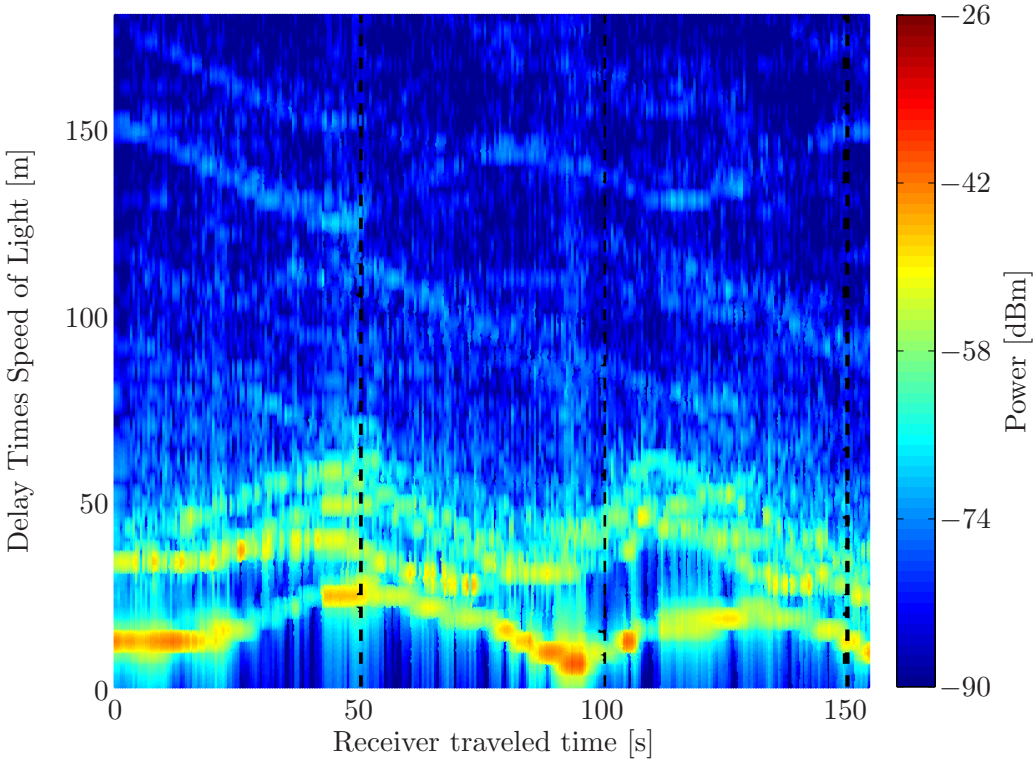

Figure 6.11. *Recorded CIRs as a function of the pedestrian moving time in seconds.*

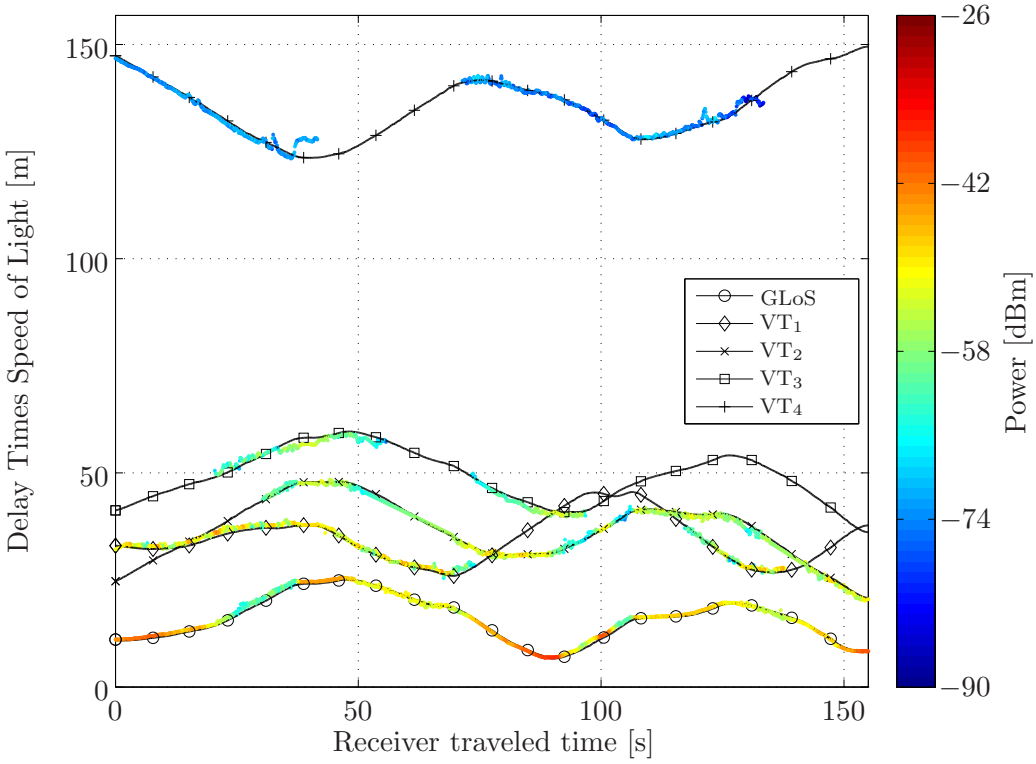

Figure 6.12. *Estimation results of KEST for the CIR as a function of the pedestrian moving time in seconds where only long tracked MPCs are visualized. Additionally the calculated propagation distances of the GLoS path and paths of VT_1, VT_2, VT_3 and VT_4 are shown.*

position, the first propagation path, i.e. $i = 0$, is considered as the LoS path to the physical transmitter and, therefore, the position $\boldsymbol{r}_{\mathrm{VT},0}(t_k) = \boldsymbol{r}_t$ is equal to the physical transmitter position and $d_{\mathrm{VT},0}(t_k) = 0$. If Channel-SLAM has no prior information on the physical transmitter position, Channel-SLAM estimates the position of the physical transmitter as a VT. During the pedestrian movement, the number of tracked MPCs changes which results in removing and initialization of sub-PFs during the movement. Additionally, because Channel-SLAM does not consider re-tracking of previous MPCs, e.g. the MPCs of VT_1 and VT_3 which are tracked multiple times, are initialized without any prior information. We set the continuous-time process noise intensity to $\sigma_{q_u}^2 = 5 \cdot 10^{-4} \frac{\mathrm{m}^2}{\mathrm{s}^3}$ and we perform 200 independent PF evaluations based on the same measurement data. For the evaluations we add an artificial clock bias to the measurements to verify the clock bias estimation capabilities.

Fig. 6.13 shows the enlarged measurement scenario with estimated PDFs for the physical transmitter, VT_1, VT_2 and the pedestrian positions. Whereas the PDFs of the physical transmitter, VT_2 and pedestrian positions are the estimation results at the end of the track, the estimated PDF of VT_1 is the estimation results when the tracking of the MPC is lost, i.e. after 75s. We see that especially the positions of both, the physical transmitter and VT_2 can be estimated with a low uncertainty. Additionally, Fig. 6.13 shows two examples of the MMSE point estimates of the receiver position with and without prior information on the physical transmitter position indicated in red and in green.

Fig. 6.14 shows the RMSEs of the estimated pedestrian positions as a function of the pedestrian moving time with and without the prior information on the physical transmitter position. Additionally, Fig. 6.14 shows the RMSE of Alg. I with perfect knowledge of the VT positions, see Table 5.2 for details about Alg. I. The measurement scenario considers only reflections, thus, Alg. I is equivalent to Alg. II. Because of the initialization of the receiver position using prior information, all algorithms perform similarly at the beginning of the track where the position error is rather low. Afterwards, the $\mathrm{RMSE}_u(t_k)$ is varying between 0.6m and 5m. Alg. I can be interpreted as a lower bound and estimates the receiver position with the lowest RMSE. Between 70s and 90s of the receiver movement, Alg. I has a slightly higher RMSE which might be due to the non-perfect reflecting surfaces, KEST estimation errors or small inaccuracies in the calculations of the VT positions. Furthermore, we see that we obtain similar RMSEs with and without the prior information on the physical transmitter position. Similar to the simulations, we can conclude that Channel-SLAM does not require the prior information on the physical transmitter position if an IMU is used.

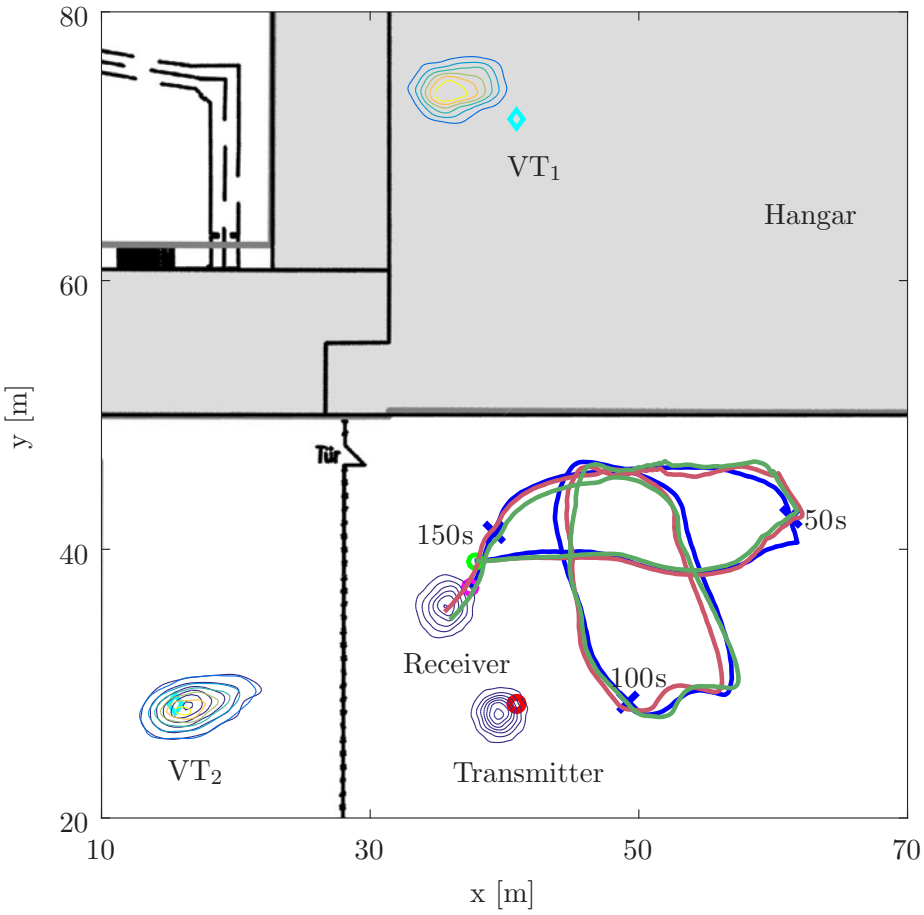

Figure 6.13. *Enlarged measurement scenario of Fig. 6.10 with the ground truth of the track in blue. The figure shows two examples of the MMSE point estimates of the receiver position with the prior information on the physical transmitter position in green and without in red. The starting-position and end-position are indicated by the green and magenta circles. Additionally, the figure shows the estimated PDFs for the physical transmitter, VT_1, VT_2 and pedestrian position.*

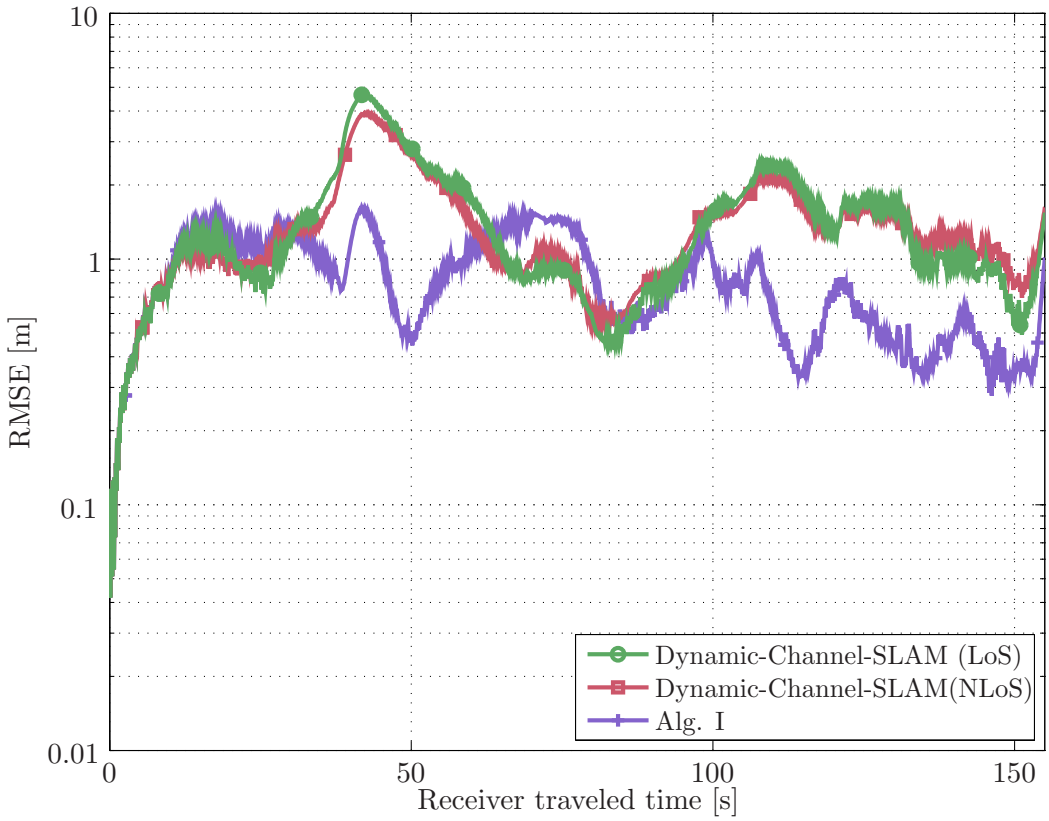

Figure 6.14. *$RMSE_u(t_k)$ as a function of the pedestrian moving time for Channel-SLAM with and without the prior information on the physical transmitter position. Additionally, Alg. I is shown which assumes perfect knowledge of the VT positions and physical transmitter position, see Table 5.2 for details about Alg. I. The measurement scenario considers only reflections, thus, Alg. I is equivalent to Alg. II.*

6.4 Walking Pedestrian - Indoor Measurements

This section evaluates Channel-SLAM based on channel measurements with a single static physical transmitter and a walking pedestrian (see Section 6.1.2) as shown in Fig. 6.15 outside and inside an office building. The pedestrian moves on the blue track for 522 s, starts at the parking lot, enters the building, walks down two corridors, walks inside the meeting room and leaves the building to the parking lot. The starting-position is indicated by the green circle, the end-position by the magenta circle and the physical transmitter position by the red circle. In the following, we divide the track into different track-sections (TSs), see Table 6.2. To measure the position of the receiver, the tachymeter was located in the lobby where the prism of the walking pedestrian is in LoS conditions to the tachymeter in the TSs I, II, IV, VI, VII and VIII. For the corridor parts, TS III and TS V, the prism of the walking pedestrian is in NLoS conditions. In order to obtain the ground truth of the moving pedestrian in TS III and TS V, we measured ground truth points (markers) in these TSs in advance. Whenever the pedestrian walks on such a marker, it is recorded in the data capturing software running on the laptop. By using these ground truth points we obtain an accuracy of the pedestrian location in the order of 20 cm. The pedestrian moves with a constant speed, except between the time instants 210s and 265s, and between 375s and 395s, where the pedestrian was standing.

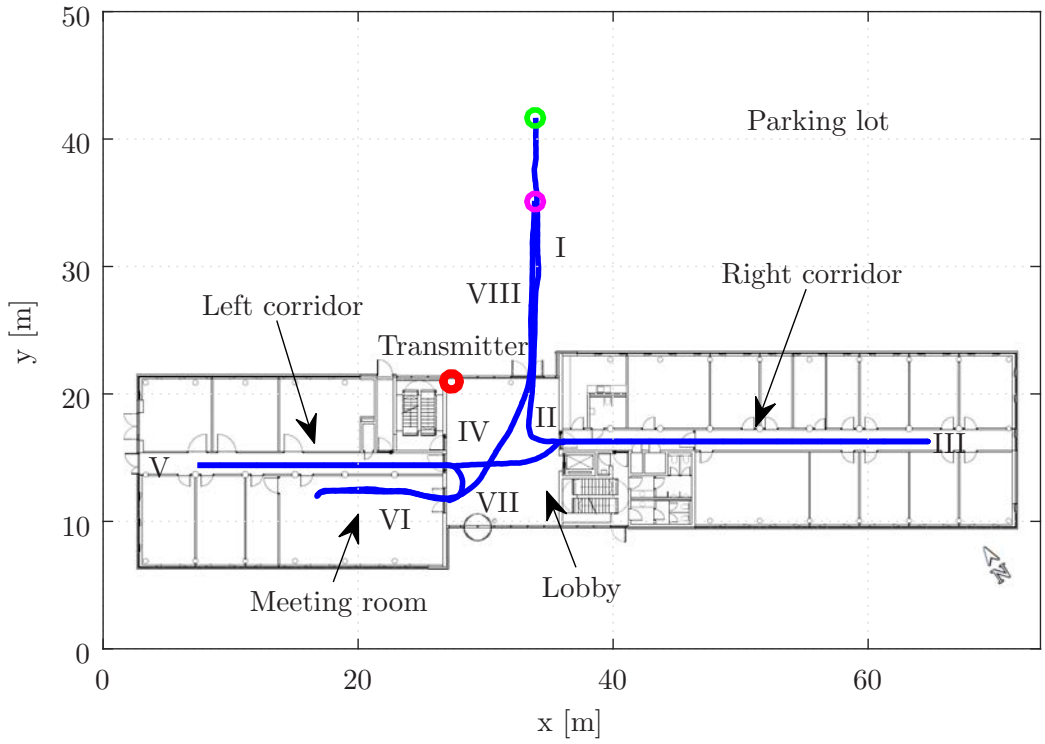

Figure 6.15. *Measurement scenario with a static physical transmitter and a moving receiver (pedestrian). The pedestrian moves on the blue track for* 522 s*: starts at the parking lot (indicated by the green circle), enters the building, walks down two corridors, walks inside the meeting room and leaves the building back to the parking lot (end-position indicated by the magenta circle). The track is divided into different TSs, see Table 6.2*

Table 6.2. *Description of the different sections of the track*

Track-section (TS)	**Beginning at**	**Description**
I	$t_k = 0\,\mathrm{s}$	Outdoor
II	$t_k = 42\,\mathrm{s}$	Lobby
III	$t_k = 73\,\mathrm{s}$	Right corridor
IV	$t_k = 213\,\mathrm{s}$	Lobby transition
V	$t_k = 295\,\mathrm{s}$	Left corridor
VI	$t_k = 384\,\mathrm{s}$	Short lobby passage & meeting room
VII	$t_k = 470\,\mathrm{s}$	Lobby
VIII	$t_k = 498\,\mathrm{s}$	Outdoor

Fig. 6.16 shows the recorded CIRs as a function of the receiver traveled time, where the color indicates the received power. Many MPCs are closely spaced regarding their delays, nevertheless for some parts of the track it is possible to determine the evolution of different MPCs. The figure shows periods with high power, when the receiver is in the lobby close to the physical transmitter, and periods with low power when the LoS path is blocked or attenuated by walls, e.g. outdoors or inside the corridors. Fig. 6.16b shows the estimation results of KEST for the CIR as a function of the receiver traveled time, where only the MPCs of KEST which are tracked for more than 3 m of the receiver movement are shown. Many MPCs can be tracked for several seconds of receiver movement. The black line in Fig. 6.16b shows the GLoS path. For TS I, the LoS path between the physical transmitter and the receiver is present. However, the signal of the LoS path is attenuated by the coated window. In TS I, the pedestrian walks towards the physical transmitter, thus, the delay of the LoS path decreases. Other MPCs behave similarly, indicating that their corresponding VTs are located in moving direction. When entering the lobby (TS II) the received power increases and drops again by the time entering the first corridor (TS III). During the time the pedestrian walks in the right corridor, one MPC with a slightly larger delay than the calculated GLoS, which is probably caused by a diffraction at the entrance door of the corridor. Furthermore, for this part of the track, also a signal most probably reflected at the end of the corridor is received. By leaving the corridor to the lobby, the received power rises again (TS IV). However, the LoS path is tracked inaccurately during the crossing of the lobby, which might be caused by the limited bandwidth and closely spaced MPCs. During the time the pedestrian walks in the left corridor (TS V), the LoS path is blocked and MPCs which are most likely caused by reflections on the right wall of the lobby are tracked by KEST. After shortly passing the lobby, the pedestrian enters the meeting room (TS VI). Although several MPCs are present, KEST is only able to track MPCs for a short period of time caused by dense multipath components (DMCs). Finally, the pedestrian leaves the meeting room and the building through the lobby (TS VII) back to the parking lot (TS VIII).

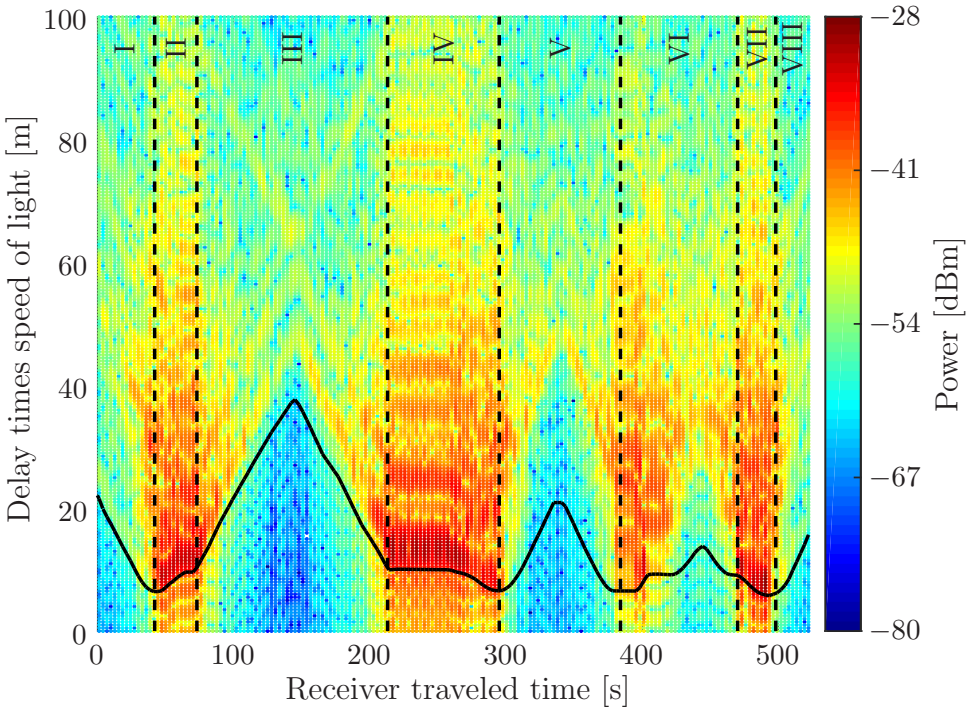

(a) *Recorded CIRs as a function of the receiver traveled time in seconds.*

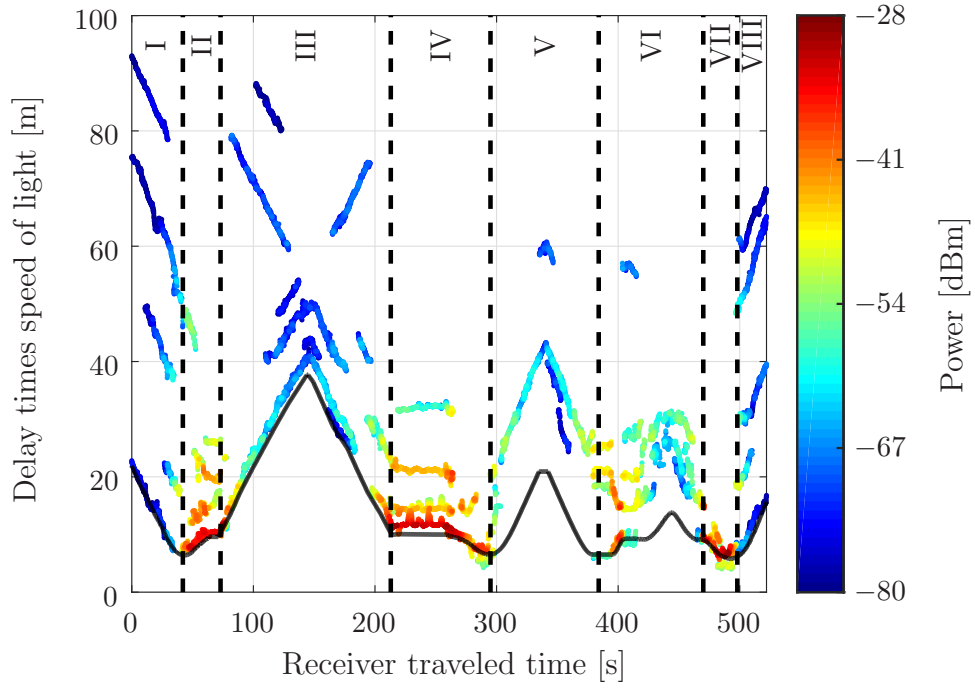

(b) *Estimation results of KEST for the CIR as a function of the receiver traveled time. Only MPCs that are visible to the receiver for more than* 3 m *are shown.*

Figure 6.16. *Recorded CIRs and estimation results of KEST. The black line indicates the GLoS path. The vertical dashed lines indicate the different TSs, see Table 6.2.*

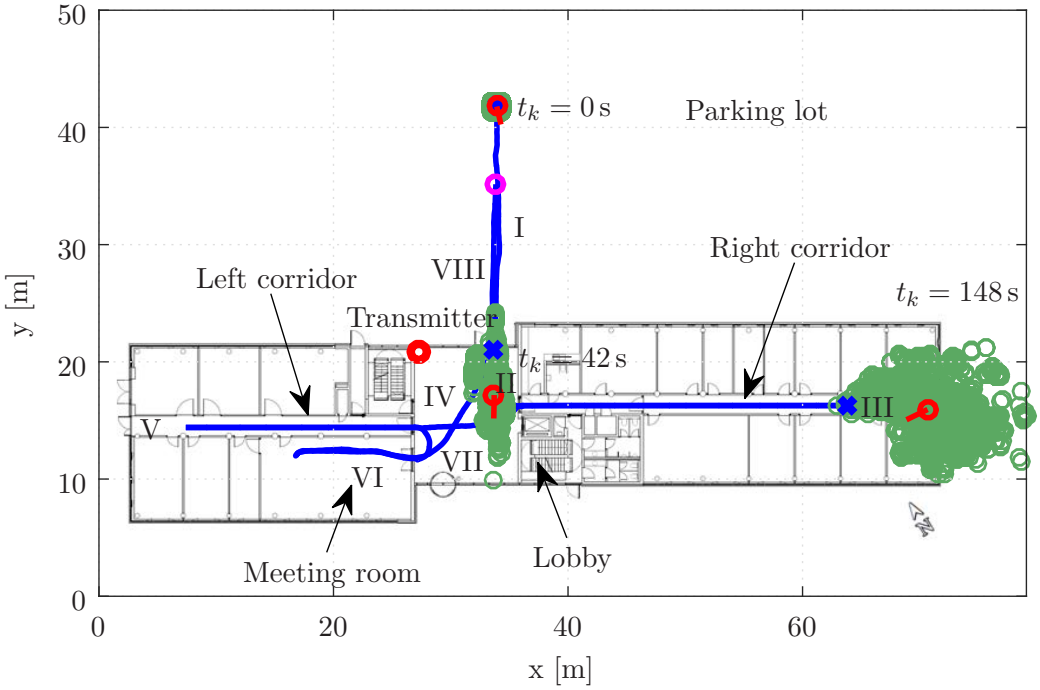

Figure 6.17. *Visualization of the particle filter estimation of the receiver position for three different time instances: $t_k = 0\,\mathrm{s}$ (initialization), $t_k = 42\,\mathrm{s}$ and $t_k = 148\,\mathrm{s}$. The green circles indicate the particle states of the receiver positions, the red circles the MMSE estimates of the receiver positions and the blue crosses the ground truths.*

Similarly to the measurement evaluation in Section 6.3, prior information on $\mathbf{x}_u(t_0)$ has been used. We apply a uniform distribution of 1 m width around the starting position $\boldsymbol{r}_u(t_0)$ and a uniform distributed speed between 0 m/s and 0.2 m/s for $\|\boldsymbol{v}_u(t_0)\|$ while the speed direction is assumed to be known. For the evaluation, Channel-SLAM uses $N_s = 2000$ particles in the super-PF. We limit the number of particles per bin to $N_m = 30$ and the grid size to $\Delta_d = 0.5\,\mathrm{m}$. Additionally, for the evaluations of Channel-SLAM, we do not assume any prior information on the physical transmitter position, i.e. Channel-SLAM estimates the position of the physical transmitter as a VT.

Fig. 6.17 illustrates different time steps of the position estimation. For simplicity we show only the estimations of the receiver position. We show by the green circles the particle states of the receiver positions, by the red circles the MMSE estimates of the receiver positions and by the blue crosses the ground truths. During the receiver movement the uncertainty on the estimated pedestrian position increases.

Fig. 6.18 shows the RMSE of the estimated receiver position as a function of the receiver traveled time. We performed 200 independent runs of the PF implementation of Channel-SLAM based on the same measurement data. Because of the initialization

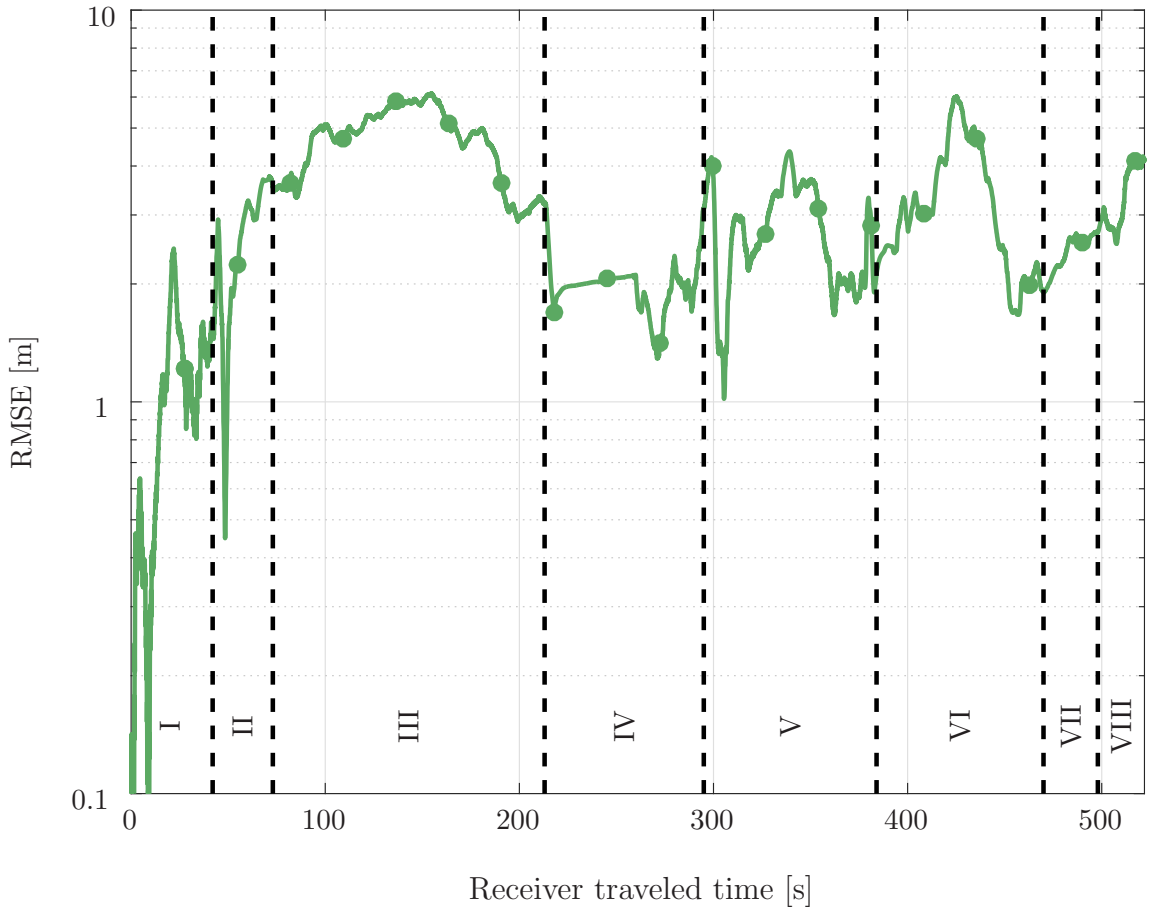

Figure 6.18. *$RMSE_u(t_k)$ as a function of the receiver traveled time in seconds. The vertical dashed lines indicate the different TSs, see Table 6.2.*

of the receiver position using prior information, the position error at the beginning of the track is rather low and increases up to 6 m when the pedestrian is inside the right corridor. Afterwards, the error decreases and varies between 1 m and 4 m. During the time when the pedestrian walks inside the meeting room (TS VI) the error grows again up to 6 m most likely caused by MPCs which have a short life time. To further decrease the positioning error, additional sensors like using signals of GNSSs as proposed in [GPU+17a] or mapping algorithms as proposed in [GMU+16, GMP+16] could be used.

Chapter 7

Conclusion and Future Work

In this thesis a novel algorithm referred to as Channel-SLAM is introduced which allows positioning of moving receivers using wireless radio signals. Channel-SLAM requires only one physical transmitter in operation and exploits multipath propagation for positioning. Thus, Channel-SLAM stands for a paradigm shift in radio based positioning where multipath propagation has so far been considered as harmful for precise positioning. We presented a Bayesian formulation and particle filter (PF) implementation of Channel-SLAM and applied Channel-SLAM to measurement data. Using Channel-SLAM on the measurement data shows that accurate position estimation is possible by exploiting multipath propagation even without the prior information on the physical transmitter position. To the knowledge of the author, this is the first time that the possibility of using multipath propagation for positioning without prior information such as room-layout or fingerprinting database has been shown. We believe that Channel-SLAM is a suitable technique for applications for global navigation satellite system (GNSS) denied areas such as inside buildings. Furthermore, the work in this thesis opens the door for precise positioning without prior information on the physical transmitter position.

The main contributions of this thesis are as follows:

- We proposed a novel transition model to describe each multipath component (MPC) as a line-of-sight (LoS) path being emitted from a virtual transmitter (VT) with unknown position. Hence, a specific detection of different propagation phenomena such as reflection, diffraction or scattering is not necessary. The VTs are inherently time synchronized to the physical transmitter and static in their positions with an additional constant propagation distance.

- We derived a novel algorithm based on recursive Bayesian filtering for Channel-SLAM. Channel-SLAM estimates the receiver position and the positions of the

VTs simultaneously. Hence, received MPCs increase the number of transmitters enabling positioning when the number of physical transmitters is insufficient or resulting in a more accurate position estimate. Additionally, the approach does not require any prior information such as a room-layout or a database for fingerprinting.

- We introduced two different implementations of Channel-SLAM: The first implementation of Channel-SLAM considers a receiver equipped with a linear antenna array. In addition to the estimated delays, Channel-SLAM uses angle of arrival (AoA) measurements to improve the positioning accuracy. The second implementation of Channel-SLAM fuses heading information coming from an inertial measurement unit (IMU) with the estimated MPC parameters. By using the heading information, Channel-SLAM requires only an initial prior information on the receiver position and moving direction to define the coordinate system. Thus, prior information on the physical transmitter position is not necessary and is estimated like a VT.

- Channel-SLAM is derived based on Rao-Blackwellization, where the state space is partitioned into subspaces. The algorithm allows to use different numbers of particles in each particle filter associated to a VT. The number of particles are dynamically adapted during runtime which enables a major performance gain in terms of computational effort.

- To verify the position accuracy of Channel-SLAM, a posterior Cramér-Rao lower bound (PCRLB) is derived which incorporates heading information. Based on simulations, the accuracy of Channel-SLAM is compared to the derived PCRLB. The evaluations show that accurate position estimation is possible when MPCs are used even without the prior information on the physical transmitter position.

- Channel-SLAM is evaluated based on three measurement campaigns covering indoor and outdoor scenarios. Using Channel-SLAM on measurement data shows that accurate position estimation is possible by exploiting MPCs.

The thesis focuses on Channel-SLAM, derives the algorithm and provides performance results. Ongoing research, beyond the results included in this thesis are:

- Channel-SLAM assumes the knowledge of the starting position to fix the coordinate system. In outdoor environments this knowledge can be obtained from GNSS. Preliminary research was done in [GPU+17a] to fuse Channel-SLAM with GNSS pseudoranges. Future research might exploit multipath propagation of GNSS signals for positioning.

- Channel-SLAM estimates the position relatively, hence, errors are cumulative and the growth in uncertainty is unbounded over time. First results published in [GMU+16] describes an algorithm to generate a map of the visited areas. The algorithm estimates the situation when the receiver revisits an area to correct estimation errors. Future research could go towards merging several maps of the visited areas collected by one or more receivers.

- The presented Channel-SLAM implementation does not consider retracking of previous MPCs or VTs. Hence, if the tracking of a MPC has been lost and might be regained, the corresponding VT is initialized without any prior information. Thus, first research was done in [GMP+16, UGJD17] to extend Channel-SLAM, to estimate, map and reuse previous estimated VT states. Especially, first results presented in [UGJD17] show that reusing VTs increases the position accuracy.

Further work in multipath assisted position may be pursued:

- The derived model for Channel-SLAM assumes a static two dimensional environment. Dynamic scatterers like in a car-to-car scenario are not included. Furthermore, Channel-SLAM assumes that the signal is reflected on a plain surface. Future work could consider MPCs which interact with uneven, curved surfaces and moving objects. Additionally, Channel-SLAM might be extended to consider three dimensional environments.

- We propose in this thesis a two level approach: on the first level, the multipath parameters for each MPC are estimated based on the received wireless signal by Kalman enhanced super resolution tracking (KEST); on the second level, Channel-SLAM estimates the receiver and VT states based on the estimated MPCs. Future research could jointly combine both levels, in order to further improve the position accuracy.

- Channel-SLAM uses solely the heading information of the IMU to solve ambiguities and improve the position accuracy. Theoretically, the inertial measurements allow to compute continuously position and attitude for inertial navigation by numerical integrations. Further extensions of Channel-SLAM could use more information provided by the IMU.

Appendix A

Inertial Measurement Units

A.1 Introduction

Today many smartphones feature a micro-electro-mechanical system (MEMS) IMU. An IMU is an electronic device that provides inertial measurements by using a combination of accelerometers and gyroscopes. The accelerometers measure the linear accelerations and the gyroscopes measure the turn rates. Numerical integrations of the inertial measurements allow to compute continuously position and attitude for inertial navigation: double integrating the acceleration yields to the position change; integrating the turn rate yields to the attitude change. IMUs are classically built as mechanical devices which consist of precision mechanical gyroscopes and accelerometers used in e.g. airplanes. In recent years, MEMS IMUs became popular with sub-cm size. However, compared to the mechanical IMUs, MEMS IMUs are not able to provide the same precision or long term stability [Woo07]. Because the position calculation involves double integrations, even small measurement errors quickly cause a drift in the position solution which makes the position solution unreliable over time.

The inertial measurements are provided from the IMU with respect to the sensor alignment [Woo07] i.e. the body frame (b-frame). In order to obtain the inertial measurements, a transformation from the b-frame to the navigation frame (n-frame) is necessary introduced in Section A.2. In our application, the position of the IMU is assumed as constant with respect to the receiving antenna. Thus, we are able to calculate the coordinate transformation matrices during a calibration phase.

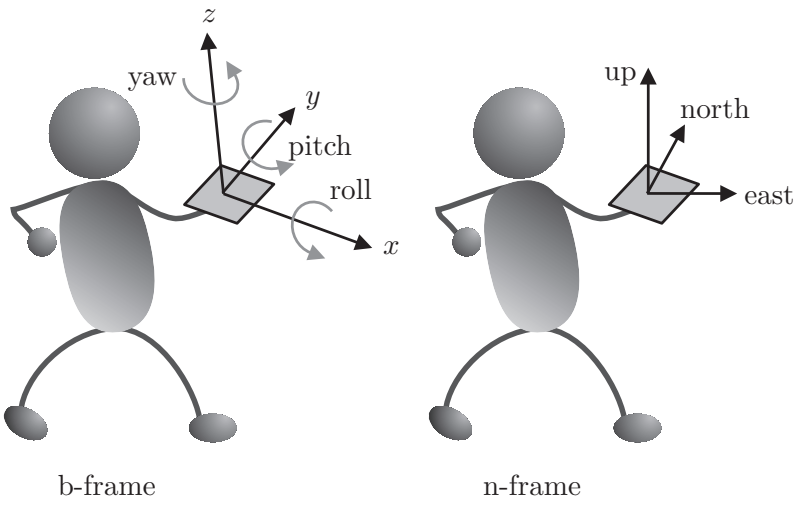

Figure A.1. *IMU coordinate systems.*

A.2 Inertial Navigation

In order to use the inertial measurements, transformations between different coordinate systems are necessary [Jek01] as shown in Fig. A.1. The accelerations are measured with respect to the b-frame, whereas the gyroscope senses the angular rates of the b-frame with respect to the inertial frame (i-frame) in the b-frame. The b-frame generally refers to the device to be navigated and is centered at the measurement device where the axes are aligned with the device axes. If the center of gravity is not correctly aligned with the axes, a transformation from the sensor frame to the b-frame is necessary. The i-frame has its origin at the center of the earth and is fixed, i.e. it does not rotate with the earth.

To estimate the heading, we need to transfer the measurements to the n-frame. As shown in Fig. A.1 on the right, the n-frame is also centered at the measurement device, but the axes are pointing towards north, east and up directions and serves as a reference frame for the attitude. The rotation from the n-frame to the b-frame depends on the heading and pitch of the IMU and is given by

$$\mathbf{R}_{n\to b}(t_k) = R_3(\psi(t_k))R_2(\theta(t_k))R_1(\phi(t_k))\,, \tag{A.1}$$

with the rotation matrices R_1, R_2 and R_3 around the x-, y- and z-axis. Roll $\phi(t_k)$, pitch $\theta(t_k)$ and yaw $\psi(t_k)$ angles refer to rotations around the x, y and z axes.

As mentioned before, the time-discrete accelerometer measurements $\boldsymbol{a}_b(t_k)$ are provided in the b-frame and can be modeled according to [Jek01, Hen15], with

$$\boldsymbol{a}_b(t_k) = \mathbf{R}_{n\to b}(t_k)\,\boldsymbol{a}_n(t_k) + \boldsymbol{b}_b(t_k) + g \begin{pmatrix} -\sin(\theta(t_k)) \\ \cos(\theta(t_k))\sin(\phi(t_k)) \\ \cos(\theta(t_k))\cos(\phi(t_k)) \end{pmatrix} + \boldsymbol{\epsilon}_b(t_k)\,, \tag{A.2}$$

with the rotation matrix $\mathbf{R}_{n\to b}(t_k)$, the acceleration in the n-frame $\boldsymbol{a}_n(t_k)$, the gravitational acceleration g, the accelerometer biases $\boldsymbol{b}_b(t_k)$ and the measurement noise $\boldsymbol{\epsilon}_b(t_k)$.

The gyroscope measures the angular rates $\boldsymbol{\omega}_{ib}^b(t_k)$ of the b-frame with respect to the inertial i-frame in the b-frame, where the relations are given by

$$\boldsymbol{\omega}_{ib}^b(t_k) = \mathbf{R}_{n\to b}(t_k)\boldsymbol{\omega}_{in}^n(t_k) + \boldsymbol{\omega}_{nb}^b(t_k) + \boldsymbol{b}_{\omega_{ib}}^b(t_k) + \boldsymbol{\epsilon}_{\omega_{ib}}^b(t_k)\,, \tag{A.3}$$

where $\boldsymbol{\omega}_{in}^n(t_k)$ are the angular rates in the n-frame with respect to the i-frame, $\boldsymbol{b}_{\omega_{ib}}^b(t_k)$ are the gyroscope biases and $\boldsymbol{\epsilon}_{\omega_{ib}}^b(t_k)$ denotes measurement noise [Hen15, Jek01]. The term $\boldsymbol{\omega}_{in}^n(t_k)$ describes the rotation of the n-frame with respect to the i-frame depending on the geographical latitude $\nu(t_k)$, the rates $\dot{\nu}(t_k), \dot{\lambda}(t_k)$ of latitude and longitude, and the angular velocity of the earth ω_e with

$$\boldsymbol{\omega}_{in}^n(t_k) = \begin{pmatrix} (\dot{\lambda}(t_k) + \omega_e)\cos(\nu(t_k)) \\ -\dot{\nu}(t_k) \\ -(\dot{\lambda}(t_k) + \omega_e)\sin(\nu(t_k)) \end{pmatrix}. \tag{A.4}$$

The angular rates of the b-frame with respect to the n-frame $\boldsymbol{\omega}_{nb}^b(t_k)$ are related to the time derivative of the Euler angles [Jek01] by

$$\boldsymbol{\omega}_{nb}^b(t_k) = \begin{pmatrix} 1 & \sin(\phi(t_k))\tan(\theta(t_k)) & \cos(\phi(t_k))\tan(\theta(t_k)) \\ 0 & \cos(\phi(t_k)) & -\sin(\phi(t_k)) \\ 0 & \sin(\phi(t_k))/\cos(\theta(t_k)) & \cos(\phi(t_k))/\cos(\theta(t_k)) \end{pmatrix} \begin{pmatrix} \dot{\phi}(t_k) \\ \dot{\theta}(t_k) \\ \dot{\psi}(t_k) \end{pmatrix}. \tag{A.5}$$

The basic relation is given by (A.3) and (A.5), however, the knowledge of the initial roll and pitch angles, i.e. the tilted position of the device as well as the sensor biases are essential, which can be determined if the device is static, see Section A.3.

A.3 Preprocessing

The purpose of the preprocessing procedure is to obtain the heading changes $\dot{\phi}(t_k)$ during runtime based on the acceleration and turn rate measurements from the IMU. In our considered scenario, the position of the IMU is assumed as constant with respect to the receiving antenna. Therefore, we are able to calculate the coordinate transformation matrices during a calibration phase at the beginning during a static phase. For a static IMU, the accelerations in the n-frame $\boldsymbol{a}_n(t_k)$ in (A.2) are zero. While in theory an object could move at a constant velocity without undergoing any acceleration or turning, this is highly unlikely in reality. Especially when considering pedestrian applications, movements will always cause shaking and vibration of the IMU. Neglecting sensor noise and biases, we only measure the acceleration due to the gravitational force of the earth. In this case, pitch $\theta(t_k)$ and roll $\phi(t_k)$ of the device can be determined by

$$\theta(t_k) = -\sin^{-1}\left(\frac{a_x^b(t_k)}{\|\boldsymbol{a}_b(t_k)\|}\right), \tag{A.6a}$$

$$\phi(t_k) = \sin^{-1}\left(\frac{-a_y^b(t_k)}{(\|\boldsymbol{a}_b(t_k)\|\cos(\theta(t_k))}\right), \tag{A.6b}$$

where $\boldsymbol{a}_b(t_k) = \left(a_x^b(t_k), a_y^b(t_k), a_z^b(t_k)\right)^T$ is the measured acceleration in the b-frame [Ped13]. As mentioned before, for simplicity we assume that the IMU has a constant tilt during the measurements. In practical applications, the sensor orientation has to be estimated continuously [FON08]. If $\theta(t_k)$ and $\phi(t_k)$ are estimated during the calibration phase, the heading change $\dot{\phi}(t_k)$ can be calculated from (A.5) during runtime.

A.4 Movement Detection

As mentioned before, we use the IMU measurements to obtain information if the IMU is in motion or static. We use a thresholding technique proposed in [SGGO05] to detect quasi-static states of the IMU based on the accelerometer and gyroscope measurements. This is particularly effective since we assume that the IMU has a constant tilt during the measurements. However, difficulties arise in selecting the optimal threshold value, which can vary between users, surfaces, etc. Especially, for an unconstrained smartphone, the freedom of movement might additionally affect the property of the accelerometer and gyroscope measurements and mistakenly trigger the threshold. Detecting levels of activity is a widely spread research topic and further information can be found in e.g. [SGGO05, RM00, FNRA10, KWM11, AGO+12, BH13].

Appendix B

Derivation of the Weight Update Equation for Channel-SLAM

In the following we derive the weight update equation of (4.20) for the approximations of (4.19), see also [AMGC02, RAG04]. According to [AMGC02], the posterior density $\mathsf{p}\big(\mathbf{x}_u(t_{0:k})|\mathbf{z}(t_{1:k})\,,\mathbf{u}(t_{1:k})\big)$ can be approximated as

$$\mathsf{p}\big(\mathbf{x}_u(t_{0:k})|\mathbf{z}(t_{1:k})\,,\mathbf{u}(t_{1:k})\big) \approx \sum_{j=1}^{N_s} w^{(j)}(t_k)\;\delta\left(\mathbf{x}_u(t_{0:k}) - \mathbf{x}_u^{(j)}(t_{0:k})\right)\,, \tag{B.1}$$

with the weight update

$$w^{(j)}(t_k) \propto \frac{\mathsf{p}\big(\mathbf{x}_u^{(j)}(t_{0:k})|\mathbf{z}(t_{1:k})\,,\mathbf{u}(t_{1:k})\big)}{\mathsf{q}\big(\mathbf{x}_u^{(j)}(t_{0:k})|\mathbf{z}(t_{1:k})\,,\mathbf{u}(t_{1:k})\big)}\,, \tag{B.2}$$

where the particles $\mathbf{x}_u^{(j)}(t_{0:k})$ are drawn from the importance density $\mathsf{q}\big(\mathbf{x}_u^{(j)}(t_{0:k})|\mathbf{z}(t_{1:k})\,,\mathbf{u}(t_{1:k})\big)$. Seeing it from an iterative perspective, at each time instant t_k, we have an approximation for $\mathsf{p}\big(\mathbf{x}_u(t_{0:k-1})|\mathbf{z}(t_{1:k-1})\,,\mathbf{u}(t_{1:k-1})\big)$ where we want to approximate $\mathsf{p}\big(\mathbf{x}_u(t_{0:k})|\mathbf{z}(t_{1:k})\,,\mathbf{u}(t_{1:k})\big)$ with a new set of particles. If we chose the importance density that

$$\begin{aligned}&\mathsf{q}\big(\mathbf{x}_u(t_{0:k})|\mathbf{z}(t_{1:k})\,,\mathbf{u}(t_{1:k})\big) \\ &\quad= \mathsf{q}\big(\mathbf{x}_u(t_k)|\mathbf{x}_u(t_{0:k-1})\,,\mathbf{z}(t_{1:k})\,,\mathbf{u}(t_{1:k})\big)\cdot\mathsf{q}\big(\mathbf{x}_u(t_{0:k-1})|\mathbf{z}(t_{1:k-1})\,,\mathbf{u}(t_{1:k-1})\big)\,,\end{aligned} \tag{B.3}$$

we can argument that we obtain the particle states $\mathbf{x}_u^{(j)}(t_{0:k}) \sim \mathsf{q}\big(\mathbf{x}_u(t_{0:k})|\mathbf{z}(t_{1:k})\,,\mathbf{u}(t_{1:k})\big)$ from the existing particle states $\mathbf{x}_u^{(j)}(t_{0:k-1}) \sim \mathsf{q}\big(\mathbf{x}_u(t_{0:k-1})|\mathbf{z}(t_{1:k-1})\,,\mathbf{u}(t_{1:k-1})\big)$ with the new particle states $\mathbf{x}_u^{(j)}(t_k) \sim \mathsf{q}\big(\mathbf{x}_u(t_k)|\mathbf{x}_u(t_{0:k-1})\,,\mathbf{z}(t_{1:k})\,,\mathbf{u}(t_{1:k})\big)$.

In order to calculate the weight update equation (B.2), we factorize $\mathsf{p}\big(\mathbf{x}_u(t_{0:k})|\mathbf{z}(t_{1:k})\,\mathbf{u}(t_{1:k})\big)$ with

$$\begin{aligned}
&\mathsf{p}\big(\mathbf{x}_u(t_{0:k})|\mathbf{z}(t_{1:k})\,\mathbf{u}(t_{1:k})\big) \qquad\qquad (B.4)\\
&= \frac{\mathsf{p}\big(\mathbf{z}(t_k)|\mathbf{x}_u(t_{0:k})\,,\mathbf{z}(t_{1:k-1})\,,\mathbf{u}(t_{1:k})\big)\cdot\mathsf{p}\big(\mathbf{x}_u(t_{0:k})|\mathbf{z}(t_{1:k-1})\,,\mathbf{u}(t_{1:k})\big)}{\mathsf{p}\big(\mathbf{z}(t_k)|\mathbf{z}(t_{1:k-1})\big)}\\
&= \frac{\mathsf{p}\big(\mathbf{z}(t_k)|\mathbf{x}_u(t_{0:k})\,,\mathbf{z}(t_{1:k-1})\,,\mathbf{u}(t_{1:k})\big)\cdot\mathsf{p}\big(\mathbf{x}_u(t_k)|\mathbf{x}_u(t_{0:k-1})\,,\mathbf{z}(t_{1:k-1})\,,\mathbf{u}(t_{1:k})\big)}{\mathsf{p}\big(\mathbf{z}(t_k)|\mathbf{z}(t_{1:k-1})\big)}\\
&\quad\times\mathsf{p}\big(\mathbf{x}_u(t_{0:k-1})|\mathbf{z}(t_{1:k-1})\,,\mathbf{u}(t_{1:k})\big)\\
&= \frac{\mathsf{p}\big(\mathbf{z}(t_k)|\mathbf{x}_u(t_{0:k})\,,\mathbf{z}(t_{k-1})\big)\cdot\mathsf{p}\big(\mathbf{x}_u(t_k)|\mathbf{x}_u(t_{k-1})\,,\mathbf{u}(t_k)\big)}{\mathsf{p}\big(\mathbf{z}(t_k)|\mathbf{z}(t_{1:k-1})\big)}\\
&\quad\times\mathsf{p}\big(\mathbf{x}_u(t_{0:k-1})|\mathbf{z}(t_{1:k-1})\,,\mathbf{u}(t_{1:k-1})\big)\\
&\propto \mathsf{p}\big(\mathbf{z}(t_k)|\mathbf{x}_u(t_{0:k})\,,\mathbf{z}(t_{k-1})\big)\cdot\mathsf{p}\big(\mathbf{x}_u(t_k)|\mathbf{x}_u(t_{k-1})\,,\mathbf{u}(t_k)\big)\\
&\quad\times\mathsf{p}\big(\mathbf{x}_u(t_{0:k-1})|\mathbf{z}(t_{1:k-1})\,,\mathbf{u}(t_{1:k-1})\big)\,.
\end{aligned}$$

Please note, $\mathsf{p}\big(\mathbf{z}(t_k)|\mathbf{x}_u(t_{0:k})\,,\mathbf{z}(t_{k-1})\big)=\mathsf{p}\big(\mathbf{z}(t_k)|\mathbf{x}_u(t_{0:k})\big)$, however, because of the calculations in Section 4.2.2, we are not doing this simplification here. With (B.3) and (B.4), the weight update equation of (B.2) is

$$\begin{aligned}
w^{(j)}(t_k) &\propto \frac{\mathsf{p}\big(\mathbf{z}(t_k)|\mathbf{x}_u^{(j)}(t_{0:k})\,,\mathbf{z}(t_{k-1})\big)\cdot\mathsf{p}\big(\mathbf{x}_u^{(j)}(t_k)|\mathbf{x}_u^{(j)}(t_{k-1})\,,\mathbf{u}(t_k)\big)}{\mathsf{q}\big(\mathbf{x}_u^{(j)}(t_k)|\mathbf{x}_u^{(j)}(t_{0:k-1})\,,\mathbf{z}(t_{1:k})\,,\mathbf{u}(t_{1:k})\big)} \qquad (B.5)\\
&\quad\times\frac{\mathsf{p}\big(\mathbf{x}_u^{(j)}(t_{0:k-1})|\mathbf{z}(t_{1:k-1})\,,\mathbf{u}(t_{1:k-1})\big)}{\mathsf{q}\big(\mathbf{x}_u^{(j)}(t_{0:k-1})|\mathbf{z}(t_{1:k-1})\,,\mathbf{u}(t_{1:k-1})\big)}\\
&= w^{(j)}(t_{k-1})\frac{\mathsf{p}\big(\mathbf{z}(t_k)|\mathbf{x}_u^{(j)}(t_{0:k})\,,\mathbf{z}(t_{k-1})\big)\cdot\mathsf{p}\big(\mathbf{x}_u^{(j)}(t_k)|\mathbf{x}_u^{(j)}(t_{k-1})\,,\mathbf{u}(t_k)\big)}{\mathsf{q}\big(\mathbf{x}_u^{(j)}(t_k)|\mathbf{x}_u^{(j)}(t_{0:k-1})\,,\mathbf{z}(t_{1:k})\,,\mathbf{u}(t_{1:k})\big)}\,.
\end{aligned}$$

Since, we are only interested in a filtered estimate $\mathsf{p}\big(\mathbf{x}_u(t_k)|\mathbf{z}(t_{1:k})\,,\mathbf{u}(t_{1:k})\big)$, we obtain for $\mathsf{q}\big(\mathbf{x}_u^{(j)}(t_k)|\mathbf{x}_u^{(j)}(t_{0:k-1})\,,\mathbf{z}(t_{1:k})\,,\mathbf{u}(t_{1:k})\big)\triangleq\mathsf{q}\big(\mathbf{x}_u^{(j)}(t_k)|\mathbf{x}_u^{(j)}(t_{k-1})\,,\mathbf{z}(t_k)\,,\mathbf{u}(t_k)\big)$ where the importance density becomes only dependent on $\mathbf{x}_u^{(j)}(t_{k-1})$, $\mathbf{z}(t_k)$ and $\mathbf{u}(t_k)$. Therefore, from (B.5) we obtain

$$w^{(j)}(t_k)\propto w^{(j)}(t_{k-1})\frac{\mathsf{p}\big(\mathbf{z}(t_k)|\mathbf{x}_u^{(j)}(t_k)\,,\mathbf{z}(t_{k-1})\big)\cdot\mathsf{p}\big(\mathbf{x}_u^{(j)}(t_k)|\mathbf{x}_u^{(j)}(t_{k-1})\,,\mathbf{u}(t_k)\big)}{\mathsf{q}\big(\mathbf{x}_u^{(j)}(t_k)|\mathbf{x}_u^{(j)}(t_{k-1})\,,\mathbf{z}(t_k)\,,\mathbf{u}(t_k)\big)}\,, \qquad (B.6)$$

where the posterior filtered density is approximated as stated in (4.19).

List of Abbreviations

AoA	angle of arrival	6
b-frame	body frame	107
CDF	cumulative distribution function	26
CIR	channel impulse response	2
DBN	dynamic Bayesian network	19
DMC	dense multipath component	98
EKF	extended Kalman filter	6
EM	expectation maximization	14
GLoS	geometrical line-of-sight	2
GNSS	global navigation satellite system	1
HMM	hidden Markov model	19
i-frame	inertial frame	108
IMU	inertial measurement unit	6
KEST	Kalman enhanced super resolution tracking	6
KF	Kalman filter	6
log-domain	logarithmic domain	23
log-weight	log-domain weight	30
LoS	line-of-sight	1
LS	least square	18
MAP	maximum a posteriori	21
MEMS	micro-electro-mechanical system	107
ML	maximum likelihood	14
MMSE	minimum mean square error	21

MPC	multipath component	2
MUSIC	multiple signal classification	14
n-frame	navigation frame	107
NLoS	non-line-of-sight	1
OFDM	orthogonal frequency-division multiplexing	79
PCRLB	posterior Cramér-Rao lower bound	7
PDF	probability density function	20
PF	particle filter	6
PSD	power spectral density	13
RBPF	Rao-Blackwellized particle filter	6
RFID	radio frequency identification	1
RMSE	root mean square error	70
RSS	received signal strength	2
SAGE	space-alternating generalized expectation-maximization	14
SIR	sequential importance resampling	23
SIS	sequential importance sampling	23
SISO	single-input single-output	79
SLAM	simultaneous localization and mapping	3
SNR	signal-to-noise-ratio	63
sub-PF	subordinate particle filter	46
super-PF	superordinate particle filter	46
TOA	time of arrival	1
TS	track-section	96
UWB	ultra-wideband	1
VT	virtual transmitter	3
WLAN	wireless local area network	1

Notation and List of Symbols

Notation

Throughout the thesis, the following notation is used:

- $(\cdot)^T$ and $(\cdot)^H$ stand for matrix (or vector) transpose and conjugate transpose, respectively.
- All vectors are interpreted as column vectors.
- Matrices are denoted by bold capital letters and vectors by bold small letters.
- $[\mathbf{A}]_{l,m}$ represents the element in row l and column m of matrix $\mathbf{A}$ and $[\mathbf{x}]_l$ denotes the l-th element of vector $\mathbf{x}$.
- $\|\mathbf{A}\|^2 = \sum_l \sum_m |\,[\mathbf{A}]_{l,m}\,|^2$ represents the square of the Frobenius norm of $\mathbf{A}$.
- $\mathrm{diag}[\mathbf{A}_1, \ldots, \mathbf{A}_k]$ denotes the diagonal block matrix with the diagonal matrices $\mathbf{A}_1, \ldots, \mathbf{A}_k$ and $\mathrm{diag}[a_1, \ldots, a_k]$ denotes the diagonal matrix with the diagonal elements $a_1, \ldots, a_k$.
- $a \sim \mathcal{N}(a; \mu_a, \sigma_a^2)$ denotes a Gaussian distributed random variable a with mean μ_a and variance σ_a^2.
- $\mathcal{U}[0, N]$ denotes the uniform distribution on the interval $[0, N]$.
- $\mathbf{E}[x]$ stands for expectation or sample mean of x and $\mathbf{E}_a[x]$ stands for expectation of x with respect to $\mathsf{p}(a)$.
- $\mathscr{F}_{t_k}\{\cdot\}$ stands for the discrete-time Fourier transform with respect to t_k and $\mathscr{F}_f^{-1}\{\cdot\}$ stands for the inverse discrete-time Fourier transform with respect to f.
- $1 : k$ stands for all integer numbers starting from 1 to k, thus $1, 2, \ldots, k$.
- $\Re\{x\}$ denotes the real part of x.

- ∇_a stands for the first-order partial derivatives with respect to a and Δ_a^b stands for the second-order partial derivatives with $\Delta_a^b \triangleq \nabla_a \nabla_b^T$.
- $\hat{x}$ denotes the estimation of x.
- $\propto$ stands for proportional.
- $\{x^{(i)}\}_{i=1}^N$ defines the set for $x^{(i)}$ with $i = 1, \ldots, N$.

List of Latin Symbols

$d_{\mathrm{SR}}(t_k)$	Distance between the scatterer S and the reflection point	41
$d_{\mathrm{SU}}(t_k)$	Distance between the scatterer S and the receiver	39
$d_{\mathrm{S_iU}}(t_k)$	Distance between the scatterer S_i and the receiver	40
$d_{\mathrm{TR}}(t_k)$	Distance between the physical transmitter and the reflection point	37
$d_{\mathrm{TS}}(t_k)$	Distance between the physical transmitter and the scatterer S	39
$d_{\mathrm{TS_i}}(t_k)$	Distance between the physical transmitter and the scatterer S_i	40
$d_{\mathrm{VT},i}(t_k)$	Additional propagation length of the i-th VT	41
$\tilde{\mathbf{d}}_{\mathrm{VT},i,l}(t_k)$	Distance between the i-th VT and the l-th antenna element	61
$d^{(j,a)}_{\mathrm{VT},i}(t_k)$	Additional propagation length of the i-th VT of j-th super- and a-th sub-particle	53
$\mathbf{F}(t_k)$	Transition matrix	22
$\mathbf{f}(\cdot,\cdot)$	System model	20
f_c	Carrier frequency	61
$\mathbf{H}(t_k)$	Measurement matrix	22
$\mathbf{h}(\cdot,\cdot)$	Measurement model	20
$h(t_k,\tau)$	Time variant CIR	10
$H_h(t_k,f)$	Time variant channel transfer function	11
$\mathbf{I}$	Identity matrix	60
$\mathbf{J}(t_k)$	Posterior information matrix	59
$\mathrm{Jacob}(\cdot)$	Function of the Jacobian algorithm	32
K	Constant value for initialization of the particles	53
$\mathbf{K}(t_k)$	Gain matrix	22
$\mathrm{K}(t_k)$	Kernel function	28
$\mathbf{m}(t_k)$	Sample mean vector	22
$\mathbf{m}$	Map which comprises a set of objects	34
$m(t_k)$	Moving indicator	44
$N(t_k)$	Number of MPCs	11
$n(\tau_m)$	White circular symmetric normal distributed receiver noise	12
N_{eff}	Effective sample size	25
$\mathbf{n}_h(t_k)$	Measurement noise	20
N_p	Number of particles	24
$N_{P,j,i}(t_k)$	Number of particles of the sub-PF of j-th super-particle and i-th MPC	46
N_s	Number of particles of the super-PF	46
$N_{\mathrm{t}}(t_k)$	Total number of particles	53
$\mathbf{n}_t(t_k)$	Transition noise	20
N_{thr}	Resampling threshold	26

$\mathbf{n}_u(t_k)$	Transition noise of the receiver states	50
$\mathbf{P}(t_k)$	Covariance matrix	22
$\mathbf{Q}(t_k)$	Covariance matrix of the process noise	22
$\mathbf{Q}_u(t_k)$	Covariance matrix for the transition of the receiver states	51
$\mathbf{R}(t_k)$	Covariance matrix of the measurement noise	22
$\mathbf{R}_{n\to b}(t_k)$	Rotation matrix	108
$r_{u,x}(t_k)$	x-coordinate of the receiver position	50
$r_{u,y}(t_k)$	y-coordinate of the receiver position	50
$\mathbf{r}_{\mathrm{VT},i}^{(j,a)}(t_k)$	State vector of the i-th VT position of j-th super- and a-th sub-particle	53
$\boldsymbol{r}_u^{(j)}(t_k)$	Receiver position state vector of j-th super-particle	46
$\boldsymbol{r}_r(t_k)$	Position of the reflection point	37
$\boldsymbol{r}_{r,i}(t_k)$	Position of the i-th reflection point	38
$\boldsymbol{r}_s$	Position of the scatterer	37
$\boldsymbol{r}_{s,i}$	Position of the i-th scatterer	40
$\boldsymbol{r}_t$	Position of the physical transmitter	37
$\boldsymbol{r}_{t,i}$	Position of the i-th physical transmitter	16
$\boldsymbol{r}_u(t_k)$	Receiver position state vector	16
$\boldsymbol{r}_{\mathrm{VT},i}$	i-th VT position	37
S_i	i-th Scatterer	40
S	Scatterer	37
$S(\nu_k, \tau)$	Doppler variant CIR	11
$t_{a,i}(t_k)$	TOA of the signal originated at the i-th transmitter	16
t_k	Discrete time step	10
$t_{t,i}(t_k)$	Transmit time of the signal originated at the i-th transmitter	16
t_δ	Time between two adjacent time instants $t_k - t_{k-1}$	50
$\mathbf{u}(t_k)$	Control input vector	35
VT_i	i-th VT	37
$v_{u,x}(t_k)$	x-coordinate of the receiver velocity	50
$v_{u,y}(t_k)$	y-coordinate of the receiver velocity	50
$\boldsymbol{v}_u^{(j)}(t_k)$	Receiver velocity state vector of j-th super-particle	46
$\boldsymbol{v}_u(t_k)$	Receiver velocity state vector	42
$W(t_k)$	Normalization factor of the weights	30
$\hat{W}(t_k)$	Normalization factor of the weights in log-domain	30
$w^{(j)}(t_k)$	Weight of the j-th (super-) particle	24
$\hat{w}^{(j)}(t_k)$	Weight of the j-th (super-) particle in log-domain	30
$\tilde{w}^{(j)}(t_k)$	Resampled weight of the j-th (super-) particle	26

List of Greek Symbols

List of Author's Publications

First Author

C. Gentner, M. Ulmschneider, and T. Jost. Cooperative Simultaneous Localization and Mapping for Pedestrians using Low-Cost Ultra-Wideband System and Gyroscope. In *Proc. IEEE/ION PLANS*, Monterey, CA, USA, April 2018

C. Gentner, S. Zhang, and T. Jost. Log-PF: Particle Filtering in Logarithm Domain. *Journal of Electrical and Computer Engineering*, 2018, January 2018

C. Gentner, R. Pöhlmann, M. Ulmschneider, T. Jost, and S. Zhang. Positioning using Terrestrial Multipath Signals and Inertial Sensors. *Mobile Information Systems*, September 2017

C. Gentner and M. Ulmschneider. Simultaneous Localization and Mapping for Pedestrians using Low-Cost Ultra-Wideband System and Gyroscope. In *Proc. IEEE Int. Conf. on Indoor Positioning and Indoor Navigation*, Saporo, Japan, September 2017

C. Gentner, R. Pöhlmann, M. Ulmschneider, T. Jost, and A. Dammann. Simultaneous Localization and Mapping using Terrestrial Multipath Signals, GNSS and Inertial Sensors. In *Proc. Int. Technical Meeting of the Satellite Division of the Institute of Navigation*, Portland, OR, USA, September 2017

C. Gentner, T. Jost, W. Wang, S. Zhang, A. Dammann, and U.-C. Fiebig. Multipath Assisted Positioning with Simultaneous Localization and Mapping. *IEEE Trans. Wireless Commun.*, 15(9):6104–6117, September 2016

C. Gentner, B. Ma, R. Pöhlmann, M. Ulmschneider, T. Jost, and A. Dammann. Simultaneous Localization and Mapping in Multipath Environments: Mapping and Reusing of Virtual Transmitters. In *Proc. Int. Technical Meeting of the Satellite Division of the Institute of Navigation*, Portland, OR, USA, September 2016

C. Gentner, B. Ma, M. Ulmschneider, T. Jost, and A. Dammann. Simultaneous Localization and Mapping in Multipath Environments. In *Proc. IEEE/ION PLANS*, Savanah, GO, USA, April 2016

C. Gentner, R. Pöhlmann, M. Ulmschneider, T. Jost, and A. Dammann. Multipath Assisted Positioning for Pedestrians. In *Proc. Int. Technical Meeting of the Satellite Division of the Institute of Navigation*, Tampa, FL, USA, September 2015

C. Gentner, R. Pöhlmann, T. Jost, and A. Dammann. Multipath Assisted Positioning using a Single Antenna with Angle of Arrival Estimations. In *Proc. Int. Technical Meeting of the Satellite Division of the Institute of Navigation*, Tampa, FL, USA, September 2014

C. Gentner, T. Jost, and A. Dammann. Accurate Indoor Positioning using Multipath Components. In *Proc. Int. Technical Meeting of the Satellite Division of the Institute of Navigation*, Nashville, TN, USA, September 2013

C. Gentner and T. Jost. Indoor Positioning using Time Difference of Arrival between Multipath Components. In *Proc. IEEE Int. Conf. on Indoor Positioning and Indoor Navigation*, Montbeliard, France, October 2013

C. Gentner, J.-M. Rawadi, E. Muñoz Diaz, and M. Khider. Hybrid Positioning with 3GPP-LTE and GPS employing Particle Filters. In *Proc. Int. Technical Meeting of the Satellite Division of the Institute of Navigation*, September 2012

C. Gentner, S. Sand, and A. Dammann. OFDM Indoor Positioning Based on TDOAs: Performance Analysis and Experimental Results. In *Int. Conf. on Localization and GNSS (ICL-GNSS)*, Starnberg, Germany, June 2012

C. Gentner, E. Muñoz Diaz, M. Khider, E. Staudinger, S. Sand, and A. Dammann. Particle Filter Based Positioning with 3GPP-LTE in Indoor Environments. In *Proc. IEEE/ION PLANS*, April 2012

C. Gentner, I. Groh, and S. Sand. False Alarm and Detection Probability for NLOS Detection in LTE Environments. In *Proc. of* 8^{th} *Int. Workshop on Multi-Carrier Systems & Solutions (MC-SS 2011), Herrsching, Germany*, May 2011

C. Gentner and I. Groh. Analytical Derivation of the False Alarm and Detection Probability for NLOS Detection. In *Proc. IEEE Vehicular Technology Conf. Spring*, April 2011

C. Gentner, I. Groh, and S. Sand. Analytical derivation of the False Alarm Probability and Detection Probability for GNSS NLOS Detection using a Dual Frequency Receiver. In *Proc. Int. Technical Meeting of The Institute of Navigation*, San Diego, CA, USA, January 2011

C. Gentner and S. Sand. NLOS Detection and Mitigation based on Confidence Metric and EKF. In *Proc. Int. Technical Meeting of The Institute of Navigation*, San Diego, CA, USA, January 2011

Co-Author

M. Arias, T. Jost, B. Gonzalez-Valdes, W. Wang, S. Zhang, M. Ulmschneider, and C. Gentner. Statistical Analysis of the Radiation Pattern of an Antenna Mounted on an Aircraft. In *Proc. IEEE European Conf. on Antennas and Propagation*, April 2016

A. Dammann, E. Staudinger, S. Sand, and C. Gentner. Joint GNSS and 3GPP-LTE Based Positioning in Outdoor-to-Indoor Environments - Performance Evaluation and Verification. In *Proc. Int. Technical Meeting of the Satellite Division of the Institute of Navigation*, September 2011

I. Groh, C. Gentner, and S. Sand. Iterative Intercarrier Interference Mitigation for Pilot-Aided OFDM Channel Estimation Based on Channel Linearizations. In *Proc. IEEE Vehicular Technology Conf. Fall*, September 2012

I. Groh, C. Gentner, and J. Selva. Analytical Computation of Mean Time to Lose Lock for Langevin Delay-Locked Loops. *IEEE Trans. on Communications*, 60(11):3491–3498, November 2012

I. Groh, C. Gentner, and J. Selva. A Novel Tracking Jitter Computation Method for Delay-Locked Loops in Spread-Spectrum Systems. *Trans. on Emerging Telecommunications Technologies*, 23(8):715–727, December 2012

I. Groh, A. Dammann, and C. Gentner. Efficient Intercarrier Interference Mitigation for Pilot-Aided Channel Estimation in OFDM Mobile Systems. In *Proc. IEEE Vehicular Technology Conf. Spring*, April 2011

S. Plass, R. Poehlmann, A. Dammann, and C. Gentner. Investigations on AIS Signal Reception on Aircraft at Higher Altitudes. In *Proc. IEEE OCEANS Conf.*, Taipei, April 2014

E. Staudinger and C. Gentner. TDoA Subsample Delay Estimator with Multiple Access Interference Mitigation and Carrier Frequency Offset Compensation for OFDM based Systems. In *Proc. IEEE Workshop Positioning Navigation and Communication*, pages 33 – 38, Dresden, Germany, April 2011

M. Ulmschneider, D. C. Luz, and C. Gentner. Exchanging Transmitter Maps in Multipath Assisted Positioning. In *Proc. IEEE/ION PLANS*, Monterey, CA, USA, April 2018

M. Ulmschneider, C. Gentner, T. Jost, and A. Dammann. Rao-Blackwellized Gaussian Sum Particle Filtering for Multipath Assisted Positioning. *Journal of Electrical and Computer Engineering*, February 2018

M. Ulmschneider, C. Gentner, T. Jost, and A. Dammann. Association of Transmitters in Multipath-Assisted Positioning. In *Proc. IEEE Global Telecommunications Conf.*, Singapore, Singapore, December 2017

M. Ulmschneider, C. Gentner, R. Raulefs, and M. Walter. Multipath Assisted Positioning in Vehicular Applications. In *Proc. IEEE Workshop Positioning Navigation and Communication*, October 2016

M. Ulmschneider, C. Gentner, R. Faragher, and T. Jost. Gaussian Mixture Filter for Multipath Assisted Positioning. In *Proc. Int. Technical Meeting of the Satellite Division of the Institute of Navigation*, Portland, OR, USA, September 2016

M. Ulmschneider and C. Gentner. Multipath Assisted Positioning for Pedestrians using LTE Signals. In *Proc. IEEE/ION PLANS*, Savanah, GO, USA, April 2016

M. Ulmschneider, C. Gentner, S. Ache, and A. Roessler. Multipath Assisted Positioning with Band-Limited Signals in an Urban Environment. In *Proc. Int. Technical Meeting of the Satellite Division of the Institute of Navigation*, Tampa, FL, USA, September 2015

W. Wang, T. Jost, C. Gentner, S. Zhang, and A. Dammann. A Semi-Blind Tracking Algorithm for Joint Communication and Ranging with OFDM Signals. *IEEE Trans. Veh. Technol.*, 65(7):5237–5250, July 2016

W. Wang, R. Raulefs, T. Jost, A. Dammann, C. Gentner, and S. Zhang. Ship-to-Land Broadband Channel Measurement Campaign at 5.2 GHz. In *Proc. of the MTS/IEEE OCEANS 2014*, St.John's, Canada, September 2014

W. Wang, R. Raulefs, T. Jost, A. Dammann, C. Gentner, and S. Zhang. Ship-to-Land Broadband Channel Measurement Campaign at 5.2 GHz. In *Proc. of the Int. Symposium Inf. on Ships*, Hamburg, Germany, September 2014

W. Wang, T. Jost, U.-C. Fiebig, and C. Gentner. Modeling Three Different Types of Multipath Components for Mobile Radio Channel. In *Proc. IEEE European Conf. on Antennas and Propagation*, The Hague, Netherlands, 2014

W. Wang, T. Jost, C. Gentner, A. Dammann, and U.-C. Fiebig. Outdoor-to-Indoor Channels at 2.45 GHz and 5.2 GHz for Geolocation Applications. In *Proc. IEEE European Conf. on Antennas and Propagation*, Rome, Italy, April 2011

A. Zeh, C. Gentner, and D. Augot. An Interpolation Procedure for List Decoding Reed Solomon Codes based on Generalized Key Equations. *IEEE Trans. Inf. Theory*, 57(9):5946 –5959, September 2011

A. Zeh, C. Gentner, and M. Bossert. Efficient List-Decoding of Reed-Solomon Codes with the Fundamental Iterative Algorithm. In *2009 Inf. Theory Workshop, Taormina*, Taormina, Sicily, Italy, 2009

S. Zhang, E. Staudinger, W. Wang, C. Gentner, A. Dammann, and E. Sandgren. DiPLoc: Direct Signal Domain Particle Filtering for Network Localization. In *Proc. Int. Technical Meeting of the Satellite Division of the Institute of Navigation*, Tampa, Florida, USA, September 2015

References

[AGO+12] D. Anguita, A. Ghio, L. Oneto, X. Parra, and J. L. Reyes-Ortiz. Human Activity Recognition on Smartphones using a Multiclass Hardware-Friendly Support Vector Machine. In *Proc. Int. Workshop on Ambient Assisted Living*, pages 216–223. Springer, 2012.

[AJG+16] M. Arias, T. Jost, B. Gonzalez-Valdes, W. Wang, S. Zhang, M. Ulmschneider, and C. Gentner. Statistical Analysis of the Radiation Pattern of an Antenna Mounted on an Aircraft. In *Proc. IEEE European Conf. on Antennas and Propagation*, April 2016.

[AMGC02] M. Arulampalam, S. Maskell, N. Gordon, and T. Clapp. A Tutorial on Particle Filters for Online Nonlinear/Non-Gaussian Bayesian Tracking. *IEEE Trans. Signal Process.*, 50(2):174–188, February 2002.

[ANU08] F. Antreich, J. Nossek, and W. Utschick. Maximum Likelihood Delay Estimation in a Navigation Receiver for Aeronautical Applications. *Aerospace Science and Technology*, 12(3):256–267, April 2008.

[AR12] M. Angermann and P. Robertson. FootSLAM: Pedestrian Simultaneous Localization and Mapping Without Exteroceptive Sensors - Hitchhiking on Human Perception and Cognition. *Proc. of the IEEE*, 100(Special Centennial Issue):1840–1848, May 2012.

[BD06] T. Bailey and H. Durrant-Whyte. Simultaneous Localization and Mapping (SLAM): Part II. *IEEE Robot. Autom. Mag.*, 13(3):108–117, 2006.

[Bel63] P. Bello. Characterization of Randomly Time-Variant Linear Channels. 11(4):360–393, December 1963.

[BH13] A. Brajdic and R. Harle. Walk Detection and Step Counting on Unconstrained Smartphones. In *Proc. of the 2013 ACM Int. Joint Conf. on Pervasive and Ubiquitous Computing*, UbiComp '13, pages 225–234, New York, NY, USA, 2013. ACM.

[BP00] P. Bahl and V. N. Padmanabhan. RADAR: an In-Building RF-Based User Location and Tracking System. In *Proc. IEEE Conf. on Comp. Commun. (INFOCOM)*, volume 2, pages 775–784 vol.2, 2000.

[BR11] L. Bruno and P. Robertson. WiSLAM: Improving FootSLAM with WiFi. In *Proc. IEEE Int. Conf. on Indoor Positioning and Indoor Navigation*, pages 1–10, 2011.

[BS87] P. Beckmann and A. Spizzichino. *The Scattering of Electromagnetic Waves from Rough Surfaces*. Artech House, 1987.

[BSLK04] Y. Bar-Shalom, X. R. Li, and T. Kirubarajan. *Estimation with Applications to Tracking and Navigation: Theory Algorithms and Software*. John Wiley & Sons, 2004.

[BVD16] S. Banville and F. Van Diggelen. Innovation: Precise Positioning using Raw GPS Measurements from Android Smartphones. *GPS World*, November 2016.

[CCF99] J. Carpenter, P. Clifford, and P. Fearnhead. Improved Particle Filter for Nonlinear Problems. *IEE Proc. Radar, Sonar and Navigation*, 146(1):2–7, 1999.

[CFPFR09] P. Closas, C. Fernández-Prades, and J. A. Fernández-Rubio. A Bayesian Approach to Multipath Mitigation in GNSS Receivers. *IEEE J. Sel. Areas Sig. Proc.*, 3(4):695–706, August 2009.

[Che03] Z. Chen. Bayesian Filtering: From Kalman Filters to Particle Filters, and Beyond. Technical report, McMaster University, 2003.

[CR96] G. Casella and C. P. Robert. Rao-Blackwellisation of Sampling Schemes. *Biometrika*, 83(1):81–94, 1996.

[Cra46] H. Cramér. A Contribution to the Theory of Statistical Estimation. *Scandinavian Actuarial Journal*, 1946(1):85–94, 1946.

[Cra16] H. Cramér. *Mathematical Methods of Statistics*, volume 9. Princeton university press, 2016.

[CS98] J. Caffery and G. L. Stuber. Subscriber Location in CDMA Cellular Networks. *IEEE Trans. Veh. Technol.*, 47(2):406–416, May 1998.

[CSMC04] K. W. Cheung, H. C. So, W. K. Ma, and Y. T. Chan. Least Squares Algorithms for Time-of-Arrival-Based Mobile Location. *IEEE Trans. Signal Process.*, 52(4):1121–1130, April 2004.

[DB06] H. Durrant-Whyte and T. Bailey. Simultaneous Localization and Mapping: Part I. *IEEE Robot. Autom. Mag.*, 13(2):99–110, June 2006.

[DCD15] D. Dardari, P. Closas, and P. M. Djuric. Indoor Tracking: Theory, Methods, and Technologies. *IEEE Trans. Veh. Technol.*, 64(4):1263–1278, April 2015.

[DFMR00] A. Doucet, N. d. Freitas, K. P. Murphy, and S. J. Russell. Rao-Blackwellised Particle Filtering for Dynamic Bayesian Networks. In *Proc. Conf. Uncertainty in Artificial Intelligence*, pages 176–183, 2000.

[DGK01] A. Doucet, N. J. Gordon, and V. Krishnamurthy. Particle Filters for State Estimation of Jump Markov Linear Systems. *IEEE Trans. Signal Process.*, 49(3):613–624, Mar 2001.

[DLR77] A. P. Dempster, N. M. Laird, and D. B. Rubin. Maximum Likelihood from Incomplete Data via the EM Algorithm. *J. Royal Statist. Soc.*, 39(1):1–38, 1977.

[DNC+01] M. G. Dissanayake, P. Newman, S. Clark, H. F. Durrant-Whyte, and M. Csorba. A Solution to the Simultaneous Localization and Map Building (SLAM) Problem. *IEEE Trans. Robot. Autom.*, 17(3):229–241, 2001.

[DPW+13] I. Dokmanic, R. Parhizkar, A. Walther, Y. M. Lu, and M. Vetterli. Acoustic Echoes Reveal Room Shape. *Proc. Natl. Acad. Sci. USA*, 110(30):12186–12191, 2013.

[DRMS07] A. J. Davison, I. D. Reid, N. D. Molton, and O. Stasse. MonoSLAM: Real-Time Single Camera SLAM. *IEEE Trans. Pattern Anal. Mach. Intell.*, 29(6), June 2007.

[DSSG11] A. Dammann, E. Staudinger, S. Sand, and C. Gentner. Joint GNSS and 3GPP-LTE Based Positioning in Outdoor-to-Indoor Environments - Performance Evaluation and Verification. In *Proc. Int. Technical*

Meeting of the Satellite Division of the Institute of Navigation, September 2011.

[DT09] T. Deissler and J. Thielecke. Feature based Indoor Mapping using a Bat-Type UWB Radar. In *Proc. IEEE Int. Conf. Ultra-Wideband*, pages 475–479, September 2009.

[DT10] T. Deissler and J. Thielecke. UWB SLAM with Rao-Blackwellized Monte Carlo Data Association. In *Proc. IEEE Int. Conf. on Indoor Positioning and Indoor Navigation*, pages 1–5, September 2010.

[EPG94] J. Erfanian, S. Pasupathy, and P. Gulak. Reduced Complexity Symbol Detectors with Parallel Structure for ISI Channels. *IEEE Trans. Commun.*, 42(234):1661–1671, February 1994.

[FFL07] B. Ferris, D. Fox, and N. D. Lawrence. WiFi-SLAM using Gaussian Process Latent Variable Models. In *Proc. Int. Joint Conf. on Artificial Intelligence (IJCAI)*, volume 7, pages 2480–2485, January 2007.

[FLMW13] M. Froehle, E. Leitinger, P. Meissner, and K. Witrisal. Cooperative Multipath-Assisted Indoor Navigation and Tracking (Co-MINT) using UWB Signals. In *Proc. IEEE Int. Conf. on Communications*, pages 16–21, June 2013.

[FNRA10] K. Frank, M. J. V. Nadales, P. Robertson, and M. Angermann. Reliable Real-Time Recognition of Motion Related Human Activities using MEMS Inertial Sensors. In *Proc. Int. Technical Meeting of the Satellite Division of the Institute of Navigation*, Portland, OR, USA, September 2010.

[FON08] W. T. Fong, S. K. Ong, and a. Y. C. Nee. Methods for In-Field User Calibration of an Inertial Measurement Unit Without External Equipment. *Measurement Science and Technology*, 19(8), 2008.

[FTH+99] B. H. Fleury, M. Tschudin, R. Heddergott, D. Dahlhaus, and K. I. Pedersen. Channel Parameter Estimation in Mobile Radio Environments using the SAGE Algorithm. *IEEE J. Sel. Areas Commun.*, 17(3):434–450, March 1999.

[GDG11] I. Groh, A. Dammann, and C. Gentner. Efficient Intercarrier Interference Mitigation for Pilot-Aided Channel Estimation in OFDM Mobile

Systems. In *Proc. IEEE Vehicular Technology Conf. Spring*, April 2011.

[Gez08] S. Gezici. A Survey on Wireless Position Estimation. *Wireless Personal Communications*, 44(3):263–282, October 2008.

[GG05] F. Gustafsson and F. Gunnarsson. Mobile Positioning using Wireless Networks. *IEEE Signal Process. Mag.*, 22(4):41–53, July 2005.

[GG11] C. Gentner and I. Groh. Analytical Derivation of the False Alarm and Detection Probability for NLOS Detection. In *Proc. IEEE Vehicular Technology Conf. Spring*, April 2011.

[GGS11a] C. Gentner, I. Groh, and S. Sand. Analytical derivation of the False Alarm Probability and Detection Probability for GNSS NLOS Detection using a Dual Frequency Receiver. In *Proc. Int. Technical Meeting of The Institute of Navigation*, San Diego, CA, USA, January 2011.

[GGS11b] C. Gentner, I. Groh, and S. Sand. False Alarm and Detection Probability for NLOS Detection in LTE Environments. In *Proc. of* 8^{th} *Int. Workshop on Multi-Carrier Systems & Solutions (MC-SS 2011), Herrsching, Germany*, May 2011.

[GGS12a] I. Groh, C. Gentner, and S. Sand. Iterative Intercarrier Interference Mitigation for Pilot-Aided OFDM Channel Estimation Based on Channel Linearizations. In *Proc. IEEE Vehicular Technology Conf. Fall*, September 2012.

[GGS12b] I. Groh, C. Gentner, and J. Selva. A Novel Tracking Jitter Computation Method for Delay-Locked Loops in Spread-Spectrum Systems. *Trans. on Emerging Telecommunications Technologies*, 23(8):715–727, December 2012.

[GGS12c] I. Groh, C. Gentner, and J. Selva. Analytical Computation of Mean Time to Lose Lock for Langevin Delay-Locked Loops. *IEEE Trans. on Communications*, 60(11):3491–3498, November 2012.

[GJ13] C. Gentner and T. Jost. Indoor Positioning using Time Difference of Arrival between Multipath Components. In *Proc. IEEE Int. Conf. on Indoor Positioning and Indoor Navigation*, Montbeliard, France, October 2013.

[GJD13] C. Gentner, T. Jost, and A. Dammann. Accurate Indoor Positioning using Multipath Components. In *Proc. Int. Technical Meeting of the Satellite Division of the Institute of Navigation*, Nashville, TN, USA, September 2013.

[GJW+16] C. Gentner, T. Jost, W. Wang, S. Zhang, A. Dammann, and U.-C. Fiebig. Multipath Assisted Positioning with Simultaneous Localization and Mapping. *IEEE Trans. Wireless Commun.*, 15(9):6104–6117, September 2016.

[GLN09] Y. Gu, A. Lo, and I. Niemegeers. A Survey of Indoor Positioning Systems for Wireless Personal Networks. *IEEE Commun. Surveys Tuts.*, 11(1):13–32, 1st Quarter 2009.

[GMK+12] C. Gentner, E. Muñoz Diaz, M. Khider, E. Staudinger, S. Sand, and A. Dammann. Particle Filter Based Positioning with 3GPP-LTE in Indoor Environments. In *Proc. IEEE/ION PLANS*, April 2012.

[GMP+16] C. Gentner, B. Ma, R. Pöhlmann, M. Ulmschneider, T. Jost, and A. Dammann. Simultaneous Localization and Mapping in Multipath Environments: Mapping and Reusing of Virtual Transmitters. In *Proc. Int. Technical Meeting of the Satellite Division of the Institute of Navigation*, Portland, OR, USA, September 2016.

[GMU+16] C. Gentner, B. Ma, M. Ulmschneider, T. Jost, and A. Dammann. Simultaneous Localization and Mapping in Multipath Environments. In *Proc. IEEE/ION PLANS*, Savanah, GO, USA, April 2016.

[GPJD14] C. Gentner, R. Pöhlmann, T. Jost, and A. Dammann. Multipath Assisted Positioning using a Single Antenna with Angle of Arrival Estimations. In *Proc. Int. Technical Meeting of the Satellite Division of the Institute of Navigation*, Tampa, FL, USA, September 2014.

[GPU+15] C. Gentner, R. Pöhlmann, M. Ulmschneider, T. Jost, and A. Dammann. Multipath Assisted Positioning for Pedestrians. In *Proc. Int. Technical Meeting of the Satellite Division of the Institute of Navigation*, Tampa, FL, USA, September 2015.

[GPU+17a] C. Gentner, R. Pöhlmann, M. Ulmschneider, T. Jost, and A. Dammann. Simultaneous Localization and Mapping using Terrestrial Multipath Signals, GNSS and Inertial Sensors. In *Proc. Int.*

Technical Meeting of the Satellite Division of the Institute of Navigation, Portland, OR, USA, September 2017.

[GPU+17b] C. Gentner, R. Pöhlmann, M. Ulmschneider, T. Jost, and S. Zhang. Positioning using Terrestrial Multipath Signals and Inertial Sensors. *Mobile Information Systems*, September 2017.

[GRMK12] C. Gentner, J.-M. Rawadi, E. Muñoz Diaz, and M. Khider. Hybrid Positioning with 3GPP-LTE and GPS employing Particle Filters. In *Proc. Int. Technical Meeting of the Satellite Division of the Institute of Navigation*, September 2012.

[GS11] C. Gentner and S. Sand. NLOS Detection and Mitigation based on Confidence Metric and EKF. In *Proc. Int. Technical Meeting of The Institute of Navigation*, San Diego, CA, USA, January 2011.

[GSD12] C. Gentner, S. Sand, and A. Dammann. OFDM Indoor Positioning Based on TDOAs: Performance Analysis and Experimental Results. In *Int. Conf. on Localization and GNSS (ICL-GNSS)*, Starnberg, Germany, June 2012.

[GSS93] N. Gordon, D. Salmond, and A. F. M. Smith. Novel Approach to Nonlinear/Non-Gaussian Bayesian State Estimation. *IEE Proc. Radar Signal Processing*, 140(2):107–113, 1993.

[GU17] C. Gentner and M. Ulmschneider. Simultaneous Localization and Mapping for Pedestrians using Low-Cost Ultra-Wideband System and Gyroscope. In *Proc. IEEE Int. Conf. on Indoor Positioning and Indoor Navigation*, Saporo, Japan, September 2017.

[GUJ18] C. Gentner, M. Ulmschneider, and T. Jost. Cooperative Simultaneous Localization and Mapping for Pedestrians using Low-Cost Ultra-Wideband System and Gyroscope. In *Proc. IEEE/ION PLANS*, Monterey, CA, USA, April 2018.

[Gus10] F. Gustafsson. Particle Filter Theory and Practice with Positioning Applications. *IEEE Aerosp. Electron. Syst. Mag.*, 25(7):53–82, 2010.

[GZJ18] C. Gentner, S. Zhang, and T. Jost. Log-PF: Particle Filtering in Logarithm Domain. *Journal of Electrical and Computer Engineering*, 2018, January 2018.

[Har15] G. H. Hardy. *On the Expression of a Number as the Sum of Two Squares*. 1915.

[Har13] R. Harle. A Survey of Indoor Inertial Positioning Systems for Pedestrians. *IEEE Commun. Surveys Tutorials*, 15(3):1281–1293, 3rd Quarter 2013.

[Hen15] P. Henkel. Tightly Coupled Precise Point Positioning and Attitude Determination. *IEEE Trans. Aerosp. Electron. Syst.*, 51(4):3182 – 3197, 2015.

[HL98] R. Harré and L. v. Lagenhove. *Positioning Theory : Moral Contexts of Intentional Action* . Malden, Mass : Blackwell, 1998.

[HM95] D. Helbing and P. Molnar. Social Force Model for Pedestrian Dynamics. *Physical Review E*, 51(5):4282–4286, 1995.

[HN95] M. Haardt and J. A. Nossek. Unitary ESPRIT: How to Obtain increased Estimation Accuracy with a Reduced Computational Burden. *IEEE Trans. Signal Process.*, 43(5):1232–1242, May 1995.

[HRMT12] M. Hardegger, D. Roggen, S. Mazilu, and G. Tröster. ActionSLAM: Using Location-Related Actions as Landmarks in Pedestrian SLAM. In *Proc. IEEE Int. Conf. on Indoor Positioning and Indoor Navigation*, pages 1–10, November 2012.

[Jek01] C. Jekeli. *Inertial Navigation Systems with Geodetic Applications*. Walter de Gruyter, 2001.

[Jos13] T. Jost. *Satellite-to-Indoor Wave Propagation for Positioning Applications*. Phd thesis, Department of Signal Theory and Communications of the University of Vigo, 2013.

[JWFP12] T. Jost, W. Wang, U.-C. Fiebig, and F. Pérez-Fontán. Detection and Tracking of Mobile Propagation Channel Paths. *IEEE Trans. Antennas Propag.*, 60(10):4875–4883, October 2012.

[JWFPF12] T. Jost, W. Wang, U.-C. Fiebig, and F. Pérez-Fontán. A Satellite-to-Indoor Channel Model: Multipath Components. In *Proc. IEEE European Conf. on Antennas and Propagation*, Prague, Czech Rep., March 2012.

[Kal60] R. E. Kalman. A New Approach to Linear Filtering and Prediction Problems. *Trans. of the ASME–Journal of Basic Engineering*, 82(Series D):35–45, 1960.

[Kap05] E. Kaplan. *Understanding GPS - Principles and Applications*. Artech House, 2nd edition edition, December 2005.

[KAT13] Y. Kuang, K. Astrom, and F. Tufvesson. Single Antenna Anchor-Free UWB Positioning based on Multipath Propagation. In *Proc. IEEE Int. Conf. on Communications*, pages 5814–5818, June 2013.

[Kay93] S. M. Kay. *Fundamentals of Statistical Signal Processing, Volume I: Estimation Theory*. Prentice Hall PTR, March 1993.

[KB90] W. Koch and A. Baier. Optimum and Sub-Optimum Detection of Coded Data Disturbed by Time-Varying Intersymbol Interference. In *Proc. IEEE Global Telecommunications Conf.*, pages 1679–1684 vol.3, December 1990.

[KD15] S. Kaiser and E. M. Diaz. PocketSLAM Based on the Principle of the FootSLAM Algorithm. In *Proc. Int. Conf. on Localization and GNSS (ICL-GNSS)*, pages 1–5. IEEE, June 2015.

[KDV16] M. Krekovic, I. Dokmanic, and M. Vetterli. EchoSLAM: Simultaneous Localization and Mapping with Acoustic Echoes. In *41st IEEE International Conference on Acoustics, Speech and Signal Processing (ICASSP 2016)*, 2016.

[Khi13] M. Khider. *Multisensor-Based Positioning for Pedestrian Navigation*. Phd thesis, University of Ulm, 2013.

[Kit96] G. Kitagawa. Monte Carlo Filter and Smoother for Non-Gaussian Nonlinear State Space Models. *J. Comput. Graph. Statist.*, 5(1):1–25, 1996.

[KK04a] K. Kaemarungsi and P. Krishnamurthy. Modeling of Indoor PositioningSsystems Based on Location Fingerprinting. In *Proc. IEEE Conf. on Comp. Commun. (INFOCOM)*, volume 2, pages 1012–1022 vol.2, March 2004.

[KK04b] K. Kaemarungsi and P. Krishnamurthy. Properties of Indoor Received Signal Strength for WLAN Location Fingerprinting. In *Proc. Int.*

Conf. on Mobile and Ubiquitous Systems: Computing, Networking and Services, pages 14–23, August 2004.

[KKR12] M. Khider, S. Kaiser, and P. Robertson. A Novel 3-Dimensional Movement Model for Pedestrian Navigation. *RIN Journal of Navigation*, 65(2):245–264, March 2012.

[KRW10] B. Krach, P. Robertson, and R. Weigel. An Efficient Two-Fold marginalized Bayesian Filter for Multipath Estimation in Satellite Navigation Receivers. *EURASIP J. Adv. Sig. Proc.*, 2010, September 2010.

[KV96] H. Krim and M. Viberg. Two Decades of Array Signal Processing Research: the Parametric Approach. *IEEE Signal Process. Mag.*, 13(4):67–94, July 1996.

[KWC13] E. Kupershtein, M. Wax, and I. Cohen. Single-Site Emitter Localization via Multipath Fingerprinting. *IEEE Trans. Signal Process.*, 61(1):10–21, January 2013.

[KWM11] J. R. Kwapisz, G. M. Weiss, and S. A. Moore. Activity Recognition using Cell Phone Accelerometers. *ACM SigKDD Explorations Newsletter*, 12(2):74–82, 2011.

[LC98] J. S. Liu and R. Chen. Sequential Monte Carlo Methods for Dynamic Systems. *Journal of the American Statistical Association*, 93(443):1032–1044, 1998.

[LDBL07] H. Liu, H. Darabi, P. Banerjee, and J. Liu. Survey of Wireless Indoor Positioning Techniques and Systems. *IEEE Trans. Syst., Man, Cybern. C*, 37(6):1067–1080, November 2007.

[LDw91] J. Leonard and H. Durrant-whyte. Simultaneous Map Building and Localization For an Autonomous Mobile Robot. In *Proc. IEEE/RSJ Int. Workshop on Intelligent Robots and Systems*, Osaka , Japan, November 1991.

[Leh05] A. Lehner. *Multipath Channel Modelling for Satellite Navigation Systems.* PhD thesis, Friedrich-Alexander-Universität Erlangen-Nürnberg, 2005.

[LFS+12] J. Lien, U. J. Ferner, W. Srichavengsup, H. Wymeersch, and M. Z. Win. A Comparison of Parametric and Sample-Based Message Representation in Cooperative Localization. *Int. Journal of Navigation and Observation*, 2012.

[LHC13] Y. Luo, O. Hoeber, and Y. Chen. Enhancing WiFi Fingerprinting for Indoor Positioning using Human-Centric Collaborative Feedback. *Human-centric Computing and Inf. Sciences*, 3(1):2, 2013.

[Li211] Performance-Based Evaluation of RFID-based Indoor Location Sensing Solutions for the Built Environment. *Adv. Eng. Inf.*, 25(3):535 – 546, August 2011.

[LKK+11] S. Lee, B. Kim, H. Kim, R. Ha, and H. Cha. Inertial Sensor-Based Indoor Pedestrian Localization with Minimum 802.15. 4a Configuration. *IEEE Trans. Ind. Informat.*, 7(3):455–466, 2011.

[LMLW15] E. Leitinger, P. Meissner, M. Lafer, and K. Witrisal. Simultaneous Localization and Mapping using Multipath Channel Information. In *Proc. IEEE Int. Conf. on Communications*, pages 754–760, June 2015.

[LTDU11] V. La Tosa, B. Denis, and B. Uguen. Joint Anchor-Less Tracking and Room Dimensions Estimation through IR-UWB Peer-to-Peer Communications. In *Proc. IEEE Int. Conf. Ultra-Wideband*, pages 575–579, September 2011.

[Mau12] R. Mautz. Indoor Positioning Technologies. ETH Zurich, Department of Civil, Environmental and Geomatic Engineering, Institute of Geodesy and Photogrammetry, February 2012.

[MCC+06] A. Molisch, D. Cassioli, C.-C. Chong, S. Emami, A. Fort, B. Kannan, J. Karedal, J. Kunisch, H. Schantz, K. Siwiak, and M. Win. A Comprehensive Standardized Model for Ultrawideband Propagation Channels. *IEEE Trans. Antennas Propag.*, 54(11):3151–3166, November 2006.

[ME05] P. Misra and P. Enge. *Global Positioning System — Signals, Measurements and Performance*. Ganga-Jamuna Press, 2nd edition, 2005. ISBN 0-9709544-1-7.

[MEL17] L. Martino, V. Elvira, and F. Louzada. Effective Sample Size for Importance Sampling Based on Discrepancy Measures. *Signal Processing*, 131:386–401, 2017.

[Men13] C. Mensing. *Location Determination in OFDM Based Mobile Radio Systems*. Phd thesis, Technische Universität München, June 2013.

[MOLG01] C. Musso, N. Oudjane, and F. Le Gland. Improving Regularised Particle Filters. In *Sequential Monte Carlo methods in practice*, pages 247–271. Springer, 2001.

[MPS14] L. Mainetti, L. Patrono, and I. Sergi. A Survey on Indoor Positioning Systems. In *Int. Conf. on Software, Telecommun. and Computer Networks (SoftCOM)*, pages 111–120, September 2014.

[MTK+02] M. Montemerlo, S. Thrun, D. Koller, B. Wegbreit, et al. FastSLAM: A Factored Solution to the Simultaneous Localization and Mapping Problem. In *Proc. AAAI Nat. Conf. on Artificial Intelligence*, pages 593–598, Edmonton, Canada, 2002.

[MWK14] P. Meissner, K. Witrisal, and K.Witrisal. UWB for Robust Indoor Tracking: Weighting of Multipath Components for Efficient Estimation. *IEEE Wireless Communications Letters*, 3(5):501–504, October 2014.

[NK11] K. A. Nuaimi and H. Kamel. A Survey of Indoor Positioning Systems and Algorithms. In *Int. Conf. on Innovations in Inf. Technol.*, pages 185–190, April 2011.

[Par00] J. Parsons. *The Mobile Radio Propagation Channel*. Wiley; 2 edition, 2000.

[PBRJ14] M. Puyol, D. Bobkov, P. Robertson, and T. Jost. Pedestrian Simultaneous Localization and Mapping in Multistory Buildings Using Inertial Sensors. *Intelligent Transportation Systems, IEEE Trans. on*, 15(4):1714–1727, Aug 2014.

[Ped13] M. Pedley. Tilt Sensing using a Three-Axis Accelerometer. Technical report, Freescale semiconductor, 2013.

[Plu13] M. D. Plumbley. Hearing the Shape of a Room. *Proc. Natl. Acad. Sci. USA*, 110(30):12162–12163, 2013.

[PPDG14] S. Plass, R. Poehlmann, A. Dammann, and C. Gentner. Investigations on AIS Signal Reception on Aircraft at Higher Altitudes. In *Proc. IEEE OCEANS Conf.*, Taipei, April 2014.

[PS96] B. W. Parkinson and J. J. Spilker Jr. *Global Positioning System: Theory and Applications, Vol. 1.* American Institute of Aeronautics and Astronautics Inc., 1996.

[Puy17] M. J. G. Puyol. Crowdsourcing Motion Maps based on FootSLAM for Reliable Indoor Pedestrian Navigation in Multistory Environments. 2017.

[RABC09] T. Robin, G. Antonini, M. Bierlaire, and J. Cruz. Specification, Estimation and Validation of a Pedestrian Walking Behavior Model. *Transportation Research Part B: Methodological*, 43(1):36–56, 2009.

[RAG04] B. Ristic, S. Arulampalam, and N. Gordon. *Beyond the Kalman Filter: Particle Filters for Tracking Applications.* Artech House, 2004.

[RAK09] P. Robertson, M. Angermann, and B. Krach. Simultaneous Localization and Mapping for Pedestrians using only Foot-Mounted Inertial Sensors. In *In Proc. UbiComp 2009, ACM*, pages 93–96, 2009.

[Rao45] C. R. Rao. Information and Accuracy Attainable in the Estimation of Statistical Parameters. *Bull. Calcutta Math. Soc*, 37(3):81–91, 1945.

[Rap96] T. S. Rappaport. *Wireless Communications - Principles and Practice.* Prentice Hall, 1996.

[Ric] A. Richter. *Estimation of Radio Channel Parameters: Models and Algorithms.* PhD thesis, Technischen Universität Ilmenau.

[RK89] R. Roy and T. Kailath. ESPRIT-Estimation of Signal Parameters via Rotational Invariance Techniques. *IEEE Trans. Acoust., Speech, Signal Process.*, 37(7):984–995, July 1989.

[RM00] C. Randell and H. Muller. Context Awareness by Analysing Accelerometer Data. In *Proc. The Fourth Int. Symp. on Wearable Computers*, pages 175–176. IEEE, 2000.

[RSZ94] C. R. Rao, C. R. Sastry, and B. Zhou. Tracking the Direction of Arrival of Multiple Moving Targets. *IEEE Trans. Signal Process.*, 42(5):1133–1144, May 1994.

[RVH95] P. Robertson, E. Villebrun, and P. Hoeher. A Comparison of Optimal and Sub-Optimal MAP decoding Algorithms Operating in the Log

Domain. In *Proc. IEEE Int. Conf. on Communications*, volume 2, pages 1009–1013, June 1995.

[SC86] R. Smith and P. Cheeseman. On the Representation and Estimation of Spatial Uncertainty. *Int. J. Robotics Research*, 5(4):56–68, 1986.

[SCGL05] G. Sun, J. Chen, W. Guo, and K. J. R. Liu. Signal Processing Techniques in Network-Aided Positioning: a Survey of State-of-the-Art Positioning Designs. *IEEE Signal Process. Mag.*, 22(4):12–23, July 2005.

[Sch86] R. Schmidt. Multiple Emitter Location and Signal Parameter Estimation. *IEEE Trans. Antennas Propag.*, 34(3):276–280, March 1986.

[SCZ+13] G. Shen, Z. Chen, P. Zhang, T. Moscibroda, and Y. Zhang. Walkie-Markie: Indoor Pathway Mapping Made Easy. In *Proc. 10th USENIX Conf. on Networked Systems Design and Implementation*, pages 85–98. USENIX Association, April 2013.

[SG11] E. Staudinger and C. Gentner. TDoA Subsample Delay Estimator with Multiple Access Interference Mitigation and Carrier Frequency Offset Compensation for OFDM based Systems. In *Proc. IEEE Workshop Positioning Navigation and Communication*, pages 33 – 38, Dresden, Germany, April 2011.

[SGGO05] A. Saxena, G. Gupta, V. Gerasimov, and S. Ourselin. In use Parameter Estimation of Inertial Sensors by Detecting Multilevel Quasi-Static States. *Knowledge-Based Intelligent Information and Engineering Systems*, 3684:595–601, 2005.

[SGLSJBLR12] G. Seco-Granados, J. López-Salcedo, D. Jiménez-Baños, and G. López-Risueño. Challenges in Indoor Global Navigation Satellite Systems. *IEEE Signal Process. Mag.*, 29(2):108–131, March 2012.

[Shu06] D. Shutin. *Multipath Tracking and Prediction for Multiple-input Multiple-output Wireless Channels*. PhD thesis, Graz University of Technology, 2006.

[SRK09] J. Salmi, A. Richter, and V. Koivunen. Detection and Tracking of MIMO Propagation Path Parameters using State-Space Approach. *IEEE Trans. Signal Process.*, 57(4):1538–1550, April 2009.

[SS04] P. Stoica and Y. Selen. Model-Order Selection: a Review of Inf. Criterion Rules. *IEEE Signal Process. Mag.*, 21(4):36–47, July 2004.

[SS16] B. Siebler and S. Sand. Posterior Cramér-Rao Bounds and Suboptimal Filtering for IMU/GNSS based Cooperative Train Localization. In *Proc. IEEE/ION PLANS*, pages 353–358, April 2016.

[SSC86] R. Smith, M. Self, and P. Cheeseman. Estimating Uncertain Spatial Relationships in Robotics. In *Proc. Second Annual Conf. on Uncertainty in Artificial Intelligence*, University of Pennsylvania, Philadelphia, USA, 1986.

[SSM62] G. L. Smith, S. F. Schmidt, and L. A. McGee. *Application of Statistical Filter Theory to the Optimal Estimation of Position and Velocity on Board a Circumlunar Vehicle.* National Aeronautics and Space Administration, 1962.

[STK05] A. H. Sayed, A. Tarighat, and N. Khajehnouri. Network-Based Wireless Location: Challenges Faced in Developing Techniques for Accurate Wireless Location Information. *IEEE Signal Process. Mag.*, 22:24–40, July 2005.

[SW08] Y. Shen and M. Z. Win. Effect of Path-Overlap on Localization Accuracy in Dense Multipath Environments. In *Proc. IEEE Int. Conf. on Communications*, pages 4197–4202. IEEE, 2008.

[SW09] Y. Shen and M. Win. On the Use of Multipath Geometry for Wideband Cooperative Localization. In *Proc. IEEE Global Telecommunications Conf.*, pages 1–6, December 2009.

[SW10a] Y. Shen and M. Win. Fundamental Limits of Wideband Localization: Part I: A General Framework. *IEEE Trans. Inf. Theory*, 56(10):4956–4980, 2010.

[SW10b] C. Steiner and A. Wittneben. Low Complexity Location Fingerprinting With Generalized UWB Energy Detection Receivers. *IEEE Trans. Signal Process.*, 58(3):1756–1767, March 2010.

[SWW10] Y. Shen, H. Wymeersch, and M. Win. Fundamental Limits of Wideband Localization: Part II: Cooperative Networks. *IEEE Trans. Inf. Theory*, 56(10):4981–5000, 2010.

[SZT08] G. Shen, R. Zetik, and R. S. Thoma. Performance Comparison of TOA and TDOA based Location Estimation Algorithms in LOS Environment. In *Proc. IEEE Workshop Positioning Navigation and Communication*, pages 71–78, March 2008.

[TBF00] S. Thrun, W. Burgard, and D. Fox. A Real-Time Algorithm for Mobile Robot Mapping with Applications to Multi-Robot and 3D Mapping. In *Proc. IEEE Int. Conf. on Robotics and Automation (ICRA)*, volume 1, pages 321–328. IEEE, 2000.

[TFvDN95] B. R. Townsend, P. C. Fenton, A. J. van Dierendonck, and D. J. R. V. Nee. Performance Evaluation of the Multipath Estimating Delay Lock Loop. *Journal of the Institute of Navigation*, 42(3):503–514, Fall 1995.

[TLRT05] R. S. Thomä, M. Landmann, A. Richter, and U. Trautwein. *Smart Antennas - State of the Art*, pages 241–270. EURASIP Book Series on SP&C. Hindawi Publishing Corporation, 2005.

[TM06] S. Thrun and M. Montemerlo. The Graph SLAM Algorithm with Applications to Large-Scale Mapping of Urban Structures. *The Int. Journal of Robotics Research*, 25(5-6):403–429, 2006.

[TMN98] P. Tichavsky, C. Muravchik, and A. Nehorai. Posterior Cramér-Rao Bounds for Discrete-Time Nonlinear Filtering. *IEEE Trans. Signal Process.*, 46(5):1386–1396, May 1998.

[TSRF06] M. Triki, D. Slock, V. Rigal, and P. Francois. Mobile Terminal Positioning via Power Delay Profile Fingerprinting: Reproducible Validation Simulations. In *Proc. IEEE Vehicular Technology Conf. Fall*, pages 1–5, September 2006.

[Tur72] G. L. Turin. A Statistical Model of Urban Multipath Propagation. *IEEE Trans. Veh. Technol.*, 21(1):1–9, February 1972.

[UG16] M. Ulmschneider and C. Gentner. Multipath Assisted Positioning for Pedestrians using LTE Signals. In *Proc. IEEE/ION PLANS*, Savanah, GO, USA, April 2016.

[UGAR15] M. Ulmschneider, C. Gentner, S. Ache, and A. Roessler. Multipath Assisted Positioning with Band-Limited Signals in an Urban Environment. In *Proc. Int. Technical Meeting of the Satellite Division of the Institute of Navigation*, Tampa, FL, USA, September 2015.

[UGFJ16] M. Ulmschneider, C. Gentner, R. Faragher, and T. Jost. Gaussian Mixture Filter for Multipath Assisted Positioning. In *Proc. Int. Technical Meeting of the Satellite Division of the Institute of Navigation*, Portland, OR, USA, September 2016.

[UGJD17] M. Ulmschneider, C. Gentner, T. Jost, and A. Dammann. Association of Transmitters in Multipath-Assisted Positioning. In *Proc. IEEE Global Telecommunications Conf.*, Singapore, Singapore, December 2017.

[UGJD18] M. Ulmschneider, C. Gentner, T. Jost, and A. Dammann. Rao-Blackwellized Gaussian Sum Particle Filtering for Multipath Assisted Positioning. *Journal of Electrical and Computer Engineering*, February 2018.

[UGRW16] M. Ulmschneider, C. Gentner, R. Raulefs, and M. Walter. Multipath Assisted Positioning in Vehicular Applications. In *Proc. IEEE Workshop Positioning Navigation and Communication*, October 2016.

[ULG18] M. Ulmschneider, D. C. Luz, and C. Gentner. Exchanging Transmitter Maps in Multipath Assisted Positioning. In *Proc. IEEE/ION PLANS*, Monterey, CA, USA, April 2018.

[VTB07] H. L. Van Trees and K. L. Bell. *Bayesian Bounds for Parameter Estimation and Nonlinear Filtering/Tracking*, volume 10. Wiley-IEEE Press, August 2007.

[Wan15] W. Wang. *Channel Measurement and Modeling for Mobile Radio Based Positioning*. PhD thesis, 2015.

[WB95] G. Welch and G. Bishop. *An Introduction to the Kalman Filter*. Chapel Hill, 1995.

[WJ12a] W. Wang and T. Jost. A Low-Cost Platform for Time-Variant Wireless Channel Measurements with Application to Positioning. *IEEE Trans. Instrum. Meas.*, 61(6):1597–1604, June 2012.

[WJ12b] W. Wang and T. Jost. A Low-Cost Platform for Time-Variant Wireless Channel Measurements with Application to Positioning. *IEEE Trans. Instrum. Meas.*, 61(6):1597–1604, June 2012.

[WJD10] W. Wang, T. Jost, and A. Dammann. Estimation and Modelling of NLoS Time-Variant Multipath for Localization Channel Model in Mobile Radios. In *Proc. IEEE Global Telecommunications Conf.*, pages 1–6, December 2010.

[WJFG14] W. Wang, T. Jost, U.-C. Fiebig, and C. Gentner. Modeling Three Different Types of Multipath Components for Mobile Radio Channel. In *Proc. IEEE European Conf. on Antennas and Propagation*, The Hague, Netherlands, 2014.

[WJG+11] W. Wang, T. Jost, C. Gentner, A. Dammann, and U.-C. Fiebig. Outdoor-to-Indoor Channels at 2.45 GHz and 5.2 GHz for Geolocation Applications. In *Proc. IEEE European Conf. on Antennas and Propagation*, Rome, Italy, April 2011.

[WJG+16] W. Wang, T. Jost, C. Gentner, S. Zhang, and A. Dammann. A Semi-Blind Tracking Algorithm for Joint Communication and Ranging with OFDM Signals. *IEEE Trans. Veh. Technol.*, 65(7):5237–5250, July 2016.

[WJMD09] W. Wang, T. Jost, C. Mensing, and A. Dammann. ToA and TDoA Error Models for NLoS Propagation Based on Outdoor to Indoor Channel Measurement. In *Proc. IEEE Wireless Commun. and Netw. Conf. (WCNC)*, pages 1–6, April 2009.

[WM12] K. Witrisal and P. Meissner. Performance Bounds for Multipath-Assisted Indoor Navigation and Tracking (MINT). In *Proc. IEEE Int. Conf. on Communications*, pages 4321–4325, June 2012.

[Woo07] O. J. Woodman. An Introduction to Inertial Navigation. Technical Report UCAM-CL-TR-696, University of Cambridge, Computer Laboratory, August 2007.

[WRJ+14a] W. Wang, R. Raulefs, T. Jost, A. Dammann, C. Gentner, and S. Zhang. Ship-to-Land Broadband Channel Measurement Campaign at 5.2 GHz. In *Proc. of the MTS/IEEE OCEANS 2014*, St.John's, Canada, September 2014.

[WRJ+14b] W. Wang, R. Raulefs, T. Jost, A. Dammann, C. Gentner, and S. Zhang. Ship-to-Land Broadband Channel Measurement Campaign at 5.2 GHz. In *Proc. of the Int. Symposium Inf. on Ships*, Hamburg, Germany, September 2014.

[WS02] M. Win and R. Scholtz. Characterization of Ultra-Wide Bandwidth Wireless Indoor Channels: a Communication-Theoretic View. *IEEE J. Sel. Areas Commun.*, 20(9):1613–1627, December 2002.

[WVDM00] E. A. Wan and R. Van Der Merwe. The Unscented Kalman Filter for Nonlinear Estimation. In *Proc. IEEE Symp. Adaptive Syst. Signal Process., Commun. Contr*, pages 153–158. IEEE, 2000.

[XRK94] G. Xu, R. H. Roy, and T. Kailath. Detection of Number of Sources via Exploitation of Centro-Symmetry Property. *IEEE Trans. Signal Process.*, 42(1):102–112, January 1994.

[YFL+03] L. Yang, W. Fang, J. Li, R. Huang, and W. Fan. Cellular Automata Pedestrian Movement Model Considering Human Behavior. *Chinese Science Bulletin*, 48(16):1695, 2003.

[ZGA11] A. Zeh, C. Gentner, and D. Augot. An Interpolation Procedure for List Decoding Reed Solomon Codes based on Generalized Key Equations. *IEEE Trans. Inf. Theory*, 57(9):5946 –5959, September 2011.

[ZGB09] A. Zeh, C. Gentner, and M. Bossert. Efficient List-Decoding of Reed-Solomon Codes with the Fundamental Iterative Algorithm. In *2009 Inf. Theory Workshop, Taormina*, Taormina, Sicily, Italy, 2009.

[Zha02] Y. Zhao. Standardization of Mobile Phone Positioning for 3G Systems. *IEEE Commun. Mag.*, 40(7):108–116, July 2002.

[ZRDS13] S. Zhang, R. Raulefs, A. Dammann, and S. Sand. System-Level Performance Analysis for Bayesian Cooperative Positioning: From Global to Local. In *Proc. IEEE Int. Conf. on Indoor Positioning and Indoor Navigation*, Montbéliard - Belfort, France, October 2013.

[ZSW+15] S. Zhang, E. Staudinger, W. Wang, C. Gentner, A. Dammann, and E. Sandgren. DiPLoc: Direct Signal Domain Particle Filtering for Network Localization. In *Proc. Int. Technical Meeting of the Satellite Division of the Institute of Navigation*, Tampa, Florida, USA, September 2015.

Please note, parts of this thesis have appeared in [GZJ18,GPU+17b,GPU+17a,GJW+16, GMP+16, GMU+16, GPU+15, GPJD14, GJD13, GJ13].